NASA Technical Memorandum 100913

Experimental Study of Bypass Transition in a Boundary Layer

Kenneth L. Suder and James E. O'Brien
Lewis Research Center
Cleveland, Ohio

and

Eli Reshotko
Case Western Reserve University
Cleveland, Ohio

May 1988

NASA

EXPERIMENTAL STUDY OF BYPASS TRANSITION IN A BOUNDARY LAYER

Kenneth L. Suder and James E. O'Brien
National Aeronautics and Space Administration
Lewis Research Center
Cleveland, Ohio 44135

and

Eli Reshotko
Case Western Reserve University
Dept. of Mechanical and Aerospace Engineering
Cleveland, Ohio 44106

SUMMARY

A detailed investigation to compare the boundary layer transition process in a low intensity disturbance environment to that in an environment in which the disturbances are initially non–linear in amplitude has been conducted using a flat plate model. Test section freestream turbulence values were varied from 0.3% to approximately 5% using rectangular–bar grids. The longitudinal integral length scale, intensity, and frequency spectra were acquired to characterize the freestream turbulence. For each level of freestream turbulence, boundary layer surveys of the mean longitudinal velocity and rms of the velocity fluctuations were obtained at several streamwise locations with a linearized hot–wire constant temperature anemometer system. From these surveys the resulting boundary layer shape factor, inferred skin friction coefficients, and distribution of the velocity fluctuations through the boundary layer were used to identify the transition region corresponding to each level of freestream turbulence. Both the initially linear and initially non–linear transition cases were identified. Hereafter, the transition process initiated by the linear growth of Tollmien

Schlichting (T–S) waves will be referred to as the T–S path to transition; whereas, the transition process initiated by finite non–linear disturbances will be referred to as the bypass transition process. The transition mechanism based on linear growth of T–S waves was associated with a freestream turbulence level of 0.3%; however, for a freestream turbulence intensity of 0.65% and higher, the bypass transition mechanism prevailed. The following detailed measurements were acquired to study and compare the two transition mechanisms: 1) simultaneous time traces of a flush–mounted hot film and a hot wire for the hot wire located at different depths within the boundary layer, 2) crosscorrelations betweeen flush–mounted hot films, 3) two–point correlations between a flush–mounted hot film and a hot wire positioned at various locations throughout the flowfield, and 4) boundary layer spectra at various streamwise distances through the transition region.

The results of these measurements indicate that there exists a critical value for the peak rms of the velocity fluctuations within the boundary layer of approximately 3 to 3.5% of the freestream velocity. Once the unsteadiness within the boundary layer reached this critical value, turbulent bursting initiated, regardless of the transition mechanism. The two point correlations and simultaneous time traces within the transition region illustrate the features of a turbulent burst and its effect on the surrounding flowfield.

TABLE OF CONTENTS

NOMENCLATURE

A	Calibration constant.
B	Calibration constant.
b	Bar width of the turbulence–generating grids.
C_f	Skin friction coefficient.
CCF_n	Normalized cross–correlation coefficient.
c	Wave propagation speed.
E	Bridge output voltage.
E_l	Linearizer output voltage.
f	Frequency (Hz).
$f'(\eta)$	Blasius similarity variable ($f'(\eta) = u/U_e$).
H	Boundary layer shape factor.
I	Intermittency factor.
K	Calibration constant.
L	Longitudinal integral length scale of the freestream turbulence.
n	Exponent.
R	Correlation coefficient.
$\mathbb{R}_x$	Reynolds number based on x–distance.
$\mathbb{R}_\theta$	Reynolds number based on momentum thickness.
$\mathbb{R}_{\delta^*}$	Reynolds number based on displacement thickness.

T	Overall time.
T_e	Integral time scale associated with the freestream turbulence.
Tu	Freestream turbulence.
t	Instantaneous time.
U	Mean velocity in the streamwise direction.
U_τ	Friction velocity.
u	Local velocity in the streamwise direction.
$u'(f)$	Power spectral density (V^2 / Hz).
u^+	Streamwise mean velocity in wall units ($u^+ = u / U_\tau$).
V	Volts.
x	Streamwise distance or direction referenced to the leading edge of the flat–plate test surface.
y	Vertical distance or direction from the flat–plate test surface.
y^+	Normalized y distance in wall units ($y^+ = y\ U_\tau / \nu$).
z	Spanwise distance or direction referenced from the centerline of the wind tunnel test section.

Greek

β	Normalized frequency ($\beta = 2\pi f$).
δ_{99}	Boundary layer thickness.
δ^*	Boundary layer displacement thickness.
η	Blasius similarity variable ($\eta = y\ [U_e/(2\nu x)]^{1/2}$).
θ	Boundary layer momentum thickness.
λ	Wavelength.
μ	Viscosity of the fluid (air).

ν	Kinematic viscosity of the fluid (air).
ρ	Density of the fluid (air).
τ	Time delay.
τ_w	Wall shear stress.
φ	Power spectral density, $\varphi = \varphi(\omega)$.
ω	Frequency (radians/second).

Subscripts

e	Referring to the value at the edge of the boundary layer.
x	Referring to the x direction, x component, or based on x distance.
∞	Referring to the value in the freestream.

Superscripts

$\overline{\quad}$	Time averaged quantity.
'	Fluctuating quantity.

CHAPTER I

INTRODUCTION

In a quiescent flow environment the initial instabilities in a laminar boundary layer are two–dimensional waves, known as Tollmien–Schlichting (T–S) waves [1,2], which are amplified with streamwise distance and eventually breakdown into bursts of turbulence which leads to the development of a turbulent boundary layer [1,3]. Linear stability theory [4,5] has been shown to predict the initial stages of this type of boundary layer transition at low freestream disturbance levels [6]. Unfortunately, at higher freestream disturbance levels the boundary layer transition process is not very well understood. In the presence of high freestream disturbance levels, Morkovin [7] introduces the term bypass transition to describe the transition process in which the traditional linear stability considerations are bypassed and finite non–linear instabilities occur. The bypass mechanism permits the formation of turbulent spots without Tollmien–Schlichting wave amplification. The intent of this investigation is to examine the features associated with the bypass transition process and to compare the bypass transition process to the transition process in which the initial instabilities are T–S waves. Hereafter, these two mechanisms will be referred to as the bypass path and the T–S path to boundary layer transition.

Some effects which are known to influence boundary layer transition

are freestream turbulence, acoustic disturbances, surface vibration, surface roughness, pressure gradient, and streamwise curvature. Several investigators [8,9,10,11] have tried to isolate the effects of freestream turbulence and pressure gradient on boundary layer transition. Each of these studies concentrated on the macroscopic parameters such as the location of the start and end of the transition region, and the distribution of the skin friction coefficient and heat transfer rates within the transition region. In the present study much effort has been taken to look at the details of the boundary layer transition by acquiring experimental data to describe the mean and disturbance freestream and boundary layer flowfields prior to and during the transition process.

Boundary layer transition results from the buildup of disturbances in the boundary layer. Therefore, in order to understand the transition process, one must understand how the disturbances are generated and amplified in the boundary layer. Dyban, Epik, and Suprun [12] have investigated the structure of laminar boundary layers under high freestream turbulence levels ranging from 0.3 to 25%. They found a peak in oscillation magnitude within the boundary layer, believed to be caused by the penetration of the freestream turbulence. They referred to these laminar boundary layers which were buffeted by the freestream turbulence as pseudo–laminar boundary layers. Their results indicated that the depth of penetration of the external disturbances into the boundary layer did not depend on the freestream turbulence and increased slightly with Reynolds number. Unfortunately, the results of this investigation by Dyban, Epik, and Suprun were limited to the distribution of disturbances within laminar

boundary layers. Elder [13] conducted a study to determine the conditions required to initiate a turbulent spot within a laminar boundary layer. Elder concluded that regardless of how disturbances are generated in a laminar boundary layer, breakdown to turbulence occurs by the initiation of a turbulent spot when the velocity fluctuations within the boundary layer exceeds about 2% of the freestream velocity over most of the boundary layer. More recent investigations to examine the details of the boundary layer transition process include the work of Paik and Reshotko [14] and Sohn and Reshotko [15]. Unfortunately, in these experiments the data was limited to centerline measurements in facilities of limited capability. In the present investigation the boundary layer development is described for six levels of freestream turbulence intensity ranging from 0.3% to 6%. In addition, the facility used in this research program provided the flexibility for off–centerline measurements and the acquisition of two–point correlations which were obtained to examine the features of the boundary layer flow in all three dimensions.

The present experiment focuses on the effect of the freestream turbulence intensity on the transition region of a smooth flat plate at zero pressure gradient and ambient test conditions. The goals of this investigation are not only to document the effects on the macroscopic features such as skin friction coefficient and boundary layer thicknesses within the transition region, but also to obtain detailed measurements within the transitioning region which will provide a better understanding of the mechanisms associated with the transition process. This research program is aimed at identifying the fundamental similarities and differences

between the T–S transition process and the bypass transition process. In addition, this information will provide a useful database which can be used to develop models and verify computational prediction schemes.

The experiments were conducted in a closed–circuit wind tunnel located at the NASA Lewis Research Center. The test surface is a smooth flat plate subjected to zero pressure gradient at ambient test conditions. Care was taken to establish spanwise uniformity over the flat plate and to insure that the boundary layer developed from the leading edge of the flat plate. Test section freestream turbulence levels were varied from 0.3% to 6% using grids. The freestream turbulence was characterized by its intensity, integral length scale, and frequency spectra. Measurements of the mean longitudinal velocity and longitudinal velocity fluctuations through the boundary layer were used to determine the transition region for each level of freestream turbulence. Once the transition region was identified for each freestream turbulence level detailed measurements within the transitioning boundary layer were acquired to establish a better understanding of the transition process. Such detailed measurements included the boundary layer spectra and two–point correlations to assess the features within the transitioning boundary layer.

CHAPTER II

RESEARCH EQUIPMENT

2.1 Facility

The data presented in this investigation were obtained in the NASA Lewis Research Center's boundary layer research facility which was designed to study the transition of a boundary layer from laminar to turbulent flow. The facility is a closed–loop wind tunnel which provides control over the velocity, pressure gradient, turbulence level, and temperature within the test section. The major components of the wind tunnel as depicted in Fig. 1 are: 1) blower, 2) flow conditioner, 3) contraction nozzle, 4) boundary layer bleed line, 5) test section, 6) diffuser, 7) air heater, 8) air filter, and 9) air cooler. The blower is a 24 1/2 inch diameter centrifugal fan with a capacity of 10 000 CFM driven by a 20 HP motor and is manufactured by the Chicago Blower Corporation (SISW Class III SQA Fan serial number 120041). A vortex valve located at the blower inlet is used to adjust the test section velocities from 20 ft/s to 120 ft/s. Upon exiting the blower, air enters the flow conditioning chamber (plenum chamber) which straightens the flow irregularities exiting the centrifugal blower and reduces the freestream turbulence level. Downstream of the plenum chamber a 2–D nozzle (no convergence in the transverse direction) with a 3.6 : 1 contraction ratio accelerates the flow to produce the required test section

Reynolds numbers. Prior to entering the test section, the boundary layer and corner vortices which developed in the contraction nozzle are drawn through a bleed line by an auxiliary suction blower and returned to the main wind tunnel circuit at the inlet of the main blower. The test section flow exits into a diffuser where the air velocity is reduced prior to entering the return duct. The return duct consisting of the air heater, filter,and cooler completes the wind tunnel circuit. More details of specific tunnel components will be discussed in the following paragraphs.

2.1.1 Flow Conditioning / Plenum Chamber

The flow conditioning chamber consists of the following: 1)perforated part span baffles which reduce the flow irregularities exiting the centrifugal blower, 2) a series of honeycombs and arrays of soda straws to straighten the large–scale flow swirls, and 3) a series of fine–mesh screens to reduce the tunnel freestream turbulence level. The flow uniformity at the exit of the flow–conditioning section was measured to be within $\pm$ 2 percent of the mean through–flow velocity. Also, the flow conditioning resulted in a freestream turbulence intensity of approximately 0.3 percent in the test section at a freestream velocity of 100 ft/s. In order to achieve higher freestream turbulence levels, space was allocated at the exit plane of the flow–conditioning chamber for insertion of rectangular–bar turbulence–generating grids.

2.1.2 Turbulence–Generating Grids

To change the freestream turbulence levels within the test section,

various turbulence–generating grids may be inserted at the exit plane of the flow–conditioning chamber (Fig. 1). The turbulence grids are located upstream of the contraction nozzle so that the resulting turbulence would be more homogeneous and have a lower decay rate along the test section length. The turbulence–generating grids consist of rectangular–bar arrays with approximately 60 percent open area. Four grids were designed to produce test section turbulence levels ranging from approximately 1 to 6 percent. An additional grid configuration in which a 20–mesh screen was placed directly in front of grid #1 was also used to generate freestream turbulence within the test section. Hereafter, this grid configuration will be referred to as the grid 0.5 configuration. Dimensions of the four rectangular bar grids are given in Fig. 2.

2.1.3 Test Section

The test section of the wind tunnel is rectangular in shape and measures 6 inches in height, 27 inches in width, and 60 inches in length. The test section was designed to be removable such that a different test surface (i.e. heated surface, cooled surface, roughened surface, etc.) could be employed to study the boundary layer transition process. The floor and sidewalls are constructed of plexiglass, whereas the top wall consists of a stainless–steel frame holding three successive interchangeable panels – two of plexiglass and the third comprising the probe traversing mechanism. The top wall of the test section is hinged at the test section inlet plane and can be pivoted to obtain either a favorable or adverse pressure gradient within the test section. The floor of the test section serves as the flat–plate test

surface. At the entrance to the test section, a series of two upstream–facing scoops are employed to bleed the boundary layer which develops in the contraction nozzle. A schematic depicting the details of this double–scoop configuration is presented in Fig. 3. The larger upstream scoop entraps the boundary layer and corner vortices generated in the contraction nozzle. The smaller downstream scoop is smoothly attached to the test surface and serves as the leading edge of the flat plate. The leading edge of the small scoop is a 4 x 1 ellipse to prevent a local separation bubble and possible tripping of the boundary layer. Both scoops discharge into the boundary layer bleed duct within which a slide valve is used to control the volume of flow through the scoops. Within each scoop a perforated plate is inserted to distribute the flow through the scoop uniformly in the spanwise direction. These perforated plates are also used to control the relative distribution of flow through each of the two scoops. Rows of static taps in the spanwise direction along the top and bottom of each of the scoops provide guidance in establishing the suction rate and spanwise uniformity at the leading edge of the flat plate.

2.1.4 Probe Traversing Mechanism

The probe traversing mechanism permitted precise probe positioning in the vertical, streamwise, and spanwise directions – relative to the flat plate test surface. An L.C. Smith actuator driven by a stepping motor enabled vertical positioning within increments of 0.001 inches. The probe and actuator assembly was mounted to a screw–driven X–Z table which provided streamwise and spanwise probe positioning within increments of

0.01 inches. In order to provide maximum flexibility in positioning the probe throughout the test section with minimal flow disturbance, an epicyclic device was used which allowed probe positioning anywhere within a 19 inch diameter circle. A brief description of this device follows. The probe is inserted in the test section through a hole in a small circular plate which is eccentrically mounted within a larger circular plate (See Fig. 4). Both circular plates are supported by ball bearings and are free to rotate in either direction, independently; thereby, permitting linear positioning of the probe via an X–Z drive mechanism. These two circular plates are located within a rectangular section which comprises one of the three panels making–up the top wall of the test section. Also, these three panels are interchangeable, such that the section containing the traverse mechanism can be positioned at different streamwise distances from the leading edge of the flat plate. However, this probe positioning system was limited in that there were certain areas of the test section where the probe could not be positioned. The most noteworthy limitations were: 1) the probe could not be positioned within the first 5 inches from the leading edge of the flat plate, and 2) due to interference with the X–Z drive mechanism the probe positioning was limited to 17 inches in the streamwise direction. In summary, the probe could be positioned anywhere within a 17 inch diameter circle and the circle center could be located at distinct streamwise positions; thereby, permitting probing throughout the test section with only one probe insertion hole in the top wall of the test section.

2.1.5 Test Configuration

For the present investigation the facility's aforementioned

control devices were configured to provide the following: 1) freestream velocity of approximately 100 ft/s (see Tables I – VI), 2) zero pressure gradient along the flat wall test surface, 3) ambient temperature within the test section which was held constant for a given test run — i.e., $\pm$ 2 ^{0}F fluctuation over an 8 hour test period, and 4) freestream turbulence levels ranging from 0.3 to 6 percent within the test section. Also, the roof panel containing the probe traversing mechanism was centered along the test section centerline and at the streamwise distances of 13 and 37 inches from the leading edge of the flat plate test surface.

2.2 **Instrumentation**

2.2.1 Wind Tunnel Instrumentation

The wind tunnel circuit is equipped with many pressure and temperature sensors which are used to monitor the tunnel operation conditions. Figs. 5 and 6, respectively, illustrate the location of the thermocouples and pressure sensing devices within the test facility. Initially, this instrumentation was used for shakedown testing of the facility. Currently, this instrumentation is used primarily to monitor the operation of each component within the wind tunnel circuit.

2.2.2 Test Section Instrumentation

The test section is instrumented with static pressure taps,

flush–mounted hot–film sensors, thermocouples, and pitot tubes. At both the test section inlet and exit planes, a pitot tube and thermocouple are located in the freestream at the centerline of the test section. From these measurements of total pressure and total temperature the freestream velocity entering and exiting the test section can be determined. Also, at the test section inlet there are static pressure taps located on the boundary layer bleed scoops as indicated in Fig. 7. The larger and most upstream scoop entraps the boundary layer which develops along the nozzle, while the smaller scoop serves as the leading edge of the flat–plate test surface. Therefore, the static taps on the larger scoop are used to monitor the rate of boundary layer bleed. The static taps on the smaller scoop are used to insure that the incoming flow has approximately a zero incidence angle to the leading edge of the flat–plate and that the flow is uniform in the spanwise direction. Additional static pressure taps are located along the flat–plate test surface as indicated in Fig. 8. The x–distance in Fig. 8 is measured from the leading edge of the flat plate. These static taps are used to check the streamwise and spanwise pressure gradient within the test section. Also, located along the flat–plate test surface are 30 flush mounted hot–film sensors (TSI model 1237). See Fig. 9. The signals from these sensors are used qualitatively to determine the state of the boundary layer (i.e. laminar, transitional, or turbulent) at the location of each sensor within the test section. In order to characterize the turbulence and document the boundary layer development within the test section, probes were inserted into the flow path and positioned via the probe traversing mechanism. The following types of probes were used in this investigation: 1) a TSI model

1210–T1.5 single sensor straight hot–wire probe was used to measure the characteristics of the freestream turbulence, 2) a TSI model 1218–T1.5 single sensor boundary layer hot–wire probe was used to measure the mean and fluctuating velocities within the boundary layer, and 3) a miniature boundary layer total pressure probe was used to measure the mean velocity boundary layer profile (see Fig. 10).

2.3 DATA ACQUISITION SYSTEMS

The test section pressure gradient, freestream velocity, and boundary layer bleed rate, as well as the remaining pressures and temperatures located throughout the rig were set, monitored, and recorded with the aid of the Escort Data Acquisition System. The Escort system is an interactive, real time data acquisition, display, and recording system which is used for steady state measurements. This system consists of a remote acquisition microprocessor (RAMP), data input and output peripherals, and a minicomputer. The minicomputer coordinates and executes all real time processing. The RAMP acquires the data from the facility instruments, sends the data to the minicomputer, and distributes the processed data from the minicomputer to the display device.

To determine the mean and rms of the signal voltages from the hot–film and hot–wire systems a TSI model 1076 True RMS Voltmeter and a Racal–Dana model 5004 digital averaging multimeter were used. The hot–wire system includes the hot–wire probe, a TSI model 1050 constant

temperature anemometer, and a TSI model 1052 linearizer. The hot–film system consists of the flush mounted hot–film sensor controlled by a TSI model 1053B constant temperature anemometer.

To acquire and analyze the analog waveform signal from the hot–film and hot–wire systems the following data acquisition systems were used: 1) Genrad 2500 Signal Analysis System, 2) Nicolet Scientific Corporation model 660A dual channel FFT (Fast Fourier Transform) analyzer, and 3) Datalab DL6000 'Multitrap' Waveform Recorder. Each of these systems were borrowed from other research facilities and therefore, were used for only a segment of this investigation. For example, the Genrad system was used to characterize the freestream turbulence (i.e. power spectra and autocorrelation functions), the Nicolet system was primarily used for boundary layer spectra and crosscorrelations, and the Datalab system was used for analysis and recording of simultaneous hot–film signals. Each of these data acquisition systems are briefly described in the following paragraphs.

The Genrad 2500 Signal Analysis System consists of 1) a four–channel analog data acquisition section, 2) a 6 μs, 10–bit analog to digital converter, 3) a digital processing section based on FFT techniques for spectrum analysis functions, 4) a data display device (a CRT and thermal printer), and 5) a hard disk drive for data storage. The maximum sampling rate of the system is 160 Khz divided by the number of active channels. Overall frequency ranges from 10Hz to 25 Khz may be selected.

The Nicolet model 660A dual channel FFT analyzer features a 12–bit analog to digital conversion at a rate of 2.56 times the selected frequency (selectable frequency range from 10 Hz to 100 Khz). This system provides

a maximum of 2K words of memory (i.e. 2K memory for single channel operation and 1K memory for dual channel operation). A Nicolet model 136A Digital Pen Plotter was used to plot the results. Unfortunately, this pen plotter was the only output storage device available with this data acquisition system. Therefore, the quantitative information was recorded by hand at the time of data acquisition.

The Datalab Dl6000 Multitrap waveform recorder provided simultaneous recording of data for up to 8 channels. Each channel had a maximum sample rate of 1 Mhz with sample intervals ranging from 50 ms to 1 μs. A waveform digitization and storage module, one dedicated for each channel, contained a 12 bit precision analog to digital converter and stored up to 128K words of digitized data. The data stored in each channel was downloaded via an IEEE DMA (Direct Memory Access) interface to an Hewlett Packard desktop computer system which was also used to control the data acquisition process.

CHAPTER III

EXPERIMENTAL PROCEDURE

3.1 Calibration

3.1.1 Hot–wire Calibration

The hot wires were calibrated in–situ against a pitot probe, over a range of about 20 wind tunnel settings. The calibrations were based on King's Law [16].

$$E^2 = A + B\ U^{1/2} \tag{1}$$

where E is the bridge output voltage of the constant temperature anemometer, U is the air velocity, and A and B are constants determined from the calibration. Fig. 11 depicts a representative calibration curve based on King's Law. A signal linearizer (TSI model 1052) is used to linearize the output of the constant temperature anemometer. This linearization is done by approximating the curve of bridge output voltage versus velocity with a fourth degree polynomial. Therefore, the next step is to determine the linearizer coefficients for the calibration data and to input the resulting coefficients into the linearizer signal conditioning circuit. Details of this procedure are given in [17]. To maximize the sensitivity of the linearizer, the coefficients were normalized to the 0 – 10 volt input and output range of the linearizer. Once the normalized coefficients have been

registered in the linearizer, the output voltage of the linearizer is related to the velocity in the following manner:

$$u = \frac{u_{max}}{10} E_l \tag{2}$$

where u is the local velocity, u_{max} is the maximum velocity of which the hot wire was calibrated, and E_l is the linearizer output voltage. Plots of bridge output voltage versus velocity and linearizer output voltage versus velocity are given in Fig. 12.

3.1.2 Hot–film Calibration

The calibration procedure for the flush–mounted hot–film sensors was not as straightforward as that described above for the hot–wire sensors. The following procedure was used to calibrate the hot–film sensors to indicate the wall shear stress. Bellhouse and Schultz [18] showed that a flush–mounted hot–film gage could be used to measure skin friction. The relationship between wall shear stress (τ_w) and the bridge output voltage (E) of the constant temperature anemometer is:

$$\tau_w^{1/3} = A\ E^2 + B \tag{3}$$

where A and B are constants determined from the calibration. Sandborn [19] pointed out that this procedure may lead to significant errors in determining the calibration constants and in evaluating skin friction if the calibration is performed in flows where there are large fluctuations in the wall shear stress (such is the case in the boundary layer transition region). In addition, a procedure, developed by Ramaprian and Tu [20], to evaluate not only the average wall shear stress but also the instantaneous wall shear

stress was attempted. Their expressions relating voltage output to wall shear stress are:

$$\bar{\tau}_w + \tau_w' = (A\ E^2 + B)^3 \tag{4}$$

and taking the time average of equation (4)

$$\bar{\tau}_w = A^3\ \overline{E^6} + 3\ A^2\ B\ \overline{E^4} + 3\ A\ B^2\ \overline{E^2} + B^3 \tag{5}$$

where $\bar{\tau}_w$ is the time–averaged wall shear stress, τ_w' is the fluctuation in wall shear stress, E is the instantaneous output voltage, and A and B are constants determined from calibration. The time–averaged wall shear stress, $\bar{\tau}_w$ must be known. The instantaneous output voltage, E is sampled and used to evaluate the time average of the moments E^2, E^4, and E^6. From a minimum of two calibration points, the values of A and B can be determined by solving equation (5). With the values of A and B, the instantaneous wall shear stress, $\bar{\tau}_w + \tau_w'$ can be calculated from equation (4).

The mean skin friction level can be determined from the velocity profile of a fully turbulent boundary layer using the Clauser plot technique [21]. The details of this procedure will be described in the Data Reduction Section. A trip wire was placed at the leading edge of the flat plate to produce a turbulent boundary layer along the entire length of the flat–plate test surface. Boundary layer velocity profiles were acquired with the hot wire, which was positioned adjacent to the hot film being calibrated. Simultaneously, the fluctuations of the output voltage of the hot–film gage were recorded with the Datalab DL6000 Multitrap Waveform Recorder.

Calibration data were taken at 5 wind tunnel speed settings and the results are indicated in Fig. 13. Note that the friction velocity, U_τ is related to the wall shear stress, τ_w as follows:

$$U_\tau = \sqrt{\tau_w / \rho} \tag{6}$$

Therefore, the friction velocity to the two–thirds power is directly proportional to the wall shear stress to the one–third power for incompressible flows. The straight line in Fig. 13 is based on the calibration procedure described by equation (3), whereas, the triangles are wall shear stress predictions based on the calibration procedure described by equations (4) and (5). Both calibration methods yield satisfactory results for this case of a fully turbulent boundary layer. Results of attempts to calibrate the hot films for the measurement of instantaneous skin friction within the boundary layer transition region will be discussed in the Results Section.

3.2 Tunnel set–up

Prior to a test, several calibration checks and adjustments are made to insure that the appropriate data are acquired. The following procedures were performed before a test was initiated: 1) all equipment was turned on to warm–up for about an hour, 2) self–tests and zero calibrations were performed on the voltmeters, 3) the hot wire was adjusted for stable operation and maximum frequency response over the test range of 0 to 120 ft/s, 4) the calibration of the hot wire was checked at several wind tunnel

speeds against a pitot probe, and 5) the test conditions of 100 ft/s and zero pressure gradient within the test section were established. The pressures from the static taps located along the flat–plate test surface are monitored and the hinged top wall of the tunnel was adjusted until the pressure gradient is as near to zero as this adjustment will allow. The damper valve on the boundary bleed duct is adjusted such that the inlet test section velocity is approximately equal to the outlet test section velocity. (Refer to Fig. 3 in the section describing the facility.) A representative spanwise and streamwise static pressure distribution on the boundary layer bleed scoops and the flat–plate test surface are illustrated in Figs. 14 and 15, respectively.

CHAPTER IV

DATA ACQUISITION – REDUCTION

The purpose of this experiment was to acquire detailed measurements describing boundary layer development from laminar flow into turbulent flow over a range of freestream disturbance levels. All boundary layer data were acquired along a flat plate subjected to a freestream velocity of 100 ft/s with zero pressure gradient at ambient temperature. Boundary layer development was characterized for several values of freestream turbulence intensity varying from 0.3% to about 6%. The following sections will address the data acquisition and reduction techniques to 1) characterize the freestream turbulence generated by the rectangular grids, 2) evaluate the properties and state of the boundary layer, 3) estimate the wall shear stress in the various stages of boundary layer development (i.e. laminar, transitional, and turbulent), 4) determine the evolution of turbulent bursts within the transition region of the boundary layer, and 5) evaluate frequency spectra and spatial correlations within the boundary layer.

4.1 Characterization of the Freestream Turbulence

Freestream turbulence is generated into the flow field by inserting

rectangular grids upstream of the test section inlet. (Refer to the section on the Facility Description for more detail on the grid configurations and location within the wind tunnel.) The wakes shed from the grid bars become turbulent close behind the grid and at some distance downstream of the grid the turbulence becomes more or less homogeneous. The turbulent energy decays in a nonlinear fashion with increasing downstream distance from the grids, because the smaller eddies dissipate faster than the larger eddies. Three parameters are used to characterize the freestream turbulence throughout the test section : 1) the intensity of the turbulence or velocity fluctuations, 2) the integral length scale of the turbulence, and 3) the frequency spectrum of the turbulence.

4.1.1 Turbulence Intensity

The turbulence intensity is defined (Schlichting [5]) as follows:

$$Tu = \sqrt{\frac{1}{3}\left[\overline{u'^2} + \overline{v'^2} + \overline{w'^2}\right]} \; / \; U_\infty \qquad (7)$$

However, grid–generated turbulence is more or less homogeneous and isotropic downstream of the grids. Results from a wind tunnel of similar design [22] have indicated that the turbulence is nearly isotropic ($\overline{u'^2} = \overline{v'^2} = \overline{w'^2}$). Therefore, only the longitudinal velocity fluctuations were measured in this investigation using a single hot wire oriented perpendicular to the flow direction. Assuming isotropic turbulence, the turbulence intensity reduces to:

$$Tu = \sqrt{\overline{u'^2}} \; / \; U_\infty \qquad (8)$$

Note that for a linearized hot wire anemometer system, as described in the instrumentation section, the local turbulence intensity is equivalent to the ratio of the rms of the voltage fluctuations to the mean voltage output of the signal linearizer. The Racal–Dana voltmeter was programmed to perform approximately 250 averages of the true rms and mean voltage of the linearizer output signal in order to determine the longitudinal turbulence intensity. Results of these measurements will be presented in the Discussion of Results Section.

4.1.2 Length Scale

The integral length scale of the turbulence is the scale that describes the average eddy size associated with the random motions in the turbulence. In order to determine the longitudinal length scales of this fluctuating motion at a specified position 'x', the correlation coefficient or covariance of the fluctuating velocity measured at position 'x' to that of the fluctuating velocity measured at position 'x + r' is integrated for all values of 'r' from zero to infinity. Expressed in mathematical terms this definition translates to the following:

$$L = \int_0^\infty R(r)\, dr \qquad (9)$$

where,
$$R(r) = \overline{u_1 \; u_2} \; / \; \sqrt{\overline{u_1^2} \;\; \overline{u_2^2}} \qquad (10)$$

and,

$$\overline{u_1\ u_2} = \overline{u_1(x)\ u_2(x+r)}$$

$$= \frac{1}{T}\int_0^T [u_1(x,t)\ u_2(x+r,t)]\ dt \qquad (11.a)$$

where L is the integral length scale, R is the correlation coefficient or covariance, r is the spatial separation in the streamwise direction, and u represents the quantity being correlated (fluctuating velocity in this case). See Ref. [23].

However, this two–point correlation requires that two hot–wire probes be inserted into the test section in such a manner that the upstream hot–wire probe does not interfere with the downstream hot–wire probe and that one probe can be moved at various positions relative to the other probe. Since this was not possible with the traversing mechanism and test section configuration used in this investigation an alternate method was used to approximate the integral length scale of the freestream turbulence. Taylor's hypothesis states that if the turbulent velocity fluctuations are small compared with the mean velocity, the eddies or vortex lines do not change appreciably in shape as they pass a given point. If Taylor's hypothesis is valid, then the autocorrelation of the fluctuating velocity u with time delay τ, $R(\tau) = u(t)\ u(t+\tau) / \overline{u'^2}$, will be the same as the spatial correlation with separation $U_\infty \tau$ in the streamwise direction [23]. Therefore, to measure a length scale, an autocorrelation of the signal from the single hot wire representing the fluctuating velocity in the streamwise direction is performed:

$$u(t+\tau) = \frac{1}{T} \int_0^T [u(x,t)\ u(x,t+\tau)]\ dt \qquad (11.b)$$

This autocorrelation function is normalized by the mean square of the velocity fluctuations in the streamwise direction to yield the autocorrelation coefficient.

$$R(\tau) = u(t)\ u(t+\tau)\ /\ \overline{u'^2} \qquad (12)$$

Integrating the autocorrelation coefficient results in the integral time scale, T_e, which is a measure of the average persistence of turbulent activity at a point.

$$T_e = \int_0^\infty R(\tau)\ d\tau \qquad (13)$$

Taylor's hypothesis can then be applied to estimate the longitudinal integral length scale as follows:

$$L = T_e\ U_e \qquad (14)$$

The Racal–Dana averaging voltmeter was programmed to perform 250 averages of the mean voltage so that an accurate measure of the mean velocity was used in the length scale calculation. The Genrad FFT signal processor was used for obtaining the autocorrelation data. The settings on the Genrad were as follows: 1) frequency range set at 25 Khz – sampling rate @ 2.56 times frequency bandwidth, 2) 1024 averages were taken, 3) frequency bandwidth of 25 Hz, and 4) Hanning window was on . The integration of the autocorrelation coefficient was performed by digitizing the resulting plot of the autocorrelation function from the Genrad signal analyzer and then performing a numerical integration (the trapezoidal rule

[24]). Data were acquired at x = –7.5, 6.0, 20., 32.6, 45.2, and 56.0 inches from the leading edge with y = 1, 2, 3, and 4 inches from the floor along the spanwise centerline of the wind tunnel for a total of 24 locations. Also, at x = 6 and x = 20 the autocorrelation function was obtained at Y = 1, 2, 3 and 4 for z = $\pm$ 5.0 inches from the centerline comprising an additional 16 locations. Thereby, bringing the total number of survey locations to 40.

4.1.3 Power Spectra

The contribution of the square of the velocity fluctuation within each frequency bandwidth to the overall turbulence level squared is referred to as the power spectral density. The distribution of the power spectral density as a function of frequency is defined as the power spectrum. Turbulence power spectra were acquired with a single hot wire and processed by the Genrad FFT analyzer. Only the u'^2 component of the turbulent kinetic energy was acquired thereby, resulting in a 1–D power spectrum. The data were acquired at y = 3 inches, z = centerline, and for x = –7.5, 6.0, 20., 32.6, 45.2, and 56.0 inches from the leading edge of the flat plate. The Genrad settings for data acquisition were as follows: 1) frequency range of 25 Khz, 2) 1024 averages,3) frequency bandwidth of 15.625 Hz (except for grid 1 in which the frequency bandwidth was 25 Hz), and 4) the Hanning window was on.

The autocorrelation coefficient and the power spectral density functions are related by the following Fourier transform pair:

$$R(\tau) = \int_0^\infty \varphi(\omega) \cos(\omega\tau)\, d\omega \tag{15}$$

$$\varphi(\omega) = \frac{2}{\pi} \int_0^\infty R(\tau) \cos(\omega\tau)\, d\tau \tag{16}$$

where $R(\tau)$ is defined in Eq. (12) and $\varphi(\omega)$ is the power spectral density as a function of frequency, ω, in radians per second. The normalized power spectral density, PSD(f) as a function of frequency in Hz is represented by the following:

$$PSD(f) = \varphi(\omega)\, 2\pi\, \overline{u}'^2 \tag{17}$$

The integral of the power spectral density function over all frequencies is the mean square of the velocity fluctuations, $\overline{u}'^2$. As mentioned in reference to Eqs. (12), (13), and (14), the integral of the autocorrelation coefficient, $R(\tau)$ over all values of τ multiplied by the freestream velocity represents the integral length scale of the turbulent velocity fluctuations. Also, evaluating the integral of the autocorrelation coefficient at $\tau = 0$ results in the mean square of the velocity fluctuations, $\overline{u}'^2$. Likewise , if we evaluate the value of the power spectral density function as the frequency approaches zero we find the following:

$$\varphi(0) = \frac{2}{\pi} \int_0^\infty R(\tau)\, d\tau \tag{18}$$

$$L = U_e \int_0^\infty R(\tau)\, d\tau = U_e\, \varphi(0)\, \frac{\pi}{2} \tag{19}$$

therefore,

$$L = \frac{U_e}{4\overline{u'}^2} \; PSD(0) \tag{20}$$

In summary, the autocorrelation function evaluated at zero represents the mean square of the velocity fluctuations, whereas its value integrated over all values of τ results in the integral time scale. Similarly, the power spectral density function evaluated at zero is proportional to the integral time scale, whereas its value integrated over the frequency spectrum results in the mean square of the velocity fluctuations. In this investigation values of the integral length scale were calculated using both the power spectrum and the autocorrelation methods.

4.2 **Boundary Layer Data Analysis**

The data reduction for three different types of boundary layers will be addressed in this section: 1) the laminar boundary layer, 2) the turbulent boundary layer, and 3) the transitioning boundary layer. For the laminar boundary layer, the velocity profiles are reduced and compared to the well–known Blasius solution for boundary layer development along a flat plate with zero pressure gradient ([5], pp. 144–148 and [1], pp. 253–273). The velocity profile is defined in terms of the similarity variables $\eta = y \sqrt{U_e / (2\nu x)}$ and $f'(\eta) = u/U_e$. The turbulent boundary layer can be broken down into four distinct regions: 1) the viscous sublayer, 2) the buffer zone, 3) the logarithmic region, and 4) the wake region (See Fig. 16).

The viscous layer is a very thin layer near the wall where the shear stress is dominated by the molecular viscosity as in the case of laminar flow. However, within the buffer zone, both the molecular and turbulent stresses (the stresses generated by the velocity fluctuations) contribute to the shear stress. In the logarithmic region of the turbulent boundary layer the turbulent stresses are the dominant contributors to the shear stress. The wake region is the mixing region where turbulent stresses decay to a value near zero at the edge of the boundary layer. The transitioning boundary layer is the least understood of the three types of boundary layers. It is believed that its structure lies somewhere between the laminar profile type and the turbulent type of boundary layer. The wall shear stress increases from the relatively low levels associated with a laminar boundary layer to the relatively higher levels associated with a turbulent profile. This change in shear stress is not only very important in drag calculations but also is not very well understood.

The mean velocity and rms of the fluctuating velocity within the boundary layer were measured with a single–wire boundary layer probe. From these measurements the boundary layer development was characterized and the following boundary layer parameters were determined: 1) displacement thickness, which indicates the distance that a steady flow would be displaced to satisfy conservation of mass, 2) momentum thickness, a measure of the momentum defect in the boundary layer related to drag, and 3) the shape factor, which is the ratio of the displacement thickness to the momentum thickness and is indicative of the shape of the boundary layer velocity profile. In mathematical form the displacement thickness is

defined as :

$$\delta^* = \int_0^\infty \left[1 - \frac{u}{U_\infty}\right] dy \tag{21}$$

and the momentum thickness is defined as:

$$\theta = \int_0^\infty \frac{u}{U_\infty} \left[1 - \frac{u}{U_\infty}\right] dy \tag{22}$$

To compare the measured velocity profile of the boundary layer to the Blasius solution for laminar flow along a flat plate at zero pressure gradient the data are reduced in terms of the similarity variable η and plots of η vs $f'(\eta)$ will be presented. Likewise, to compare the boundary layer mean velocity profile to the turbulent type of boundary layer the mean profile data was compared to Musker's expression in wall units for the velocity distribution in the wall region of a turbulent boundary layer [25]:

$$\begin{aligned} U^+ &= 5.424 \text{ ATAN } [(2\ Y^+ - 8.15)/\ 16.7] \\ &+ \text{LOG}_{10}\ [(Y^+ + 10.6)^{9.6}/(Y^{+^2} - 8.15Y^+ + 86)^2] \\ &- 3.52, \end{aligned} \tag{23}$$

where, $U^+ = u\ /\ U_\tau$ (23.a)

and, $Y^+ = y\ U_\tau\ /\ \nu$ (23.b)

and, $U_\tau = \sqrt{\tau_w\ /\ \rho}$ (23.c)

The mean velocity was normalized by the friction velocity, U_τ, and the y distance was normalized by the ratio of the kinematic viscosity, ν, to the

friction velocity, U_τ. The data was then plotted on the universal or U^+ versus Y^+ coordinates and compared to the correlation indicated by Eq. (23). The determination of the friction velocity will be discussed in the next section. The Blasius solution was also transformed to U^+ vs Y^+ coordinates so that the measured velocity profile could be compared to both a laminar and turbulent boundary layer velocity profile. If the data lie on the Blasius curve the velocity profile will be laminar; whereas, if the data fall on the turbulent curve the profile will be assumed to be fully–turbulent. However, if the data fall on neither curve, but lie somewhere between the two curves, then the boundary layer is considered to be in transition from laminar to turbulent flow.

A brief description of this transformation from Blasius coordinates to universal coordinates follows. From White ([1], p. 264) we find the following relations for the Blasius solution of a flat plate at zero pressure gradient:

$$\theta = 0.664 \sqrt{\nu \, x \, / \, U_\infty} \tag{24}$$

$$\tau_w \, / \, \rho = 0.4696 \, \nu \, U_e \sqrt{U_e \, / \, (2 \, \nu \, x)} \tag{25}$$

Therefore, from the definition of Reynolds number based on momentum thickness and from equation (25) we obtain:

$$\mathbb{R}_\theta = \frac{0.664}{\sqrt{2}} \, \frac{U_e}{\nu} \sqrt{\frac{2 \, \nu \, x}{U_e}} \tag{26}$$

$$\tau_w \, / \, \rho \; = 0.22049 \, U_e^2 \, / \, \mathbb{R}_\theta \tag{27}$$

Substituting the value for τ_w/ρ from equation (27) into equation (23.c), it is easily seen that the Blasius solution can be represented in terms of the U^+ and Y^+ coordinates as follows:

$$U^+ = \frac{u}{U_\tau} = 2.1296 \sqrt{\mathbb{R}_\theta}\ f'(\eta) \tag{28}$$

$$Y^+ = \frac{y\ U_\tau}{\nu} = \frac{.4696}{\sqrt{\mathbb{R}_\theta}}\ U_e \frac{y}{\nu} = \eta \sqrt{\mathbb{R}_\theta} \tag{29}$$

The U^+ vs Y^+ coordinates require the evaluation of U_τ, the friction velocity, which requires knowledge of the wall shear stress or skin friction coefficient. It is known that the wall shear stress varies dramatically from the laminar to turbulent regimes and its path is unknown in the transition region. Therefore, it is important to get a handle on this parameter. The following paragraphs will address the determination of the friction velocity.

4.3 Determination of Friction Velocity

In this section the determination of the friction velocity, wall shear stress and skin friction coefficient within each of the boundary layer development regions will be discussed. The friction velocity, wall shear stress, and skin friction coefficient are related to one another as follows: $U_\tau = \sqrt{\tau_w / \rho}$, $C_f = 2\ \tau_w / (\rho\ U_e^2) = 2\ U_\tau^2 / U_e^2$. The wall shear stress is defined as follows: $\tau_w = \mu \frac{du}{dy}|_{y=0}$. In the laminar region very near the wall, the change in velocity is linear with distance from the wall.

Therefore, the approximation of $\Delta u/\Delta y$ is used to determine the wall shear stress. However, for the turbulent boundary layer this viscous sublayer is very thin and it was not possible to get close enough to the wall to use this approximation. For the turbulent case the 'law–of–the–wall' correlation was used to estimate the wall shear stress. For a flat plate at zero pressure gradient the 'law–of–the–wall' correlation of Clauser [21] is:

$$U^+ = 5.6 \ LOG_{10} \ Y^+ + 4.9 \tag{30}$$

An initial value of U_τ was obtained from the following correlation ([1] page 518):

$$C_f = \frac{0.288 \ e^{-1.37 \ H}}{(LOG_{10} \ \mathbb{R}_\theta)^{1.753 \ + \ 0.283 \ H}} \tag{31}$$

and used in Eq (30). A least squares fit of the data falling within $50 < y^+ < 200$ to the correlation given in Eq. (30) is performed and the goodness of fit is determined by how well the slope of the curve–fitted data agree with the slope of Clauser's correlation given in Eq. (30). If the slopes are in agreement then the boundary layer is assumed turbulent and the value of U_τ has been estimated. This procedure is sometimes referred to as a Clauser fit or Clauser plot technique [21]. For the transitioning boundary layer neither of the above methods were applicable. In this region the momentum–integral equation for two–dimensional, incompressible boundary layers was used to estimate the value of shear stress at the wall. From Schlichting ([5], p. 160), the expression for the momentum integral equation is:

$$\frac{\tau_w}{\rho} = \frac{d}{dx}(U_e^2\,\theta) + \delta^*\,U_e\,\frac{d}{dx}(U_e) \qquad (32)$$

However, for a flat plate at zero incidence this equation reduces to :

$$\frac{\tau_w}{\rho} = U_e^2\,\frac{d\theta}{dx} \qquad (33)$$

Therefore, from the mean velocity profiles the momentum thickness, θ, can be determined and plotted as a function of x, distance from the leading edge of the plate. Then this data of θ vs. x was approximated with a polynomial curve fit. The resulting polynomial equation was differentiated with respect to x so that the value of $d\theta/dx$ could be determined. The value of wall shear stress was then estimated from Eq. (33).

4.4 Measurement of Turbulent Bursting

To track the evolution of the turbulent bursting with downstream distance, simultaneous records of up to eight hot–film time traces were recorded with the Datalab Waveform Recorder. For each of the eight channels, 128K of data were acquired at a rate of 50 Khz, thereby resulting in a time trace over approximately 2.62 seconds. At each freestream turbulence level, these data were acquired and recorded for the hot films located within the boundary layer transition region. From these data the evolution of the turbulent bursts as indicated by a positive voltage fluctuation on the hot–film signal, could be observed. Also,

crosscorrelations of the signals between succeeding hot films were performed to estimate the average convective velocity of the turbulent bursts. The convection velocity is determined by dividing the distance between the hot films by the τ value corresponding to the peak in the crosscorrelation coefficient (refer to Eq. 12). The hot–film time signatures were also used to evaluate the boundary layer intermittency factor. The intermittency factor is defined as the percentage of time that the flow is turbulent. Therefore, an intermittency factor of zero implies a laminar flow, whereas, an intermittency factor of one indicates that the flow is turbulent.

4.5 **Boundary Layer Spectra**

Boundary layer spectra were obtained with the normal hot wire located at a distance off the test surface which corresponded to the point of maximum amplitude of the velocity fluctuations within the boundary layer. Data were acquired for grid configurations 0, 0.5, and grid 1 at streamwise distances corresponding to locations where the boundary layer mean velocity profiles were obtained. The spectra were acquired with the Nicolet 660A dual–channel signal analyzer. For grid 0.5 and grid 1, the data were acquired over the 10 Khz frequency range and resolved within a frequency bandwidth of 12.5 Hz. Also, for all three grid configurations the power spectra were averaged 250 times to get a representative power spectrum. For the grid 0 configuration the data were acquired over the 500 Hz. frequency range (sampling frequency equal 500 * 2.56) with 800 lines

resolution or a frequency bandwidth of 0.625 Hz.

Crosscorrelations between a flush–mounted hot film and a hot wire were acquired with the Nicolet dual–channel FFT analyzer. These correlations were performed throughout the transition region for the grid 0, grid 0.5, and grid 1 configurations. All data were acquired with the Nicolet set at the 10 Khz frequency range and 200–250 averages per correlation.

CHAPTER V

PRESENTATION AND DISCUSSION OF RESULTS

5.1 Characterization of the Freestream Turbulence

The longitudinal turbulence intensity, the integral length scale of the turbulence, and the frequency spectrum of the turbulence are the three parameters used in this investigation to characterize the freestream turbulence. Data used to extract the longitudinal turbulence intensity and integral length scale information were acquired at x = –7.5, 6.0, 20., 32.6, 45.2, and 56.0 inches from the leading edge with y = 1, 2, 3, and 4 inches from the floor along the spanwise centerline of the wind tunnel for a total of 24 locations. Also, at x = 6 and x = 20 the autocorrelation function was obtained at Y = 1, 2, 3 and 4 for z = $\pm$ 5.0 inches from the centerline comprising an additional 16 locations; thereby, bringing the total number of survey locations to 40. Data were acquired at these 40 survey points for each of the following grid configurations: grid 1, grid 2, grid 3, and grid 4. A limited number of survey locations were studied for the grid 0.5 configuration.. The frequency spectra were acquired at y = 3 inches, z = 0 inches, and at the same streamwise positions where the turbulence intensity and length scale data were acquired.

5.1.1 Longitudinal Turbulence Intensity

The distribution within the test section of the freestream longitudinal turbulence intensity generated by grids 0, 0.5, 1, 2, 3, and 4 is presented in Fig. 17. The x – distance is measured from the leading edge of the flat–plate test surface. Refer to Fig. 2 for the dimensions of the rectangular turbulence generating grids. Note that the data presented in Fig. 17 represents the arithmetic average of the turbulence intensity acquired at all of the positions mentioned in the previous paragraph. The variations in the values of turbulence intensity in the y–direction and spanwise direction at each streamwise position lie within the size of the symbol in Fig. 17. Also from Fig. 17 note that for grids 0, 0.5, 1, and 2 that the turbulence intensity is relatively constant with x – distance. Therefore, the turbulence is nearly homogeneous. However, data from grids 3 and 4 indicate a decay of turbulence intensity with increasing distance from the leading edge of the flat plate. These results were compared to the empirical correlation developed by Baines and Peterson [26] for isotropic grid generated turbulence. See Fig. 18. Baines and Peterson established the following relationship between the freestream turbulence intensity, Tu_∞, the bar width, b, of the turbulence generating grid, and the distance, l, from the turbulence generating grid:

$$Tu_\infty = 1.12\ (l/b)^{-5/7} \tag{34}$$

Agreement with this correlation, Eq. (34) implies that the turbulence is 'typical' for grid generated turbulence and therefore, the turbulence is nearly isotropic. In this investigation the turbulence–generating grids were located

upstream of the contraction nozzle. Therefore the distance, l, from the turbulence generating grid was modified to account for the effect of the contraction nozzle on the turbulence development. An effective distance of 90 inches plus the distance from the turbulence generating grid was employed to achieve a satisfactory agreement with the correlation of Baines and Peterson. Therefore, the effect of the contraction nozzle is equivalent to a displacement of the grids by an additional 90 inches ahead of the test section.

5.1.2 Integral Length Scale

Measurements of the longitudinal integral scale of the freestream turbulence were obtained to depict the average eddy size associated with the fluctuations in the turbulent flow behind grids 1, 2, 3, 4, and grid 0.5. Fig. 19 shows the distribution of the integral length scale as a function of distance from the leading edge of the flat–plate test surface. These length scales were determined from the power spectrum at each x location plotted in Fig. 19 with the wire positioned at the vertical and spanwise centerline of the test surface. The values for the integral length scale for the grid 0 configuration, not shown in Fig. 19, were 7.5 and 7.7 inches for $x = 36.3$ and $x = 45.7$ inches, respectively. In Fig. 19 note the increase of the longitudinal length scale with downstream distance. This increase is due to the smaller eddies dissipating faster than the larger eddies with increasing streamwise distance. The average eddy size therefore appears to be growing with downstream distance when in reality the intensities of all eddy sizes are decreasing. Also from this same figure we see that for increasing grid

bar width (refer to Fig. 2) the integral length scale increases. Baines and Peterson [26] and Compte–Bellot and Corrsin [27] have indicated that the length scale is proportional to the distance from the grid raised to some exponent. Baines and Peterson [26] showed that the following relationship held for several grid sizes:

$$\frac{L}{b} = K \left[\frac{x}{b}\right]^n \tag{35}$$

where K is a constant and n is an exponent in the range of 0.53 to 0.56. The data shown in Fig. 19 were forced to fit the relationship indicated in Eq. (35). The results of the fit are shown in Fig. 20 and indicate that the length scale is correlated to the bar width of the rectangular–bar grid. Recall that x is the distance from the turbulence–generating grid and that an x–shift of 90 inches was required to account for the contraction nozzle effects. Additional length scale measurements were taken for grids 1, 2, 3, and 4 at the same locations that the measurements for the longitudinal turbulence intensity were taken. The integral length scales acquired at each streamwise cross section were arithmetically averaged and are plotted in Fig. 21. At each survey plane the standard deviation of the data ranged from approximately 0.05 for grid 1 to about 0.1 for grid 4. Comparison of Figs. 20 and 21 indicate that the length scale distributions are in agreement with previous researchers and the length scale values are representative for isotropic turbulence.

5.1.3 Frequency Spectra

For each turbulence–generating grid configuration the power spectrum data were acquired along the spanwise and vertical centerline within the test section at x locations of –7.5, 6.2, 20.2, 36.2, 45.7, and 56.0 inches from the leading edge of the flat–plate test surface. Figs. 22, 23, 24, 25, and 26 illustrate the power spectra for turbulence–generating grids 0.5, 1, 2, 3, and 4 respectively. The power spectrum is presented in dimensionless parameters: the dimensional spectrum is $U_e\ u'(f) / \overline{u'^2}\ L$; where U_e is the freestream velocity, u'(f) is the power spectral density, $\overline{u'^2}$ is the mean square of the fluctuations of the longitudinal velocity, and L is the longitudinal integral length scale, and the dimensionless wavenumber is $L\ f / U_e$; where f is frequency and L and U_e are defined the same as in the previous expression for dimensionless spectrum. The power spectrum is normalized in this manner so that it can be compared to Taylor's theoretical spectrum [28] for one–dimensional isotropic turbulence since isotropic turbulence is expected in the freestream far downstream of the turbulence generating grids. Figs. 22 thru 26 do not indicate any unusual spikes in the frequency spectra and each plot follows the features of Taylor's one–dimensional frequency spectra for isotropic turbulence. Therefore, based on the measured values of turbulence intensity, longitudinal length scale, and distribution of frequencies, the rectangular–bar grid–generated turbulence has the characteristics associated with isotropic turbulence. In addition, the results for grids 0.5, 1, and 2 indicate that the turbulence is nearly homogeneous and isotropic.

5.2 Determination of the Transition Region

5.2.1 Mean Velocity Profiles

Mean velocity profiles within the boundary layer were acquired to determine where the transition region was located for each level of freestream turbulence. All boundary layer profiles were obtained along the spanwise centerline of the test surface. In order to characterize the boundary layer development the data are plotted in dimensionless form. The local velocity within the boundary layer at a given distance from the flat–plate test surface (the y distance) is normalized by the freestream velocity, while the y distance is normalized by the boundary layer thickness (δ_{99}). Therefore, plots of y/δ vs. u/U_e are scaled from a value of zero at the test surface to a value of one at the edge of the boundary layer. Carpet plots of y/δ vs u/U_e at each x distance from the leading edge of the flat plate depict the boundary layer development along the flat–plate test surface. See Figs. 27, 28, 29, 30, 31, and 32. Each of these plots indicate typical boundary layer development in that the velocity at a given y distance from the test surface decreases with increasing streamwise distance for either laminar or turbulent boundary layer flow; whereas for a transitioning boundary layer flow the velocity at a given y – distance increases with increasing streamwise distance.

The boundary layer mean velocity profiles were plotted in terms of the similarity variables η and $f'(\eta)$ (see section 4.2 Boundary Layer Data Analysis) and were compared to the Blasius solution for a laminar boundary layer along a flat plate with zero pressure gradient. See Figs. 33 thru 38.

For a laminar boundary layer the plots of η versus f'(η) are similar and therefore profiles acquired at various x–distances from the leading edge of the flat plate should lie on top of one another. Also, for a laminar boundary layer along a flat plate at zero pressure gradient the velocity profiles should agree with the Blasius solution. Therefore, the data which correspond to a laminar profile should lie on top of one another and also should agree with the Blasius solution. The remaining data points therefore, are representative of boundary layer flow which is either transitioning from laminar to turbulent or is approaching fully turbulent behavior. Therefore, these plots of η versus f'(η) indicate when the boundary layers begin to deviate from a similar laminar flow and therefore mark the region where the transition process begins. For example from Fig. 33, the transition region for the no grid case apparently starts at a streamwise distance somewhere in the region between 40 and 42 inches from the leading edge of the flat plate. Similarly, the transition region for the other grid configurations are as follows: 1) from Fig. 34, the transition region for the grid 0.5 case begins between x = 8.3 and 10.3 inches, 2) from Fig. 35, the transition region for the grid 1 case begins between x = 9.0 and 10.0 inches, and 3) from Figs. 36, 37, and 38, the boundary layer has started to transition prior to the first measuring station at x = 5.0 inches from the leading edge of the flat plate.

To determine the end of the transition region the boundary layer mean velocity profiles were plotted on the U^+ versus Y^+ coordinates and compared to the empirical correlation of Musker (Eq. 23) for a fully turbulent boundary layer. The value of skin friction coefficient was

determined by using the Clauser fit technique – refer to sections 4.2 and 4.3 of this report. The resulting best–fit value of the skin friction coefficient was used to plot the data on the U^+ versus Y^+ coordinates. A subjective judgement was required to determine how well the data should fit the correlation in order to be considered a turbulent boundary layer. To assess the sensitivity of the data to Musker's correlation, the above procedure was applied to a fully–turbulent boundary layer. A trip wire was placed at the leading edge of the flat plate and several boundary layer mean velocity profiles were obtained. The Clauser fit technique was applied to these tripped boundary layer profiles and the resulting value of skin friction coefficient was used to plot the data on U^+ versus Y^+ coordinates. See Fig. 39. As indicated in Fig. 39, the data obtained in this facility for a fully turbulent profile fits the correlation of Musker very well. The goodness of fit is judged by how well the slope of the data compares to the slope of the log–linear region ($50 < y^+ > 200$) of Musker's correlation. The skin friction coefficient obtained by the Clauser fit technique was compared to the following empirical correlations [1] and [29]:

$$C_f = 0.0250\ \mathbb{R}_{\theta}^{-0.25} \tag{36}$$

and,

$$C_f = 0.455\ [\ln^2(0.06\ \mathbb{R}_x)]^{-1.0} \tag{37}$$

The value of skin friction coefficient obtained from the Clauser fit technique was 0.00379 as compared to $C_f = 0.00365$ from Eq. (36) and $C_f = 0.00379$ from Eq. (37). This test of the Clauser fit technique gives confidence in

applying the technique to the data from a post–transition turbulent boundary layer. For the grid 0 configuration, the result of the Clauser fit technique is shown in Fig. 40. The results indicate that at the last streamwise measurement location of x = 45.7 inches that the boundary layer is not yet fully turbulent. For the grid 0.5 configuration the first streamwise position that the profile appears fully turbulent is at x = 18.3 inches – see Fig. 41. Fig. 42 shows that for the grid 1 configuration that the boundary layer profile does not appear to be fully turbulent even at the last streamwise measurement position of x = 21 inches. However, the profile is very close to being turbulent as indicated in Fig. 42. For grid configurations 2, 3, and 4 the boundary layer profile is turbulent at streamwise locations of x = 8.2, 5.0, and 5.0 inches, respectively as indicated in Figs. 43, 44, and 45. Recall that the first survey station is at x = 5 inches; therefore, grids 3 and 4 will not be considered in this investigation focused on the boundary layer transition region.

An alternate method of locating the boundary layer transition region is to look at the behavior of the boundary layer parameters such as momentum thickness and displacement thickness. The ratio of displacement thickness to the momentum thickness is defined as the shape factor. The Blasius value for the shape factor is 2.59 and turbulent values are on the order of about 1.4 to 1.6. Therefore, the value of the boundary layer shape factor can be used also to estimate the beginning and end of the transition region. Fig 46 shows the shape factor as a function of x–distance for the no grid, grid 0.5, grid 1, and grid 2 configurations. The following observations can be made from Fig. 46: 1) for the no grid case the

transition region begins at x = 40 inches and does not end at the last survey station of x = 45.7 inches, 2) for the grid 0.5 case the transition region begins at about x = 9 inches and ends at x = 18 inches, 3) for the grid 1 case the transition region begins at x = 11 inches and does not end by the last survey station at x = 21 inches, and 4) for the grid 2 case the boundary layer transition region begins before the first survey station at x = 5.0 inches and ends approximately at the x location of 10 inches.

The above paragraphs indicate the dependence of the method used to determine the location of the transition region. The following sections focus on various other methods to determine this region.

5.2.2 Skin Friction

The value of the skin friction coefficient varies significantly between that of a laminar boundary layer to that of a turbulent boundary layer. Fig. 47 shows a representative distribution of C_f versus $\mathbb{R}_x$ for a flat plate. From Fig. 47 note that at an $\mathbb{R}_x \approx 4 \times 10^5$, the value of C_f varies from the laminar value of about 1.05×10^5 to $C_f \approx 4.35 \times 10^5$ for the fully turbulent boundary layer. Therefore due to large variations in the skin friction coefficient from the laminar to turbulent flow regimes, the value of the skin friction coefficient, C_f , can be used to detect the transition region. Recall, from the section describing the data acquisition and reduction, that the skin friction coefficient within the transition region was determined by the relation: $C_f = 2 \frac{d\theta}{dx}$. A plot of θ versus x and the corresponding curve fit for the grid 1 case is shown in Fig. 48. Fig. 49 illustrates the distribution of skin friction coefficient versus x–distance from the leading edge of the

flat plate for the various grid configurations of interest. Fig. 49 shows that the transition onset for grids 0.5 and 1 occur at approximately the same location. However, the grid 0.5 case approaches the turbulent values of C_f at a much faster rate than the grid 1 case. The reason for this occurrence is not clear at this time, especially since the value of the freestream turbulence is lower for grid 0.5 as compared to grid 1. Also, note that the regions of transition as determined by the skin friction coefficient are in agreement with the locations determined by the shape factor distribution. The value of the skin friction coefficient was then used to plot the mean velocity profiles on U^+ versus Y^+ coordinates – see Figs. 50 thru 55. These plots illustrate the smoothness of the transition from laminar to turbulent flow and therefore, indicate that the values obtained for the skin friction coefficient are consistent with the gradual development of a laminar profile transitioning to a turbulent profile with increasing downstream distance. Note that the theoretical Blasius curve shown in Figs. 50 thru 55, was plotted for the most streamwise laminar profile preceding the transition region. Tables I, II, III, IV, V, and VI summarize the distribution of the skin friction coefficient (also included are the other boundary layer parameters discussed in this report) with streamwise distance for each of the grid configurations.

As mentioned in the calibration section of this report, an effort was made to calibrate the flush–mounted hot–film sensors to measure the wall shear stress. At an x location corresponding to a flush–mounted hot–film location, boundary layer profiles were obtained at different wind tunnel speed settings. A trip wire was placed at the leading edge of the flat plate

to insure that the boundary layer would be fully turbulent. The value of wall shear stress was obtained by using the Clauser fit technique and was correlated to the bridge voltage output of the hot–film constant temperature anemometer system. The values of skin friction coefficient obtained from the boundary layer profiles are compared to the aforementioned empirical correlation (Eq. 36) in Fig. 56. The calibration curve was shown in Fig. 13 and discussed in section 3.1. However, when the hot film was subjected to a transitioning boundary layer flow, it was realized that the calibration was not applicable to the boundary layer transition region. Fig. 57 shows simultaneous time traces of the hot film, located within the boundary layer transition region, and a hot wire, which was located as close to the flush–mounted hot film as possible. The velocity fluctuations of the hot wire vary by a factor of approximately three, whereas the mean voltage fluctuations of the hot film vary only by a factor of about 1.003. Recall, from Fig. 47 that for $\mathbb{R}_x \approx 4 \times 10^5$ (the Reynolds number for this situation) the skin friction should vary by a factor of about 4 – if the transitioning boundary layer flow can be assumed to be jumping between the laminar and turbulent flow regimes. Approximating the shear stress as $\mu\ \Delta u/\Delta y$, the hot–wire fluctuations indicate a factor of 3 swing in the shear stress from the laminar flow to the turbulent flow. Note that since the wire is at a distance of about 0.007 inches from the test surface that the assumption of a linear velocity distribution between this point and the wall would result in a lower–than–actual value of shear stress. Therefore, it seems reasonable that the fluctuations in the hot film signal should represent a swing in skin friction of at least a factor of 3. Recall from the calibration section in this

report that the mean voltage output of the hot film is proportional to the shear stress to the $1/6^{th}$ power. Therefore to get a shear stress or skin friction coefficient variation of a factor of 4 would require that the voltage output of the hot film should vary by a factor of 1.26. As indicated in Fig. 57 the hot–film fluctuations depict only a factor of 1.003 variation in the bridge output voltage. Therefore, it was not possible to extract the instantaneous shear stress in the transition region from the hot films which were calibrated at turbulent flow conditions. Cook [30] attributes this inability of the flush–mounted hot–film sensor to follow rapid flow changes to a thermal lag due to heat conduction in the substrate of the hot film.

5.2.3 RMS Profiles

The rms of the longitudinal velocity fluctuations within the boundary layer were recorded at the same time the data for the mean velocity profiles were acquired. These velocity fluctuations (the square of which represents the x–component of Reynolds normal stress) can also be used as an indicator of the type of flow in the boundary layer. In the laminar boundary layer the longitudinal velocity fluctuations should be much smaller than the velocity fluctuations associated with a turbulent velocity profile. However, the amplitude of the fluctuations in a transitioning boundary layer will be the greatest of all because the velocity is jumping intermittently from a laminar type of flow to a turbulent type of flow. This increase in the velocity fluctuations can be seen by examining the signal from the hot wire and/or hot film shown in Fig. 57 where the sensors are within the transition region. Figs. 58 thru 63 show the profiles of the rms of the longitudinal

velocity fluctuations for the various levels of freestream turbulence used in this investigation. The plot for the no grid case – Fig. 58 – shows that for the laminar profiles the rms values are relatively low. As the flow begins to transition from laminar to turbulent, the rms of the velocity fluctuations increases rapidly. Also notice that for increasing values of y the rms values rise to a peak and drop off to the freestream value of the longitudinal turbulence intensity. This peak in the curves marks the region in which the turbulence production is balanced by the turbulence dissipation. The trend in the streamwise direction of the profiles of the rms of the velocity fluctuations is depicted in Fig. 59. The magnitude of the peak rms value gradually increases for each streamwise location when the boundary layer flow is laminar (x=5 and x=6.4). However, when the flow is intermittent the peak rms value increases rapidly with increasing streamwise distance (x = 8.3, 10.3, and 12.3) to a point where it reaches a maximum value (x = 14.3 inches). The peak rms value subsequently decreases as the flow approaches turbulent behavior.

For a turbulent boundary layer it has been shown [31] that the peak value of u'/U_τ should be approximately 2.5 to 3 and should occur within the boundary layer at $y^+ \cong 17$. Therefore, to determine how well the data obtained in this investigation agrees with these trends, the rms of the velocity fluctuations were normalized by the friction velocity and plotted in wall units. The results of this normalization is shown in Fig 64 for the grid 2 data. Note that the data plotted for values of x greater than 12 inches are post–transitioning boundary layers. From Fig. 64, the maximum value of u'/U_τ is approximately 1.7 for the post–transitioning boundary

layers and occurs at the measurement location nearest to the wall which is at $y^+ \cong 20$. The reason that the peak value of u'/U_τ was less than the expected value of 2.5 to 3.0 is explained in a publication by Ligrani and Bradshaw [31]. Ligrani and Bradshaw measured the turbulence intensity and spectra within the viscous sublayer of a turbulent boundary layer using various hot–wire probes of different dimensions. They concluded that in order to obtain the spatial resolution to accurately measure the turbulence properties within the viscous sublayer of a fully turbulent boundary layer the hot wire sensing element must have a viscous length of 20 or less. The viscous length, l^+, is defined as follows: $l^+ = l_{wire}\, U_\tau / \nu$. For the hot wires used in this investigation the value of l^+ was approximately 60. For hot wires of l^+ greater than 20 the peak value of u'/U_τdecreases, but the location of the peak value remains at $y^+ \cong 17$. Therefore, the results shown in Fig. 64 are in agreement with the findings of Ligrani and Bradshaw [31] in that the magnitude of $(u'/U_\tau)_{max}$ is slightly lower than expected value but appears to occur at $y^+ \cong 20$. Also shown in Fig. 64 is the occurrence of a 'hump', located at $y^+ \cong 95$, in the rms data for the transitioning and post–transitioning boundary layers.. This 'hump' appears to be a remnant of the intermittent behavior during the transition process. As the boundary layer approaches fully turbulent flow, the magnitude of this 'hump' diminishes and the profiles become more and more similar with increasing streamwise distance.

In addition, to check the validity of the rms measurements, data were acquired for a fully turbulent boundary layer and compared to the

'classical' results of Klebanoff [32]. For these profiles a trip wire was placed at the leading edge of the test surface. The rms of the velocity fluctuations is plotted against the results of Klebanoff in Fig. 65. The data agree very well with Klebanoff's results. The differences at least at the outer edge of the boundary layer are due to the fact that Klebanoff's measurements were obtained at a lower value of freestream turbulence than the data acquired in this investigation. Also, from this figure, we can see the shape of the longitudinal turbulence intensity within the boundary layer for a turbulent profile.

Reviewing Figs. 58 thru. 63, we find the following: 1) for grid 0 (Fig. 58) transition onset begins at about x = 40 inches and does not appear to approach fully turbulent behavior by the last survey station at x=44.3 inches, 2) for grid 0.5 (Fig. 59) transition onset occurs at approximately 8.3 inches and does not become fully turbulent even by x = 20 inches, 3) for grid 1 (Fig. 60) transition onset occurs at approximately x = 9 inches and does not become fully turbulent by x = 21 inches, 4) for grid 2 (Fig. 61) the transition onset begins prior to the first survey station at x = 5 inches and becomes fully turbulent by approximately x = 12.2 inches. The results obtained from the profiles of the rms of the velocity fluctuations imply transition regions that are slightly different than those inferred from the mean velocity profiles and distributions of the skin friction coefficient. The next section discusses a different method used to determine the location of the transition region.

5.2.4 Intermittency Factor

The intermittency factor is defined as the percentage of time the boundary layer is turbulent. Simultaneous time traces of up to eight hot films located along the centerline of the test surface were recorded for the grid 0, grid 0.5, and grid 1 configurations. From these time traces the intermittency factor was determined by choosing an arbitrary value of the mean voltage output from the hot films to use as the threshold value. All voltage levels below this threshold value would be assigned a value of zero – corresponding to laminar flow; whereas, all voltages above this threshold value would be assigned a value of one – corresponding to a turbulent flow. At each discrete time step the assigned values of either zero or one were added and the total was averaged over all time. Fig. 66 illustrates this calculation procedure for a time trace of a hot film located in the boundary layer transition region. The voltage threshold value was individually selected for each time trace such that it distinguished between laminar and turbulent regimes of the time trace as accurately as possible. Recall, from the data reduction section, that the hot film time traces were recorded at a rate of 50 Khz over a time of approximately 2.62 seconds.

The above procedure was performed on all flush–mounted hot–film time traces and the resulting values of intermittency factor are plotted in Fig. 67. The transition regions for each grid configuration is as follows: 1) grid 0 transition region from x = 38.3 inches to x = 50.2 inches, 2) grid 0.5 transition region from x = 6.2 inches to x = 24.2 inches, grid 1 transition region from x = 4.2 inches to x = 18.24 inches, 3) grid 2 transition region begins before x = 4.2 inches and ends at x = 10.2 inches,

and 4) grid 3 transition region begins before the location of the first hot film at x = 4.2 inches and ends at x = 8.2 inches. These results agree very well with the results obtained by Blair [33]. Blair located the transition region from steady–state heat transfer measurements which were made in a wind tunnel of similar construction to the tunnel used in this investigation [22]. Blair's results are shown in Fig. 68. The data shown in Fig. 68 were acquired along a flat plate with zero pressure gradient at a freestream velocity of 100 ft/s with the freestream turbulence levels indicated in Fig. 68. The excellent agreement between Blair's results and the results reported herein indicate the use of the flush–mounted hot films to determine the transition region was an appropriate technique. In the following section the results of the various methods to determine the boundary layer transition region will be summarized, compared to one another, and compared to predictions based on empirical correlations.

5.2.5 Comparison of Methods

The location of the transition region has been determined by the following methods: 1) Initially the mean velocity profiles in the boundary layer were compared to 'classical' laminar and turbulent profiles. Deviation from these classical profiles indicated the beginning and end of the transition region. 2) The boundary layer shape factor was compared to the traditional laminar and turbulent values to detect the location of the transition region. 3) The value of the skin friction coefficient was compared to the theoretical laminar value and empirical turbulent value to determine when the profile deviated from the laminar type of flow to the turbulent

type of flow. 4) The value of the rms of the longitudinal velocity fluctuations was used to determine where the transition region was located. 5) Finally, the intermittency factor obtained from flush–mounted hot–film sensors was used to gauge the type of boundary layer flow. The results of each of these methods are summarized in Table VII and they are compared to predictions of the onset of the transition region (see Table VIII) based on the empirical correlations developed by Van Driest and Blumer [8], Seyb [34], Abu–Ghannam and Shaw [10], and Dunham [35]. The agreement of the data depicted in Table VII with the empirical correlations (depicted in Table VIII) indicates that the results presented herein are reasonable. In addition, Mack's [36] modified e^n method, a more theoretically based method, was used to predict the onset of transition for each grid configuration. Based on Mack's method [36], the predicted locations for the onset of transition were as follows: 1) at $x \cong 36$ inches for grid 0, 2) at $x > 20$ inches for grid 0.5, 3) at $x \cong 17$ inches for grid 1, and 4) at $x \cong 8$ inches for grid 2. The modified e^n method [36] is based largely on linear stability theory; therefore, it is understandable that the method fails to predict the location of transition onset for the bypass transition cases (i.e. grids 0.5, 1, and 2). However, for the case of transition via the T–S path (i.e. grid 0) the location of the onset of transition as predicted by Mack's modified e^n method [36] is in good agreement with the locations determined experimentally in this investigation (see Table VII).

In Table VII, note that the intermittency factor method detected the transition region at an earlier streamwise location than the other methods. However, the intermittency factor was determined from measurements of the

flush–mounted hot films which detected the unsteadiness near the test surface, whereas, the other methods were based on measurements throughout the boundary layer. Therefore it is apparent that the mean profiles are not affected by small amounts of intermittency. The only surprising feature depicted from these results is that even though the turbulence associated with grid 0.5 was less than that of grid 1, the transition region not only started at about the same location for each of those grid configurations but also that the boundary layer flow became turbulent for the grid 0.5 configuration before it became turbulent for the grid 1 configuration. Recall, that grid 0.5 consists of a 20–mesh screen located directly in front of grid 1. The differences in the characteristics of the freestream turbulence for each case is documented in Figs. 17, 19, 22 and 23. However, the flush–mounted hot films detected the beginning and end of the transition regions in the anticipated order – see Fig. 67. This indicates that something is happening throughout the boundary layer in one of these cases to either retard (grid 1) or accelerate (grid 0.5) the boundary layer transition process. One possible explanation could be related to the integral length scales associated with each level of freestream turbulence. Recall from Fig. 19 that the integral length scale of the freestream turbulence for the grid 0.5 configuration was approximately 0.3 inches whereas, for the grid 1 configuration the integral length scale of the freestream turbulence was approximately 0.5 inches. Therefore, for the grid 0.5 configuration, the boundary layer would be buffeted by more freestream turbulent eddies in comparison to the number of eddies buffeting the boundary layer associated with the grid 1 configuration, within a given time period.

The intent of this investigation is to study the bypass transition process as compared to transition via the T–S path. Thus far, for each grid configuration, the characteristics of the freestream turbulence have been documented and the corresponding boundary layer transition region has been identified. However, for grids 2, 3, and 4, the transition process started upstream of the first measurement location at which boundary layer surveys were acquired. Only a portion of the transition region was therefore captured for these configurations. Therefore, the remainder of this report will focus on the transition region for the grid 0, grid 0.5, and grid 1 configurations.

5.3 Documentation of the Transition Process via the T–S Path

5.3.1 Description of the Transition Process via the T–S Path

The transition process for low disturbance flow past a smooth flat plate is described by White [1]. Fig. 69 depicts White's [1] representation of the steps that take place as the flow develops downstream. Near the leading edge of the flat plate the flow is a stable laminar flow. Then there is an initiation of unstable two–dimensional Tollmien–Schlichting (T–S) waves. Linear stability theory can be used to predict the critical Reynolds number at which the T–S waves begin to grow. After a period of growth of the T–S waves, they begin to vary in the spanwise direction and streamwise vortices develop. A periodic streamwise vorticity system

develops into counter–rotating vortices. Shear layers develop in the boundary layer and the vortices, which have been stretched in an S–shape in the spanwise direction, begin to break down. The vortices continue to break down into smaller and smaller vortices until the unsteadiness is characterized by fully three–dimensional fluctuations. Next, turbulent bursts occur and three dimensional turbulent spots form. These turbulent spots are believed (Schubauer and Klebanoff [37]) to be wedge shaped and are continuously being distorted due to the downstream end of the spot traveling faster than the upstream end. The turbulent spots grow and merge with other turbulent spots until the flow is fully turbulent.

5.3.2 Verification of T–S Waves

For the grid 0 configuration, time traces of the flush–mounted hot films depict the existence and amplification of T–S waves along the test surface. These T–S waves were not artificially excited but rather develop from the disturbances inherent in the wind tunnel. The time traces shown in Fig. 70 were acquired simultaneously. At $x = 30$ inches the first occurrence of a periodic waveform is recognized. The succeeding traces of $x = 32.3$, and $x = 34.3$ inches illustrate the amplification of the periodic waveform, first noticed at $x = 30.3$ inches, with increasing streamwise distance. At $x = 38.3$ inches bursting of turbulence is first evident. (Note the change in scales of the $y -$ axis.) The intermittency (i.e. the fraction of the time that the flow is turbulent) increases with increasing streamwise distance until the flow, as sensed by the flush–mounted hot films, becomes fully turbulent. These results were compared to results from linear stability theory. Fig 71 depicts the curves of neutral stability for neutral frequencies

of disturbance on a flat plate at zero incidence. This figure was extracted from Schlichting ([5], p.479). The curve labeled 'measurements' was generated from the results of Schubauer and Skramstad [6] and the theoretical curve was generated from the works of Tollmien [4]. The area between these two curves shown in Fig. 71 indicates the conditions at which the T–S waves grow in amplitude. In this investigation the initial growth of T–S waves occurs at x = 30.3 inches as indicated in Fig. 70. At x = 30.3 inches the displacement thickness was measured to be 0.039 inches. Therefore, at a freestream velocity of 100 ft/s the Reynolds number based on displacement thickness is approximately 1900. The periodic waveform shown in Fig. 70 for x = 30.3 inches exhibits a characteristic frequency of 400 Hz. Therefore, the normalized frequency, $\beta_r \nu / U_e^2 \equiv 2\pi f \nu / U_e^2$ is approximately 45×10^{-6}. These values of $\mathbb{R}_{\delta^*} \cong 1900$ and normalized frequency $\cong 45 \times 10^{-6}$ were plotted, as the solid triangle, on the neutral stability plot of Fig. 71 . The agreement of this experiment with the linear stability theory indicates that the periodic waveforms shown in Fig. 70 behave as T–S waves and therefore the transition process for the grid 0 configuration simulates the transition process via the T–S path, which was described in section 5.3.1.

5.3.3 Features of the T–S Waves

Determination of the streamwise wavelength. To determine the streamwise wavelength of the T–S waves, the periodic signal of a flush–mounted hot film was cross–correlated with the signal from a hot

wire which was positioned at different locations relative to the hot film. An example of such a crosscorrelation is shown in Fig. 72. The crosscorrelation of two periodic functions is also a periodic function and the frequency of the crosscorrelation function represents the streamwise frequency of the T–S waves. The crosscorrelation coefficient was normalized by the product of the rms of the voltage fluctuations of the hot wire and hot film so that its values would range from +1 to −1. A value of +1 for this normalized crosscorrelation coefficient, CCF_n, would indicate that the signals from the hot film and hot wire are exactly in phase with each other. Similarly, if $CCF_n = -1$, then the hot–film and hot–wire signals are 180^0 out of phase. Initially, when the hot wire is positioned directly over the hot film (this is the case in Fig. 72), the signals are in phase with one another. As the hot wire was positioned at increasing downstream distances relative to the fixed location of the flush–mounted hot film, the signals went out of phase with each other and eventually, returned to the state in which they were once again in phase with each other. The streamwise distance that the hot wire traversed, such that the hot–wire and hot–film signals were back in phase with each other, was the streamwise wavelength of the T–S waves, λ_x. This procedure was applied to hot film #16 (see Fig. 9) with the hot wire positioned from x = 34.3 inches to x = 38.5 inches. The wavelength was found to slightly increase with downstream distance. For hot–wire locations near the hot film, the measured value of λ_x was 0.9 inches and at the hot–wire locations corresponding to the furthest downstream positions relative to the hot film the value of λ_x was found to be 1.1 inches. The resulting streamwise wavelength, λ_x, was

averaged over the distance of x = 34.3 to x = 38.5 inches and was found to be approximately 0.98 inches.

T–S wave propagation speed. For a periodic function the wave propagation speed, c, is directly related to the streamwise wavelength, λ_x, and the frequency, f, of the waveform as follows: $c = \lambda_x f$. For each of the streamwise wavelengths (discussed in the previous paragraph) the corresponding wave propagation speed was calculated. The average T–S wave propagation speed was 30.8 ft/s. This result was then compared to the linear stability theory. Fig. 73 illustrates the curves of neutral stability for the disturbance frequency, $\beta = 2\pi f$, and the wave velocity, c, as a function of Reynolds number based on displacement thickness. For this investigation at the x location of x = 34.3 inches, the Reynolds number based on displacement thickness is approximately 1900. Therefore, from Fig. 73, the value of the wave velocity normalized by the freestream velocity for amplified disturbances is in the range of 0.25 to 0.33. The measured value was 0.31 and is indicated in Fig. 73 by the solid triangle. Likewise, the value of the streamwise wavelength can be calculated. The T–S wave frequency was estimated from Fig. 70 to be approximately 400 Hz. Since $\lambda_x = c / f$, and for a freestream velocity of 100 ft/s we know from Fig 73 that $25 \text{ ft/s} \leq c \leq 33 \text{ ft/s}$, then the calculated value of the streamwise wavelength is: $0.75 \leq \lambda_x \leq 0.99$ inches. The agreement of the measured values of streamwise wavelength and wave propagation velocity with those values calculated from linear stability theory indicate that the periodic waveforms shown in Fig. 70 for x = 30.3, 32.3, and 34.3 inches do indeed represent T–S waves.

Spanwise wavelength. The spanwise wavelength of the T–S waves

was measured in a similar manner to that used to measure the streamwise wavelength. Crosscorrelations between a flush–mounted hot film and a hot wire were acquired for hot film #16. The hot wire was traversed in the spanwise direction in increments of 0.25 inches. At each spanwise position the crosscorrelation coefficient was obtained and the phase relationship between the hot–film signal and the hot–wire signal was observed. A phase shift corresponding to one period of the waveform resulted a spanwise wavelength of approximately 2.0 inches, or about twice λ_x.

5.4 Bypass Transition & Comparison with the T–S Path to Transition

The bypass transition process occurs when a laminar boundary layer which is perturbed with finite non–linear disturbances originating in the freestream displays turbulent spot formation without first displaying linear disturbance growth. In such a disturbance environment the linear growth domain is bypassed, that is to say that there is no evidence of T–S waves associated with the bypass transition process. The transition region for the grid 0.5 and grid 1 configurations is identified by the simultaneous time traces of the flush–mounted hot films. These time traces are shown in Figs. 74 and 75. The time trace at x = 4.2 inches in Fig. 74 is indicative of a laminar boundary layer flow. However by x = 6.2 inches bursts of turbulence occur. The time traces at the remaining x locations show the coalescence of the turbulent spots with increasing streamwise distance until the flow is fully turbulent. Similarly, in Fig. 75 the hot–film time traces

show no evidence of any periodic waveforms such as those identified with the grid 0 configuration (see Fig. 70). In order to check for periodic waveforms between hot films, the hot–wire probe was located near the flat–plate test surface (within $\cong$ 0.007 inches) and traversed from the first survey station at x = 5 inches to the hot film where the turbulence bursting was first sited. In addition, a crosscorrelation between the hot film located closest to the leading edge of the flat plate (x = 4.2 inches) and the hot wire located at x = 5.0 inches was performed. This crosscorrelation, shown in Fig. 76, is representative of a correlation of random signals [38]. If there were any periodic waveforms present in the flow, the crosscorrelation function would exhibit some periodicity as was evidenced in Fig. 72. Therefore, for the grid 0.5 and grid 1 configurations, the linear instabilities are bypassed and the first indication of transition is evidenced by bursts of turbulence near the test surface.

The macroscopic results of the bypass mode as compared to the T–S path to transition indicate that the transition occurs much earlier for the bypass mode. Consider that for transition via the T–S path, i.e grid 0, the transition region occurred at x $\cong$ 40 inches for a freestream turbulence of 0.3%. However for the bypass mode with grid 0.5, the boundary layer transition took place at x $\cong$ 8 – 9 inches from the leading edge of the flat–plate test surface for a freestream turbulence of only 0.65%. Also, note from Tables I, II, and III, that the transition occurred for the bypass mode at a smaller value of displacement thickness and momentum thickness.

What causes bypass transition to occur? What disturbance levels are required to make the bypass occur? How do the disturbances propagate

into the boundary layer? In order to investigate the features of the bypass transition process and to make comparisons with the linear growth transition process the results of the following measurements will be discussed: 1) simultaneous time traces of a flush–mounted hot film and a hot wire with the hot wire traversed throughout the boundary layer, 2) two–point correlations between a hot film and hot wire in both the x–z plane and y–z plane of the test section, and 3) boundary layer spectra acquired for both the bypass transition case and the case of transition via the T–S path.

5.4.1 Simultaneous Hot–Wire / Hot–Film Time Traces

To determine what happens through the boundary layer as a turbulent burst occurs, simultaneous time traces of a flush–mounted hot film and a hot–wire probe positioned at different y – locations throughout the boundary layer were acquired. The time traces were acquired with the grid 1 configuration at the x – location of 8.2 inches and they are shown in Fig. 77. Each plot corresponds to a different y–location for the hot wire. The top trace and the y–axis on the right–hand–side of each plot in Fig. 77 correspond to the hot–film signal; whereas, the lower trace and the y–axis on the left–hand–side of each plot in this figure correspond to the hot–wire signal. Near the test surface, the hot–film and hot–wire probes sense a positive voltage excursion with each turbulent burst. As the hot wire is positioned further from the test surface the mean velocity increases and the fluctuations associated with the passing of a turbulent burst decrease. For the hot wire located at y positions of 0.027 and 0.037 inches

the fluctuations are both positive and negative about the mean velocity. As the hot–wire probe is positioned from a y location of 0.052 inches to the edge of the boundary layer the fluctuations associated with the turbulent bursting are negative. This change of phase between the flush–mounted hot film and the hot wire can be rationalized as follows. The effect of the passing of the turbulent spot effectively makes the boundary layer flow switch instantaneously from a laminar flow to a turbulent boundary layer flow. Fig. 78 shows a typical laminar and turbulent boundary layer profile. As indicated in Fig. 78, near the wall a jump from a laminar to turbulent flow would result in a positive velocity fluctuation whereas near the edge of the boundary layer an instantaneous switch from laminar to turbulent flow would result in a negative velocity excursion. Also from Fig. 78, note that there exists a point where the laminar and turbulent boundary layer profiles intersect. At this crossover point, the velocity excursion due to the passing of a turbulent spot would be essentially zero. Returning to Fig. 77, note that for y = 0 to 0.027 inches the velocity excursions are positive. At y = 0.027 and 0.032 inches both positive and negative velocity fluctuations occur, which would correspond to the flow bouncing about the crossover point of the laminar and turbulent velocity profiles illustrated in Fig. 78. Note also that the amplitude of the velocity fluctuations, sensed by the hot wire, are highest near the wall, reach a minimum at the crossover point, increase immediately after the crossover point, and then decrease to the freestream turbulence level. This same trend of the velocity fluctuations through the transitioning boundary layer was also depicted in the rms profiles (see Figs. 58, 59, and 60), and explains the 'hump' in Fig. 64.

The excellent correlation between the hot–film and hot–wire signals (as shown in Fig. 77) through the boundary layer indicates that disturbances are communicated through the boundary layer. Also shown in Fig. 77 is that as the hot wire was traversed in the vertical direction above the hot film, the passage of the turbulent burst is sensed at an earlier instant in time by the hot wire. This result agrees with findings of Schubauer and Klebanoff [37] that indicate that the turbulent spot extends vertically through the entire thickness of the boundary layer and that the turbulent spot is convected at a higher velocity near the edge of the boundary layer than it is near the test surface within the boundary layer (see Fig. 79). Also note that for the hot wire at y locations greater than or equal to 0.052 inches, the freestream turbulence is detected between the turbulence bursts. At y – locations lower than 0.052 the high frequencies associated with the freestream turbulence is damped within the boundary layer and only bursts of turbulence can be identified. Note that at this position the theoretical edge of a laminar profile would occur at $y \cong 0.06$ inches. All of the above observations support the claim that a burst occurs and is transported downstream at speeds which are dependent on the distance from the wall and that the passing of the turbulent spot has the same effect as an instantaneous shift from laminar flow to turbulent flow.

5.4.2 Two–Point Correlations

Due to the excellent correlation between the hot–film and the hot–wire signal through the boundary layer as is evidenced in Fig. 77, a

series of crosscorrelations were performed with the hot film located at x = 8.2 inches, y = 0 inches, and z = 0 inches and the hot wire located at x = 8.2 inches, y = 0.007, 0.017, 0.027, 0.037, 0.050, 0.065, 0.080, 0.095, and 0.110 inches for each spanwise position of z = 0.0, ± 0.25, ± 0.50, ± 0.75, ± 0.1, and 1.5 inches from the centerline of the tunnel. To obtain these crosscorrelations the data acquisition was triggered by a passing of a turbulent burst over the flush–mounted hot film. From each of these (90) crosscorrelations the peak value of the normalized crosscorrelation coefficient, CCF_n, was determined and a contour plot showing the distribution of the CCF_n in the y–z plane was constructed. See Fig. 80. This contour plot shows the change of phase between the hot–film and hot–wire voltage fluctuations and the reduction in the amplitude of the velocity fluctuations sensed by the hot wire as the hot wire is moved vertically through the boundary layer. These results were noted earlier in section 5.4.1 from the plots in Fig. 77. In addition to these results, Fig. 80 shows the effect of a burst passing the hot film (located at z = y = 0) on the surrounding flowfield. The crosscorrelations between the flush–mounted hot film and the hot wire, as the hot wire was traversed along the floor of the tunnel in the spanwise direction, indicated the spanwise region of the flowfield which was affected by the passing of a turbulent burst over the hot film. For example, Fig. 80 shows that the normalized crosscorrelation coefficient between the hot film and hot wire deteriorated to a value of 0.5 by the time the hot wire was traversed ± 0.4 inches in the spanwise direction from the hot film located at z = 0 inches (see the contour labeled 'L' in Fig. 80 which represented a CCF_n value of approximately 0.5). As the hot wire was traversed in the spanwise direction, at larger vertical distances from the

flush–mounted hot film, the correlation between the hot wire and hot film was confined to a more narrow spanwise region. Note that the edge of the boundary layer corresponds to a vertical distance of approximately 0.12 inches. Therefore, the turbulence bursts are propagated throughout the boundary layer but indicate no evidence of spanwise periodicity in the mean.

Additional crosscorrelations were obtained to study the effect of the turbulent burst on the flowfield in the streamwise and spanwise directions. Crosscorrelations between the same hot film used in Fig. 80 and the hot wire were acquired in the x–z plane near the test surface for the grid 1 configuration. Figs. 81 and 82 depict the survey locations and the resulting contour showing the distribution of the maximum CCF_n for the grid 1 configuration. Similar crosscorrelations were obtained for the grid 0.5 configuration. Fig. 83 shows the survey locations and Fig. 84 shows the resulting contours for the grid 0.5 case. Figs. 82 and 84 depict the average spanwise and streamwise persistence of a turbulent spot passing over the hot film. For example, choosing an arbitrary cut–off value of $CCF_n = 0.5$, the spanwise extent of the turbulent spot passing over the hot film would be approximately ± 0.4 inches for both the grid 1 and grid 0.5 configurations. Note that these crosscorrelations were acquired within the boundary layer transition region using the hot film which exhibited an intermittency of about 50%.. Figs. 82 and 84 indicate that the passing of an event at the hot film is highly correlated in the streamwise direction as compared to the spanwise direction.

Crosscorrelations between succeeding flush–mounted hot films located throughout the boundary layer transition region were also obtained

in order to determine an average convective velocity for the bursts of turbulence near the wall. A representative crosscorrelation between two succeeding hot films is provided in Fig. 85. The crosscorrelation shown in Fig. 85 indicates that the time it took for an event passing the upstream hot film to reach the downstream hot film was approximately 2.4 ms. Since the hot films were separated by a distance of 2 inches, the average convective velocity of the turbulent bursts is approximately 70 ft/s or 0.7 U_e. This procedure was applied to the transition regions for the grid 0 and the grid 1 configurations and the same value (0.7 U_e) for the average convective velocity of the turbulent bursts was determined. Note that this average convective burst velocity is in agreement with the measurements of Schubauer and Klebanoff [37] — see Fig. 79.

5.4.3 Boundary Layer Spectra

Bypass transition is usually described as a transition process which occurs when large finite non–linear disturbances perturb the laminar boundary layer. Therefore it is important to determine how the freestream disturbances are transmitted to the boundary layer. In section 5.2.3 the overall level of the disturbances within the boundary layer was characterized by the rms of the velocity fluctuations (see Figs. 58 thru 63). The boundary layer frequency spectra provide the distribution of the square of these velocity fluctuations as a function of frequency bandwidth. Boundary layer spectra were acquired for the grid 0, grid 0.5 and the grid 1 configurations at the various streamwise positions encompassing the

transition region. The boundary layer spectra were acquired at the position in the boundary layer where the rms of the fluctuating velocities was a maximum so that the power spectrum would be obtained at the highest level of signal quality. The boundary layer spectra were checked at different y locations through the boundary layer and similar features resulted.

The boundary layer spectra for the grid 0 configuration are shown in Fig. 86. The spectra at x locations of 28.9 thru 38.3 inches show an increase in the power spectral density (PSD) at frequencies of 350 Hz to approximately 440 Hz which correspond to the frequencies associated with the T–S waves. The increase in the PSD at approximately 50 to 70 Hz is caused by a structural vibration related to a support of the wind tunnel located at $x \cong 29$ inches. When the support was removed the floor of the tunnel vibrated; therefore the support was left intact. This figure shows the increase of the overall energy level (note the overall energy level is directly proportional to the integral of the PSD over all frequencies) within the boundary layer with increasing streamwise distance. This increase in the velocity fluctuations within the boundary layer with increasing streamwise distance was also shown in Fig. 58. From the neutral stability curve shown in Fig. 71, for $\mathbb{R}_{\delta^*} \cong 1900$, the velocity fluctuations occurring at frequencies between 100 Hz and 500 Hz would be expected to be amplified, whereas velocity fluctuations occurring outside of this frequency range would be damped. Prior to the turbulent bursting (turbulent bursting began between $x = 36.3$ and $x = 38.3$ inches) the power spectra shown in Fig. 86 follow the behavior predicted by linear stability theory in that the velocity

fluctuations occurring below a frequency of 100 Hz are not amplified with increasing streamwise distance; whereas, the velocity fluctuations occurring within the frequency bandwidth of 100 to 500 Hz are amplified with increasing streamwise distance. The power spectra at x = 28.9, 30.3, 32.3, and 34.3 inches in Fig. 86 show that the overall energy level is largely comprised of velocity fluctuations within two main frequency regions: 1) the frequencies below 100 Hz and 2) the frequencies corresponding to the T–S waves. From x = 38.3 to x = 40.3 inches the energy levels produced at the frequencies associated with the T–S waves became overshadowed by the increase of the PSD at all frequencies due to the bursts of wide–band turbulence within the boundary layer. As the turbulent bursting continued, i.e x = 40.3, 42.3, and 44.3, the power spectra resembled that of a fully turbulent flowfield in that the PSD was highest at lower frequencies and decreased monotonically with increasing frequencies.

Figs. 87 and 88 show the frequency spectra for the grid 0.5 and grid 1 configurations, respectively. From Fig. 87 note that the energy level was lowest for the laminar cases (x = 5.0 and 6.3 inches). From the neutral stability curve shown in Fig. 71, for $\mathbb{R}_{\delta^*} \cong 1000$, the velocity fluctuations occurring at frequencies between 500 Hz and 1300 Hz would be expected to be amplified, whereas velocity fluctuations occurring outside of this frequency range would be damped. Prior to the turbulent bursting (i.e before x = 8.3 inches) the power spectra shown in Fig. 87 partially follow the behavior predicted by linear stability theory in that the velocity

fluctuations occurring below a frequency of 500 Hz are not amplified with increasing streamwise distance. However, the velocity fluctuations occurring at frequencies greater than 1300 Hz were not damped as predicted by linear stability theory, but rather were amplified with increasing streamwise distance. As turbulent bursting was initiated (x = 8.3 inches) the value of the PSD increased at all frequencies – even for the frequencies within the 0 – 500 Hz range. With the increase in the intermittency with x distance the value of the PSD increased over the whole frequency spectra. The energy level remains relatively constant once the boundary layer is fully turbulent (i.e. x = 18.3 inches). Fig. 88 for the grid 1 configuration shows the same trends as the grid 0.5 case. The primary difference between the grid 0.5 and grid 1 configuration is that the grid 1 configuration has a higher energy content at the higher frequencies. The values of the PSD within the 0 – 1000 Hz frequency range are essentially the same for these two cases.

Compare Figs. 86, 87, and 88. All three figures show that for increasing streamwise distance the PSD increased over most of the frequency range, regardless of whether the flow is laminar or turbulent. In the laminar region this may indicate that the buffeting effect of the freestream turbulence on the laminar or pseudo–laminar boundary layer strengthens with increasing streamwise distance. Also for x locations where there was no evidence of turbulent bursting, the PSD remained relatively constant at the lowest frequency bandwidth – which is consistent with predictions based on linear stability. When the turbulent bursting occurred the PSD corresponding to the lowest frequency bandwidth increased. From Figs. 58

thru 60 recall that the rms of the velocity fluctuations increased through the laminar region, increased significantly during the burst of turbulence to a peak, and then dropped off as the boundary layer became fully turbulent. Likewise, in Figs 86, 87, and 88, the value of the PSD within the lowest frequency bandwidth increased and decreased in the same aforementioned manner. Therefore the low frequency portion of the power spectra is most sensitive to the changes in the rms of the velocity fluctuations within the boundary layer. This observation is more clearly shown in Fig. 89 in which values of the PSD (in this case obtained from Fig. 88) for a given frequency were plotted versus x distance. Fig 89 shows that the values of the PSD for the frequencies of 25, 50, and 100 Hz increased and decreased in a similar manner as the peak rms value shown in Fig. 59.

For the T–S path to transition case (grid 0 – Fig. 86) the unsteadiness within the boundary layer increases with streamwise distance in accordance with stability theory until the degree of unsteadiness reaches a level in which the turbulent bursting begins. To determine what value of unsteadiness is required to initiate turbulent bursting within the boundary layer, return to Figs. 70 and 58. From Fig. 70, turbulent bursting was first initiated somewhere between x = 34.3 inches and x = 38.3 inches. From Fig. 58 the peak rms of the fluctuating velocities within the boundary layer corresponding to the x locations where turbulent bursting first occurred was approximately 2–4% U_e. Similarly, for the bypass transition case (i.e. grid 0.5 – Fig. 87) the level of unsteadiness required to initiate turbulent bursts can be estimated from Figs. 74 and 59. Fig. 74 indicates that turbulent bursting first occurs at x $\cong$ 6 inches, and from Fig. 59 the peak rms of the

fluctuating velocities prior to turbulent bursting is approximately 3–4% U_e. Likewise for grid 1, the peak rms value of the fluctuating velocities within the boundary layer before turbulence bursts occur is approximately 3.5% U_e. There appears to be a critical value ($\simeq$ 3 to 3.5% U_e) of the peak rms of the velocity fluctuations within the boundary layer at which the breakdown to turbulence bursting occurs. This idea of a critical intensity of the velocity fluctuations within a boundary layer was also proposed by Elder [13]. Elder conducted an investigation to determine the conditions required to initiate a turbulent spot within a laminar boundary layer. Elder's results indicated that regardless of how disturbances are generated within a laminar boundary layer, turbulent spots will occur when the velocity fluctuations over most of the boundary layer thickness exceed 2% U_e. In this investigation not only does turbulent bursting occur when the velocity fluctuations within the boundary layer exceed 2% U_e, but when the peak value of the velocity fluctuations exceed a critical value of 3 to 3.5% U_e. Therefore, regardless of the transition mechanism, once the disturbances in the laminar boundary layer reach a critical value turbulence bursting begins.

Why do we have transition via the T–S path for grid 0 whereas, for grid 0.5 and grid 1 bypass transition occurs? The bypass transition case is usually considered to result from large non–linear disturbances. Yet, in this investigation the bypass was caused by relatively low disturbances (relatively low because they were on the same order as the disturbances associated with the T–S path transition case). In addition, recall that the boundary layer transition via the T–S path occurred from disturbances

inherent to the wind tunnel. For the T–S path to transition case, the disturbances in the freestream occurring at certain frequencies were received by the boundary layer and amplified in accordance with linear stability theory until the critical level of the unsteadiness was reached and turbulence bursting began. For the bypass transition case, the freestream disturbances buffeted the boundary layer until the unsteadiness within the boundary layer reached the critical value and turbulent bursting initiated. In both the T–S path and bypass path to transition the value of $\mathbb{R}_{\delta^*}$ was within the range shown on the neutral stability curve, yet in the bypass case, the growth of the disturbances did not follow the linear stability theory. Although the reason for this is not quite clear at this time, the following explanation is plausible.

Freestream frequency spectra for the grid 0, 0.5, and 1 configurations are shown in Figs. 90, 91, and 92. The freestream turbulence intensity (recall from Fig. 17) for the grid 0 case was 0.3%, whereas for the grid 0.5 and grid 1 configurations the freestream turbulence intensity was approximately 0.65% and 0.95%, respectively. For the grid 0 case the freestream disturbances are largely composed of velocity fluctuations within the 0 to 100 Hz frequency range. The viscous region of the boundary layer damps these low frequency disturbances. However, the disturbances within the frequency range which can be (according to linear stability theory) received and amplified by the boundary layer are relatively small in magnitude. However, for the grid 0.5 and grid 1 cases the freestream disturbances within the frequency range of 500 to 1300 Hz (recall this is the

frequency range in which the disturbances should be received and amplified in the boundary layer according to the neutral stability curve) are approximately two orders of magnitude higher than the freestream disturbances shown for the grid 0 case. Apparently, the freestream disturbances generated by grid 0.5 and grid 1 are sufficiently large so as to overwhelm the boundary layer such that the critical value for the velocity fluctuations is obtained immediately and turbulence bursting initiates. Also note that the unsteadiness level within the laminar boundary layer for the grid 0.5 case is higher than the level observed within a laminar boundary layer for the T–S path to transition case. For example the values of the PSD corresponding to the laminar boundary layers for transition via the T–S path range from 10^{-4} to 10^{-7} V^2 / Hz over a 500 Hz frequency range (see Fig. 86) and the values of the PSD corresponding to the laminar boundary layers for the bypass transition case (Fig. 87) range from 10^{-3} to 10^{-6} V^2 / Hz over a 1300 Hz frequency range. So, even though the freestream turbulence intensities varied only from 0.3% for transition via the T–S path to 0.65% for the bypass transition process, the values of the disturbances within the frequency range of the linear stability curve varied by two orders of magnitude. Therefore, possibly, the frequency distribution of the freestream disturbances and not only the overall value of the freestream disturbance influence the mechanism of boundary layer transition.

CHAPTER VI

SUMMARY & CONCLUSIONS

A detailed investigation to compare the boundary layer transition process via the T–S path to the boundary layer transition process in which the disturbances are initially non–linear in amplitude has been conducted. The flat–plate test surface with zero pressure gradient and ambient test conditions was used as the research vehicle. The freestream turbulence levels were measured to be 0.3% for grid 0, 0.65% for grid 0.5, 0.95% for grid 1, 1.95% for grid 2, 3–5% for grid 3, and 4–6% for grid 4. The turbulence intensities for all grids agreed with the empirical correlation of Baines and Peterson [26] where $Tu \cong 1.12\ (\frac{l}{b})^{-5/7}$. Integral length scale measurements grew with downstream distance according to the following power law: $\frac{L}{b} \propto (\frac{x}{b})^{0.56}$ which also agrees with experimental findings of Baines and Peterson [26]. The power spectra of the freestream turbulence agreed with Taylor's [28] one–dimensional power spectrum for isotropic turbulence. Therefore based on the measured values of turbulence intensity, integral length scale, and frequency spectra, it was concluded that the rectangular–bar grid–generated turbulence exhibited the characteristics of isotropic turbulence. In addition, the results for grids 0.5, 1 and 2 indicated that the turbulence is homogeneous and isotropic.

For each level of freestream turbulence, boundary layer surveys of the

mean velocity and rms of the velocity fluctuations were acquired at several streamwise locations with a linearized hot–wire constant temperature anemometer system. From these surveys the resulting boundary layer shape factor, inferred skin friction coefficients, and distribution of the velocity fluctuations through the boundary layer were used to identify the transition region corresponding to each level of freestream turbulence. Also, the intermittency factor determined from time traces of flush–mounted hot films located along the centerline of the flat plate was used to indicate the location of the transition region. The location of the transition region as determined by the flush–mounted hot–films was found to be in good agreement with the transition regions indicated by steady state heat transfer measurements – Blair [33] –which were acquired within a similar wind tunnel operating under similar conditions as those associated with this investigation. Not only did the different methods in determining the transition region compare well with each other but they also were in agreement with predictions of van Driest and Blumer [8], Abu–Ghannam and Shaw [10], Seyb [34], and Dunham [35]. One discrepancy arose from these results depicting the location of the transition region. The boundary layer surveys indicated that for grid 0.5 the boundary layer was turbulent by x = 18.3 inches, whereas for grid 1 the boundary layer was not fully turbulent at x = 21 inches. However, the intermittency factor determined from the flush–mounted hot films indicated an earlier transition start and end for the grid 1 configuration than was indicated for the grid 0.5 case, as would be expected based on the freestream turbulence level associated with each grid. A possible explanation could be that since the length scale of

the freestream turbulence for the grid 1 case was approximately twice that resulting from grid 0.5, the mean velocity profile for grid 1 could withstand a higher intermittency. Another result was that for the turbulent boundary layers the skin friction coefficients, determined by the Clauser fit technique, agreed well with empirical correlations of White [1] and Kays [29]. Attempts to calibrate the flush–mounted hot films for wall shear stress within the boundary layer transition region were not successful due to the thermal lag associated with the heat conduction in the substrate of the hot film [30]. In summary, the initiation of the transition region was identified for freestream turbulence levels of 0.3%, 0.65% and 0.95%. At higher freestream disturbance levels the boundary layer transition was in progress at the first survey location.

Simultaneous time traces of the flush–mounted hot films revealed that for the lowest freestream turbulence level of 0.3% the initial disturbances were the unstable two–dimensional Tollmien Schlichting (T–S) waves. However, for the higher freestream turbulence levels of 0.65% and 0.95%, the T–S waves were bypassed and the initial disturbances were finite and non–linear in amplitude. The effect of the bypass transition was to move the starting location of the transition region from $x \cong 40.3$ inches for the transition process via the T–S path ($Tu \cong 0.3\%$) to $x \cong 8$ inches for the bypass transition process ($Tu \cong 0.65\%$). Once both the T–S and bypass transition mechanisms were identified the following detailed measurements were acquired to study and compare the two transition mechanisms: 1) simultaneous time traces of a flush–mounted hot film and a hot wire were acquired for the hot wire located at different depths within the boundary

layer, 2) crosscorrelations between flush–mounted hot films were performed, 3) two–point correlations between a flush–mounted hot film and a hot wire positioned at various locations throughout the flowfield were acquired, and 4) boundary layer spectra at various streamwise distances through the transition region were obtained. The following conclusions resulted from these measurements:

1. The bursting of turbulence at the onset of the bypass transition was characteristic of a sudden explosion of the boundary layer from laminar flow behavior to fully turbulent flow behavior.
2. The turbulent burst appears to encompass the entire boundary layer thickness and is convected downstream at a higher velocity near the edge of the boundary layer than it is near the test surface.
3. The convective velocity in the streamwise direction of the turbulent bursting near the wall was measured to be 0.7 U_e, independent of the transition mechanism.
4. Two–point correlations indicated that the turbulent bursting was a highly random process with no hint of any periodicity or two–dimensionality. Also, the characteristics of the turbulent bursting were similar for both the T–S path and the bypass path to transition.
5. The velocity fluctuations associated with the T–S path to transition occurred at low frequencies (0 – 500 Hz.); whereas, the velocity fluctuations associated with the bypass transition

process occurred over a higher frequency range (0 – 10 Khz).

6. The low frequency end of the boundary layer spectra depicted the development of the boundary layer in that the energy contribution from the low frequency end of the spectra was constant for laminar flow, increased with the initiation of the turbulent bursting up to the 50% intermittency point, and then decreased as the flow became fully turbulent. In contrast, the high frequency end of the spectra increased until the flow was turbulent.

7. A critical value for the peak rms of the velocity fluctuations within the boundary layer of 3 to 3.5% U_e was identified. Once the unsteadiness in the boundary layer reached the critical value, turbulent bursting initiated, regardless of the transition mechanism.

8. The freestream turbulence intensities varied only from 0.3% for the case of transition via the T–S path to 0.65% for the bypass transition process. However, the values of the disturbances within the frequency range for which amplification would occur according to linear stability considerations varied by two orders of magnitude. Therefore, possibly, the frequency distribution of the freestream disturbances and not only the overall value of the freestream disturbance influence the mechanism of boundary layer transition.

These results emphasize the importance of the frequency spectra, length

scale and rms intensity of the freestream disturbances in predicting the transition region. Clearly, more effort must be put forth to establish the effect of each of these parameters on the receptivity of the boundary layer.

REFERENCES

1. White, F.M., *Viscous Fluid Flow*, McGraw–Hill, New York, NY, 1974.

2. Schubauer, G.B. and Skramstad, H.K., "Laminar Boundary Layer Oscillations on a Flate Plate", *NACA Report*, No. 909, 1948.

3. Klebanoff, P.S., Tidstrom, K.D., and Sargent, L.H., "The Three–Dimensional Nature of Boundary Layer Instability," *Journal of Fluid Mechanics*, Vol. 12, 1962, pp. 1–34.

4. Tollmien, W., " Uber die Entstehung der Turbulenz", English Translation in NACA TM 609, 1931.

5. Schlichting, H., *Boundary Layer Theory*, Seventh Edition, McGraw–Hill, New York, NY, 1959.

6. Schubauer, G.B., and Skramstad, H.K., "Laminar Boundary Layer Oscillations and Stability of Laminar Flow," National Bureau of Standards Paper 1772.

7. Morkovin, M.V., "Instability Transition to Turbulence and Predictability," *NATO AGARDograph No. 236*, 1978.

8. van Driest, E.R. and Blumer, C.B., "Boundary Layer Transition: Free–stream Turbulence and Pressure Gradient Effects," *AIAA Journal*, Vol. 1, No. 6, June 1963, pp. 1303–1306.

9. Hall, D.J. and Gibbings, J.C., "Influence of Stream Turbulence and Pressure Gradient Upon Boundary Layer Transition," *Journal of Mech. Engr. Div.*, Vol. 14, No. 2, 1972, pp. 134–136.

10. Abu–Ghannam, B.J., and Shaw, R., "Natural Transition of Boundary Layers – The Effects of Turbulence, Pressure Gradient, and Flow History," *Journal of Mech. Engr. Sci.*, Vol. 22, No. 5, 1980, pp. 213–228.

11. Blair, M.F., "Influence of Free–Stream Turbulence on Boundary Layer Transition in Favorable Pressure Gradients," *Trans. of ASME, Journal of Engr. for Power*, Vol. 104, October 1982, pp. 743–750.

12. Dyban, YE. P., Epik, E. YA., and Suprun, T. T.," Characteristics of the Laminar Boundary Layer in the Presence of Elevated Free–Stream Turbulence," *Fluid Mech.–Soviet Research*, Vol. 5, No. 4, 1976, pp. 31–36.

13. Elder, J.W., "An Experimental Investigation of Turbulent Spots and Breakdown to Turbulence," *Journal of Fluid Mechanics*, Vol. 9, 1960, pp. 235–246.

14. Paik, D.K., and Reshotko, E., "Low Reynolds Number Boundary Layers in a Disturbed Environment," NASA CR–175031, Jan. 1986.

15. Sohn, K.H. and Reshotko, E., "Transition in a Disturbed Environment," Case Western Reserve University Report FTAS/TR–87–189, (Also, M.S. Thesis of K.H. Sohn, Case Western Reserve University, 1986).

16. Perry, A.E., *Hotwire Anemometry*, Oxford University Press, New York, 1982.

17. *Model 1052 Linearizer Instruction Manual* TSI Incorporated, P.O. Box 43394 ,500 Cardigan Rd., St. Paul MN 55164.

18. Bellhouse, B.J. and Schultz, D.L., "Determination of Mean and Dynamic Skin Friction, Separation and Transition in Low Speed Flow with a Thin–Film Heated Element," *Journal of Fluid Mechanics*, Vol. 24, Part 2, 1966, pp. 379–400.

19. Sandborn, V.A., "Evaluation of the Time–Dependent Surface Shear Stress in Turbulent Flows," ASME Paper 79–WA/FE–17, 1979.

20. Ramaprian, B.R. and Tu, S.W., "Calibration of a Heat Flux Gage for Skin Friction Measurement," *Journal of Fluids Engineering*, Vol. 105, Dec. 1983.

21. Clauser, F.H., "The Turbulent Boundary Layer," *Advances in Applied Mechanics*, Vol. IV, 1956, Academic Press, New York, NY , pp. 1–51.

22. Blair, M.F., Bailey, D.A., and Schlinker, R.H., "Development of a Large–Scale Wind Tunnel for the Simulation of Turbomachinery Airfoil Boundary Layers," *Transactions of the ASME Journal of Engineering for Power*, Vol. 103, October 1981, pp. 678–687.

23. Bradshaw, P., *An Introduction to Turbulence and its Measurement*, Pergamon Press, New York, NY, 1971.

24. Southworth, R.W., and Deleeuw, S.L., *Digital Computation and Numerical Methods*, McGraw–Hill, New York, NY, 1965, pp. 368–385.

25. Musker, A.J., "Explicit Expression for the Smooth Wall Velocity Distribution in a Turbulent Boundary Layer," *AIAA Journal*, Vol. 17, No. 6, June 1979, pp. 655–657.

26. Baines, W.D., and Peterson, E.G., "An Investigation of Flow through Screens," *Transactions of the ASME*, Vol. 73, No. 5, July 1951, pp. 467–480.

27. Compte–Bellot, G. and Corrsin, S., "The use of a Contraction Nozzle to Improve Isotropy of Grid Generated Turbulence," *Journal of Fluid Mechanics*, Vol. 25, 1966, pp. 657–682.

28. Hinze, J.O., *Turbulence, an Introduction to its Mechanism and Theory*, McGraw–Hill, New York, NY, 1959, p. 61.

29. Kays, W.M. and Crawford, M.E., *Convective Heat and Mass Transfer*, McGraw–Hill, New York, NY, 1980, p. 174.

30. Cook, W.J., Giddings, T.A., and Murphy, J.D., "Response of Hot Element Wall Shear Stress Gage in Laminar Oscillating Flow," AIAA/ASME 4^{th} Fluid Mechanics, Plasma Dynamics and Lasers Conference, May 1986, Atlanta, Georgia, AIAA–86–1100.

31. Ligrani, P.M. and Bradshaw, P., "Spatial Resolution and Measurement of Turbulence in the Viscous Sublayer using Subminiature Hot–Wire Probes", *Experiments in Fluids*, Vol. 5, 1987, pp.407–417.

32. Klebanoff, P.S., "Characteristics of Turbulence in a Boundary Layer with Zero Pressure Gradient," *NACA Report, No. 1247*, 1955.

33. Blair, M.F., "Influence of Free–Stream Turbulence on Turbulent Boundary Layer Heat Transfer and Mean Profile Development, Part I – Experimental Data," *Trans. of ASME, Journal of Heat Transfer*, Vol. 105, February 1983, pp. 33–40.

34. Seyb, N.J., "The Role of Boundary Layers in Axial Flow Turbomachines and Prediction of their Effects," AGARD–AG–164, April 1972, pp. 261–274.

35. Dunham, J., "Predictions of Boundary Layer Transition on Turbomachinery Blades," AGARD–AG–164, 1972.

36. Mack, L.M., "Transition Prediction and Linear Stability Theory," AGARD–CP–224, 1977.

37. Schubauer, G.B., and Klebanoff, P.S., "Contributions on the Mechanics of Boundary Layer Transition," *NACA TN 3489*, 1955.

38. Bendat, J.S., and Piersol, A.G., *Random Data: Analysis and Measurement Procedures*, Wiley–Interscience, NY, 1971.

TABLE I

SUMMARY OF GRID 0 VELOCITY PROFILES

X (in.)	θ (in.)	H	R_θ	$C_f x10^6$	U_τ (ft/s)	U_e/U_τ	U_c(ft/s)
29.0	0.01484	2.629	716	571	1.647	59.18	97.5
30.3	0.01463	2.682	706	551	1.613	60.25	97.2
32.3	0.01543	2.680	740	525	1.565	61.72	96.6
34.3	0.01556	2.620	726	518	1.514	62.14	94.1
36.3	0.01628	2.550	772	524	1.552	61.78	95.9
38.3	0.01635	2.615	752	512	1.502	62.50	93.9
40.3	0.01803	2.536	835	609	1.627	57.31	93.2
42.3	0.01972	2.075	908	965	2.038	45.52	92.8
44.3	0.02179	1.783	1005	1487	2.532	36.67	92.9
45.7	0.02377	1.691	1101	1971	2.919	31.85	93.0

TABLE II

SUMMARY OF GRID 0.5 VELOCITY PROFILES

X (in.)	θ (in.)	H	R_θ	$C_f \times 10^6$	U_τ (ft/s)	U_e/U_τ	U_e(ft/s)
5.0	0.006158	2.762	310	1233	2.504	40.26	100.8
6.3	0.006946	2.735	350	1109	2.370	42.25	100.6
8.3	0.008319	2.665	420	1070	2.333	43.21	100.8
10.3	0.010090	2.310	512	1404	2.680	37.76	101.2
12.3	0.011941	2.079	607	2143	3.315	30.56	101.3
14.3	0.014208	1.748	737	2867	3.929	26.42	103.8
16.3	0.017920	1.642	934	3934	4.627	22.54	104.3
18.3	0.020562	1.424	1079	4704	5.093	20.62	105.0
20.3	0.023191	1.408	1217	4569	5.023	20.90	105.0

TABLE III

SUMMARY OF GRID 1 VELOCITY PROFILES

X (in.)	θ (in.)	H	R_θ	$C_f x10^6$	U_τ (ft/s)	U_e/U_τ	U_e(ft/s)
4.92	0.006899	2.585	325	1302	2.542	39.18	99.6
5.84	0.007336	2.649	344	1198	2.433	40.85	99.4
6.34	0.007740	2.595	364	1178	2.416	41.18	99.5
7.00	0.008288	2.533	390	1129	2.368	42.10	99.7
8.00	0.008851	2.530	417	1073	2.309	43.18	99.7
9.00	0.009295	2.534	440	1172	2.423	41.27	100.0
10.0	0.009437	2.565	444	1401	2.639	37.78	99.7
11.0	0.009876	2.470	465	1666	2.877	34.65	99.7
12.0	0.011414	2.269	538	1949	3.118	32.04	99.9
13.0	0.012120	2.156	573	2233	3.343	29.91	100.0
14.0	0.013598	2.016	643	2505	3.541	28.24	100.0
15.0	0.015370	2.094	728	2757	3.722	26.92	100.2
16.0	0.016422	2.023	777	2980	3.868	25.90	100.2
17.0	0.019010	1.895	902	3172	4.000	25.10	100.4
18.0	0.019595	1.868	929	3331	4.096	24.49	100.3
19.0	0.020797	1.826	984	3460	4.167	24.05	100.2
20.0	0.022632	1.774	1070	3565	4.227	23.68	100.1
21.0	0.024310	1.738	1152	3654	4.288	23.37	100.2

TABLE IV

SUMMARY OF GRID 2 VELOCITY PROFILES

X (in.)	θ (in.)	H	R_θ	$C_f \times 10^6$	U_τ (ft/s)	U_c/U_τ	U_c(ft/s)
5.0	0.00795	1.794	391	3395	4.120	24.10	99.3
6.2	0.01010	1.663	498	3752	4.331	22.95	99.4
7.2	0.01349	1.553	667	3922	4.406	22.58	99.5
8.2	0.01348	1.527	668	5308	5.132	19.41	99.6
9.2	0.01604	1.499	796	5034	5.005	19.92	99.7
10.2	0.01768	1.478	878	4885	4.925	20.24	99.7
12.2	0.02167	1.468	1073	4590	4.775	20.88	99.7
14.2	0.02524	1.447	1254	4391	4.672	21.34	99.7
16.2	0.02827	1.473	1405	4248	4.601	21.69	99.8
18.2	0.03223	1.437	1605	4125	4.547	21.97	99.9
20.2	0.03589	1.421	1792	4016	4.495	22.25	100.0

TABLE V

SUMMARY OF GRID 3 VELOCITY PROFILES

X (in.)	θ (in.)	H	R_θ	$C_f x 10^6$	U_τ (ft/s)	U_e/U_τ	U_e(ft/s)
5.0	0.01046	1.515	531	5670	5.44	18.78	102.2
10.2	0.02079	1.444	1059	4693	4.964	20.65	102.5
20.2	0.03759	1.357	1916	4118	4.649	22.05	102.5

TABLE VI

SUMMARY OF GRID 4 VELOCITY PROFILES

X (in.)	θ (in.)	H	R_θ	$C_f x10^6$	U_τ (ft/s)	U_c/U_τ	U_c(ft/s)
5.0	0.01265	1.502	634	5445	5.267	19.18	101.0
10.2	0.02266	1.419	1151	4651	4.927	20.74	102.2
20.2	0.05518	1.330	2133	4124	4.692	21.97	103.1

TABLE VII

SUMMARY OF TRANSITION REGIONS

Grid	Method	Onset (in.)	End (in.)
0	Mean Profiles	40.3	> 45.7
	Shape Factor	40.3	> 45.7
	Skin Friction	38.0	> 45.7
	RMS Profiles	40.0	> 45.7
	Intermittency	38.3	≈ 50.2
0.5	Mean Profiles	9.3	≈ 18.3
	Shape Factor	9.3	≈ 18.3
	Skin Friction	9.3	≈ 20.3
	RMS Profiles	8–9	> 20.3
	Intermittency	6.2	≈ 24.2
1	Mean Profiles	9–10	> 21
	Shape Factor	11	> 21
	Skin Friction	9	> 21
	RMS Profiles	9	> 21
	Intermittency	4.2	≈ 18
2	Mean Profiles	< 5	≈ 8.2
	Shape Factor	< 5	≈ 10.2
	Skin Friction	< 5	≈ 9.2
	RMS Profiles	< 5	≈ 12.2
	Intermittency	< 4	≈ 10.2

TABLE VIII

TRANSITION ONSET BASED ON EMPIRICAL CORRELATIONS

Grid	Method	Onset (in.)
0	Van Driest & Blumer	≈ 38
	Seyb	<< 29
	Abu–Ghannam & Shaw	≈ 41
	Dunham	< 29
0.5	Van Driest & Blumer	≈ 18
	Seyb	≈ 10
	Abu–Ghannam & Shaw	≈ 13
	Dunham	< 5
1	Van Driest & Blumer	≈ 11
	Seyb	≈ 10
	Abu–Ghannam & Shaw	≈ 12
	Dunham	≈ 12
2	Van Driest & Blumer	≈ 3
	Seyb	≈ 5
	Abu–Ghannam & Shaw	< 5
	Dunham	≈ 5

Van Driest & Blumer (1): $\sqrt{\mathbb{R}_x} = \dfrac{-1 + (1 + 132500\ T_u^{\,2})}{39.2\ T_u^{\,2}}$

Seyb (32): $$\mathbb{R}_\theta = \frac{1000}{1.2 + 70\ T_u} + 10\left[\frac{0.09}{0.0106 + 3.6\ T_u}\right]^{2.62}$$

Abu–Ghannam & Shaw (4): $$\mathbb{R}_\theta = 163 + \exp^{(6.91 - 100\ T_u)}$$

Dunham (33): $$\mathbb{R}_\theta = \left[0.027 + 0.73\ \exp^{-80\ T_u}\right]\left[550 + \frac{680}{1 + 100\ T_u}\right]$$

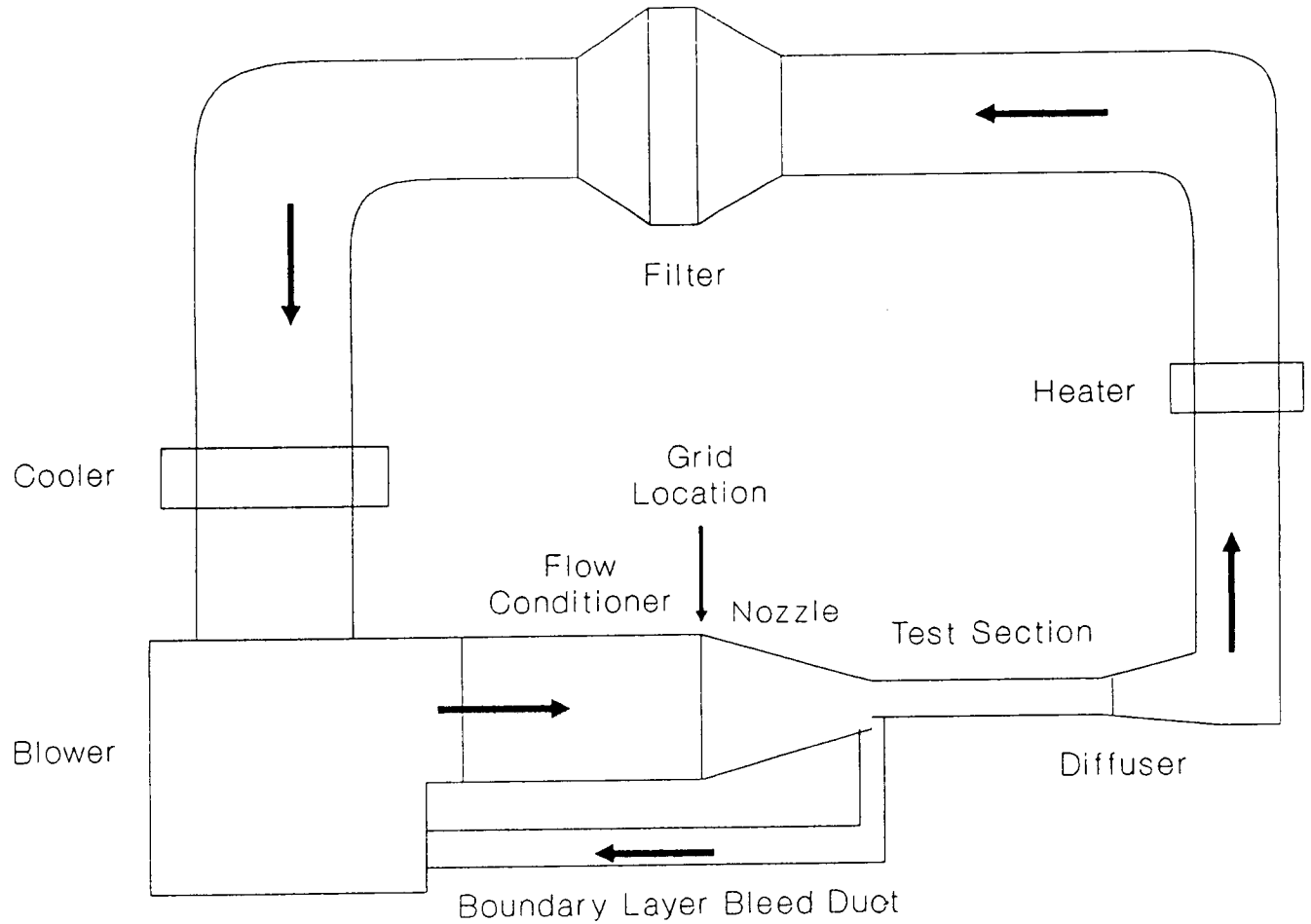

Fig. 1 Schematic diagram of the wind tunnel.

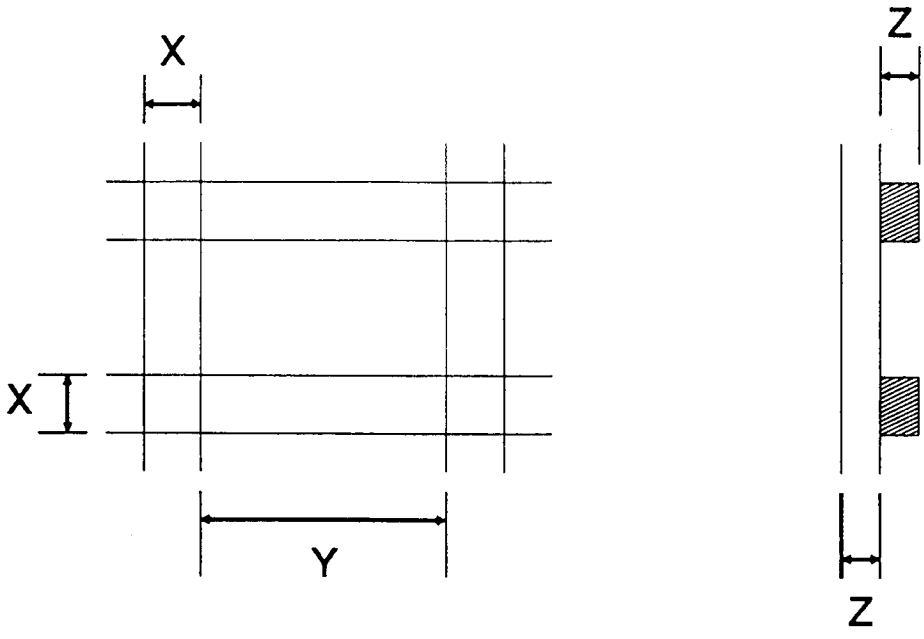

GRID	X (IN.)	Y (IN.)	Z (IN.)	% OPEN AREA
1	0.19	0.69	3/16	62
2	0.50	2.06	3/8	65
3	1.50	5.50	1/2	62
4	2.00	7.00	1/2	61

Fig. 2 Turbulence grid dimensions.

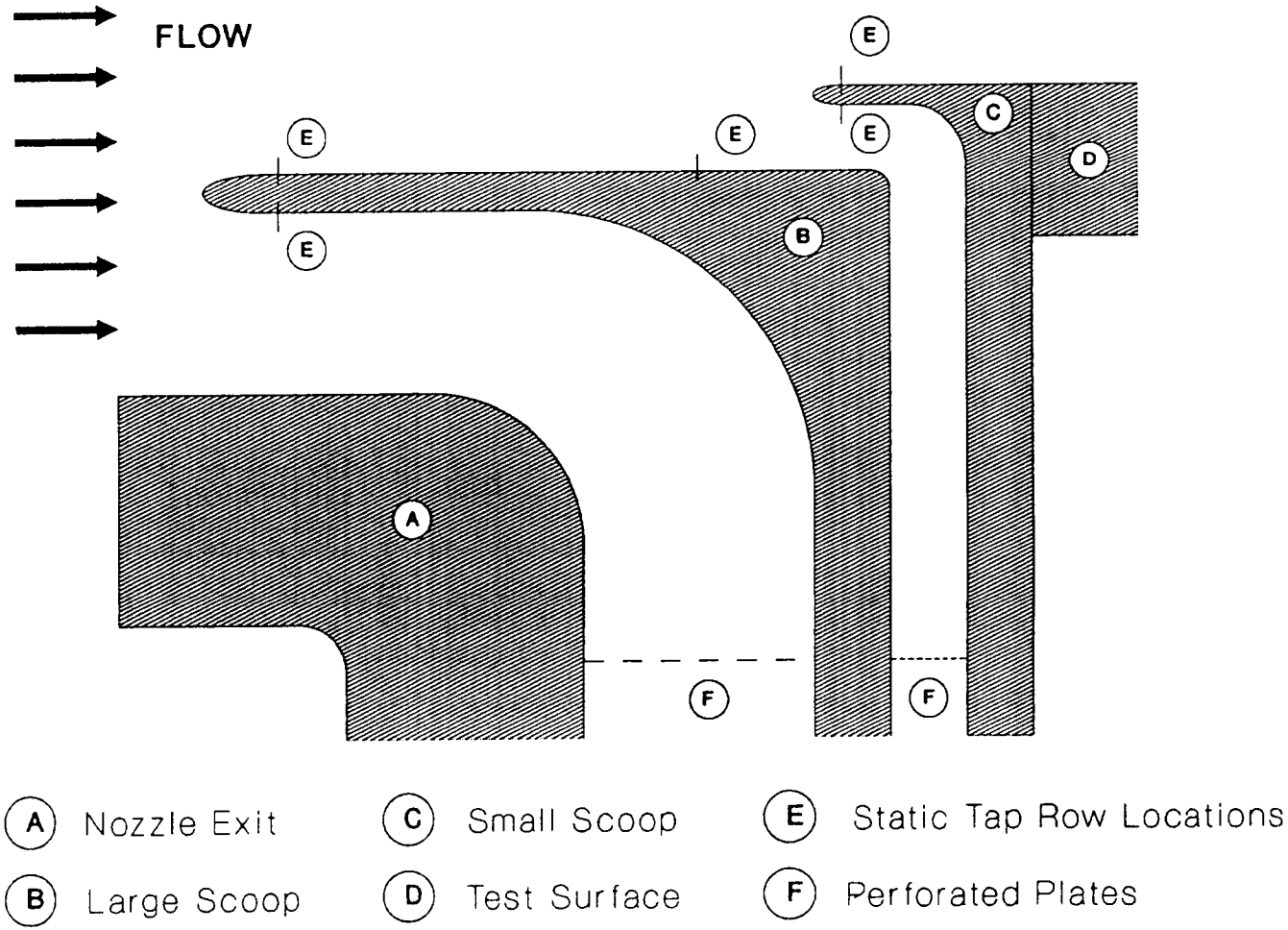

Fig. 3 Boundary bleed scoop arrrangement.

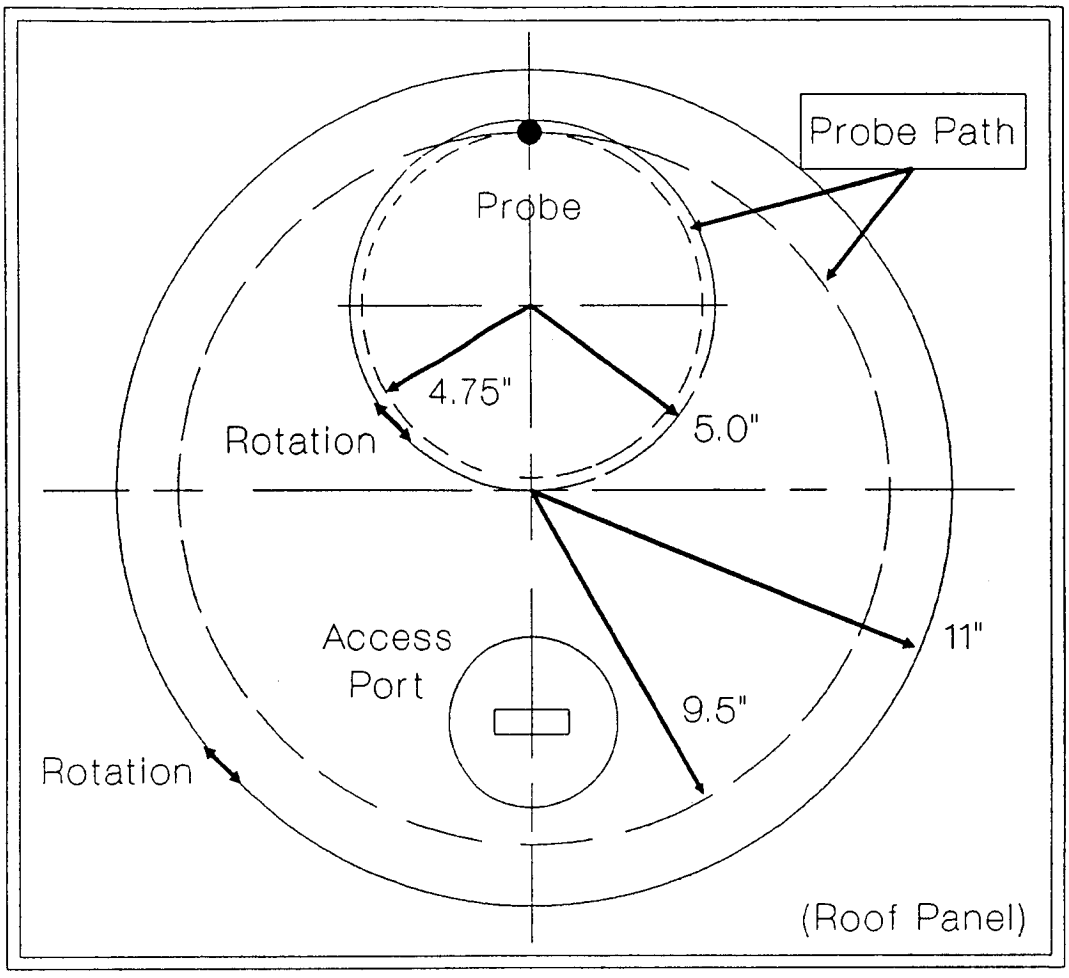

Fig. 4 Double–eccentric plate arrangement.

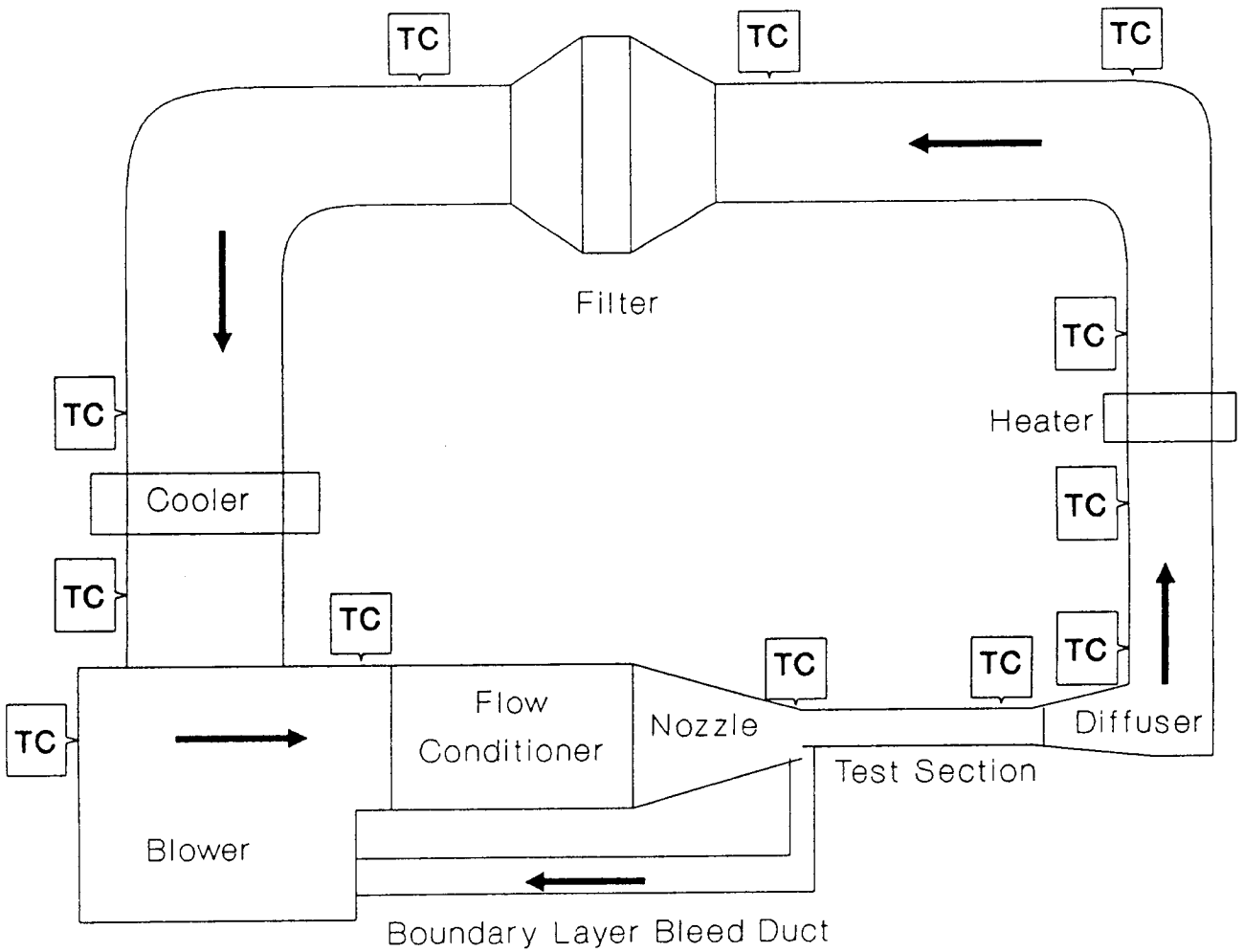

Fig. 5 Location of rig thermocouples.

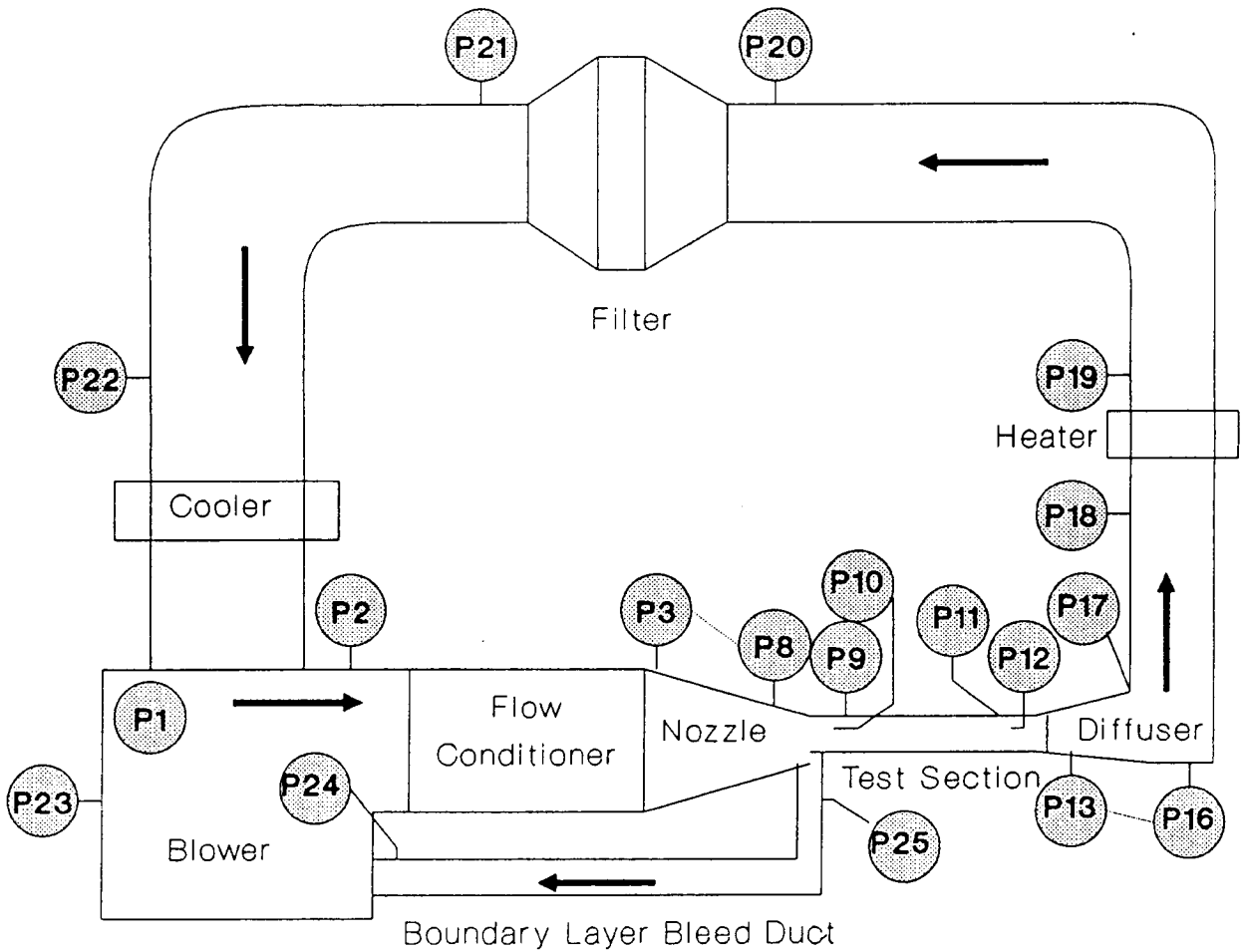

Fig. 6 Location of rig pressure taps.

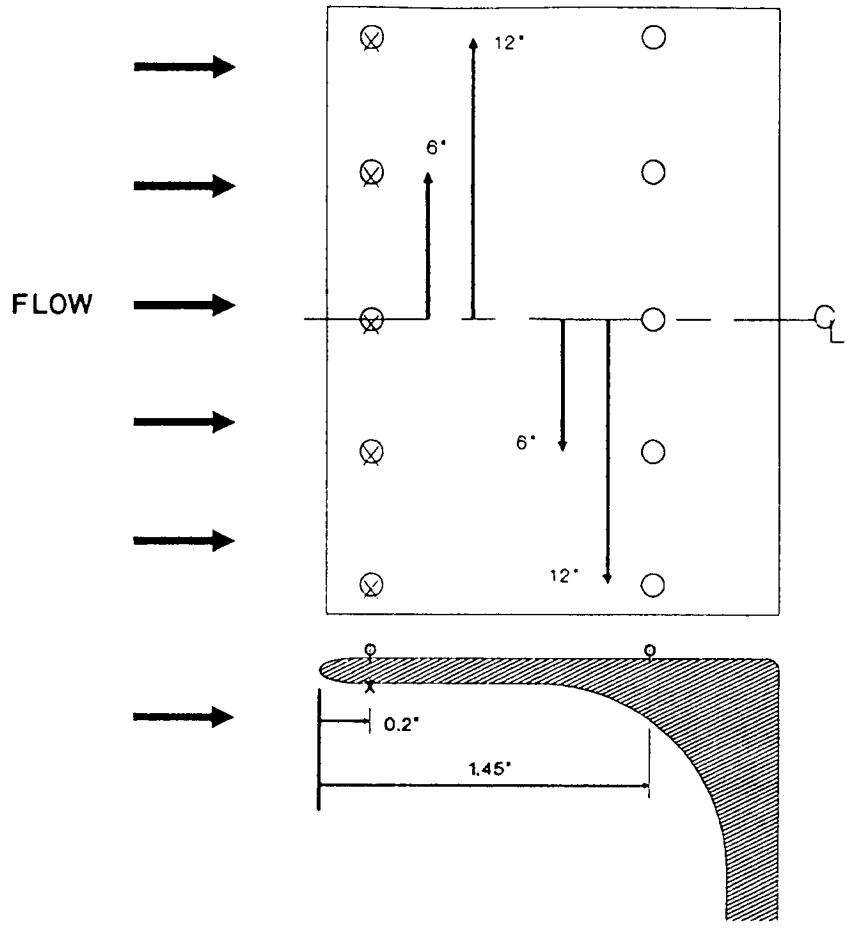

Fig. 7a Boundary layer bleed scoop statics – large scoop.

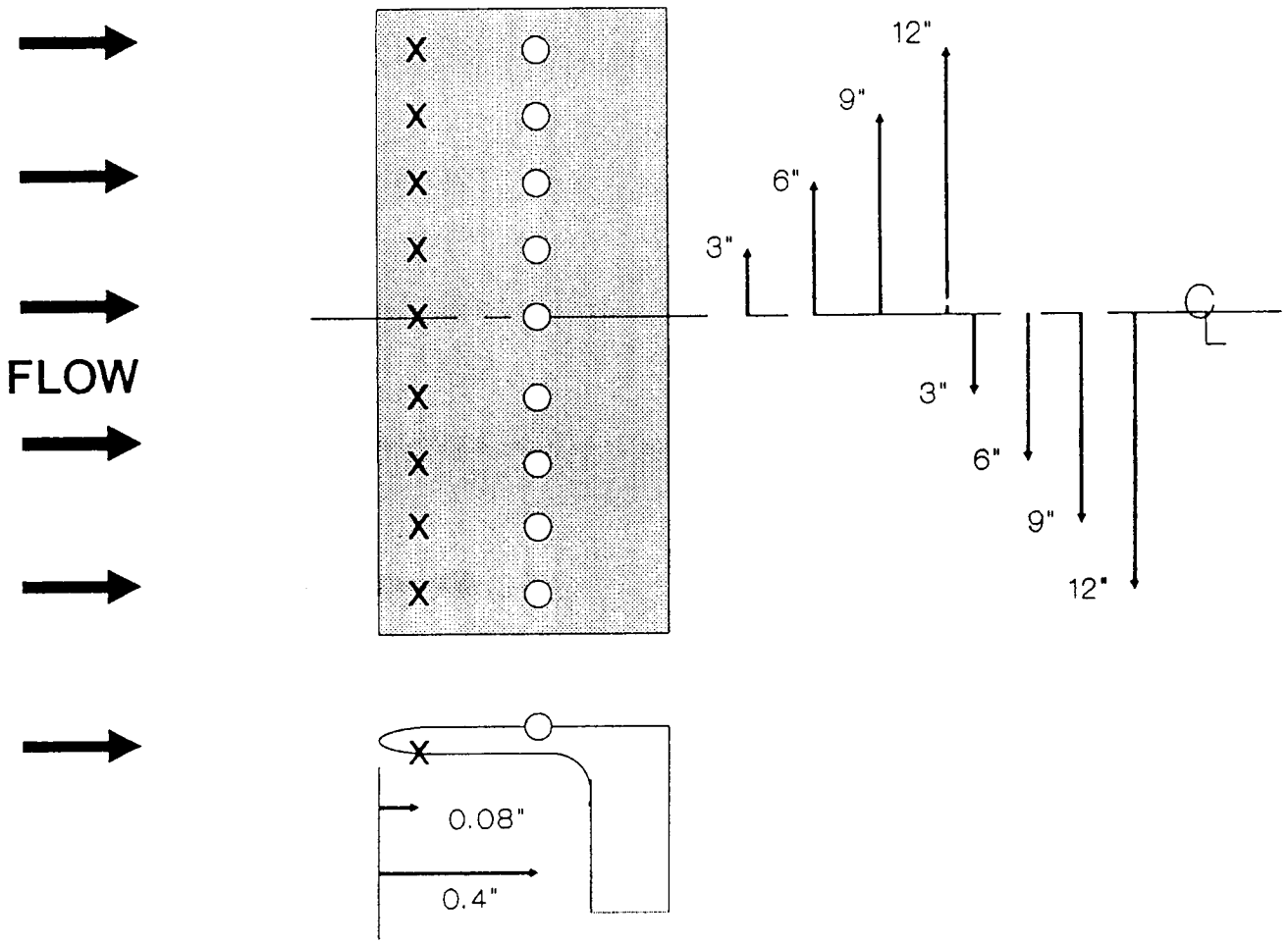

Fig. 7b Boundary layer bleed scoop statics – small scoop.

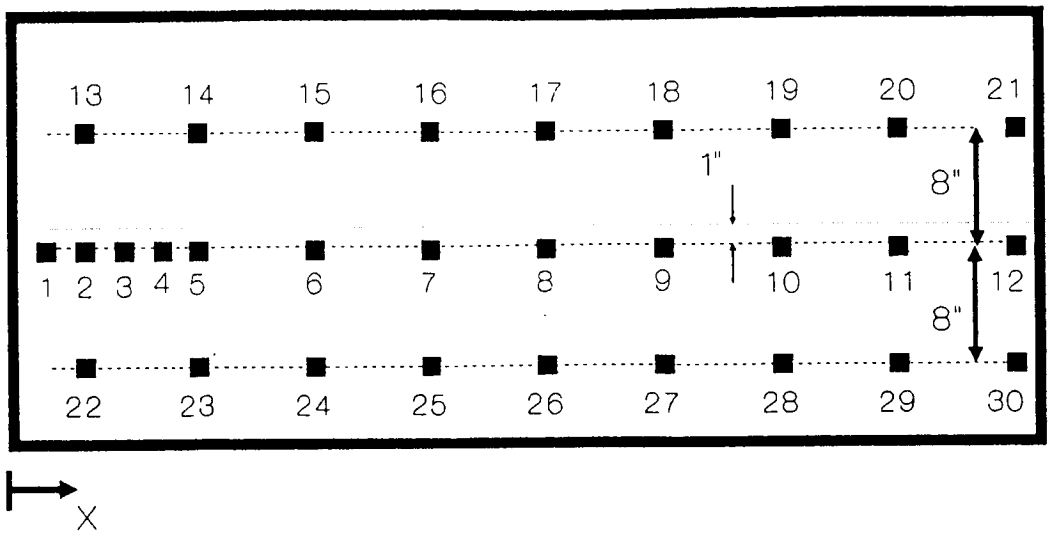

LOCATION #	X (IN.)	LOCATION #	X (IN.)	LOCATION #	X (IN.)
1	3.24	11	47.20	21	53.19
2	5.24	12	53.20	22	5.23
3	7.23	13	5.22	23	11.23
4	9.23	14	11.21	24	17.22
5	11.22	15	17.21	25	23.22
6	17.21	16	23.20	26	29.23
7	23.22	17	29.22	27	35.23
8	29.21	18	35.20	28	41.24
9	35.22	19	41.19	29	47.24
10	41.21	20	47.19	30	53.25

Fig. 8 Test section static pressure taps.

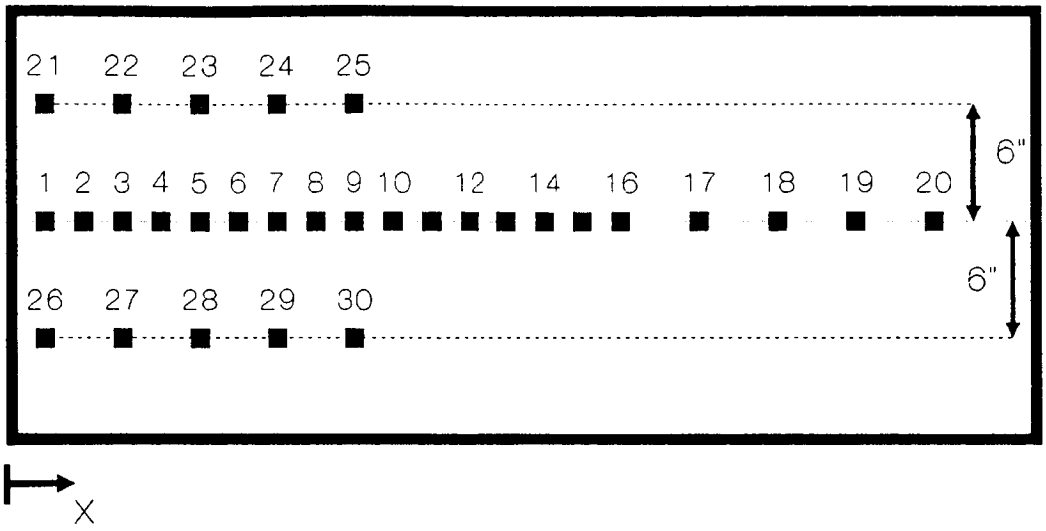

HOT FILM #	X (IN.)	HOT FILM #	X (IN.)	HOT FILM #	X (IN.)
1	4.22	11	24.25	21	6.20
2	6.22	12	26.25	22	12.31
3	8.22	13	28.26	23	18.21
4	10.22	14	30.26	24	24.20
5	12.23	15	32.26	25	30.20
6	14.23	16	34.26	26	6.22
7	16.23	17	38.27	27	12.22
8	18.24	18	42.26	28	18.22
9	20.24	19	46.25	29	24.22
10	22.24	20	50.25	30	30.22

Fig. 9 Test section hot–film locations.

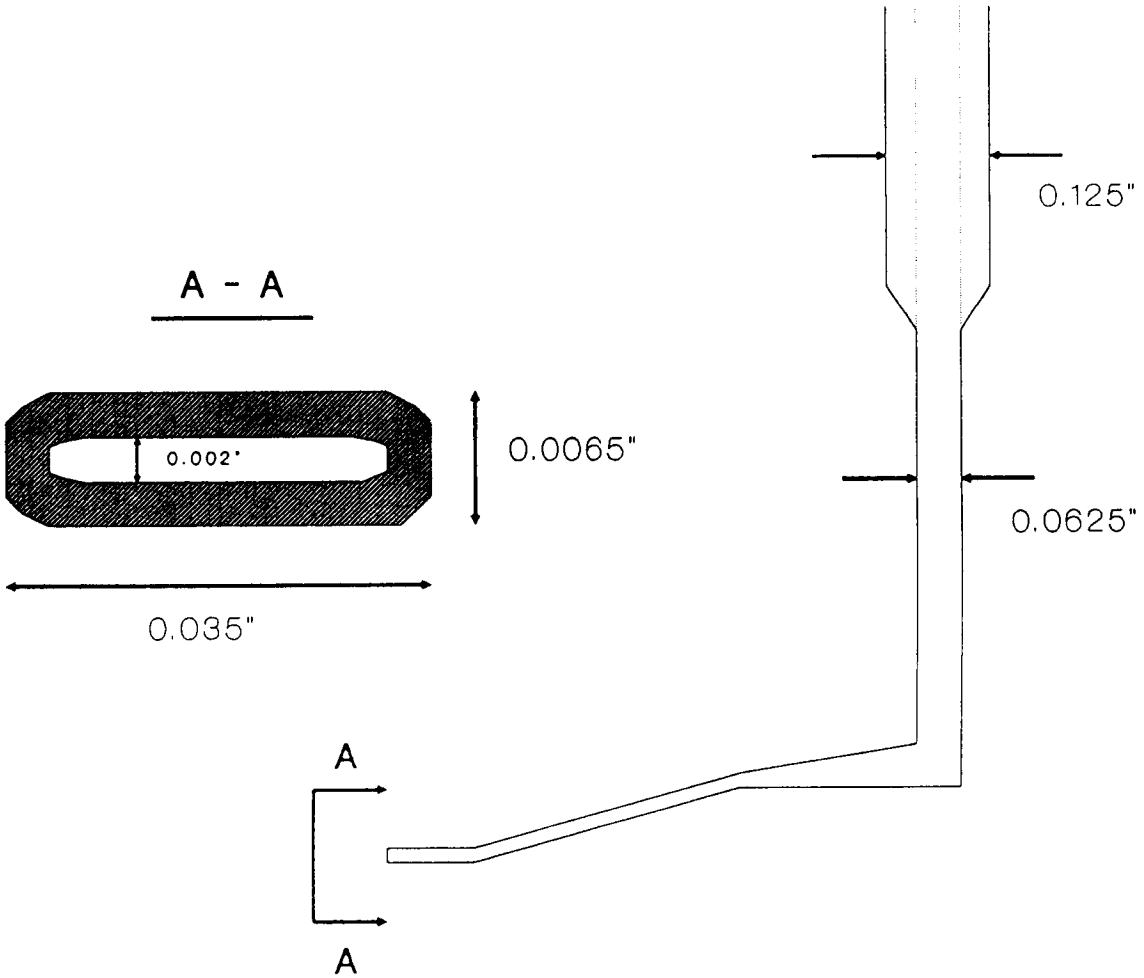

Fig. 10 Boundary layer pitot probe dimensions.

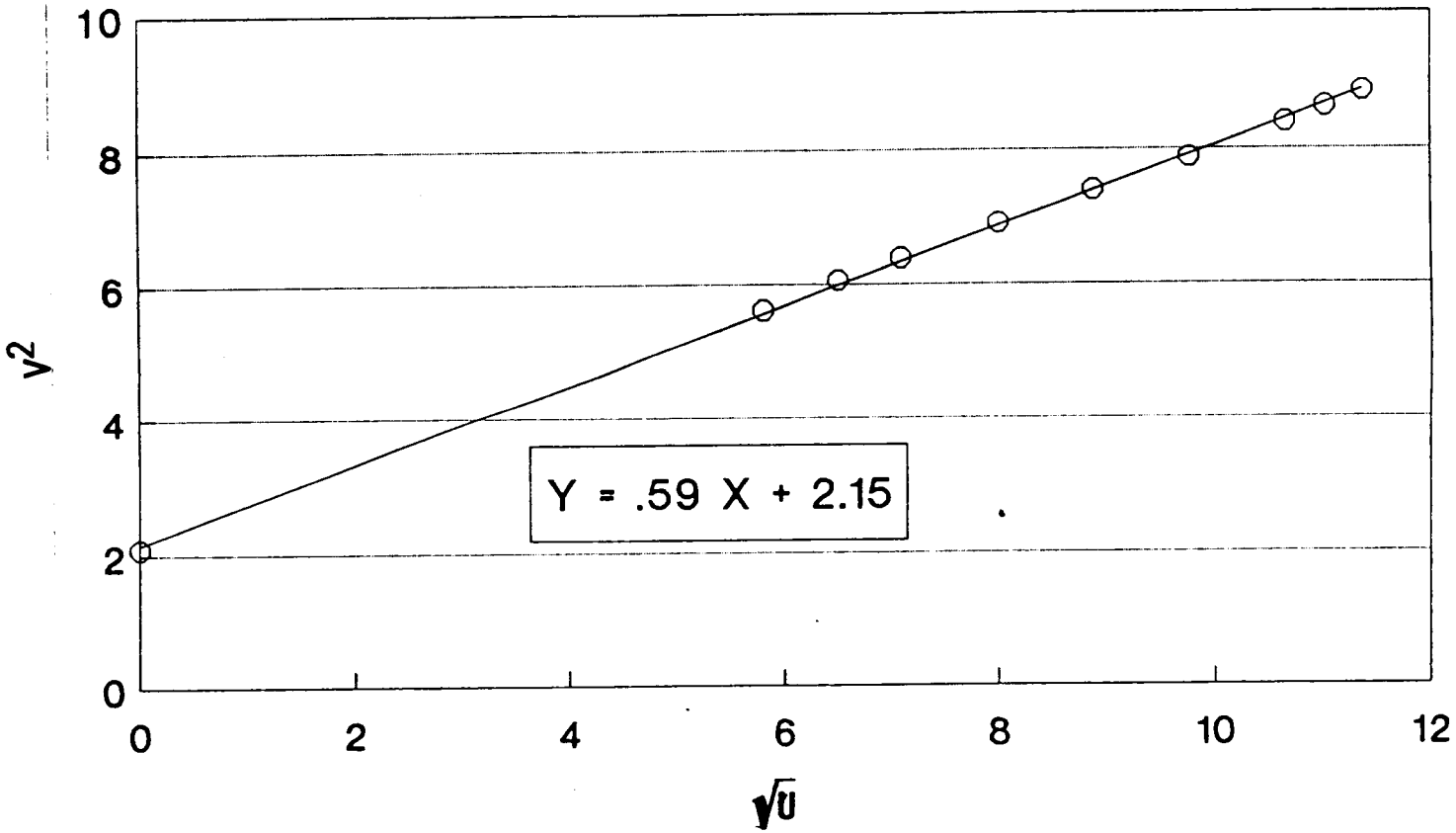

Fig. 11 Hot–wire calibration – King's law.

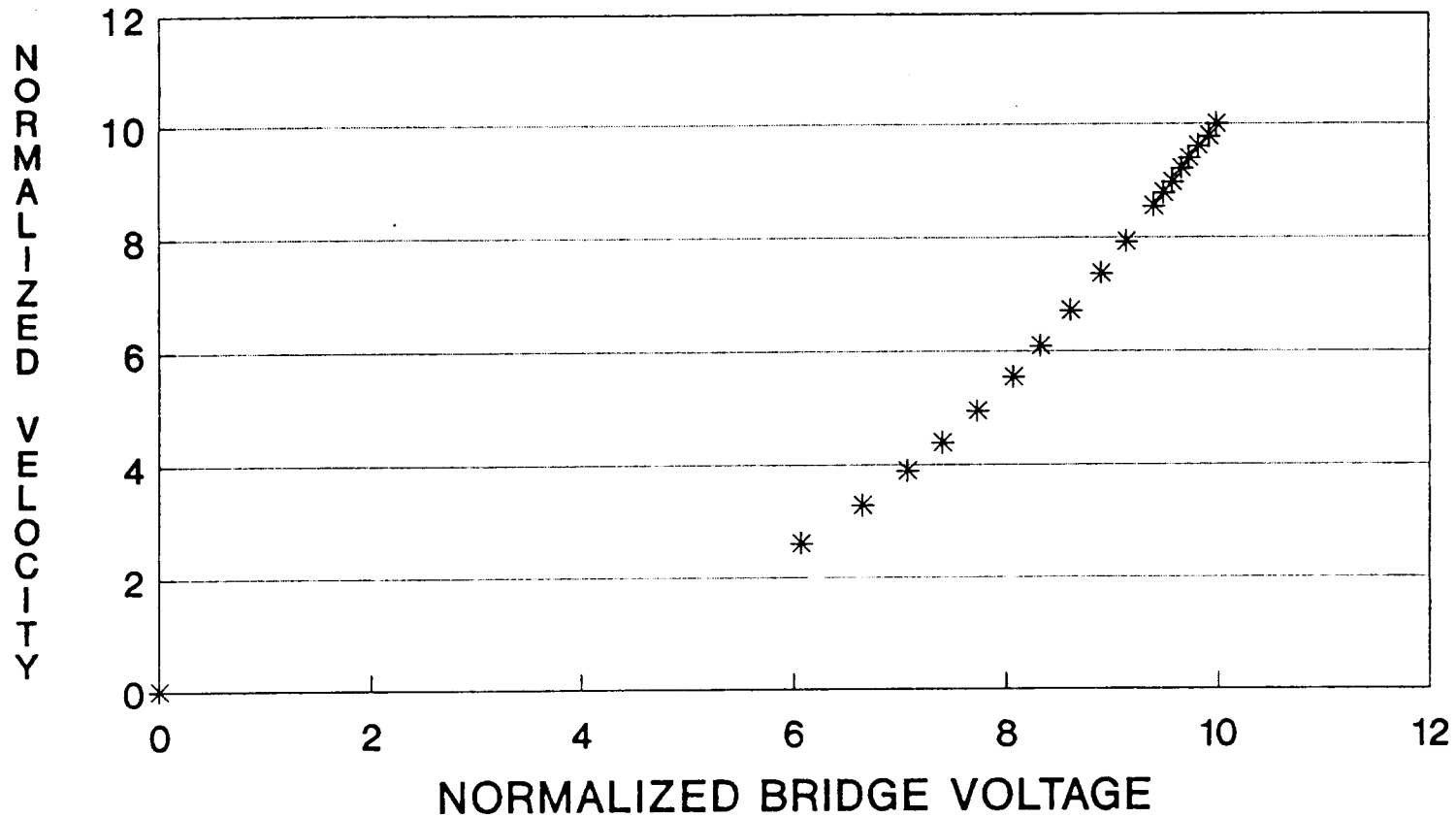

Fig. 12a Hot–wire calibration – raw data before linearization.

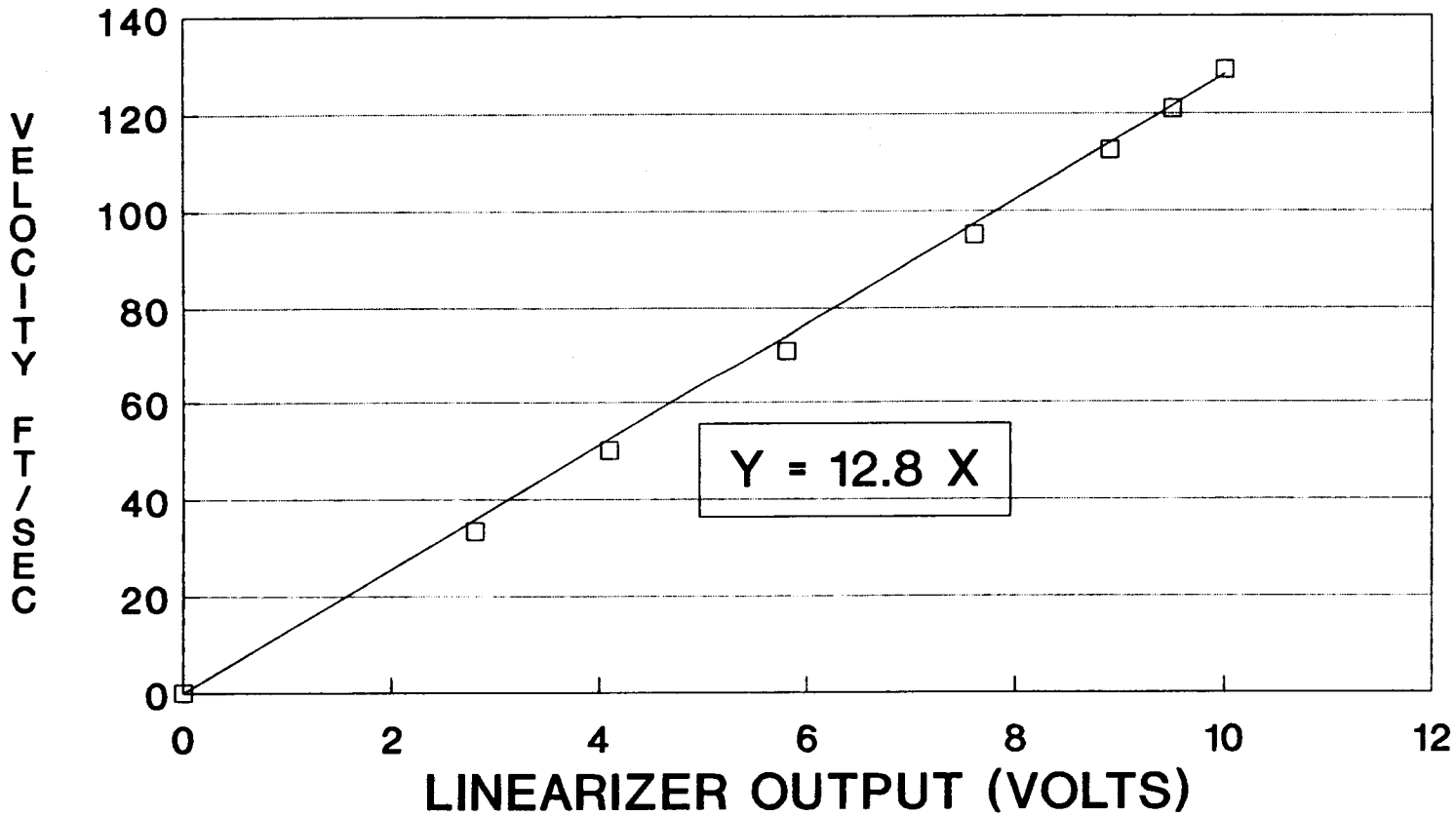

Fig. 12b Hot–wire calibration – raw data after linearization.

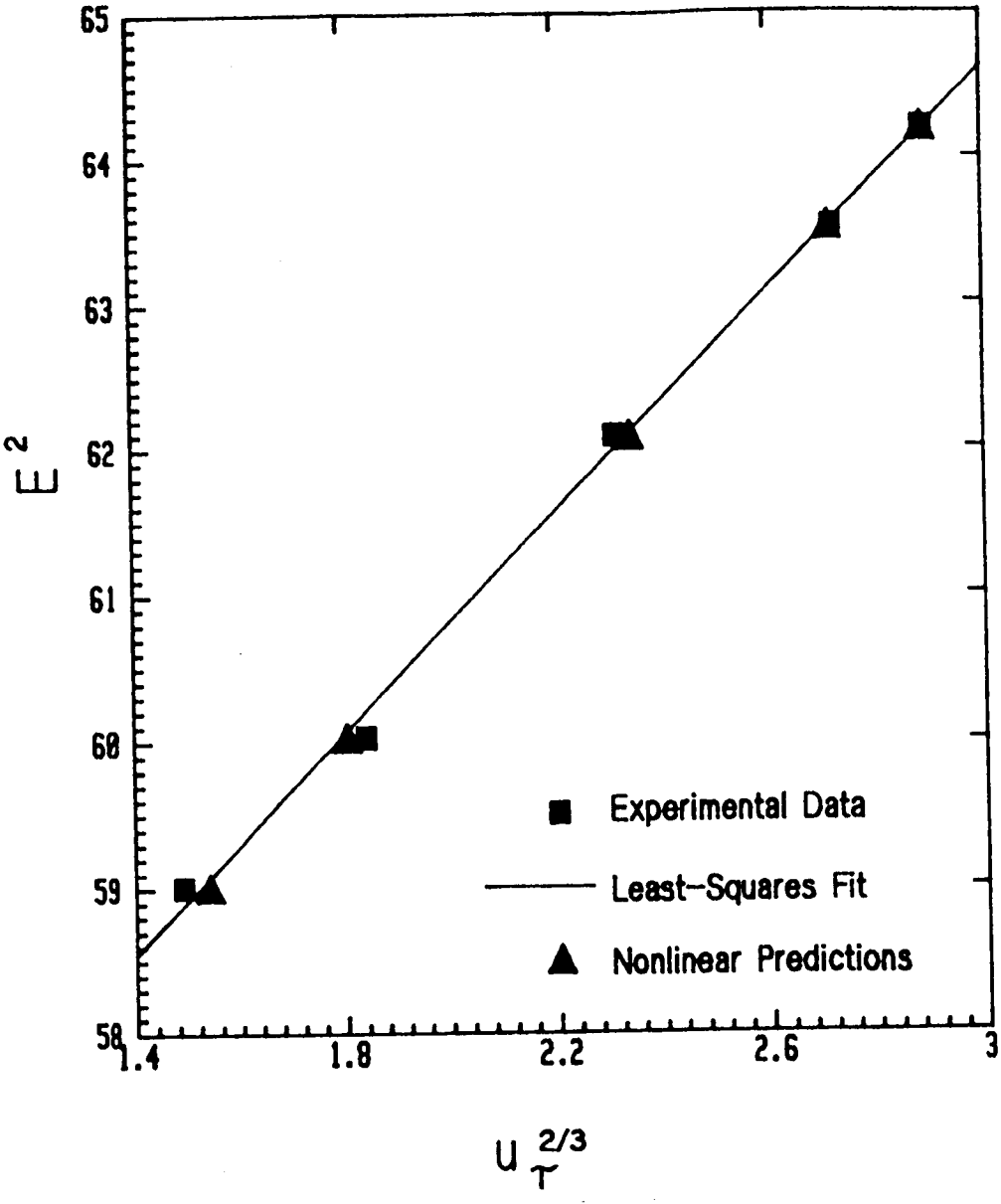

Fig. 13 Hot–film calibration.

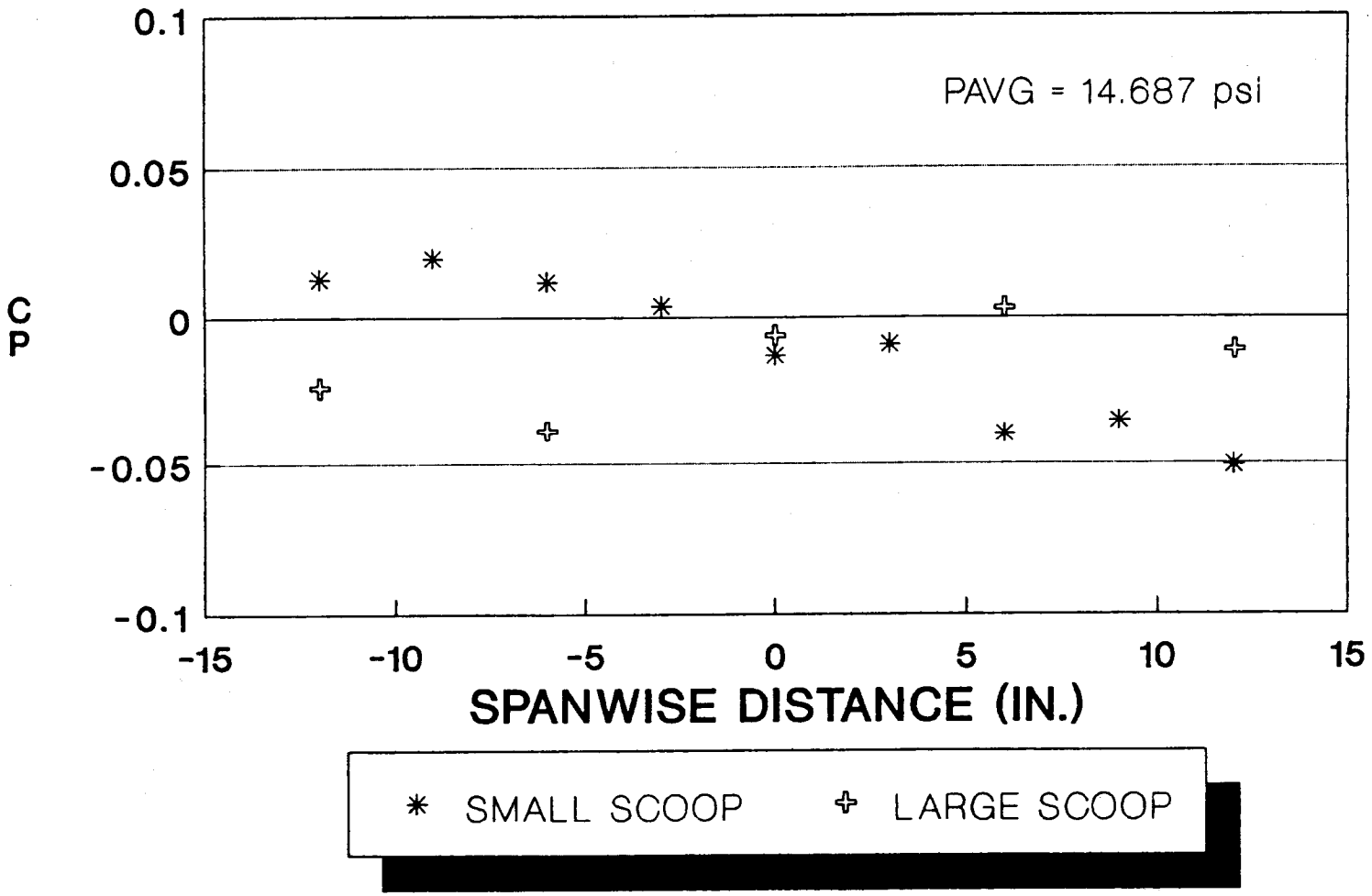

Fig. 14 Boundary layer bleed scoop static pressure distribution.

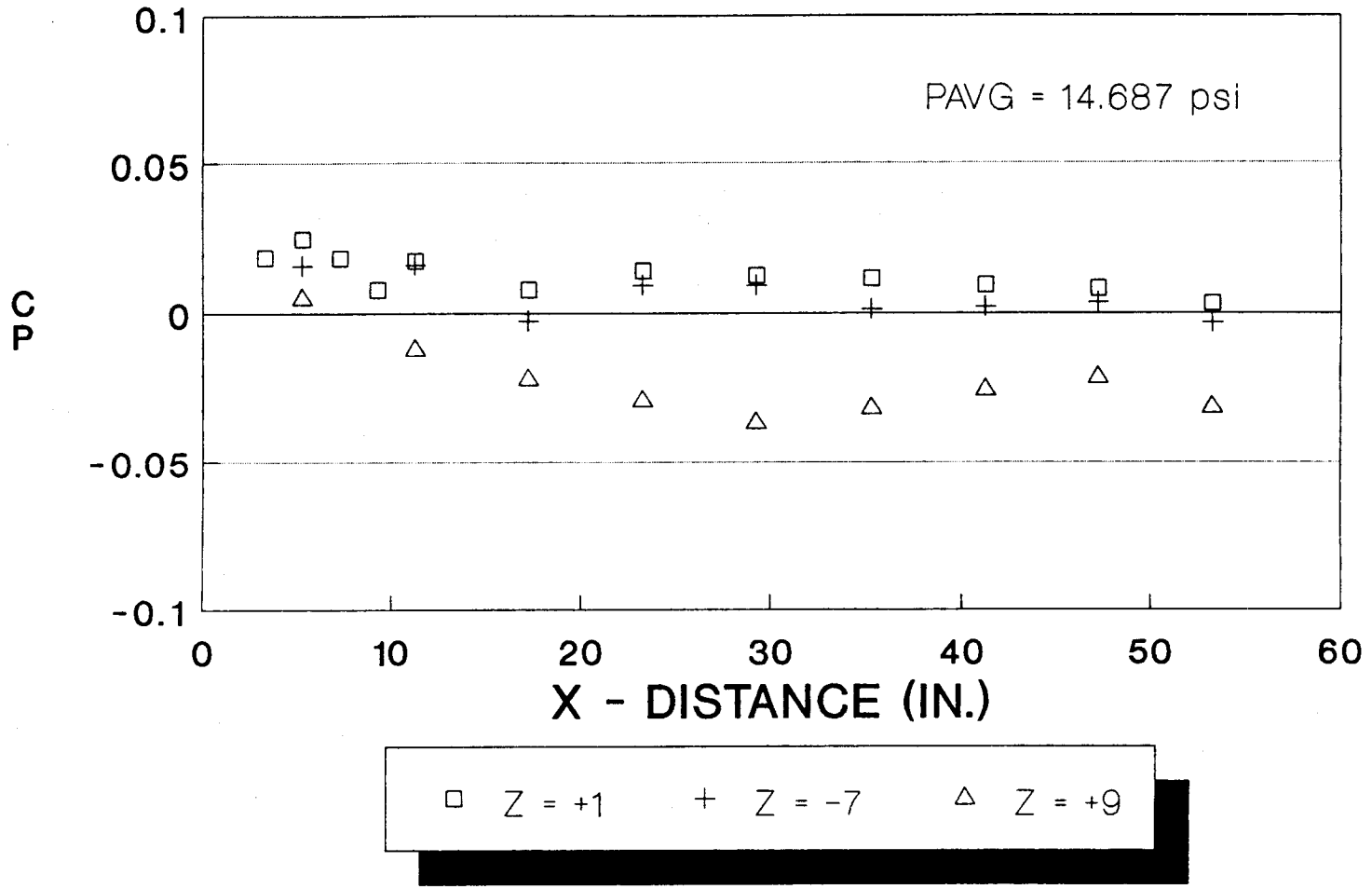

Fig. 15 Test section static pressure distribution.

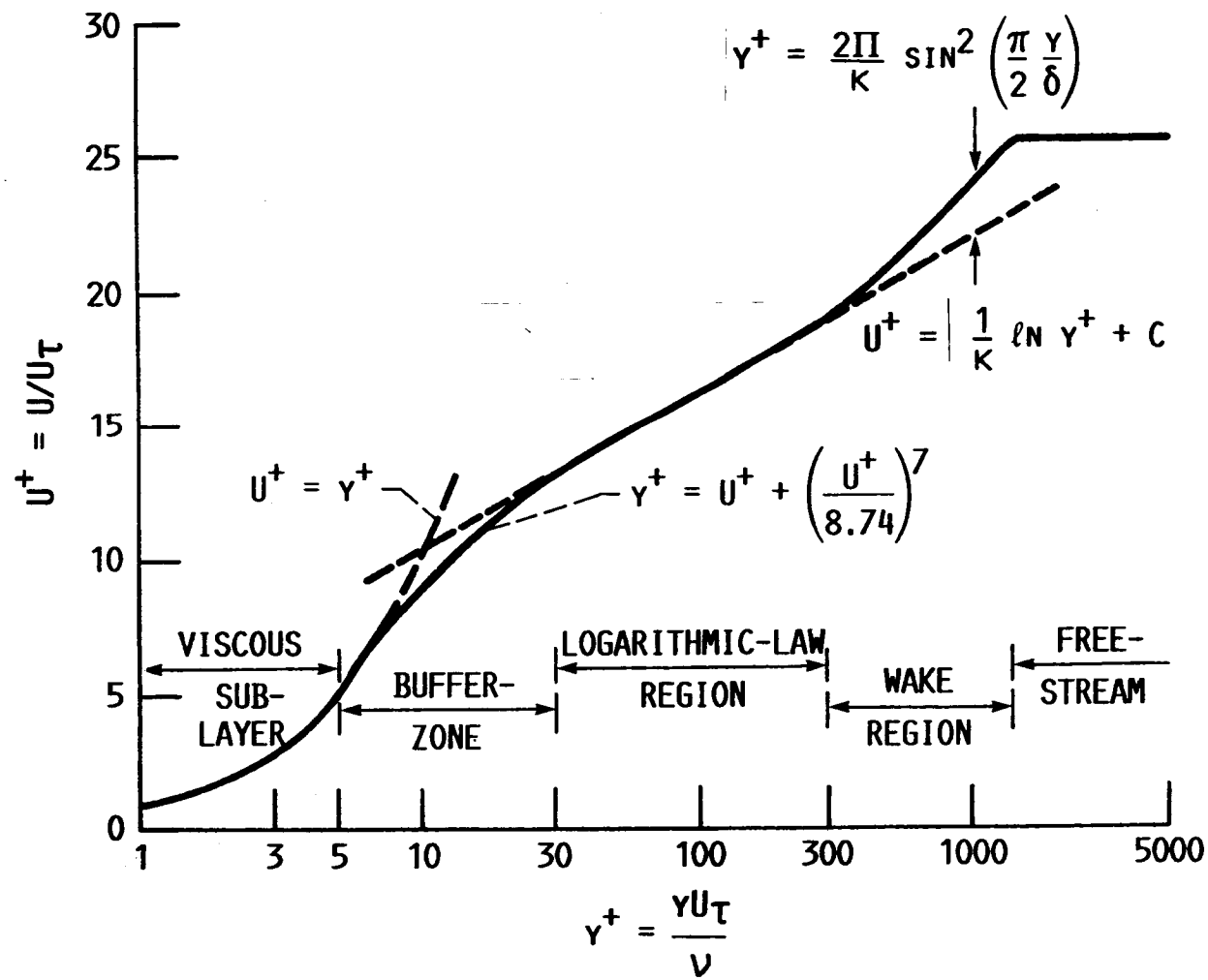

Fig. 16 Regions of a turbulent boundary layer.

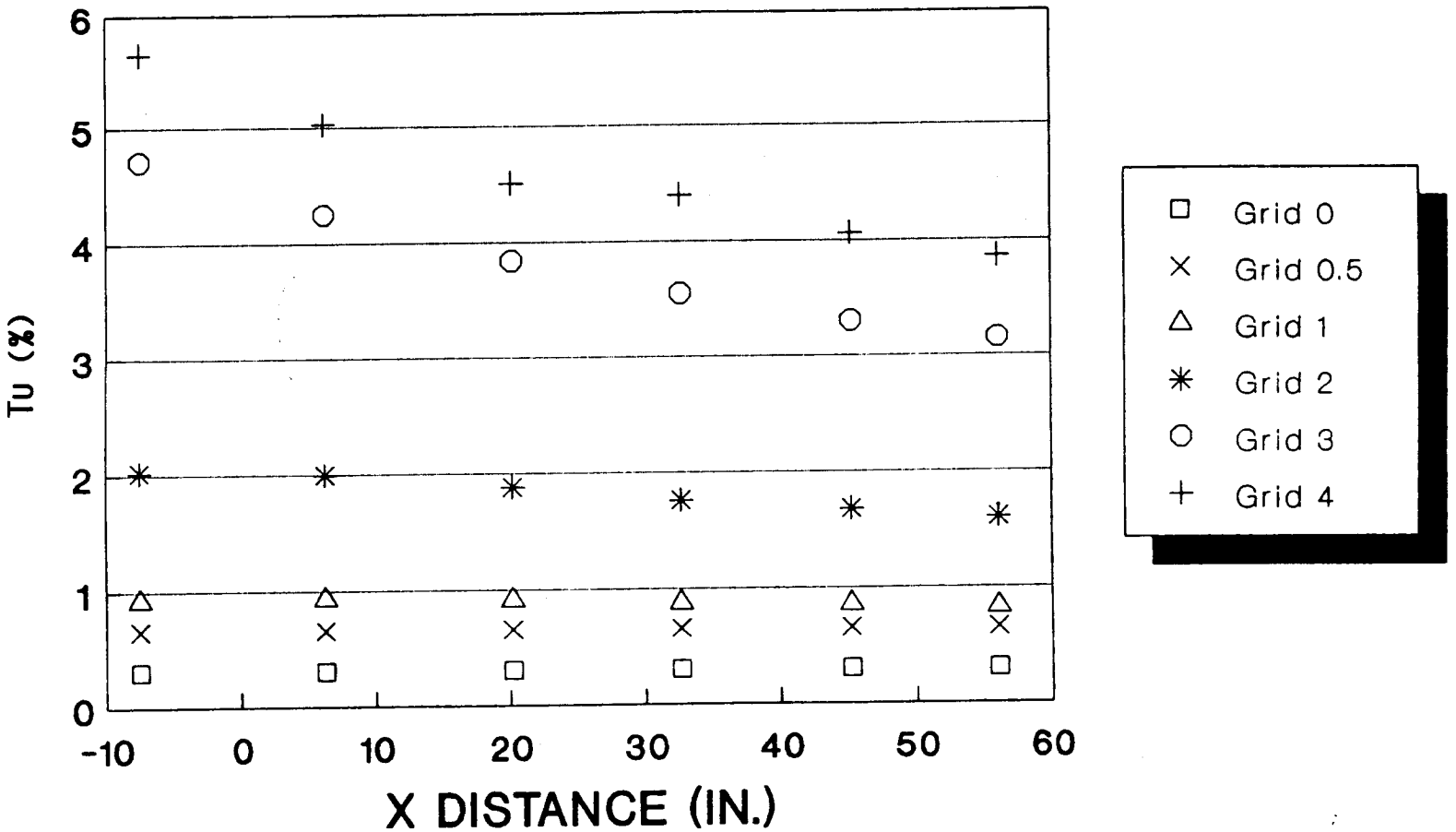

Fig. 17 Longitudinal freestream turbulence through the test section for all grids.

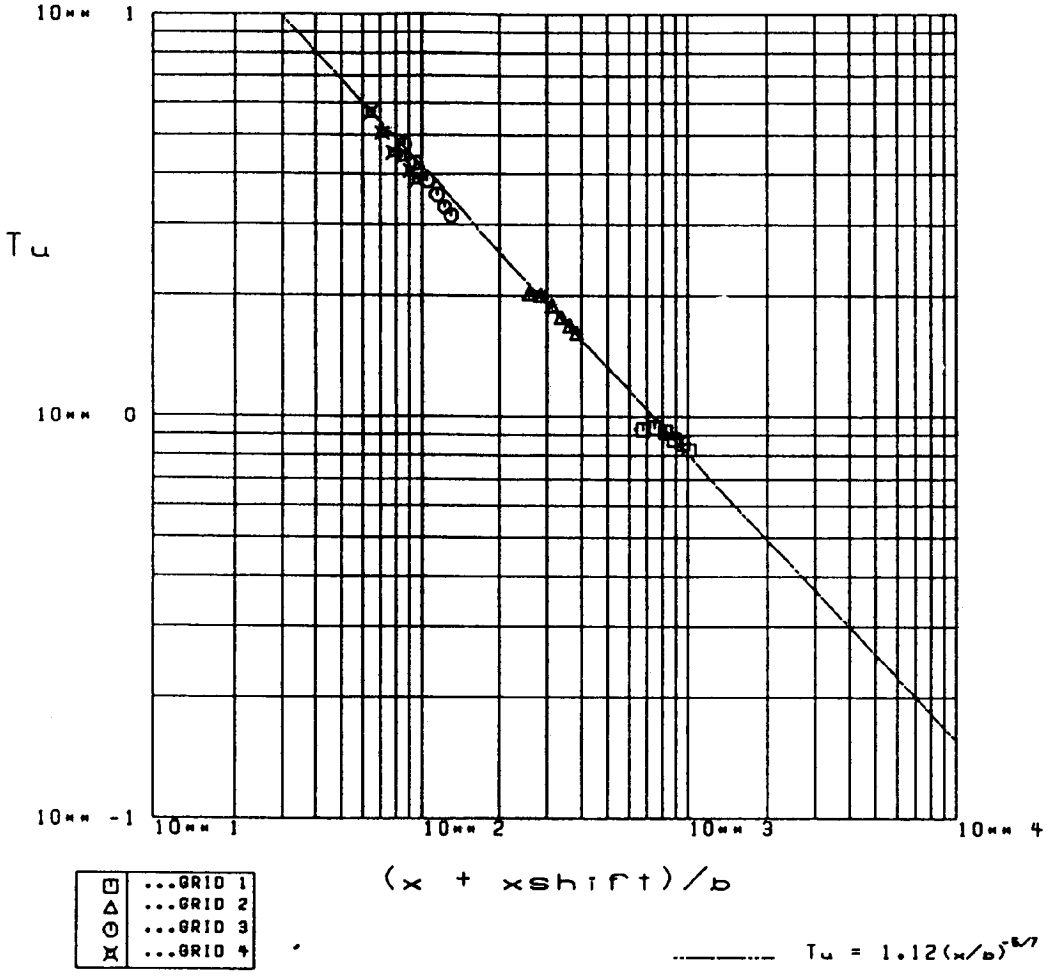

Fig. 18 Comparison of freestream turbulence intensity to results of Baines and Peterson (xshift = 90 inches).

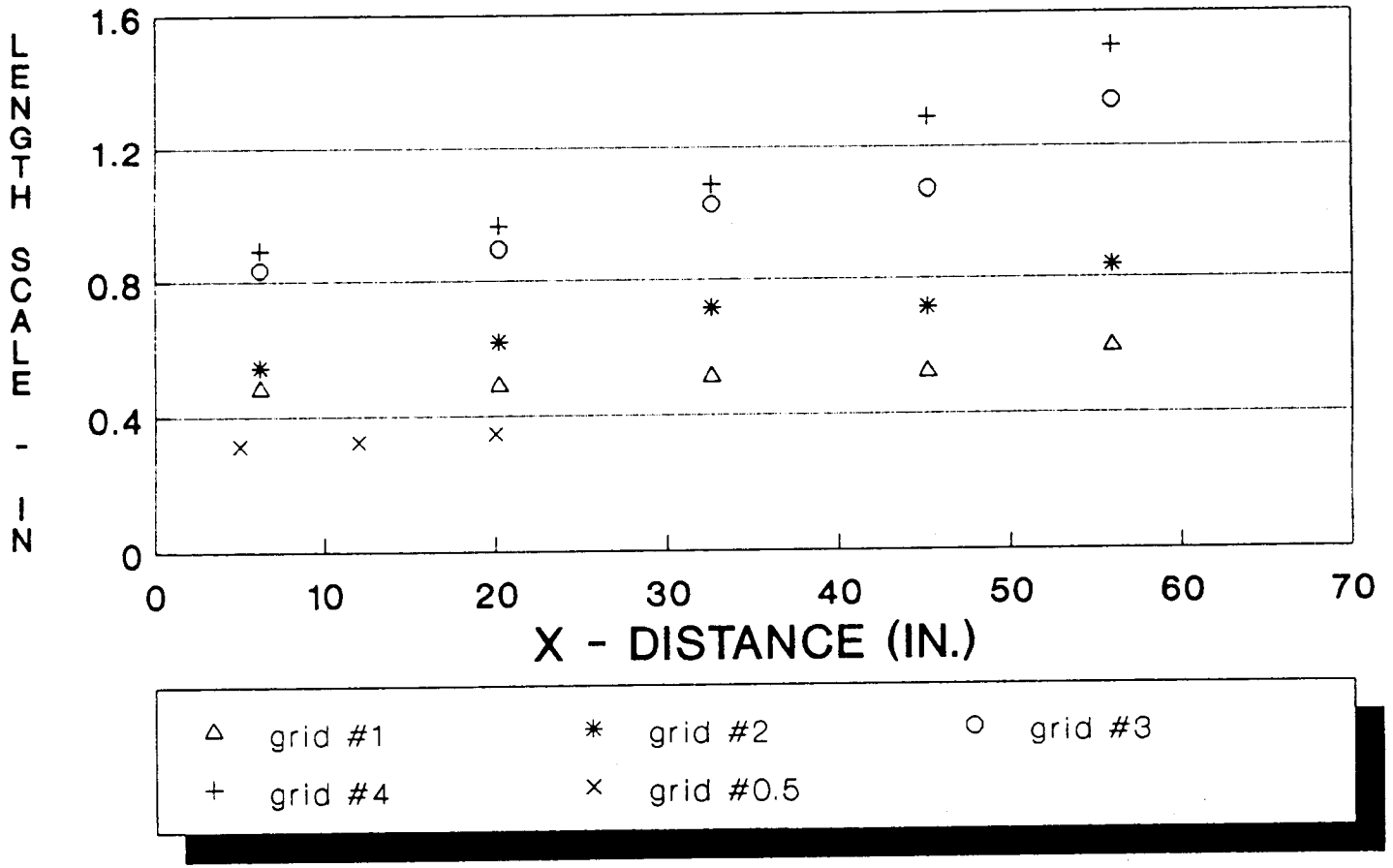

Fig. 19 Distribution of the longitudinal length scale of the freestream turbulence for all grid configurations.

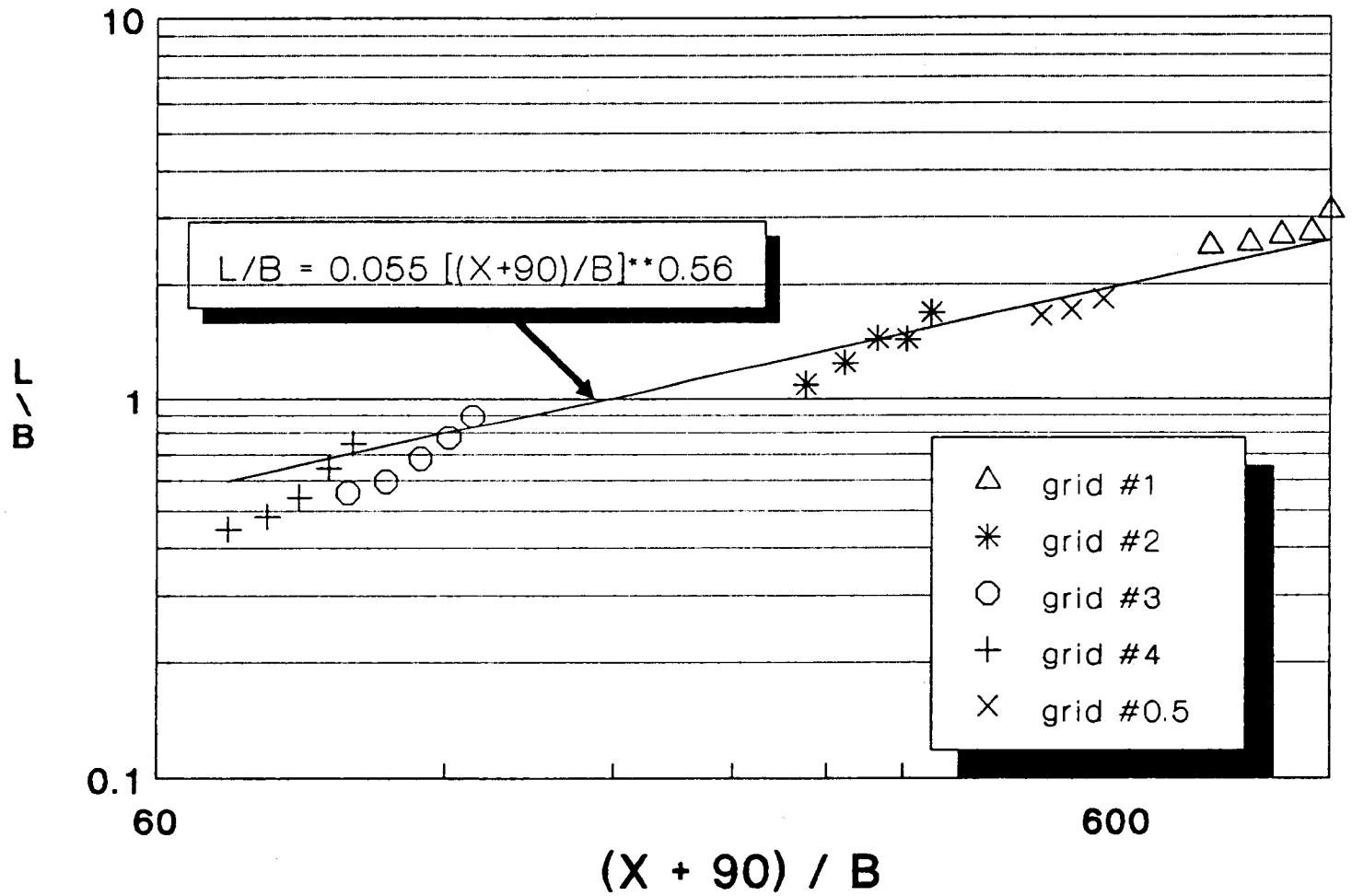

Fig. 20 Comparison of the length scales to results of Baines and Peterson.

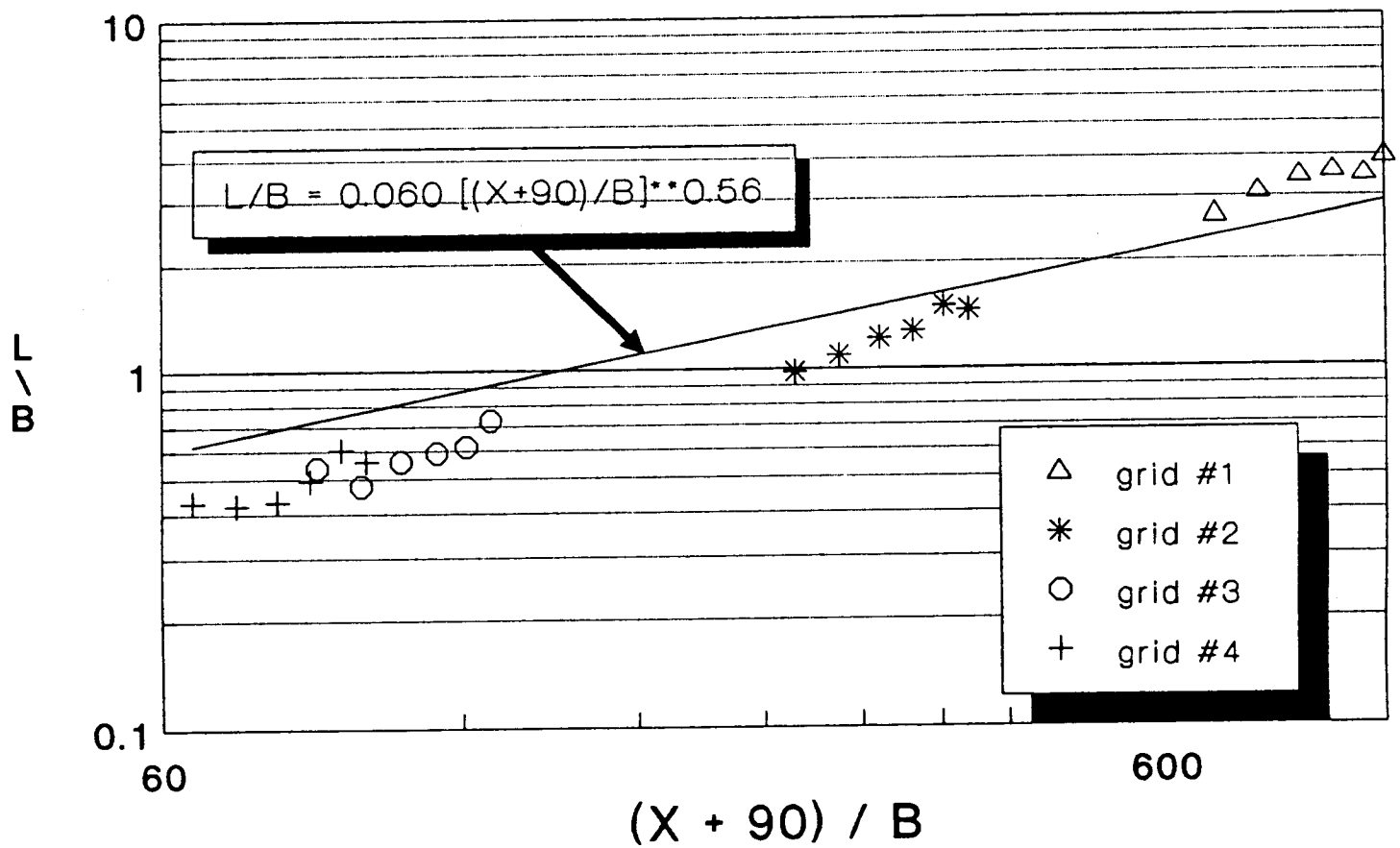

Fig. 21 Comparison of the length scales (from autocorrelations) to results of Baines and Peterson.

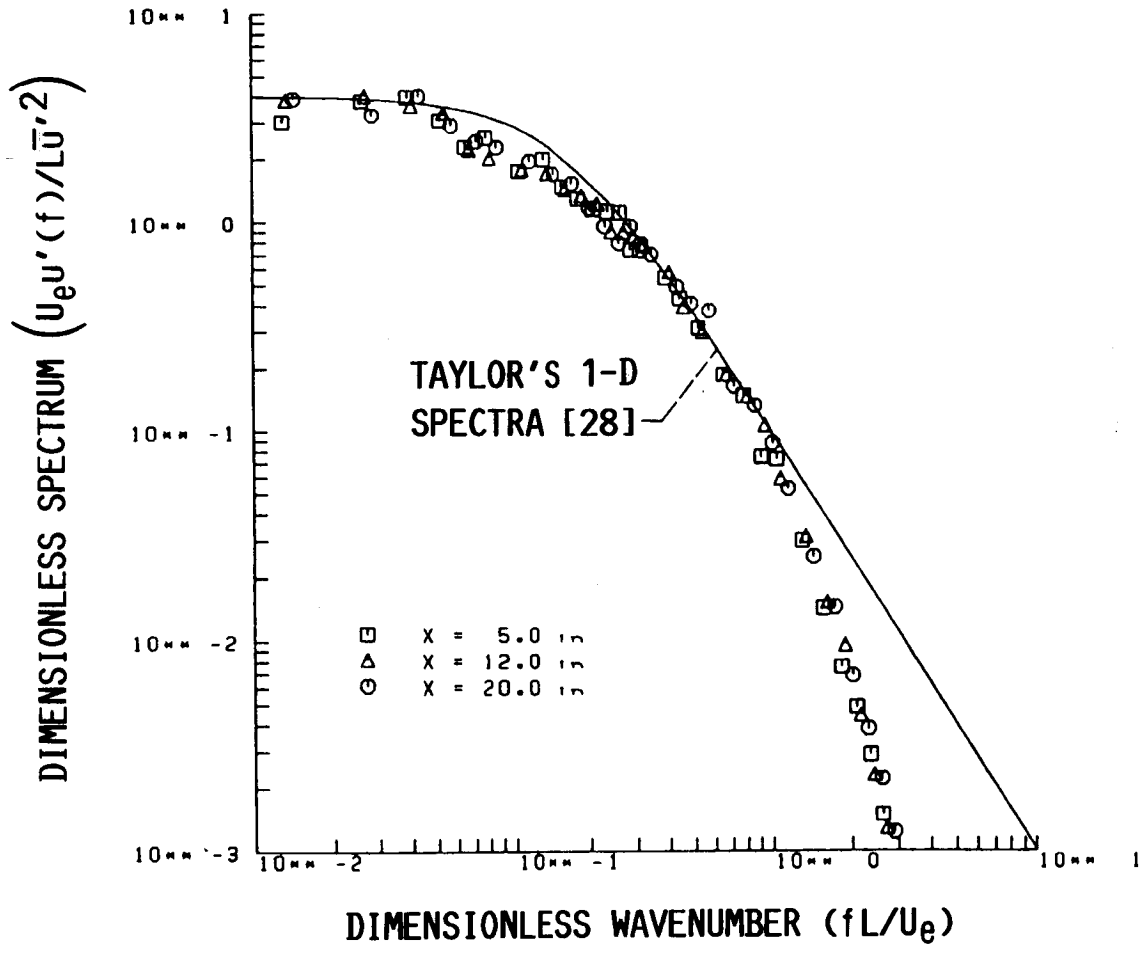

Fig. 22 Grid 0.5 – power spectrum.

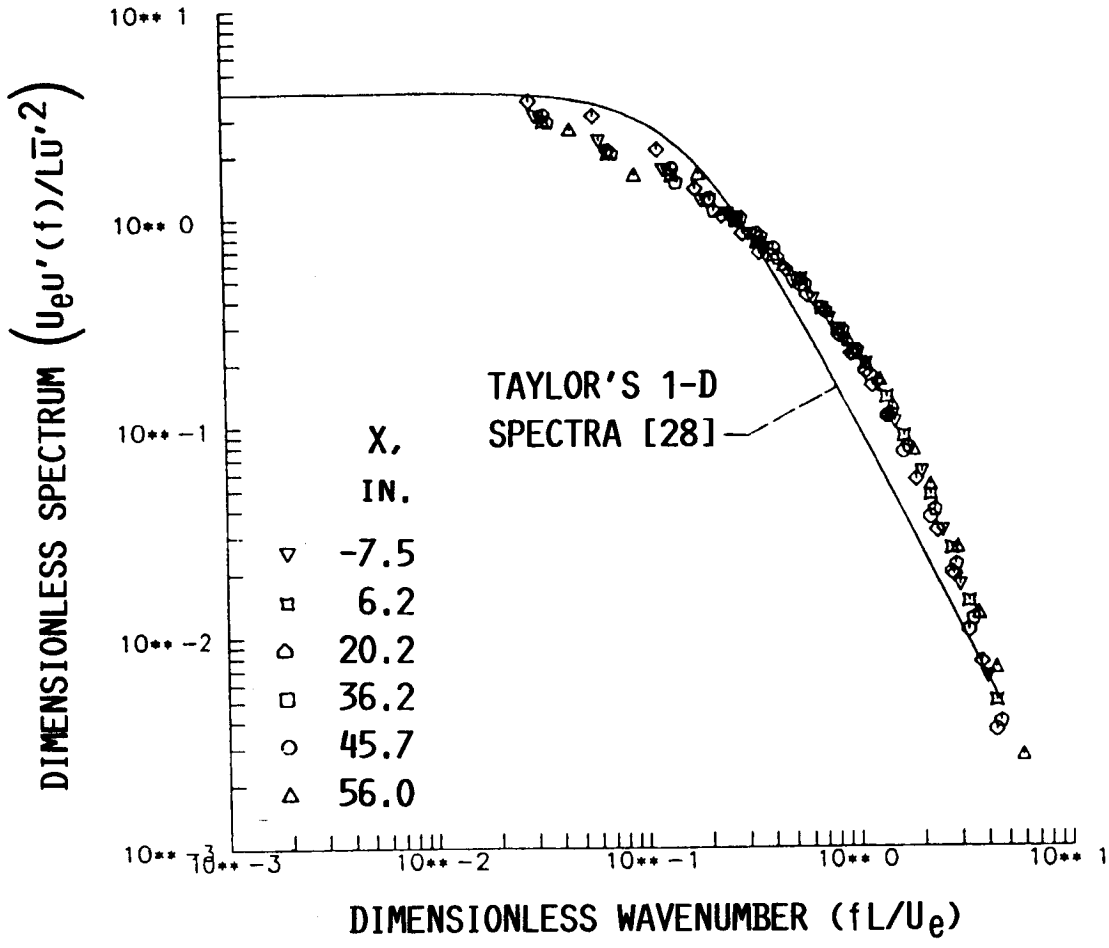

Fig. 23 Grid 1 – power spectrum.

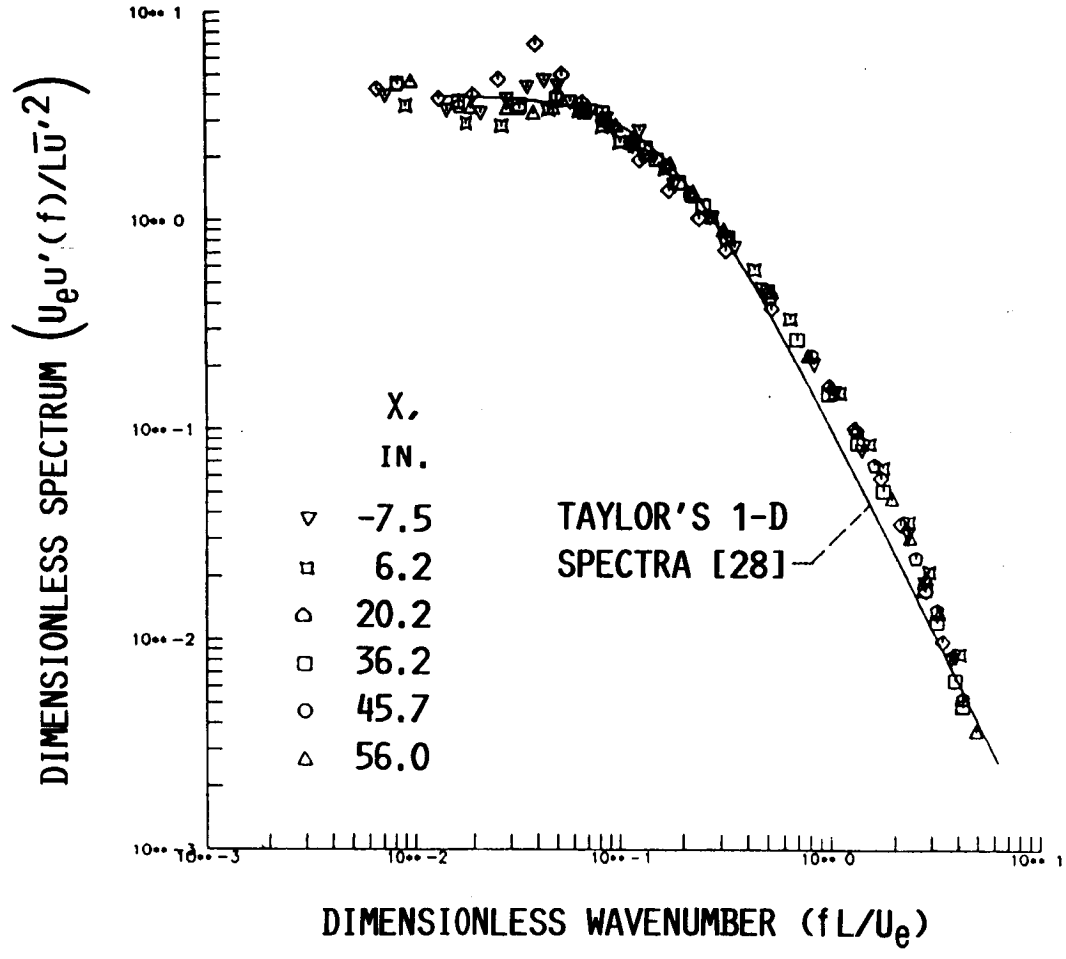

Fig. 24 Grid 2 – power spectrum.

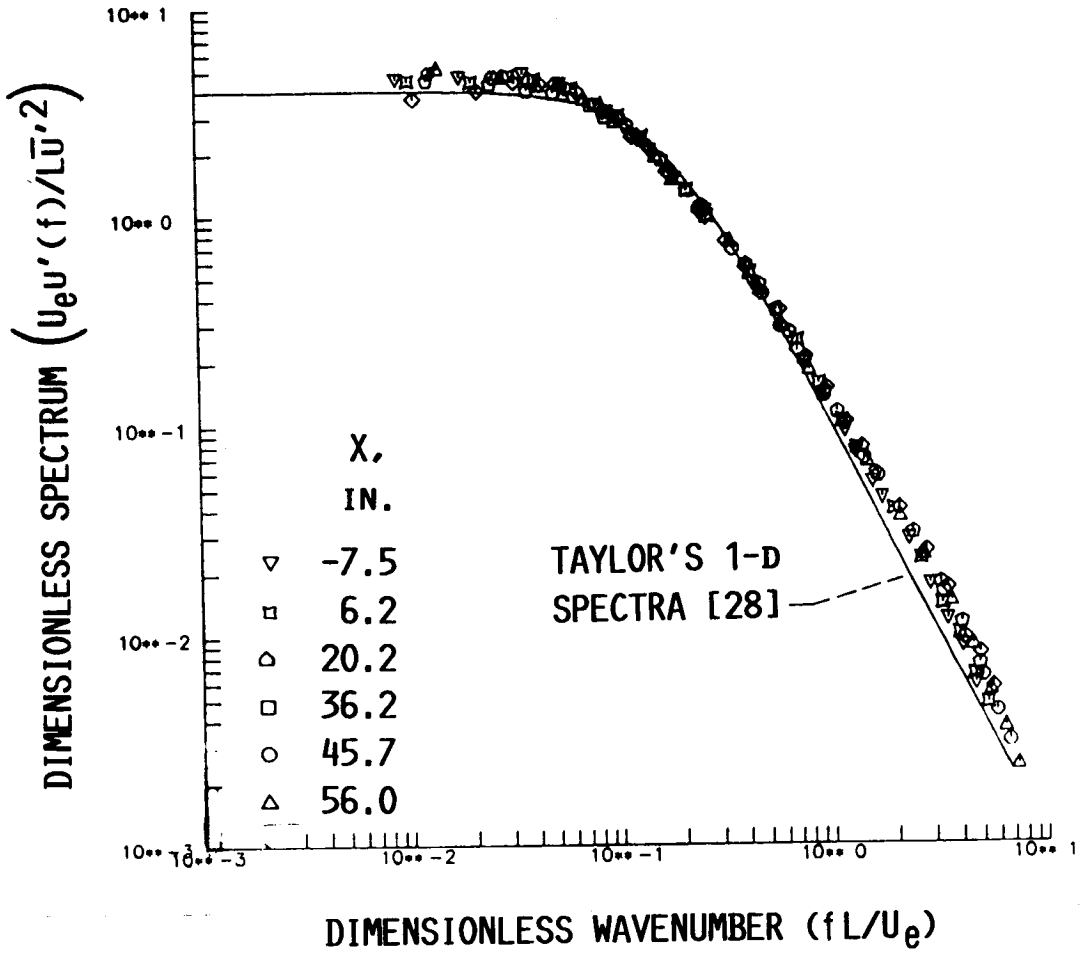

Fig. 25 Grid 3 – power spectrum.

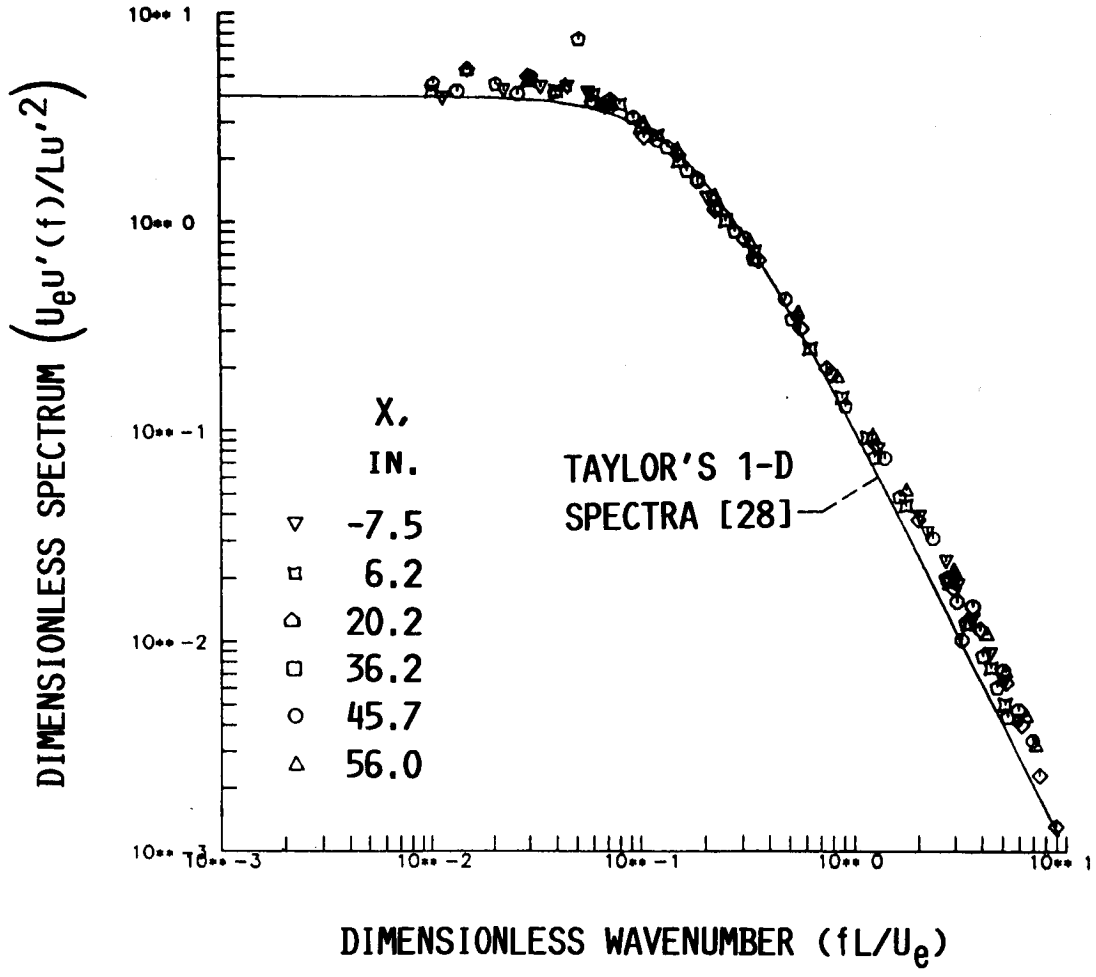

Fig. 26 Grid 4 – power spectrum.

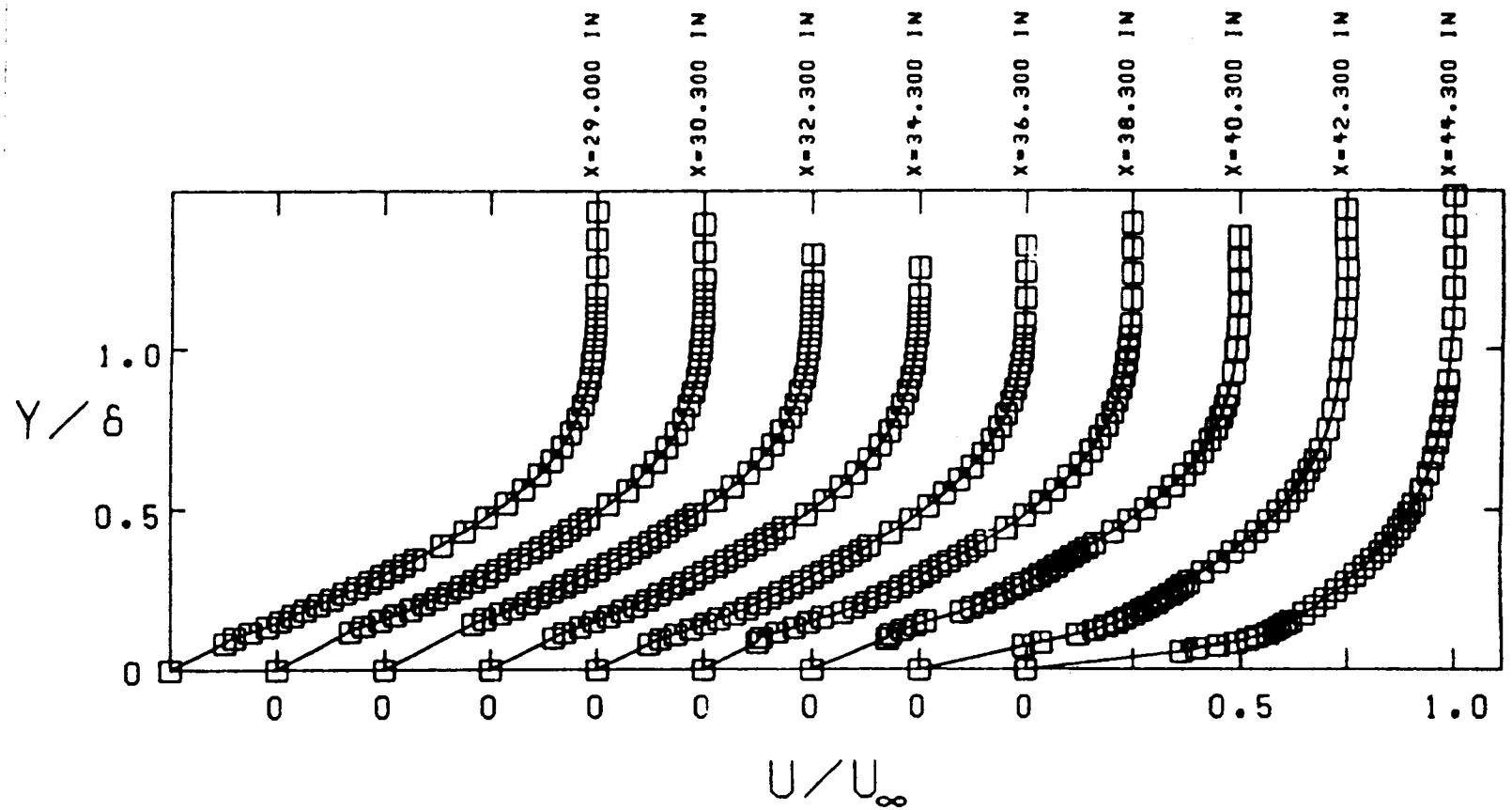

Fig. 27 Grid 0 – carpet plots of y/δ vs. u/U_e.

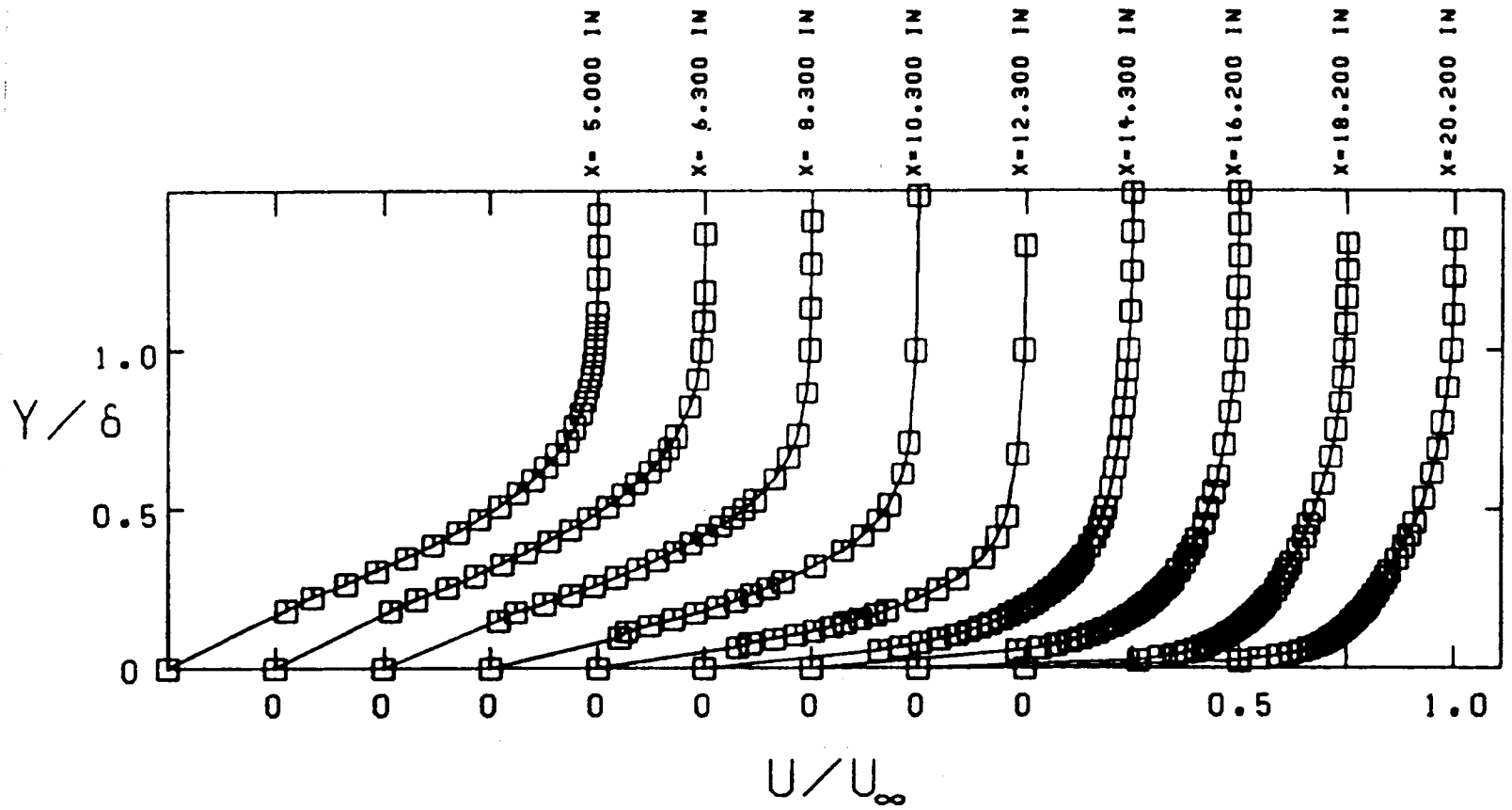

Fig. 28 Grid 0.5 – carpet plots of y/δ vs. u/U_e.

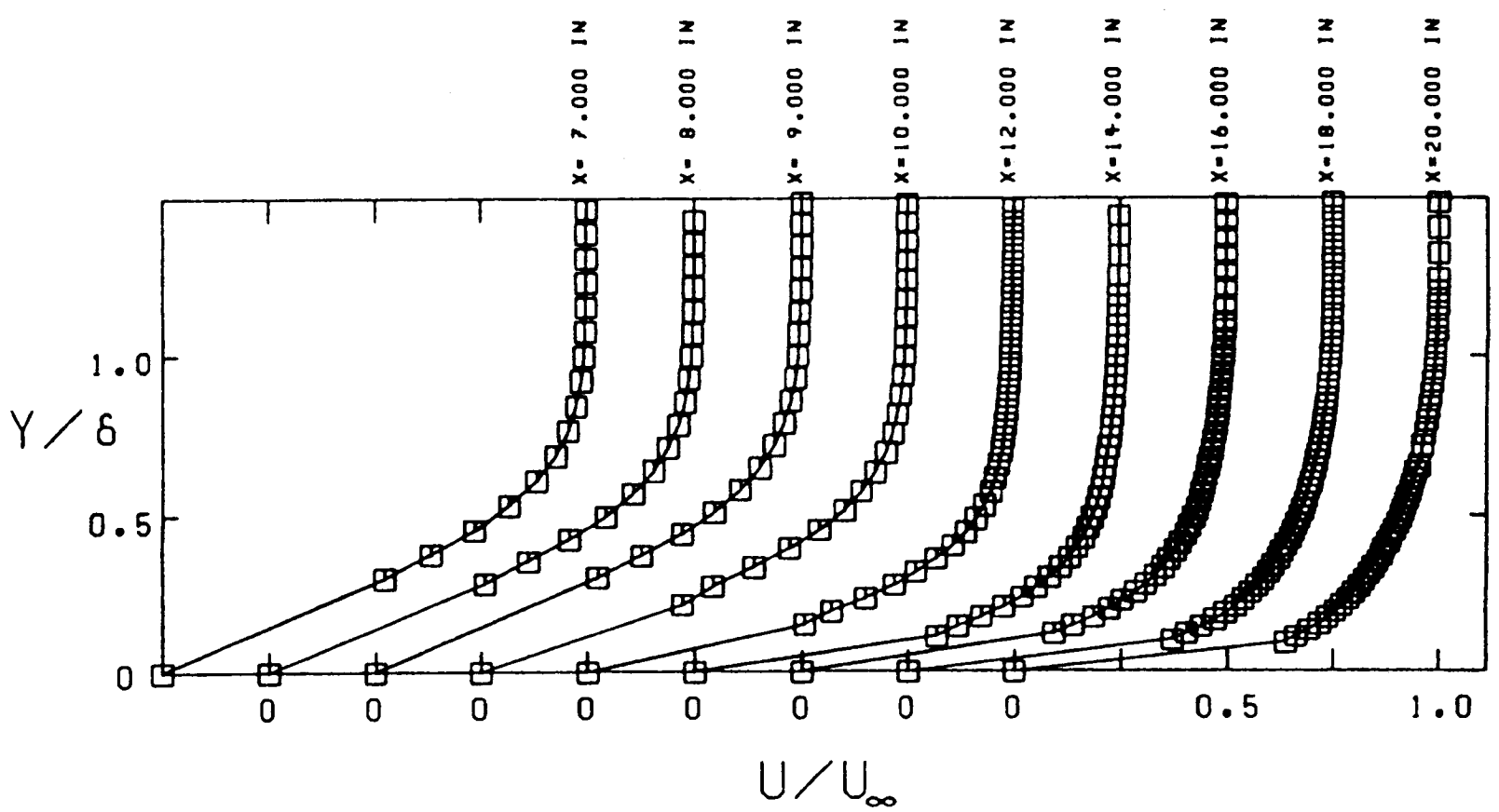

Fig. 29 Grid 1 – carpet plots of y/δ vs. u/U_e.

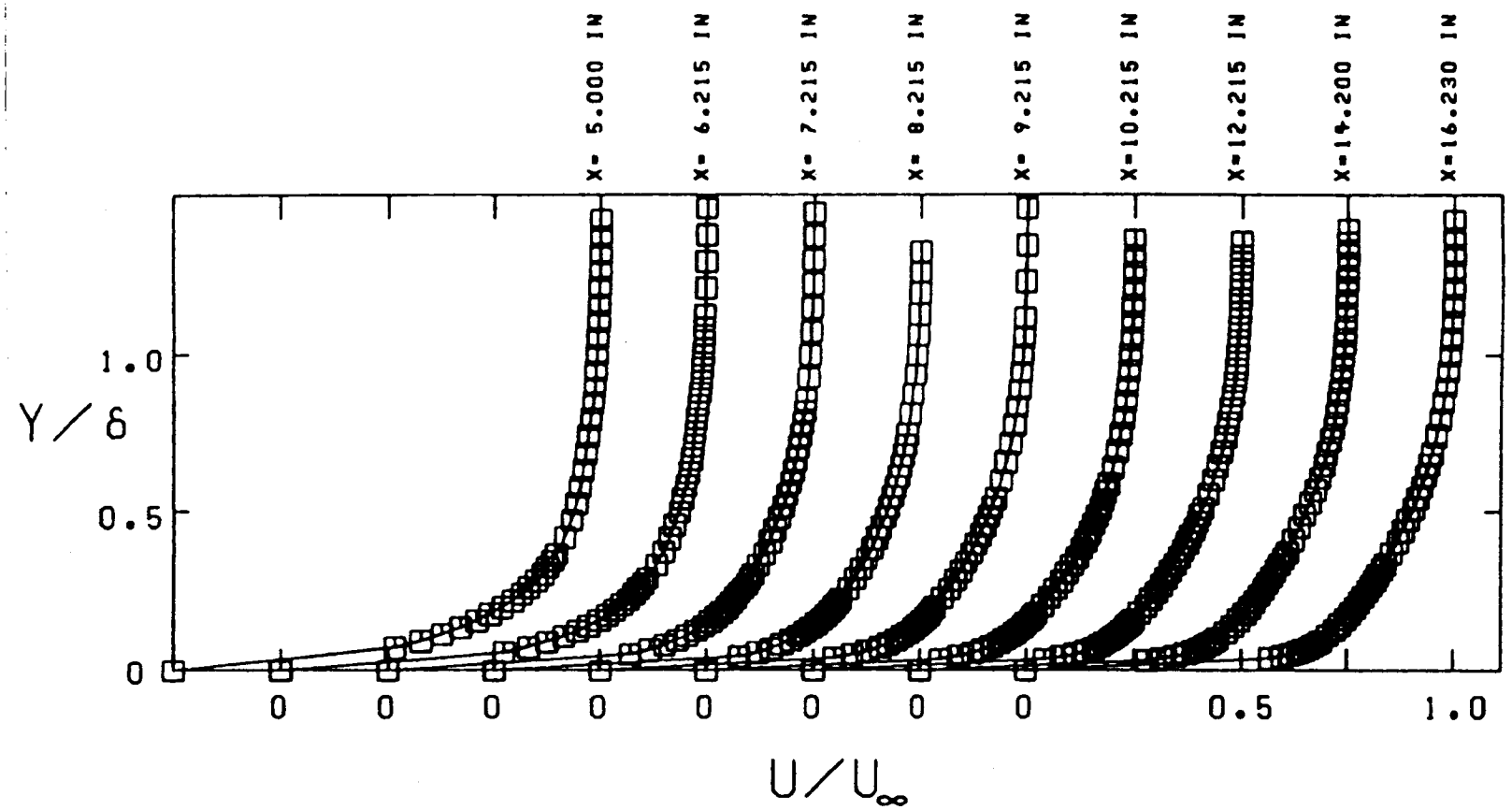

Fig. 30 Grid 2 – carpet plots of y/δ vs. u/U_e.

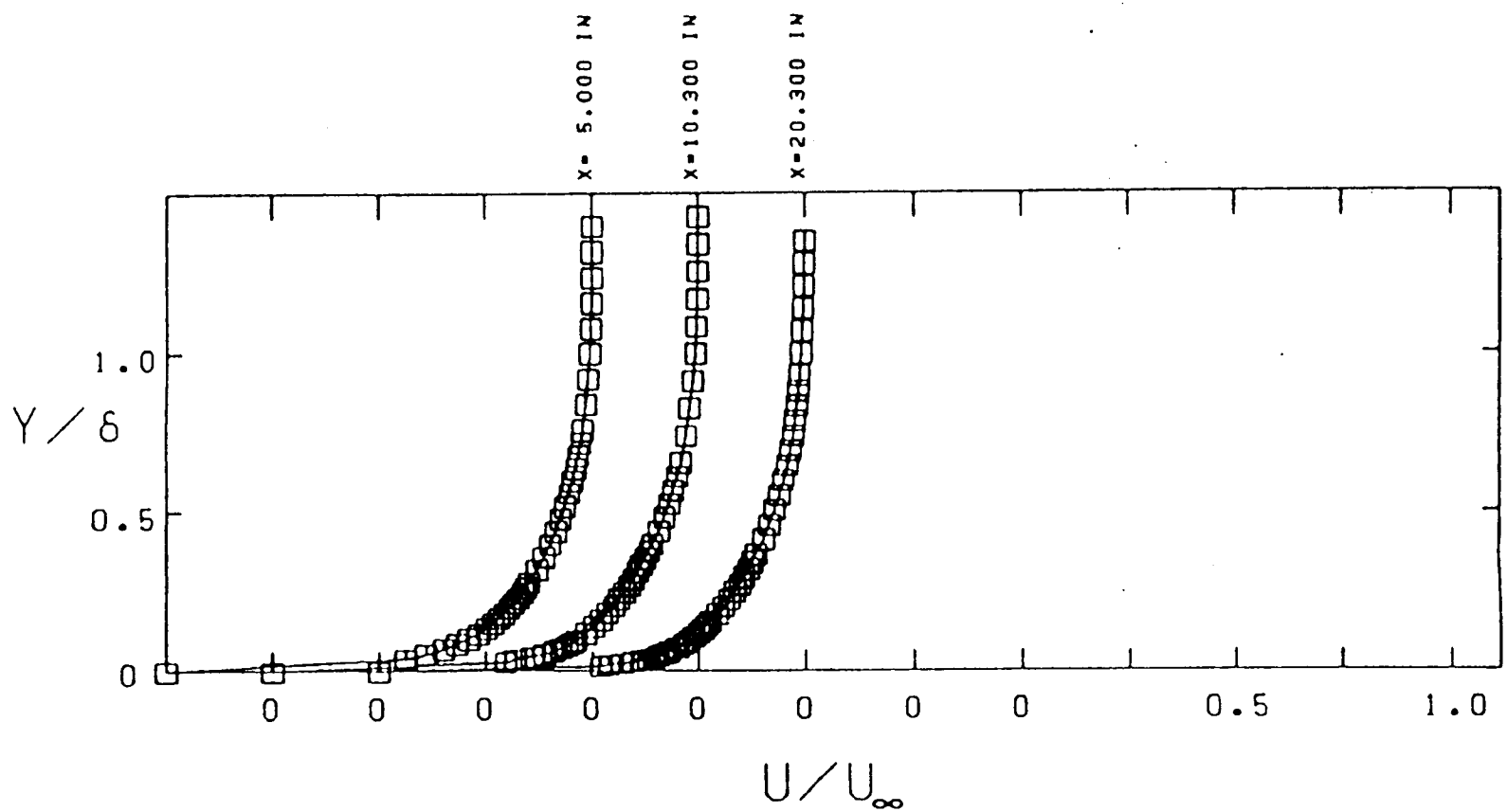

Fig. 31 Grid 3 – carpet plots of y/δ vs. u/U_e.

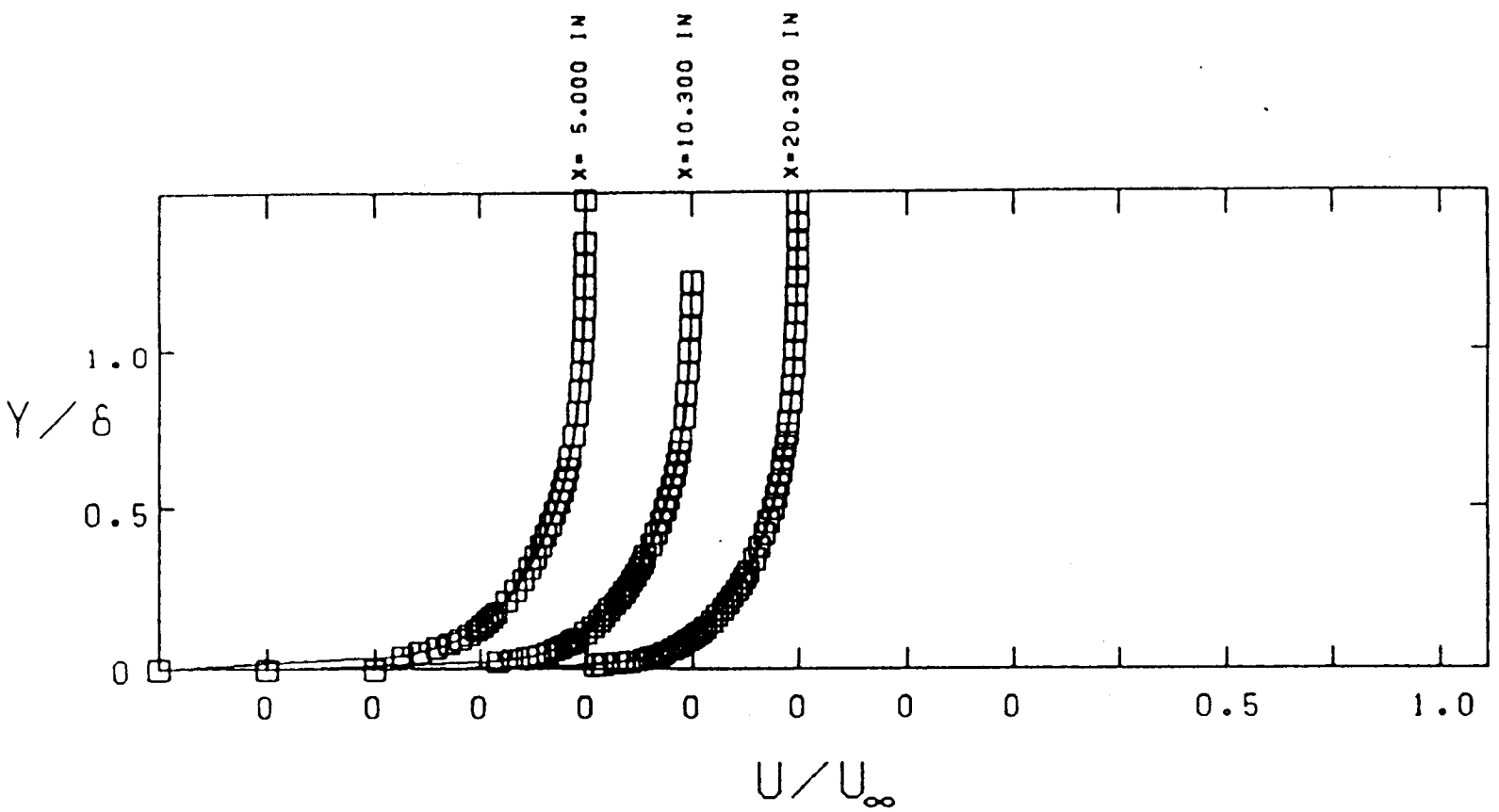

Fig. 32 Grid 4 – carpet plots of y/δ vs. u/U_e.

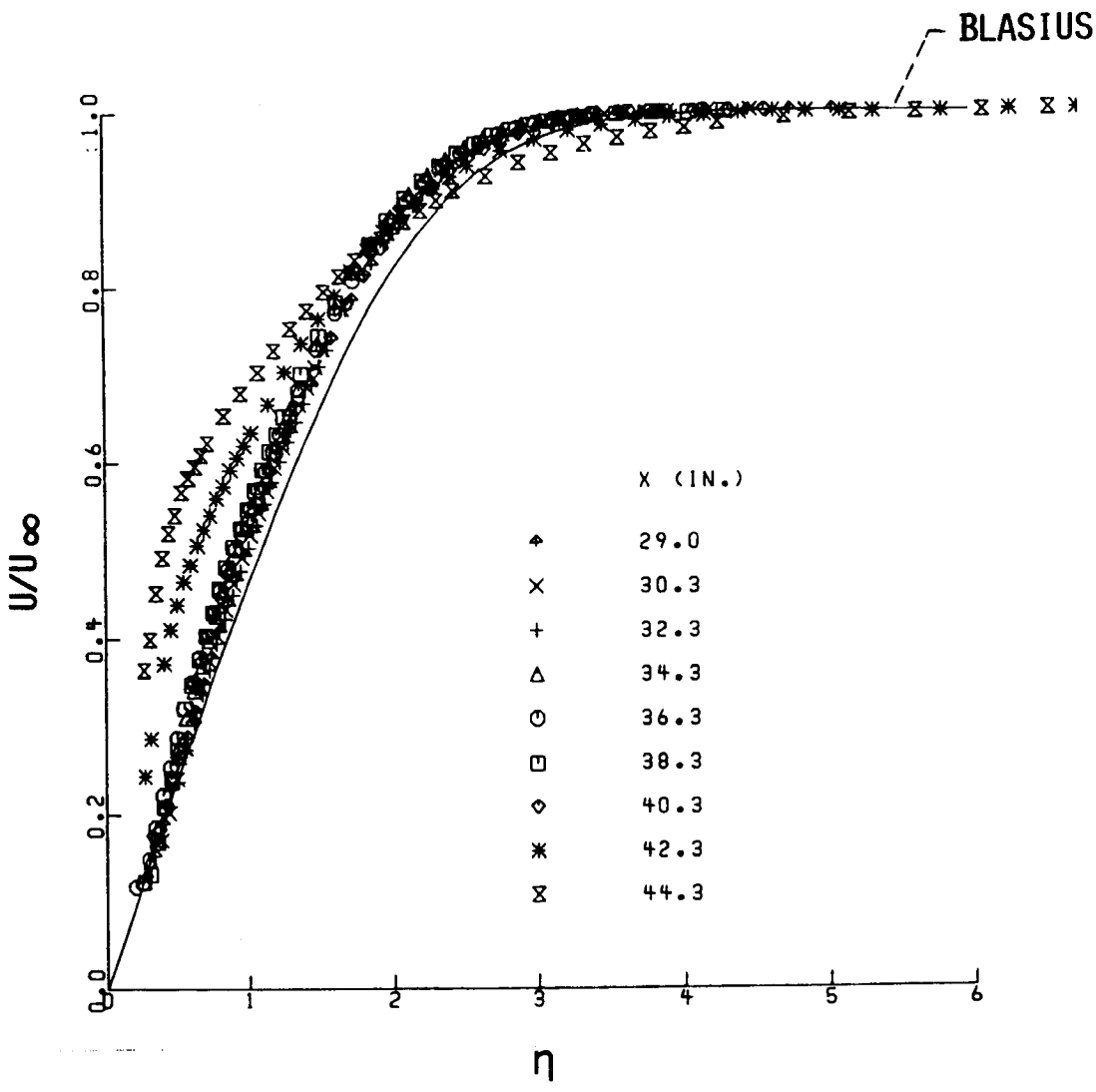

Fig. 33 Grid 0 – plots of η vs. f'(η) overlaid.

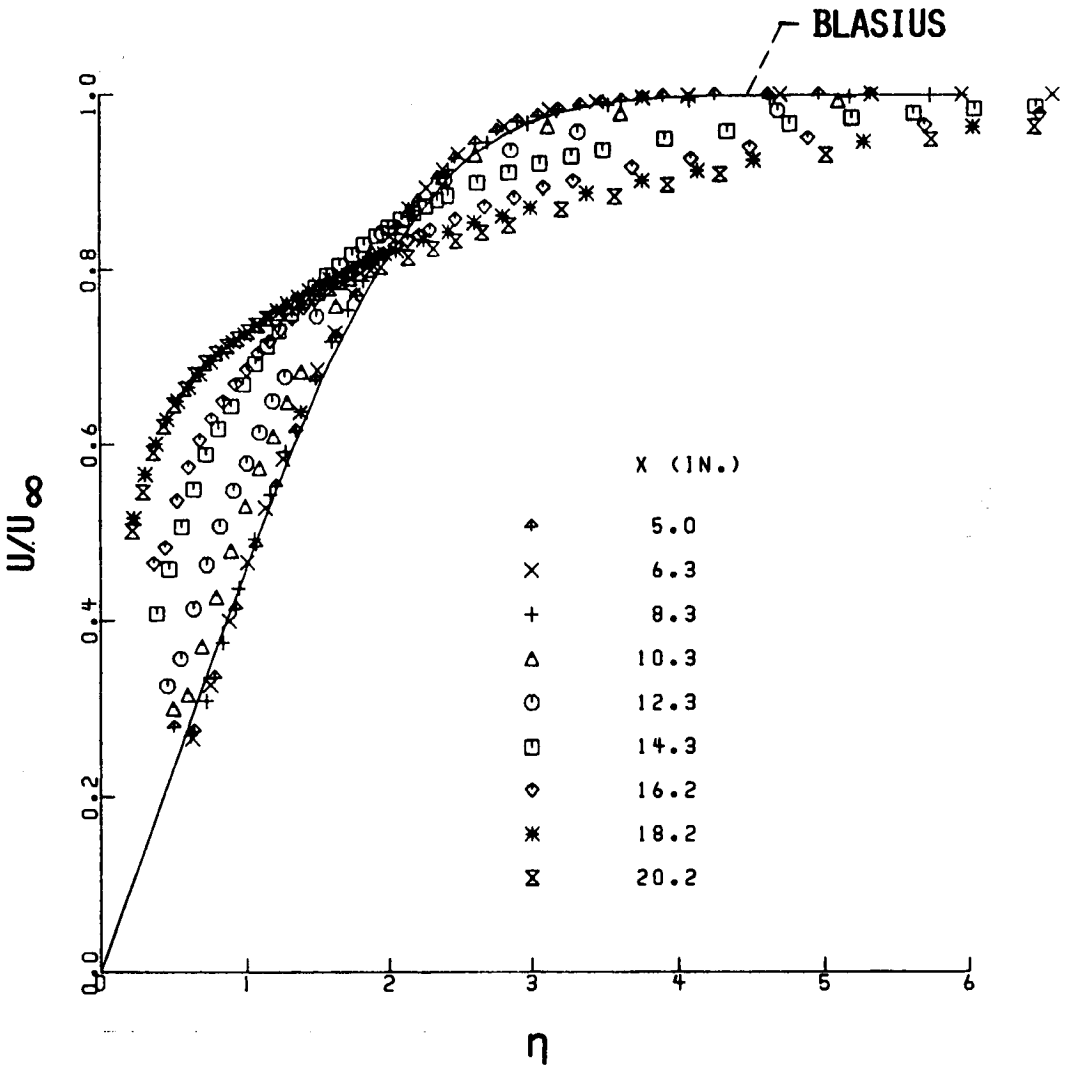

Fig. 34 Grid 0.5 – plots of η vs. f'(η) overlaid.

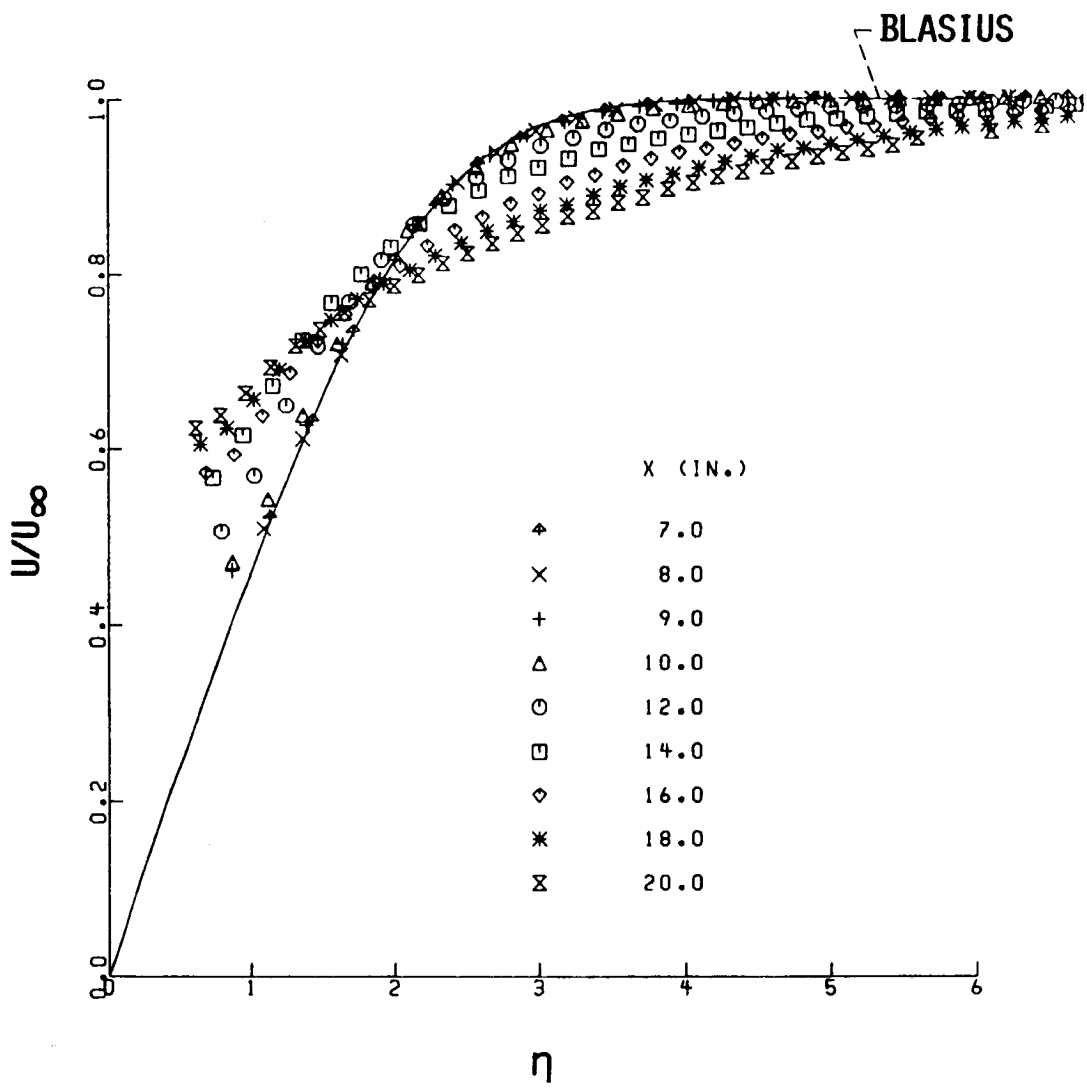

Fig. 35 Grid 1 – plots of η vs. f'(η) overlaid.

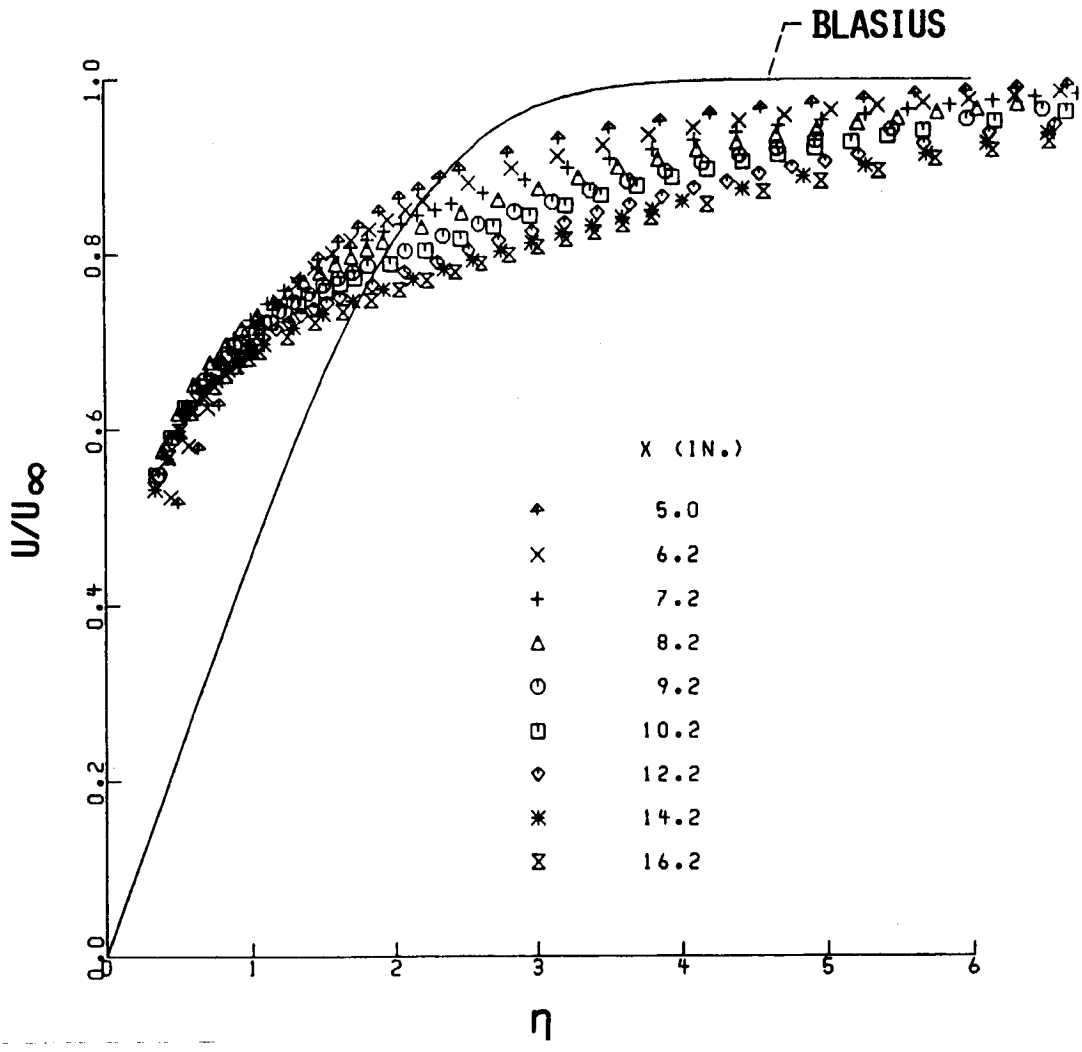

Fig. 36 Grid 2 – plots of η vs. f'(η) overlaid.

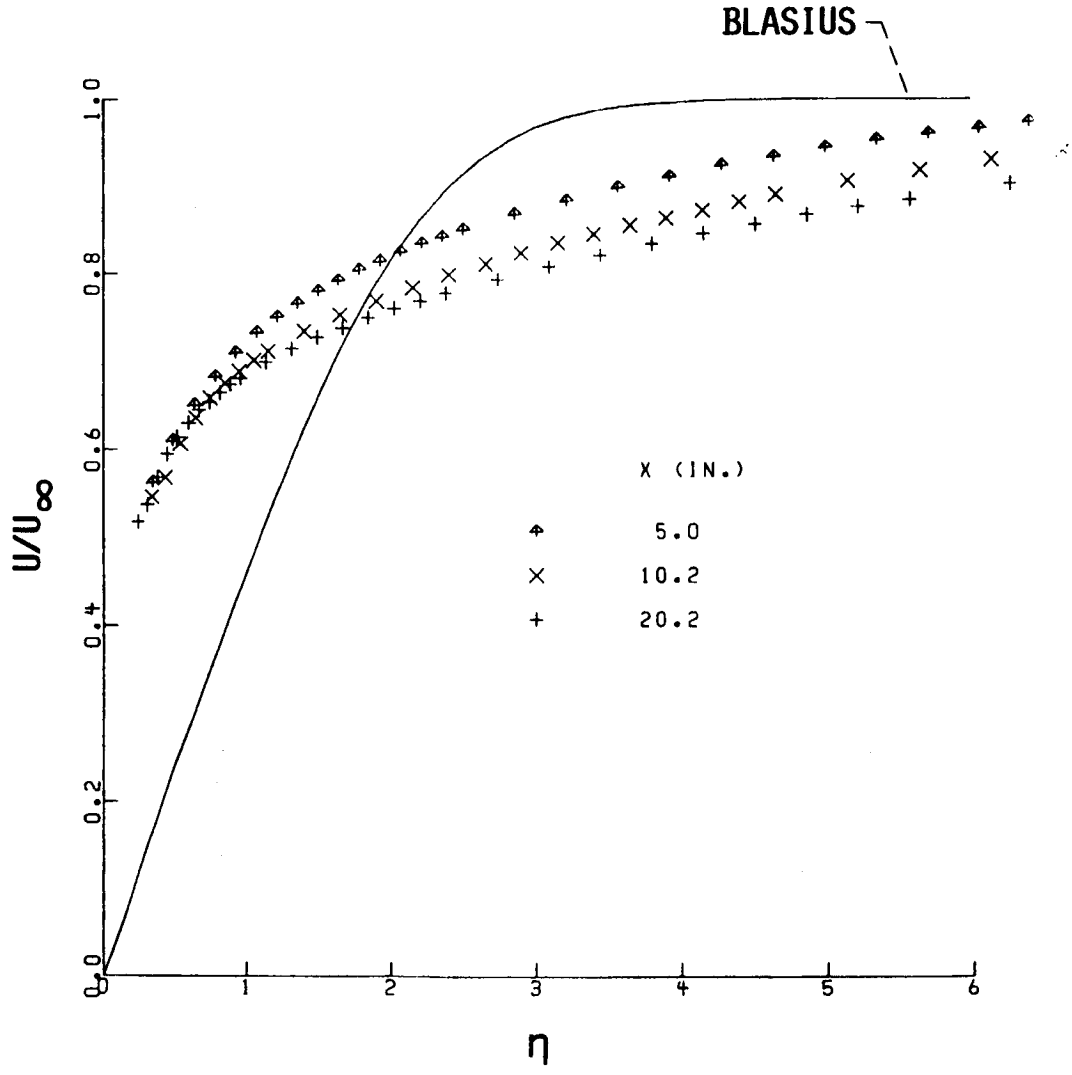

Fig. 37 Grid 3 – plots of η vs. f'(η) overlaid.

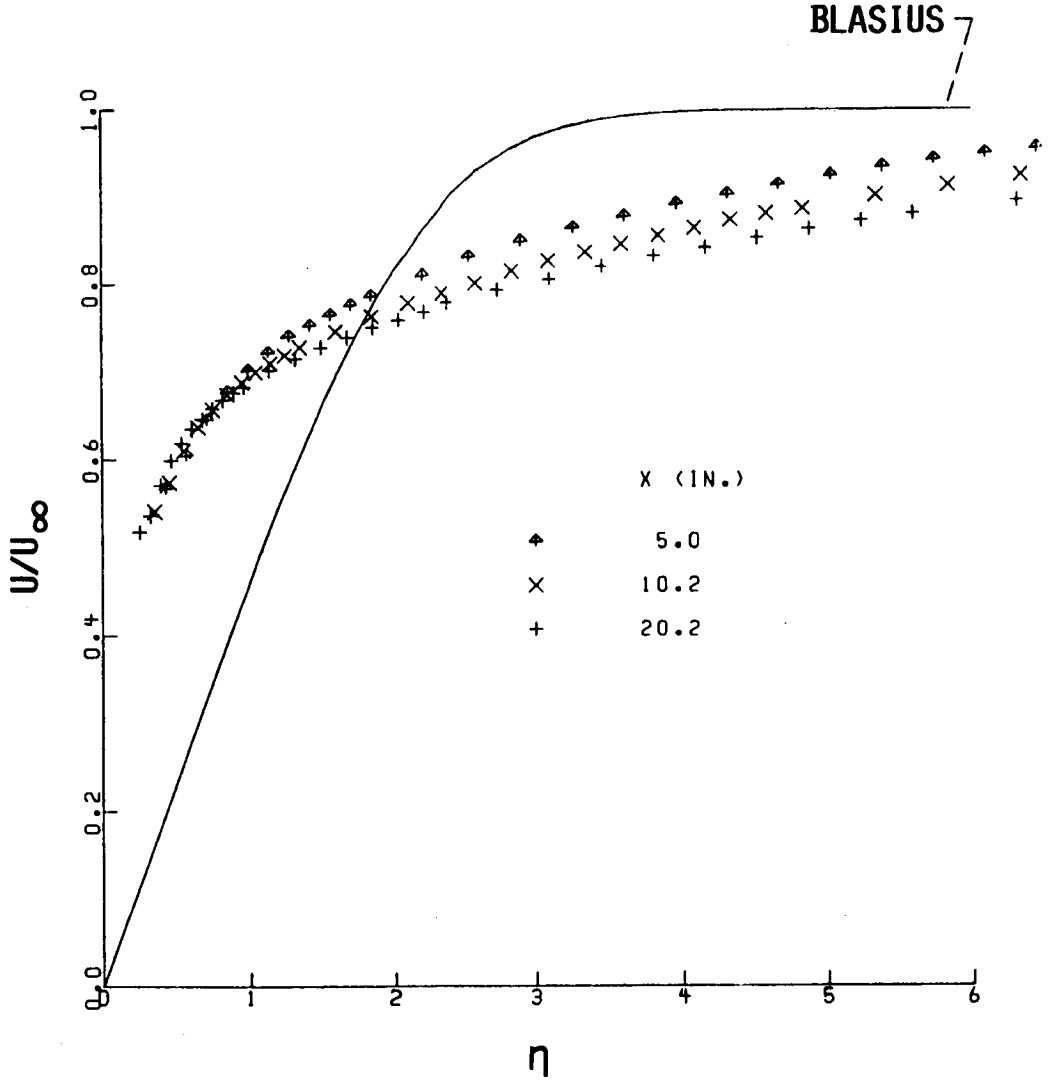

Fig. 38 Grid 4 – plots of η vs. f'(η) overlaid.

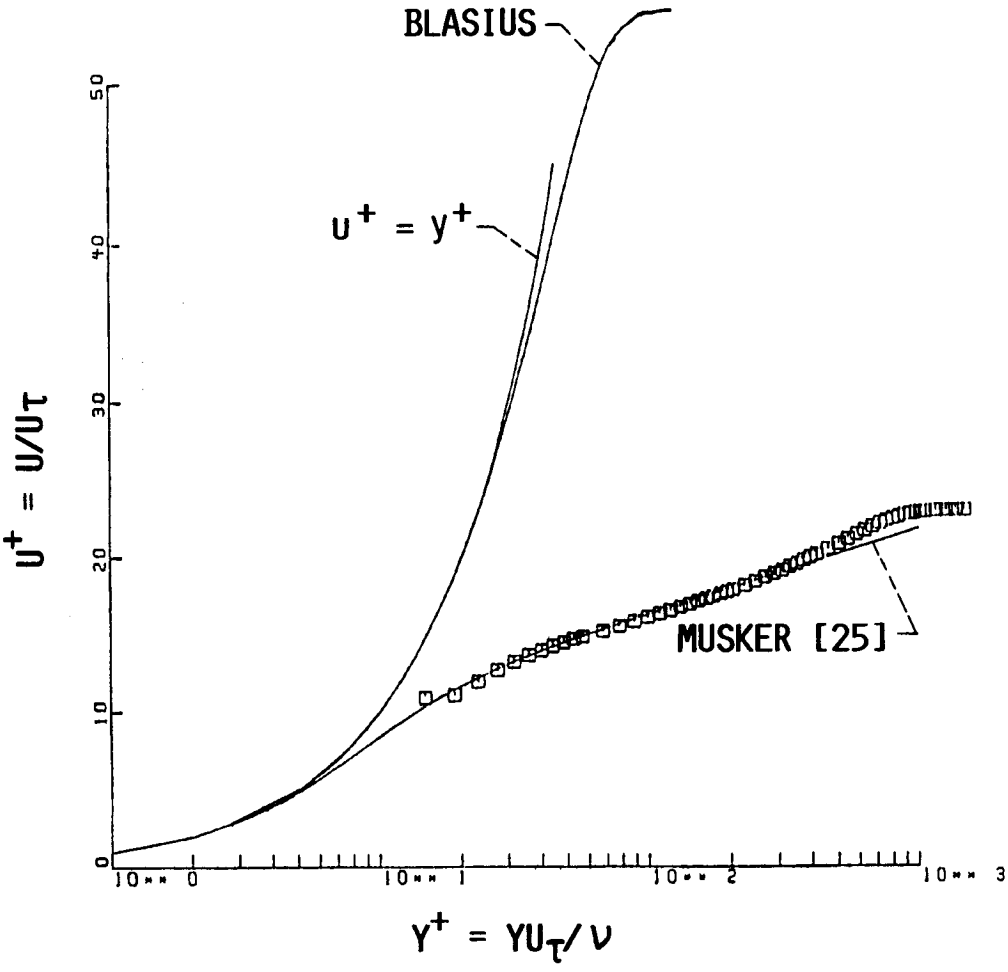

Fig. 39 Application of the Clauser technique to determine the friction velocity for a turbulent boundary layer.

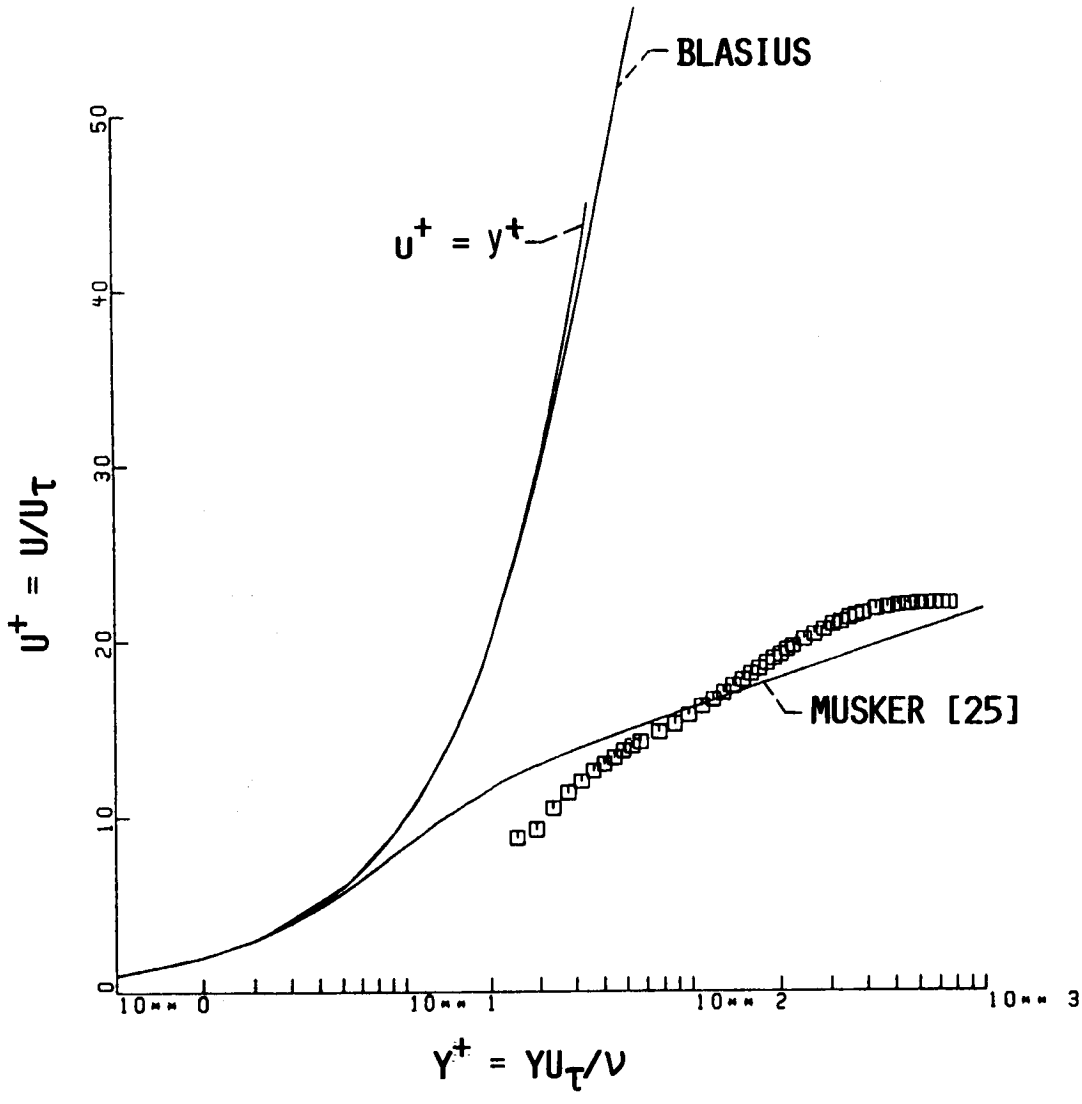

Fig. 40 Grid 0 – Clauser technique applied to the boundary layer at the last survey station.

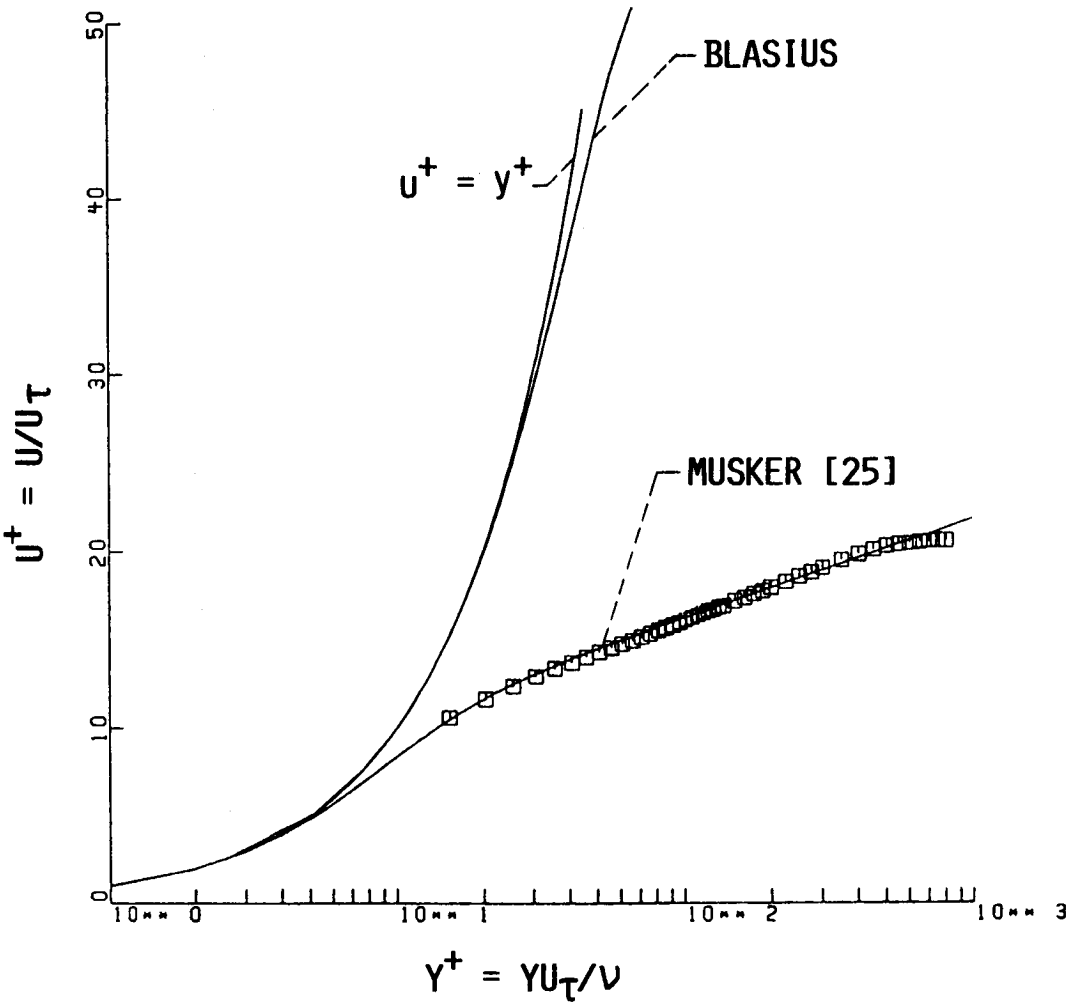

Fig. 41 Grid 0.5 – Clauser technique applied to post–transition turbulent boundary layer.

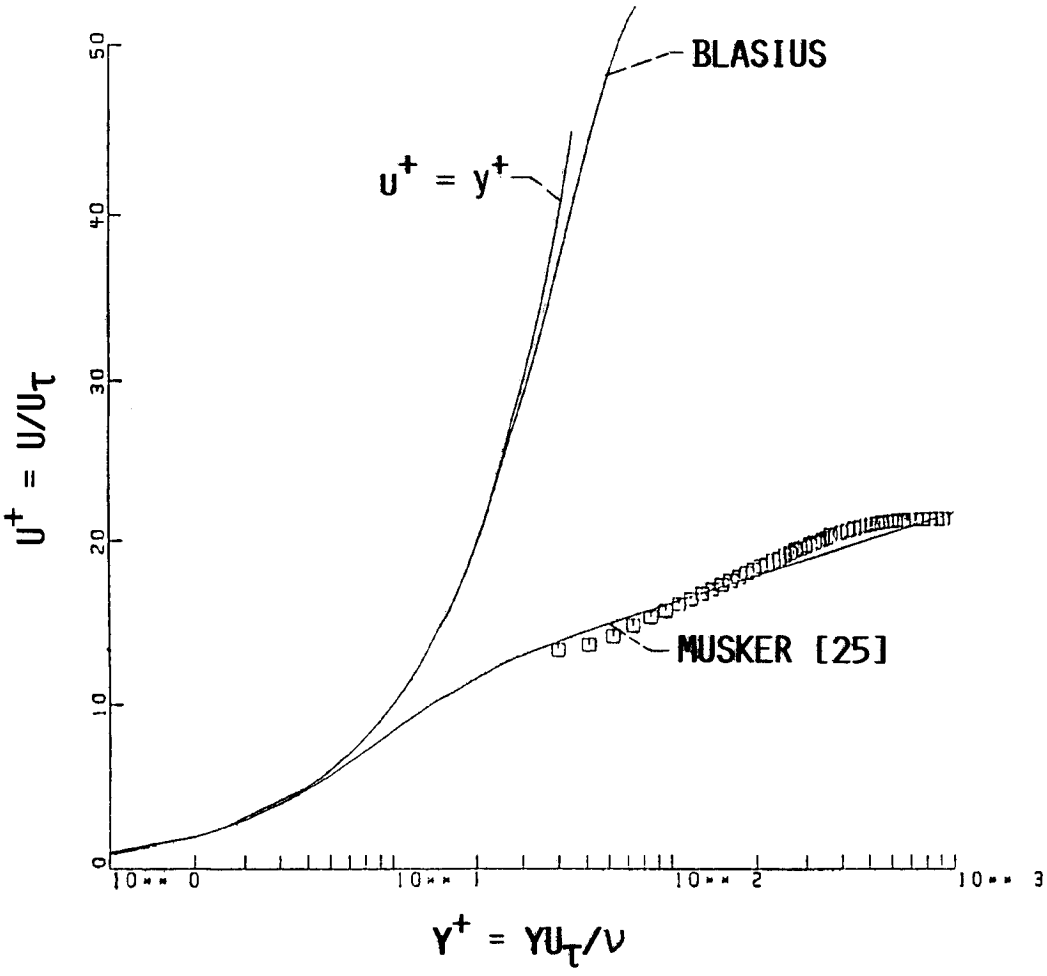

Fig. 42 Grid 1 – Clauser technique applied to the boundary layer at the last survey station.

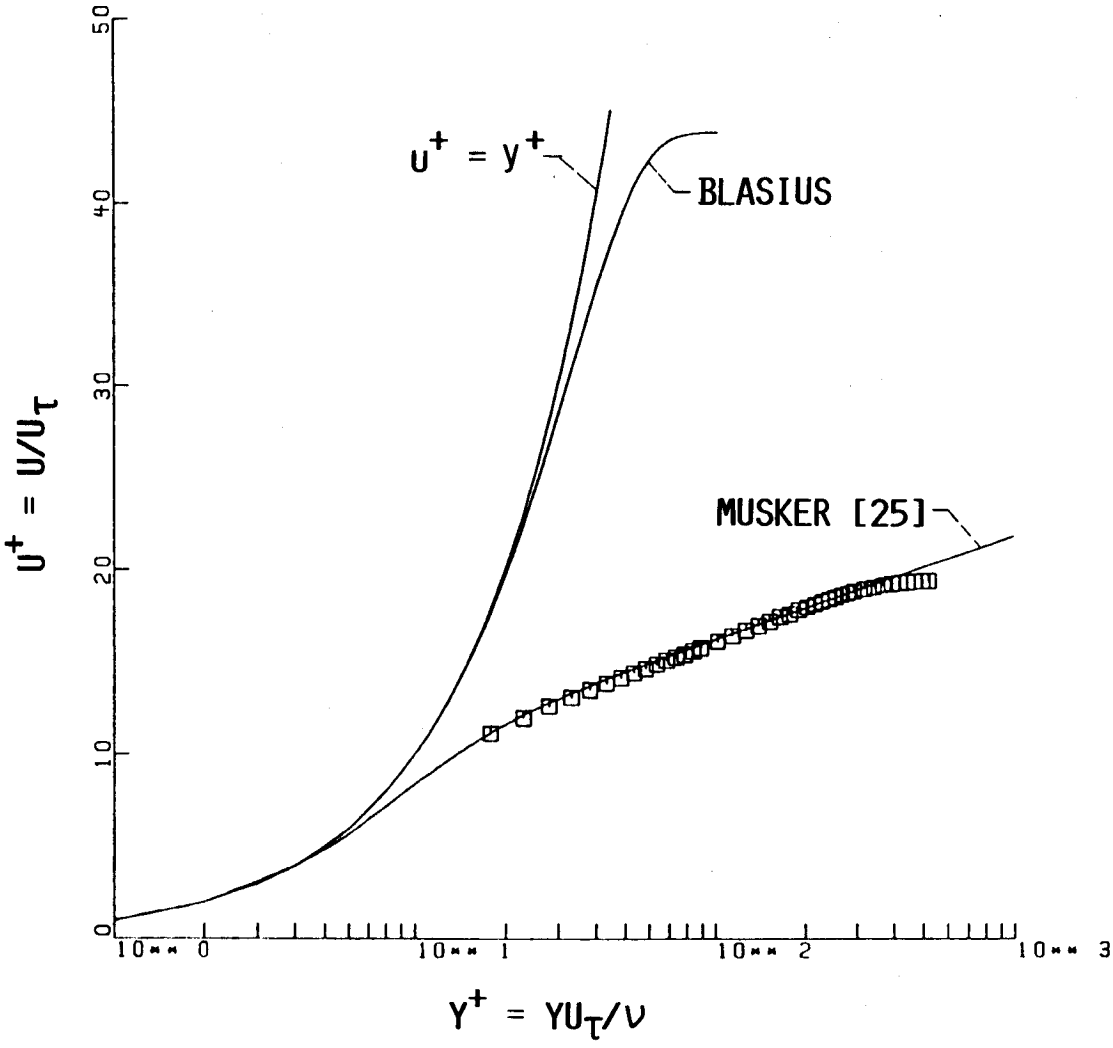

Fig. 43 Grid 2 – Clauser technique applied to post–transition turbulent boundary layer.

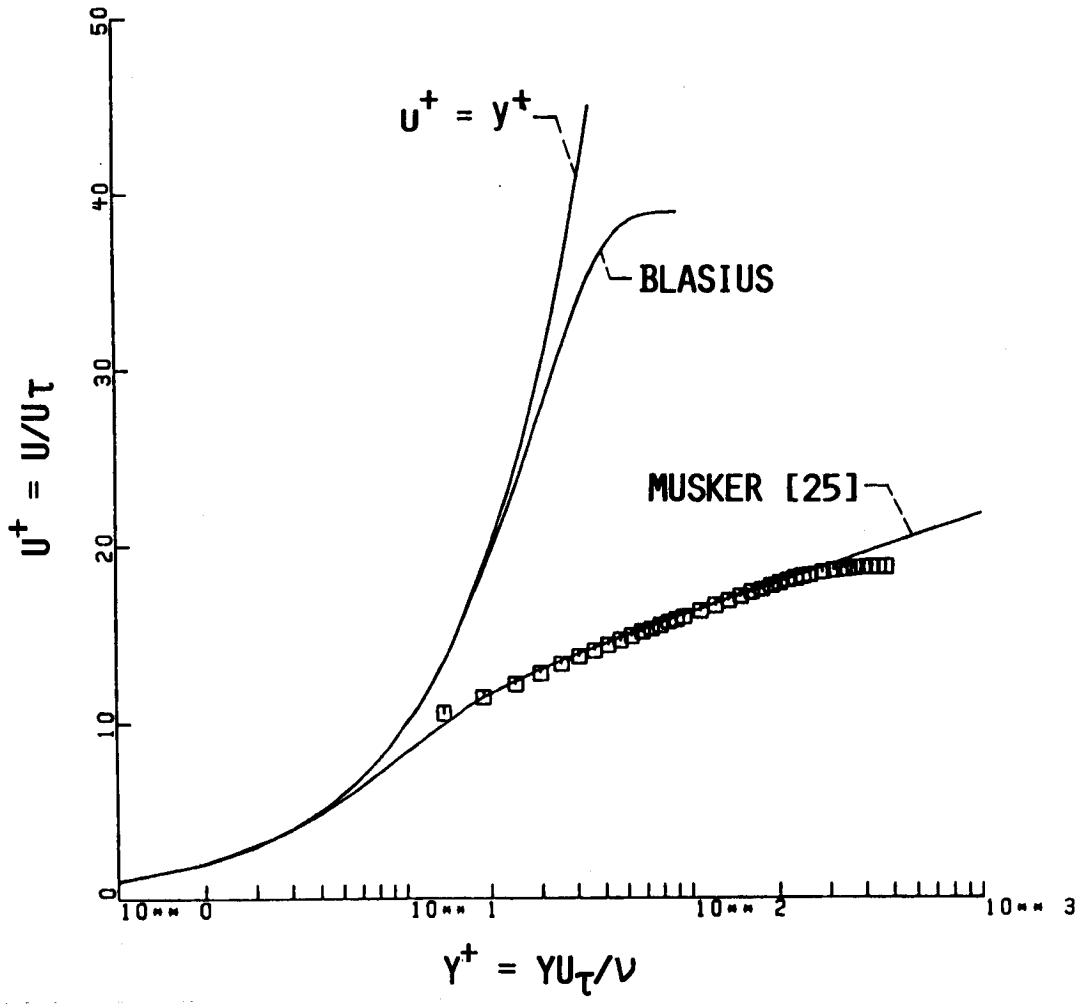

Fig. 44 Grid 3 – Clauser technique applied to post–transition turbulent boundary layer.

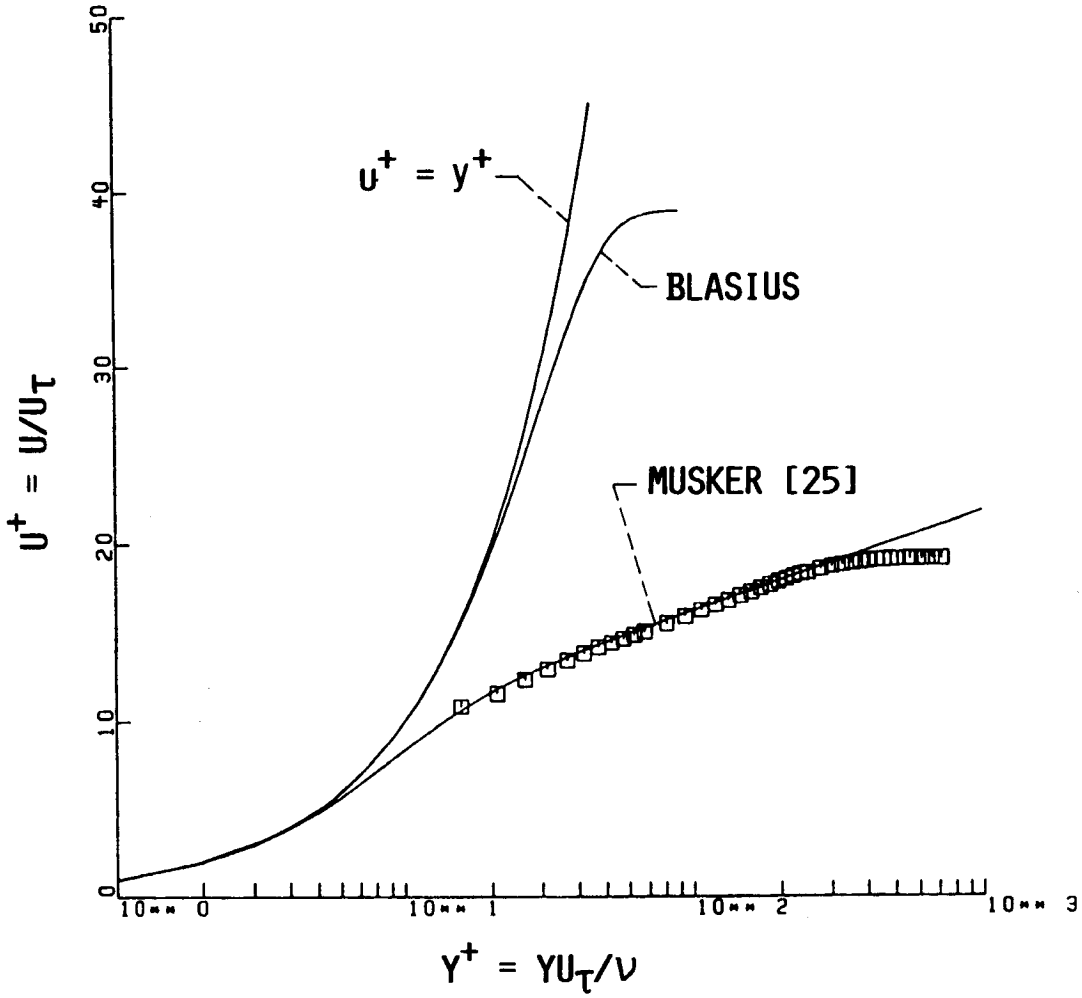

Fig. 45 Grid 4 – Clauser technique applied to post–transition turbulent boundary layer.

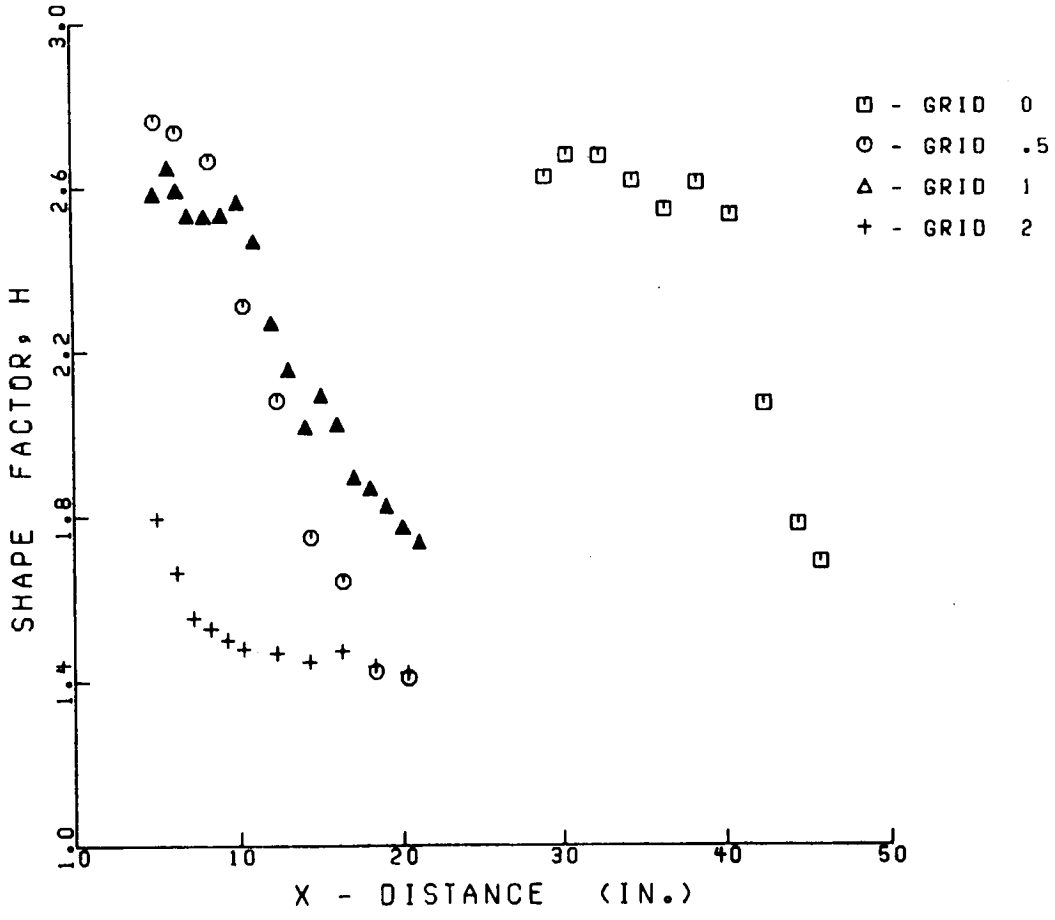

Fig. 46 Boundary layer shape factor versus x distance.

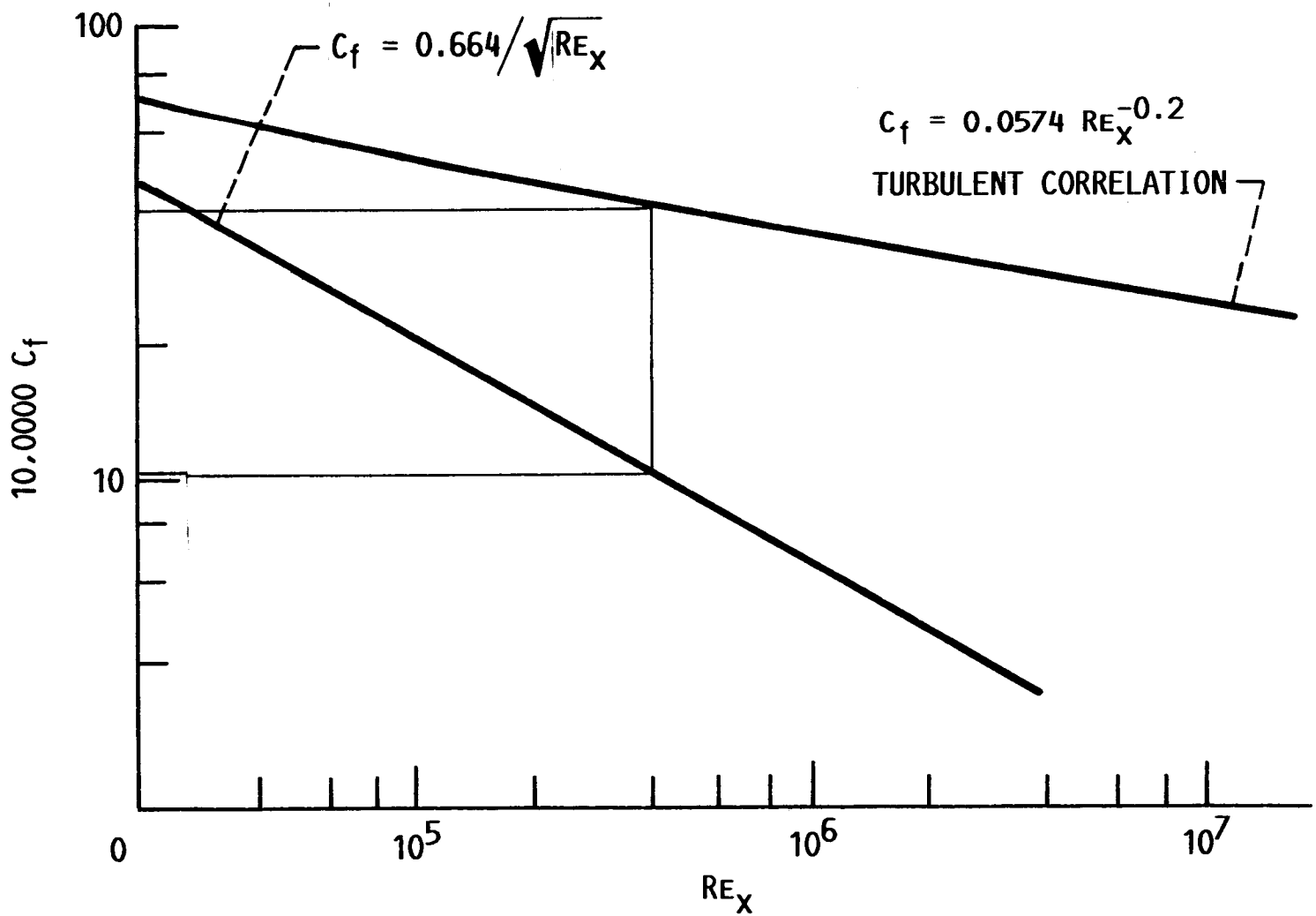

Fig. 47 Typical plot of skin friction coefficient versus x distance.

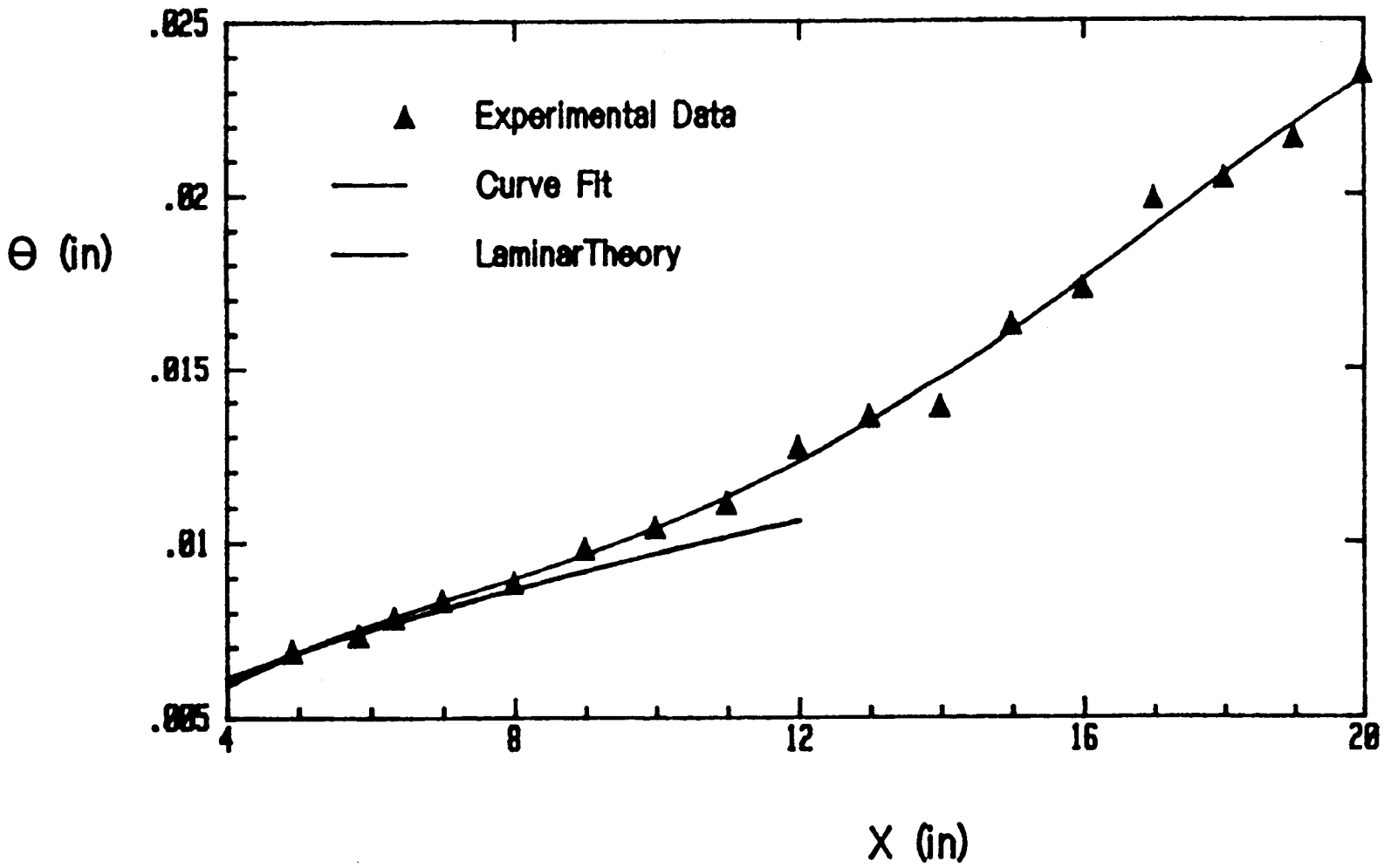

Fig. 48 Boundary layer momentum thickness versus x distance – grid 1.

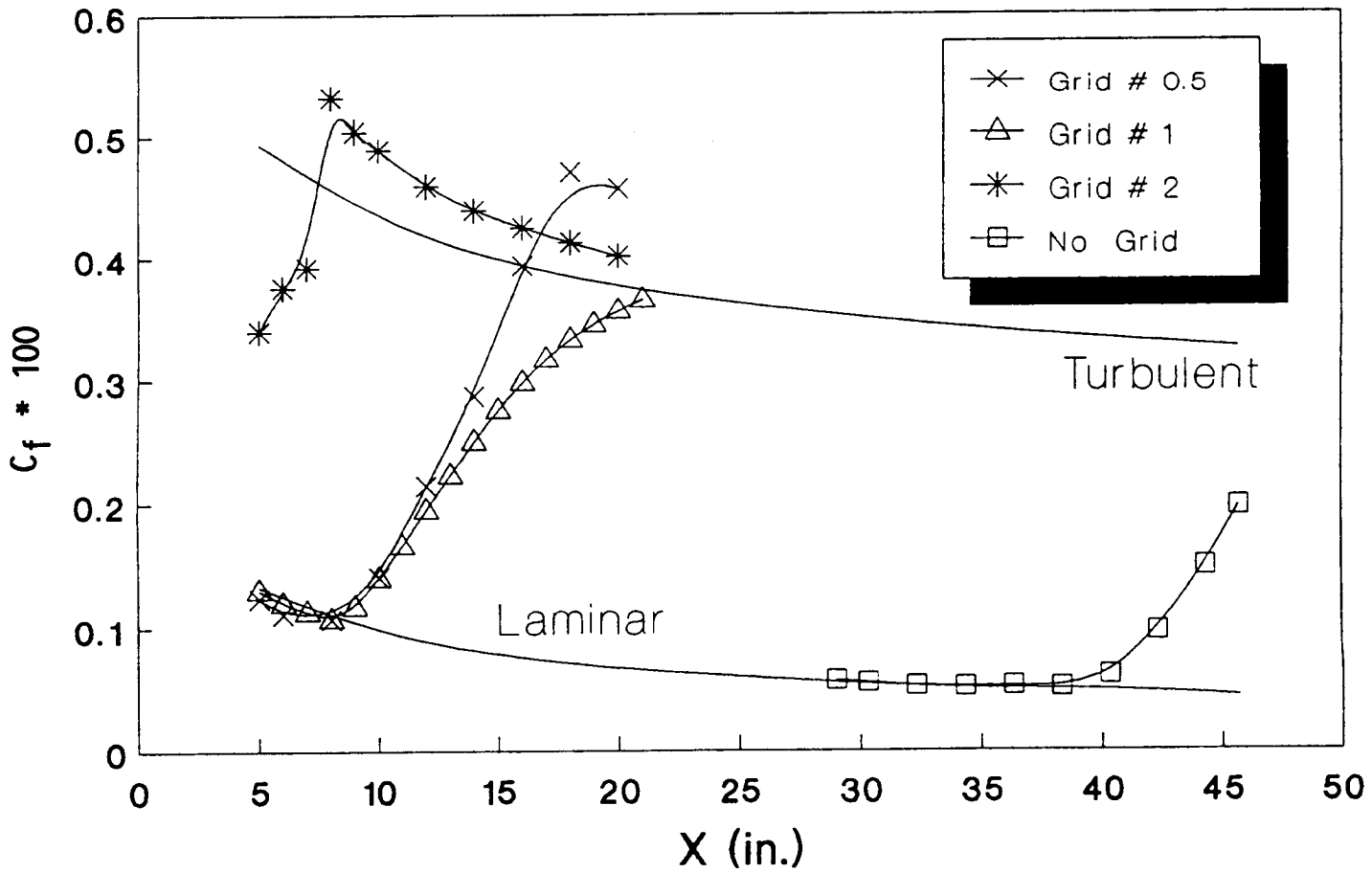

Fig 49 Skin friction coefficient versus x distance.

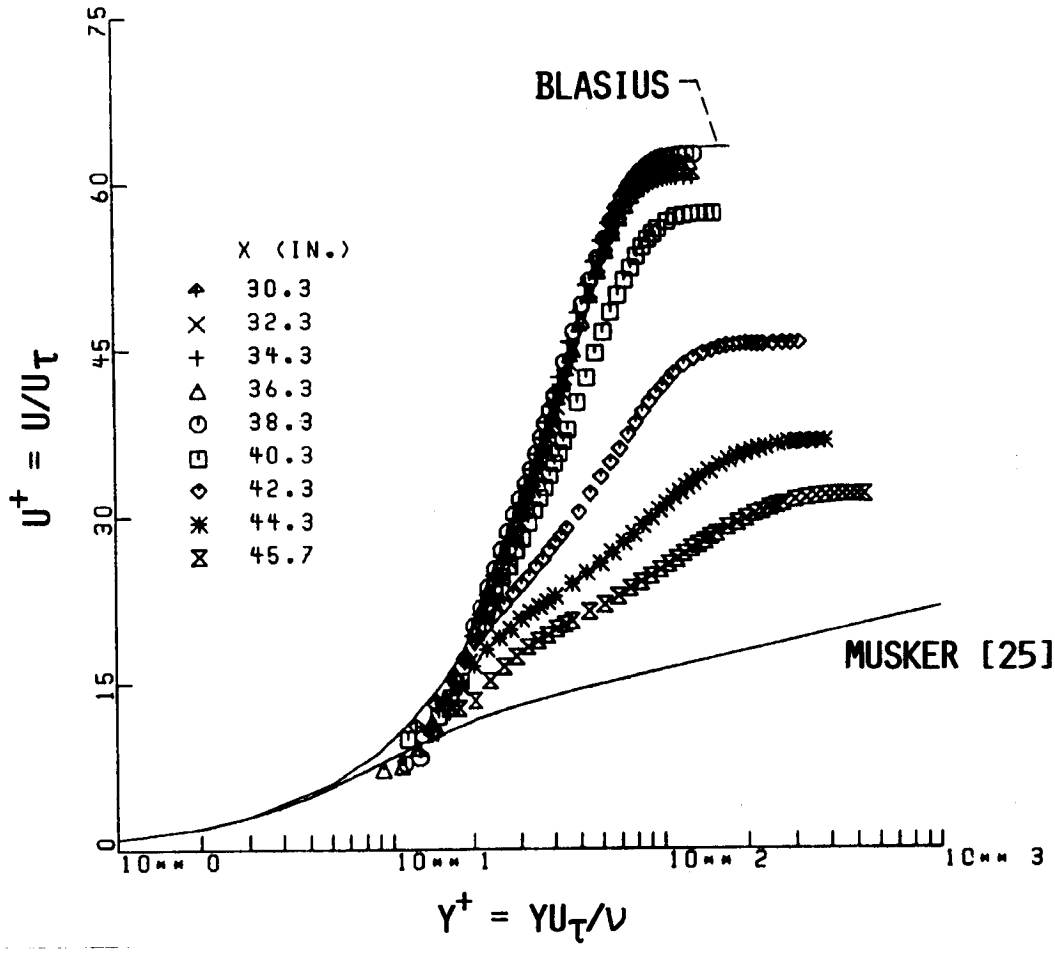

Fig. 50 Grid 0 — Mean velocity profiles in wall units.

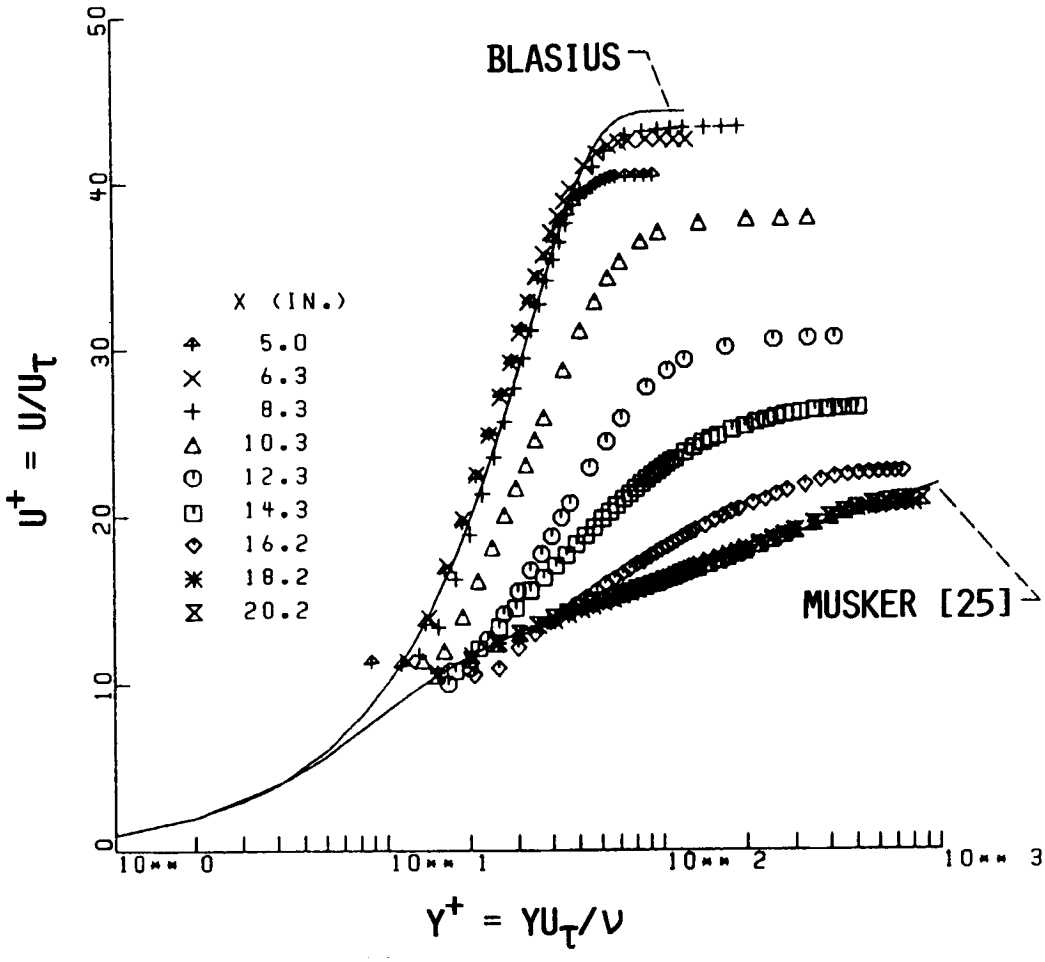

Fig. 51 Grid 0.5 – Mean velocity profiles in wall units.

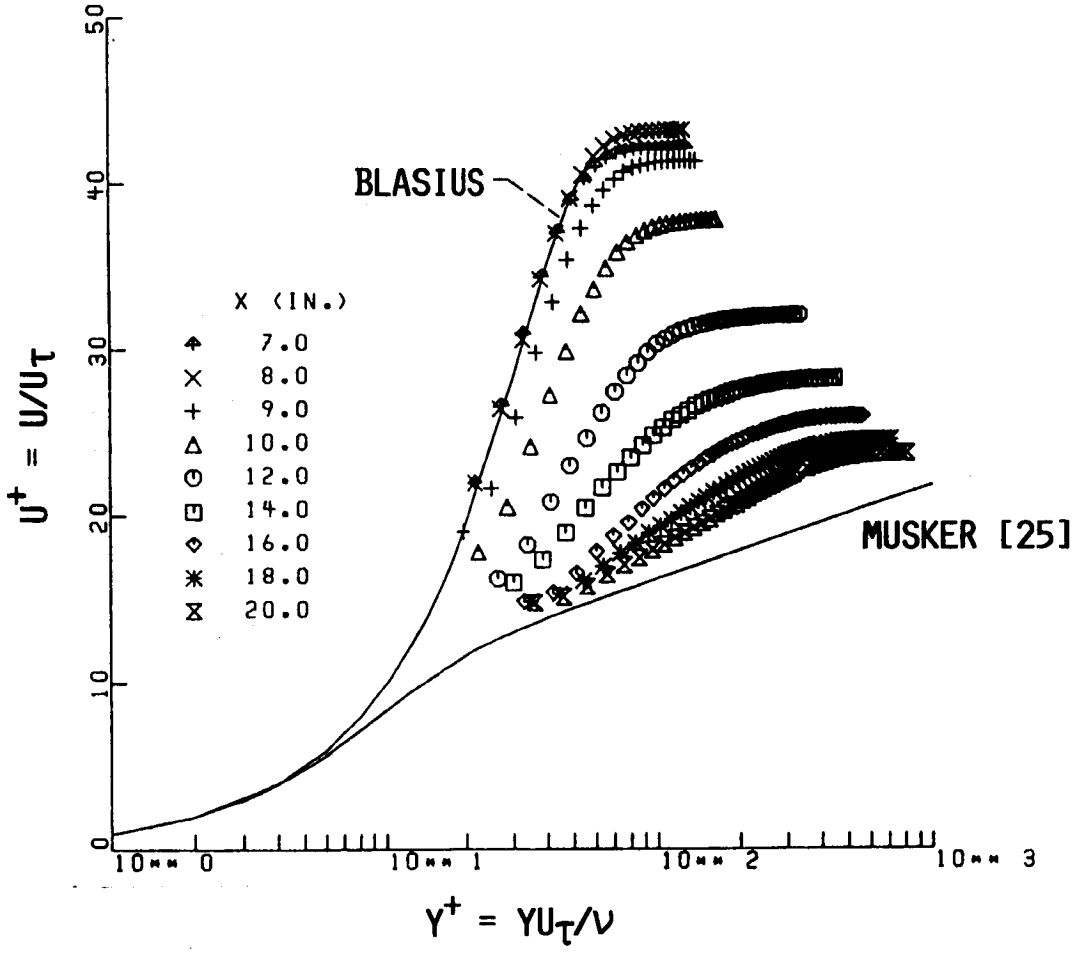

Fig. 52 Grid 1 — Mean velocity profiles in wall units.

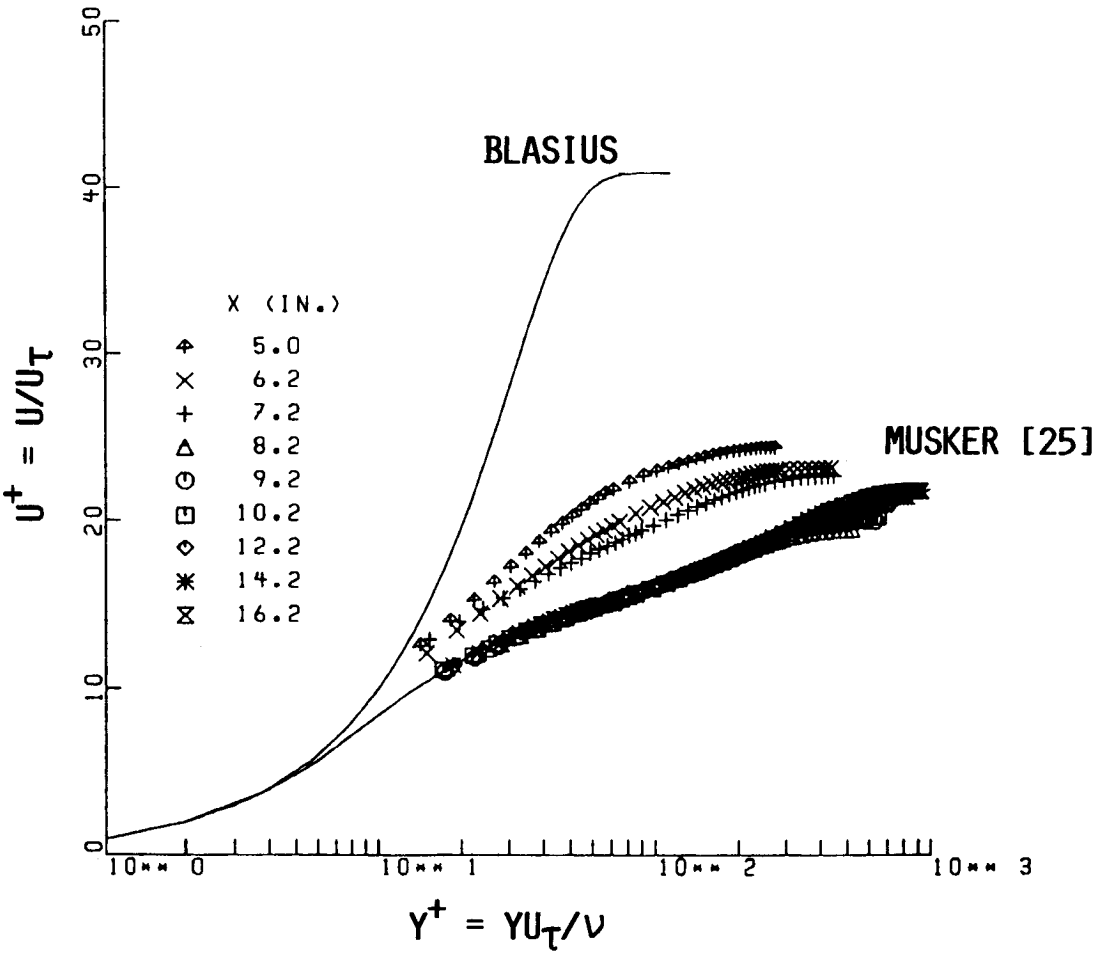

Fig. 53 Grid 2 – Mean velocity profiles in wall units.

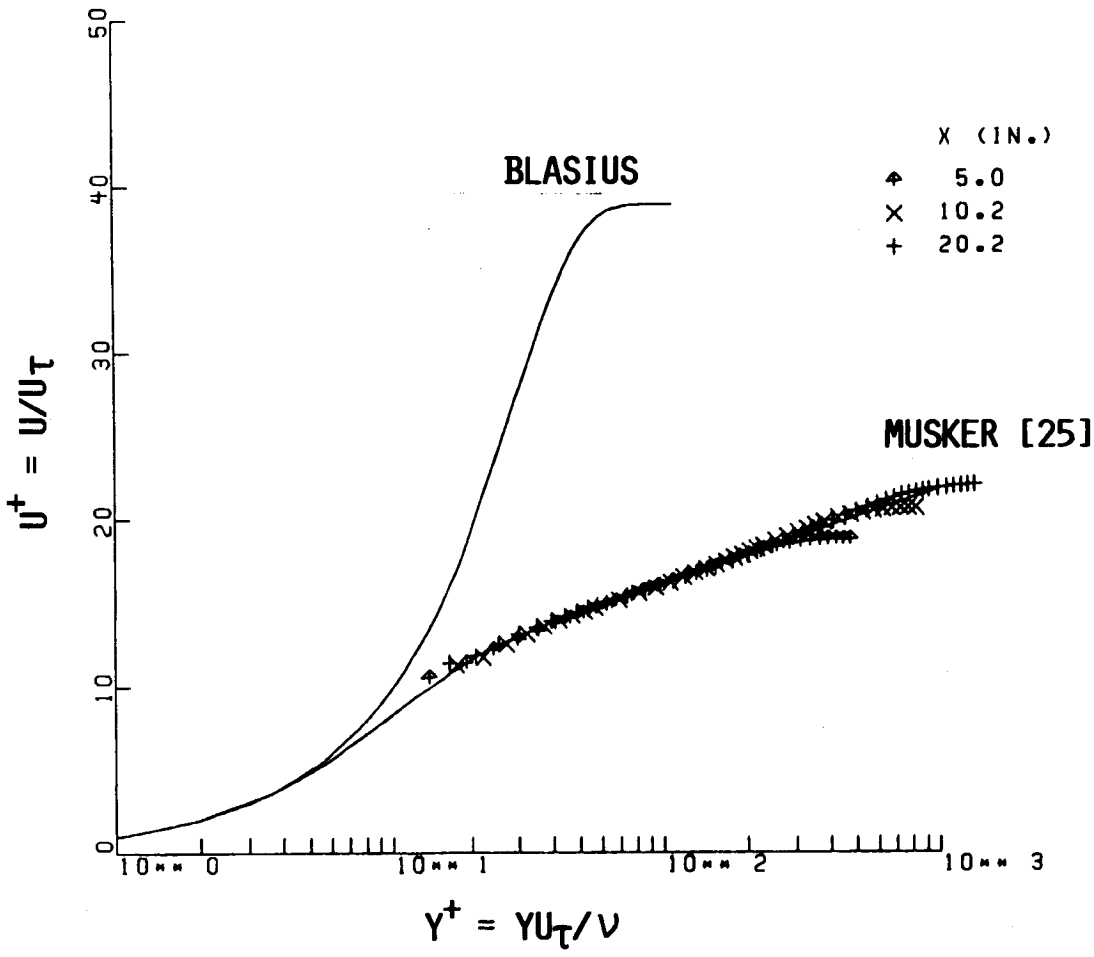

Fig 54 Grid 3 — Mean velocity profiles in wall units.

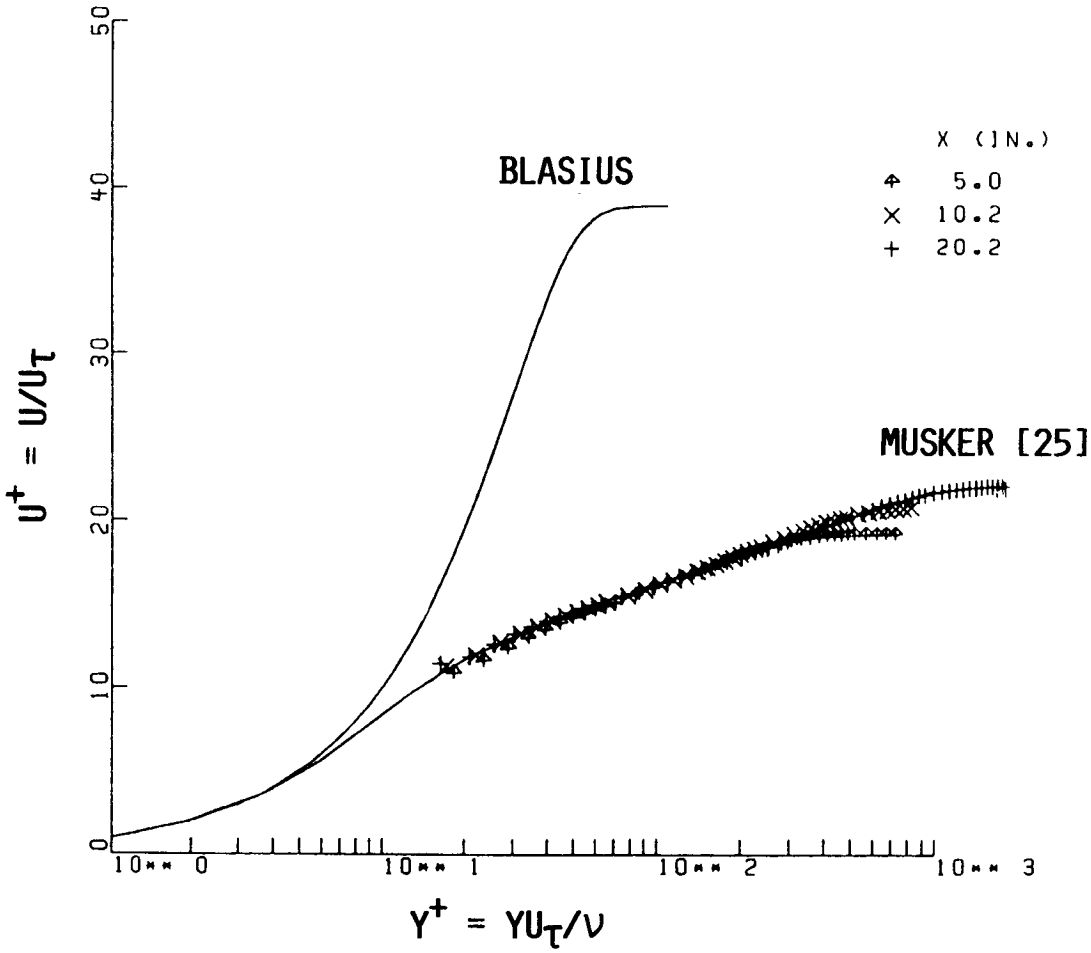

Fig. 55 Grid 4 – Mean velocity profiles in wall units.

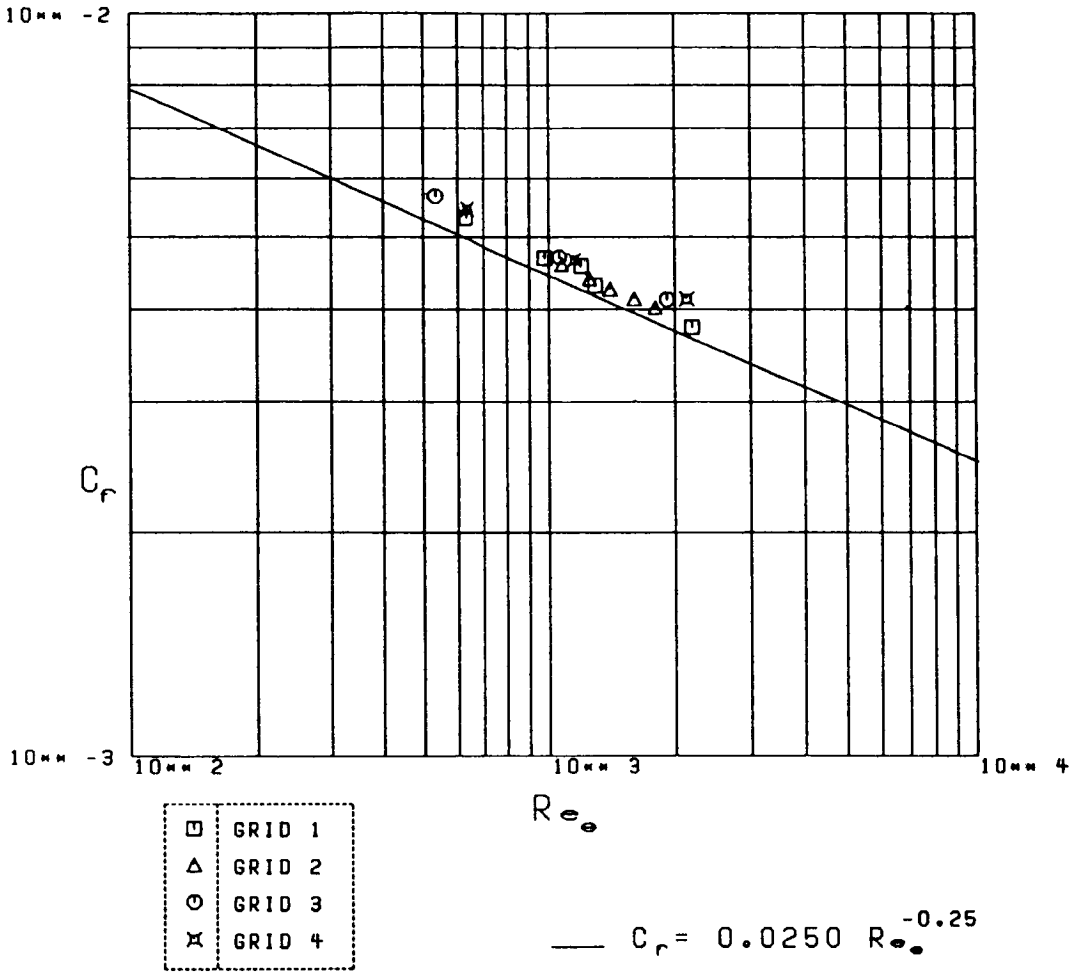

Fig. 56 Comparison of skin friction resulting from the Clauser technique to empirical correlations.

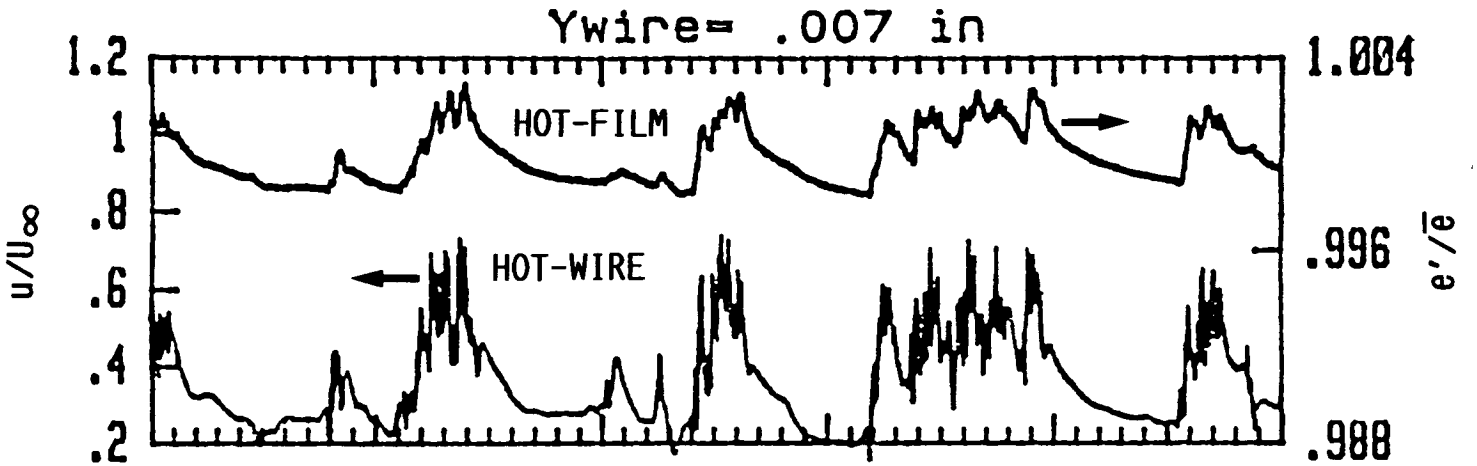

Fig. 57 Comparison of voltage swings due to the passing of a turbulent burst between a flush–mounted hot–film and a hot–wire located adjacent to the hot–film.

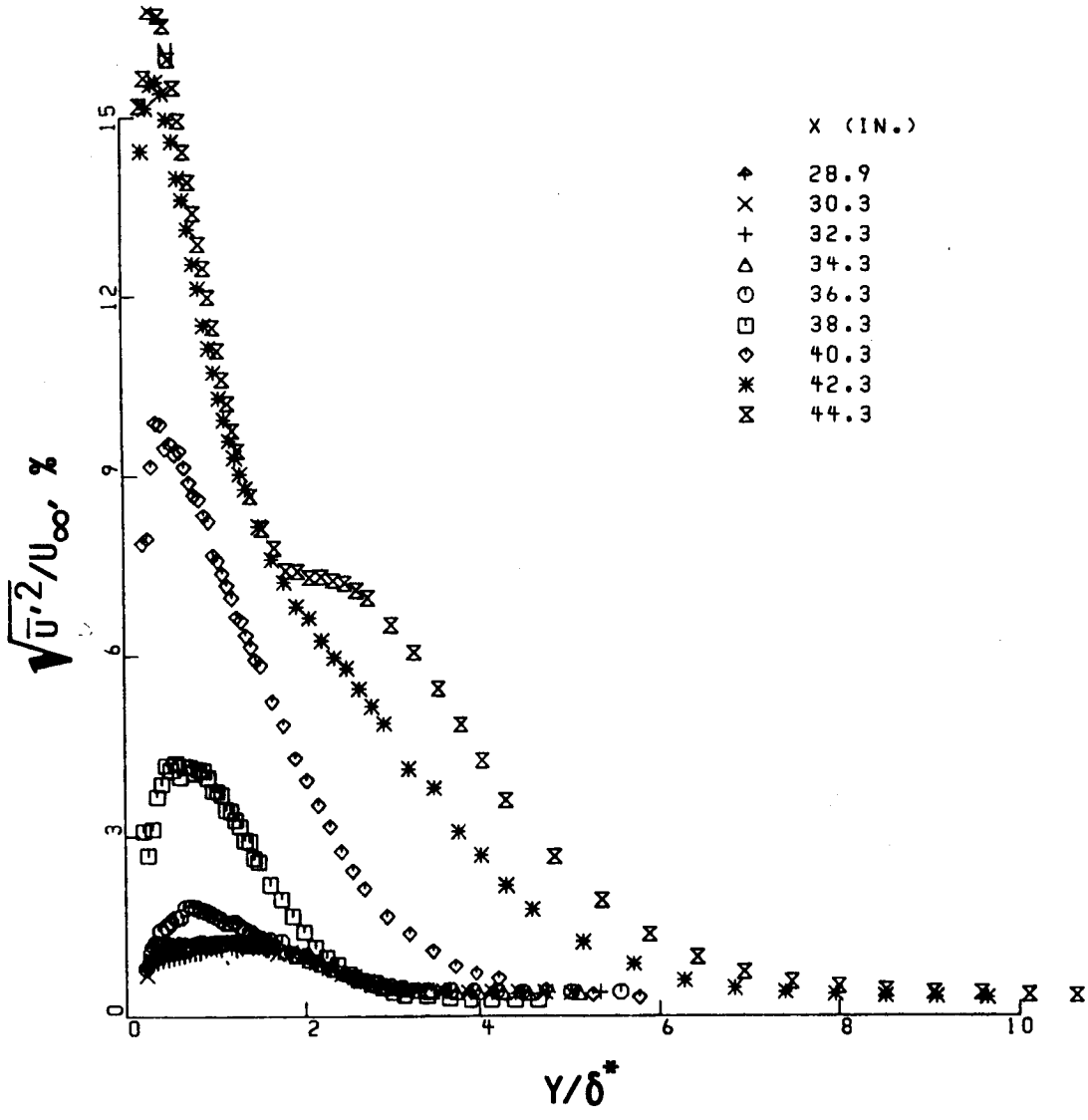

Fig. 58 Grid 0 – Boundary layer profiles of the RMS of the velocity fluctuations within the boundary layer.

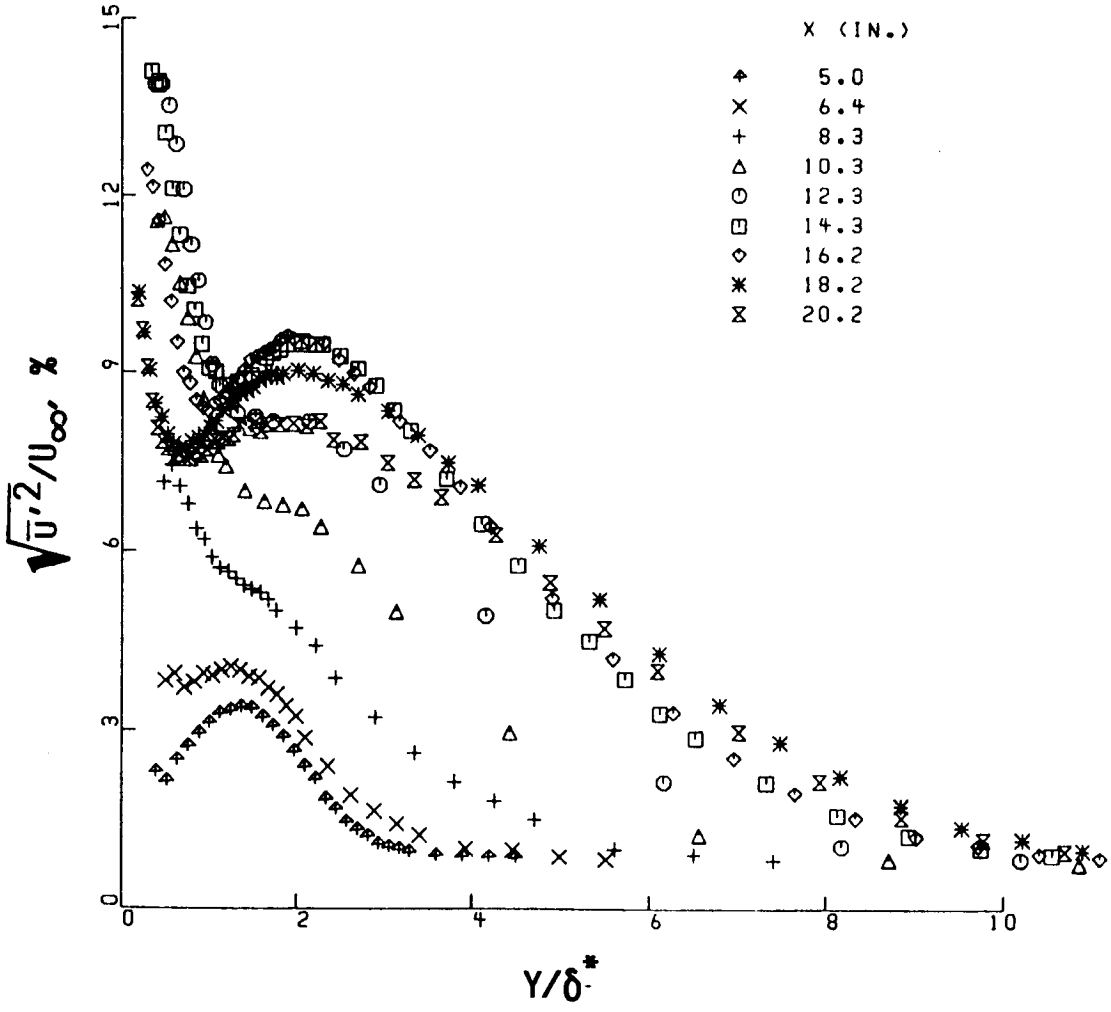

Fig. 59 Grid 0.5 – Boundary layer profiles of the RMS of the velocity fluctuations within the boundary layer.

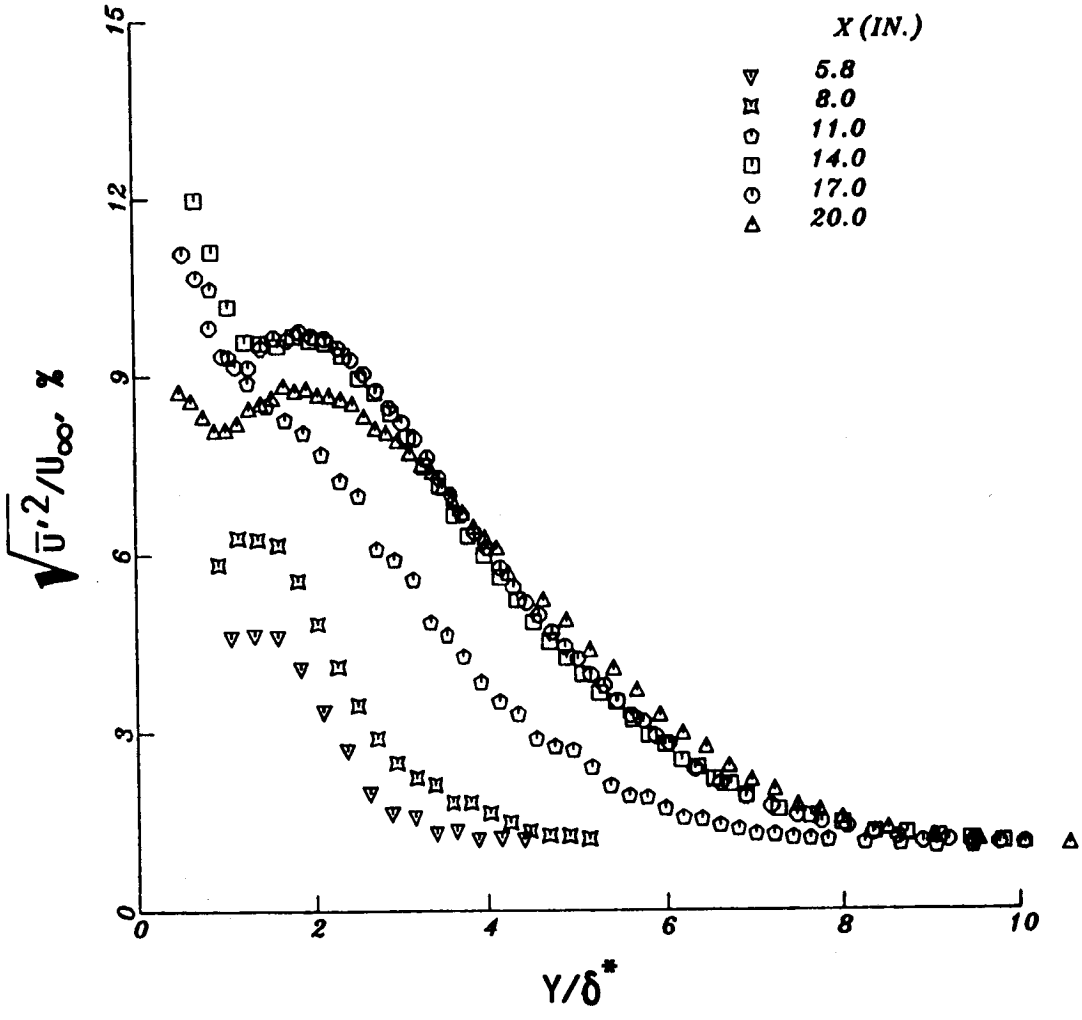

Fig. 60 Grid 1 – Boundary layer profiles of the RMS of the velocity fluctuations within the boundary layer.

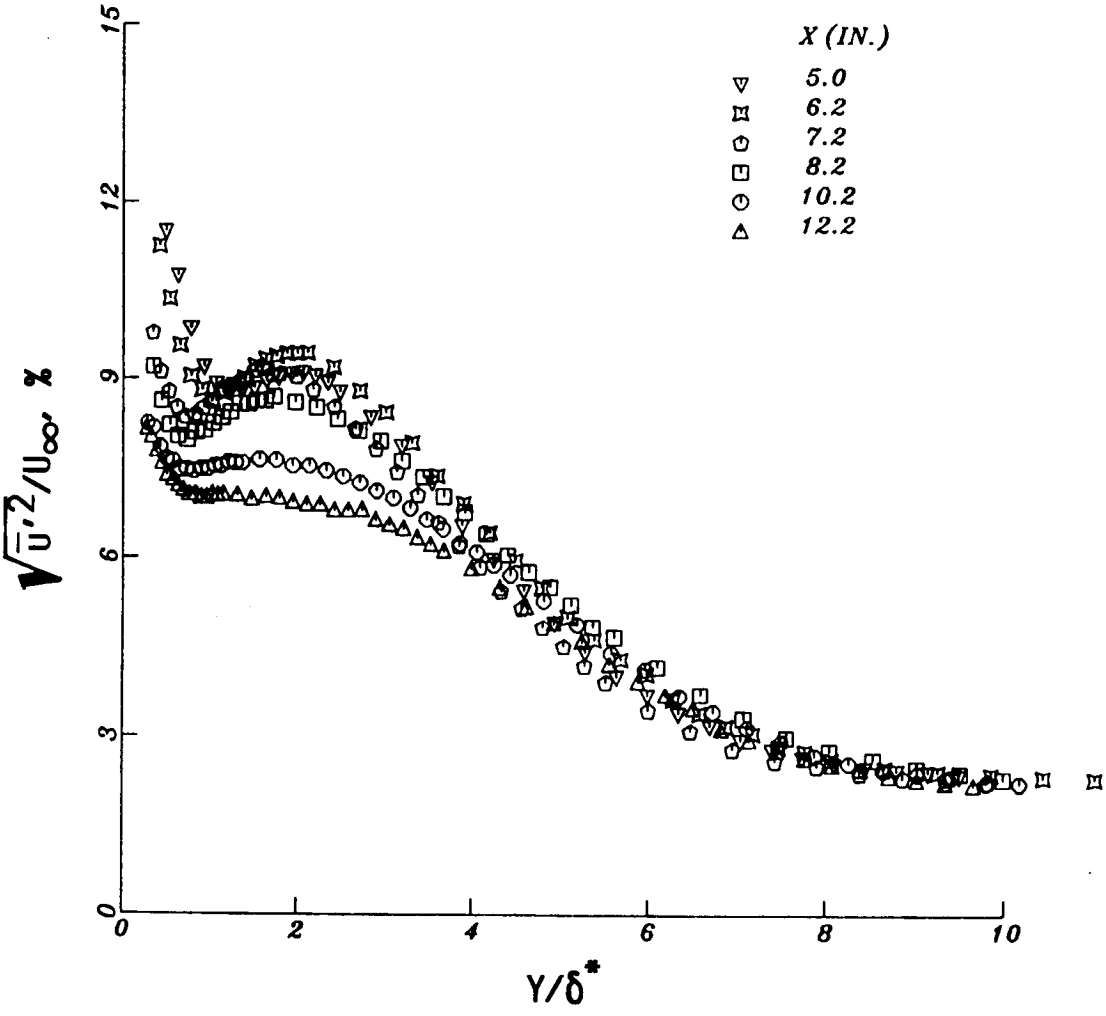

Fig. 61 Grid 2 – Boundary layer profiles of the RMS of the velocity fluctuations within the boundary layer.

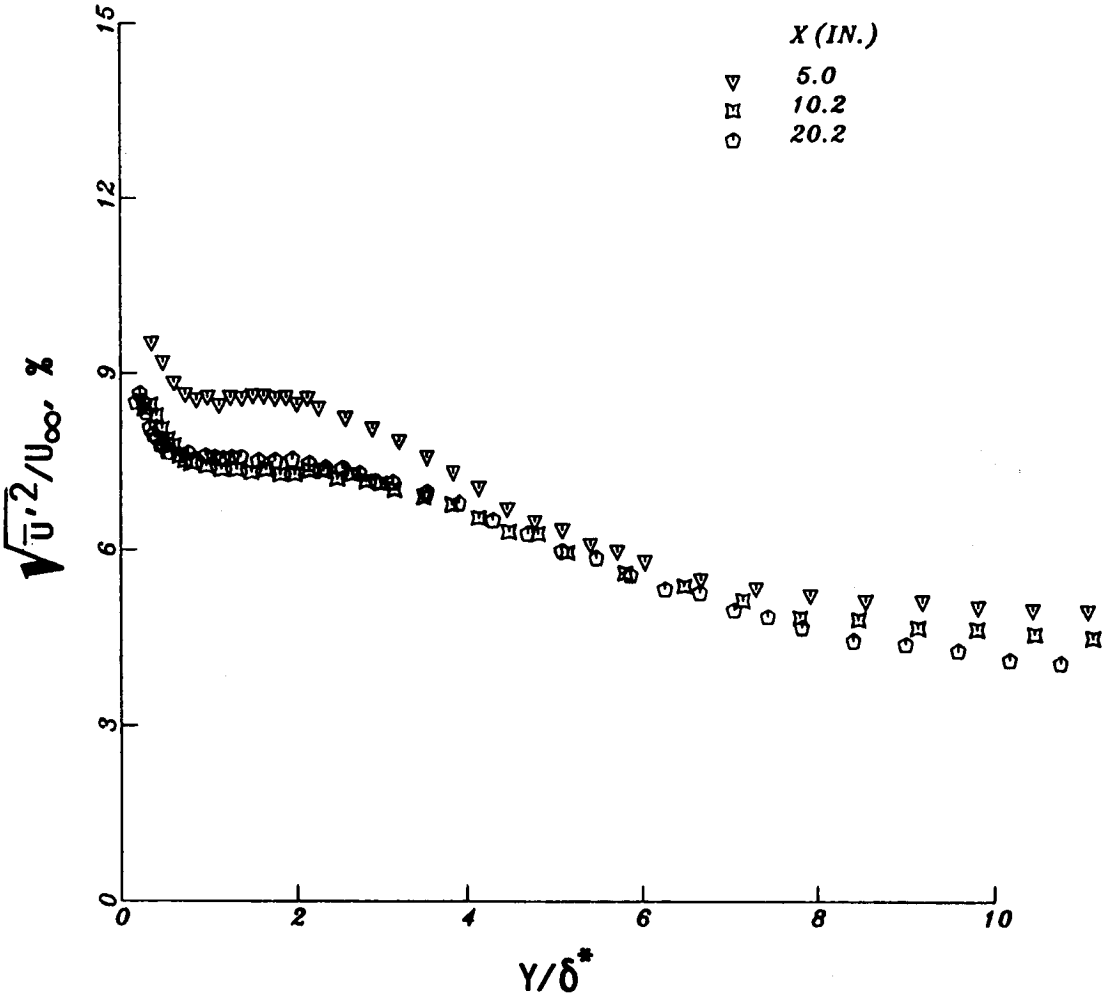

Fig. 62 Grid 3 – Boundary layer profiles of the RMS of the velocity fluctuations within the boundary layer.

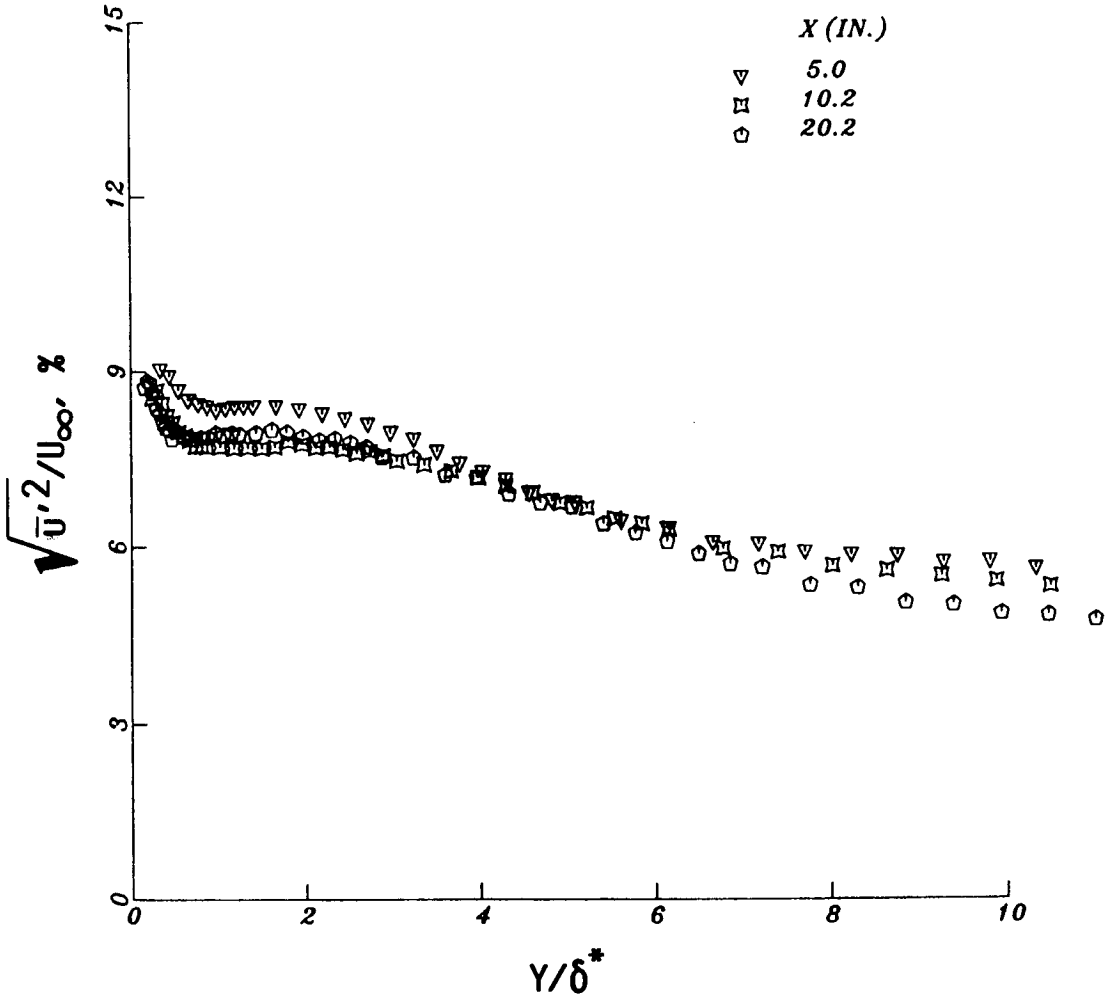

Fig. 63 Grid 4 – Boundary layer profiles of the RMS of the velocity fluctuations within the boundary layer.

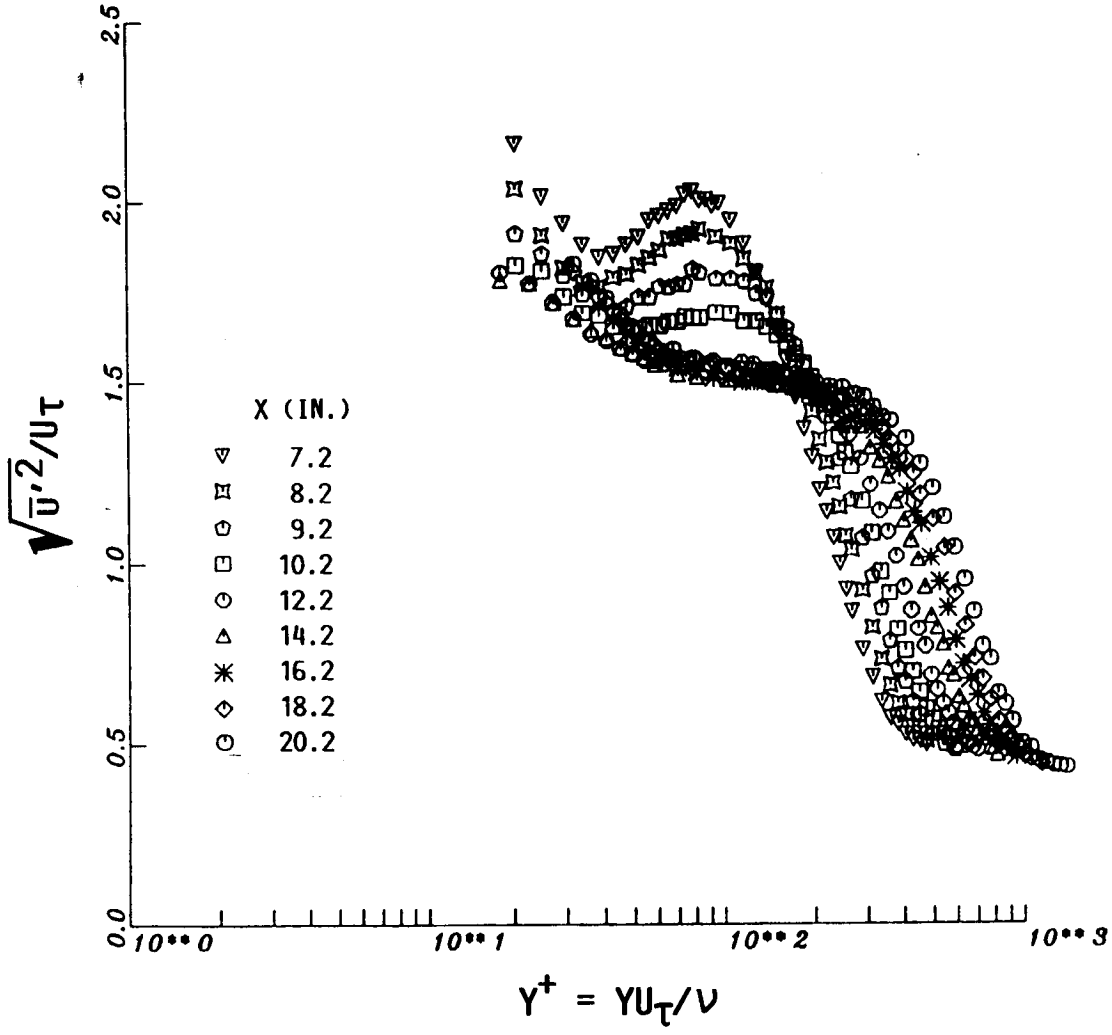

Fig. 64 Normalized profiles of the RMS of the velocity fluctuations within the boundary layer in wall units – grid 2.

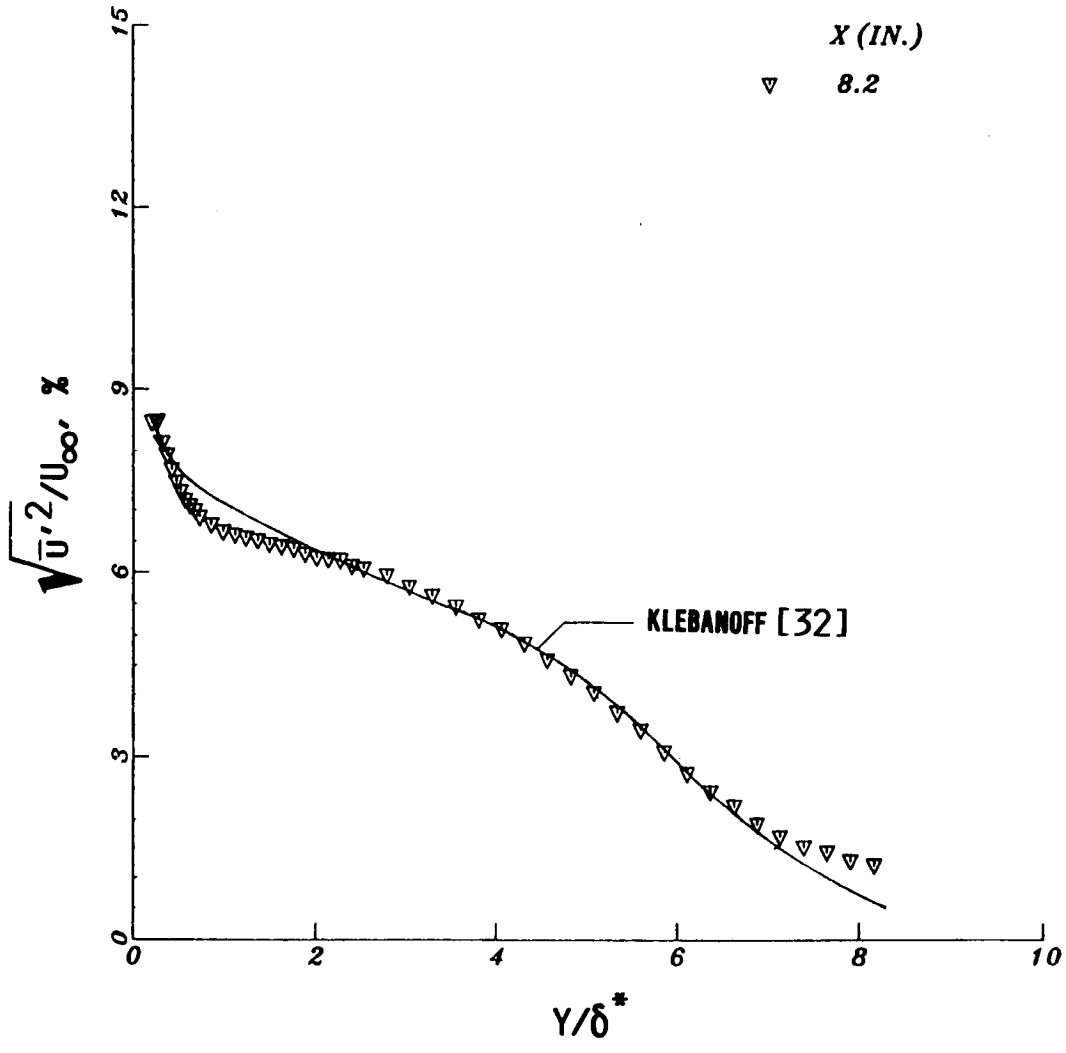

Fig. 65 Comparison of the RMS measurements to the results of Klebanoff for a fully turbulent boundary layer.

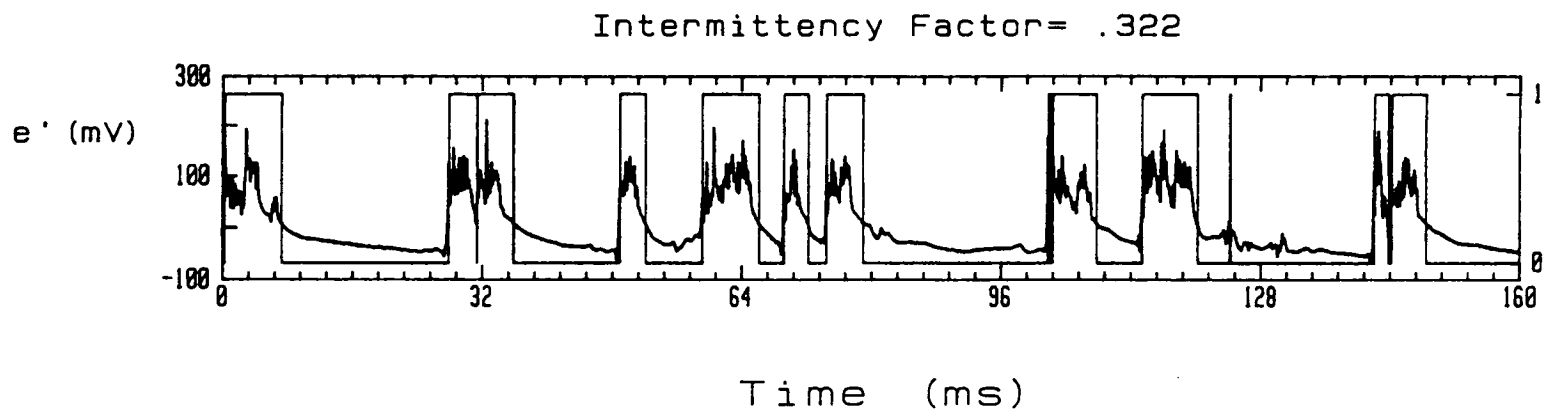

Fig. 66 Procedure to determine the intermittency factor.

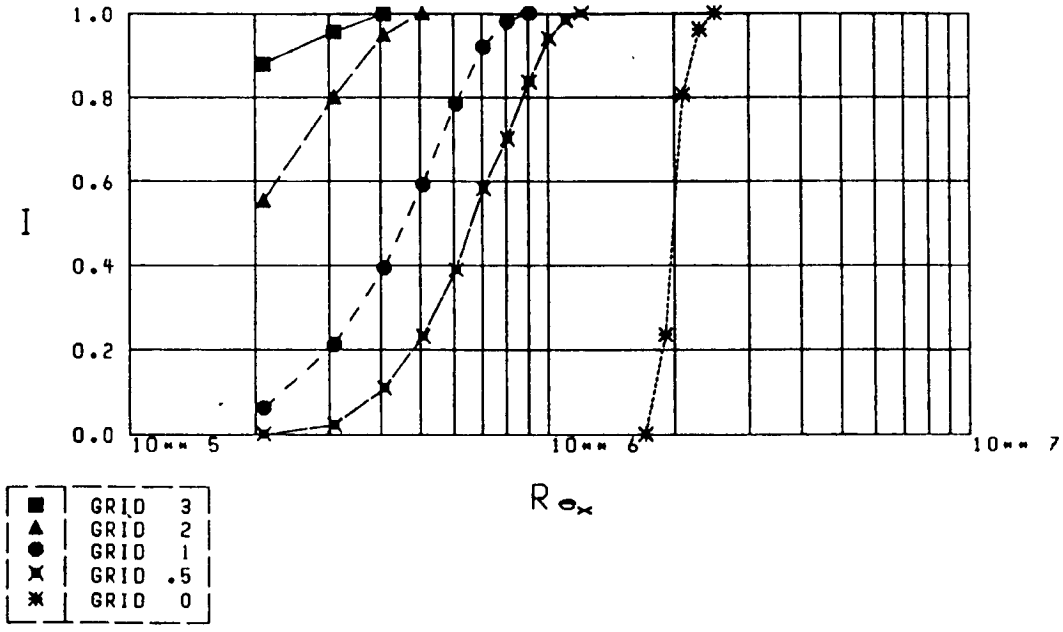

Fig. 67 Intermittency factor versus Reynolds number based on x distance.

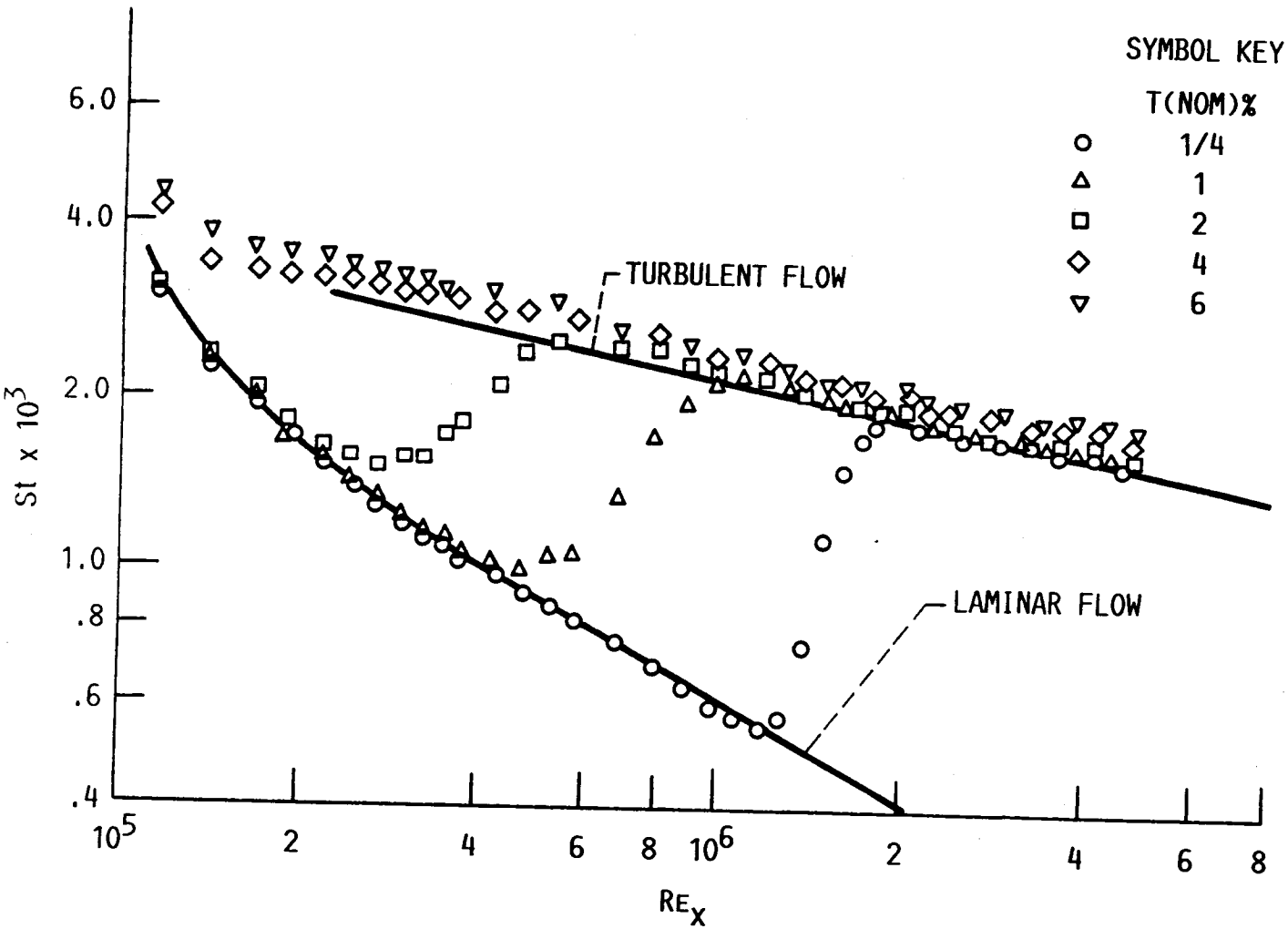

Fig. 68 Stanton number versus Reynolds number based on x distance — from Blair [33].

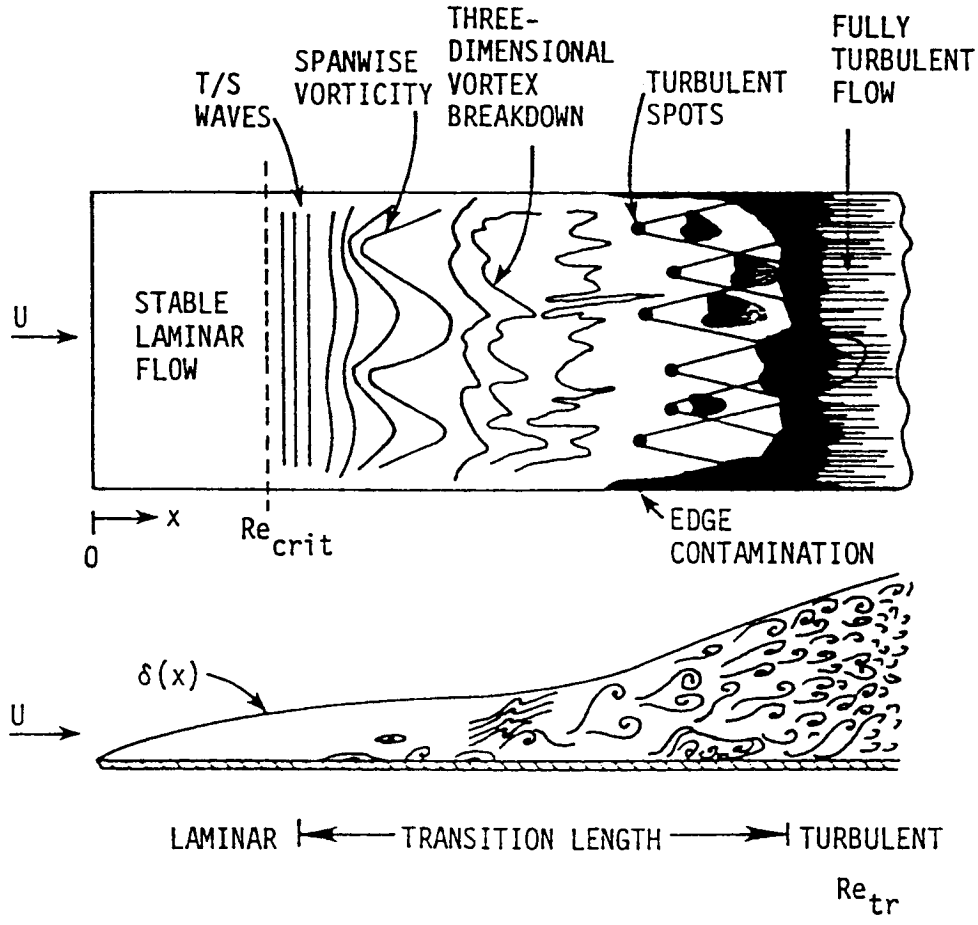

Fig. 69 Transition via the T–S path – from White [1].

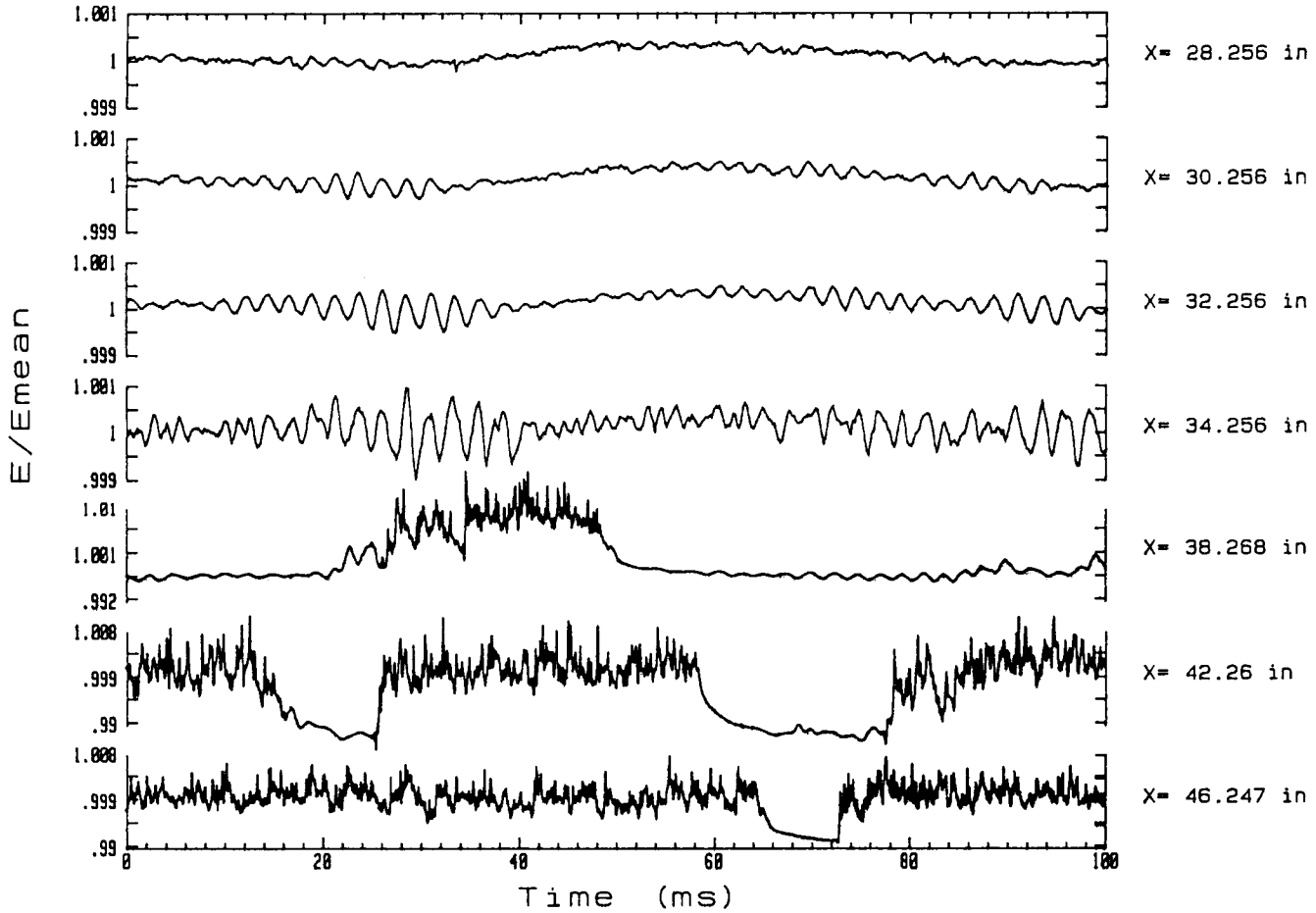

Fig. 70 Grid 0 – Simultaneous traces of the flush–mounted hot films encompassing the transition region.

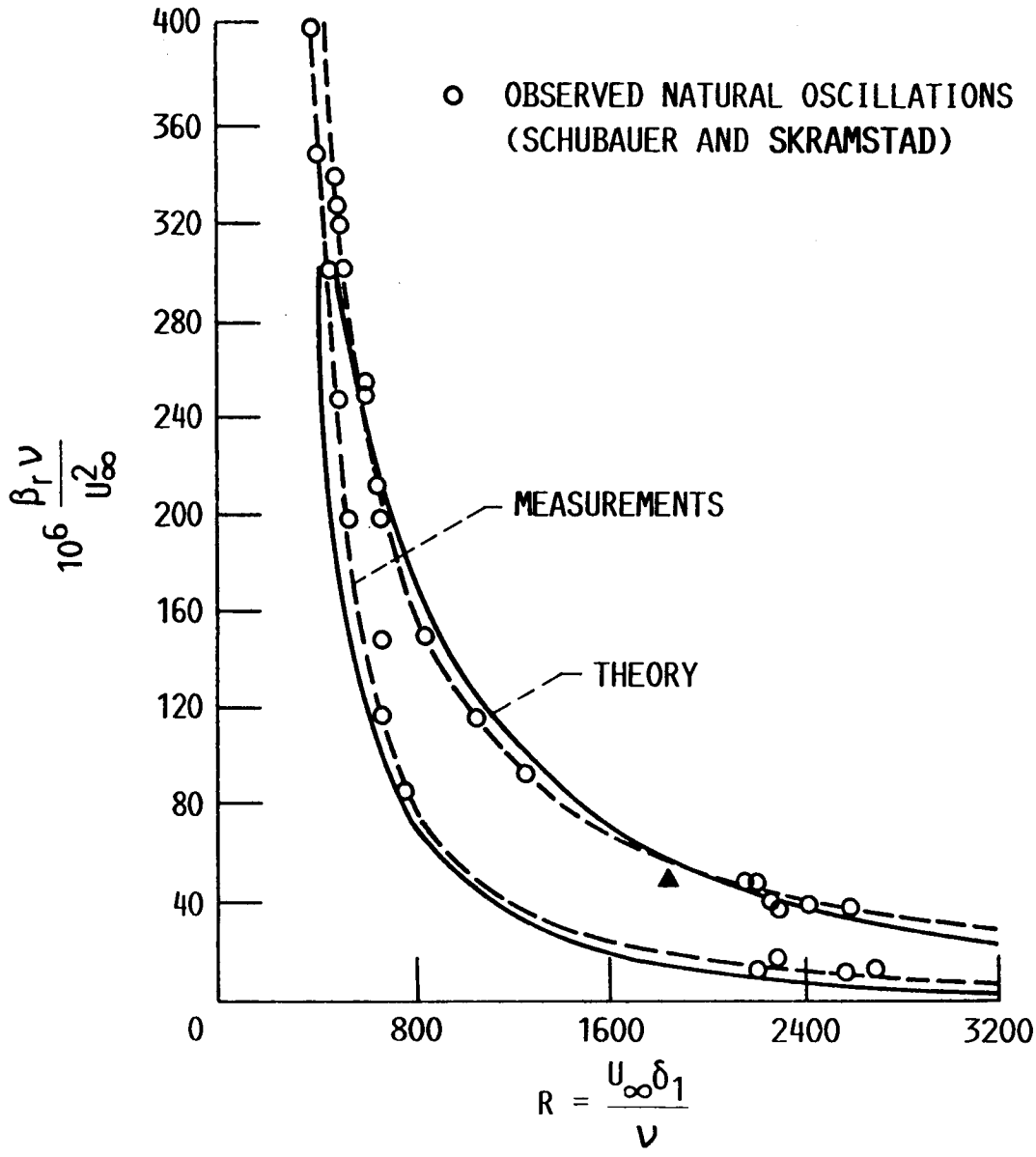

Fig. 71 Neutral stability curve – from Schlichting [5].

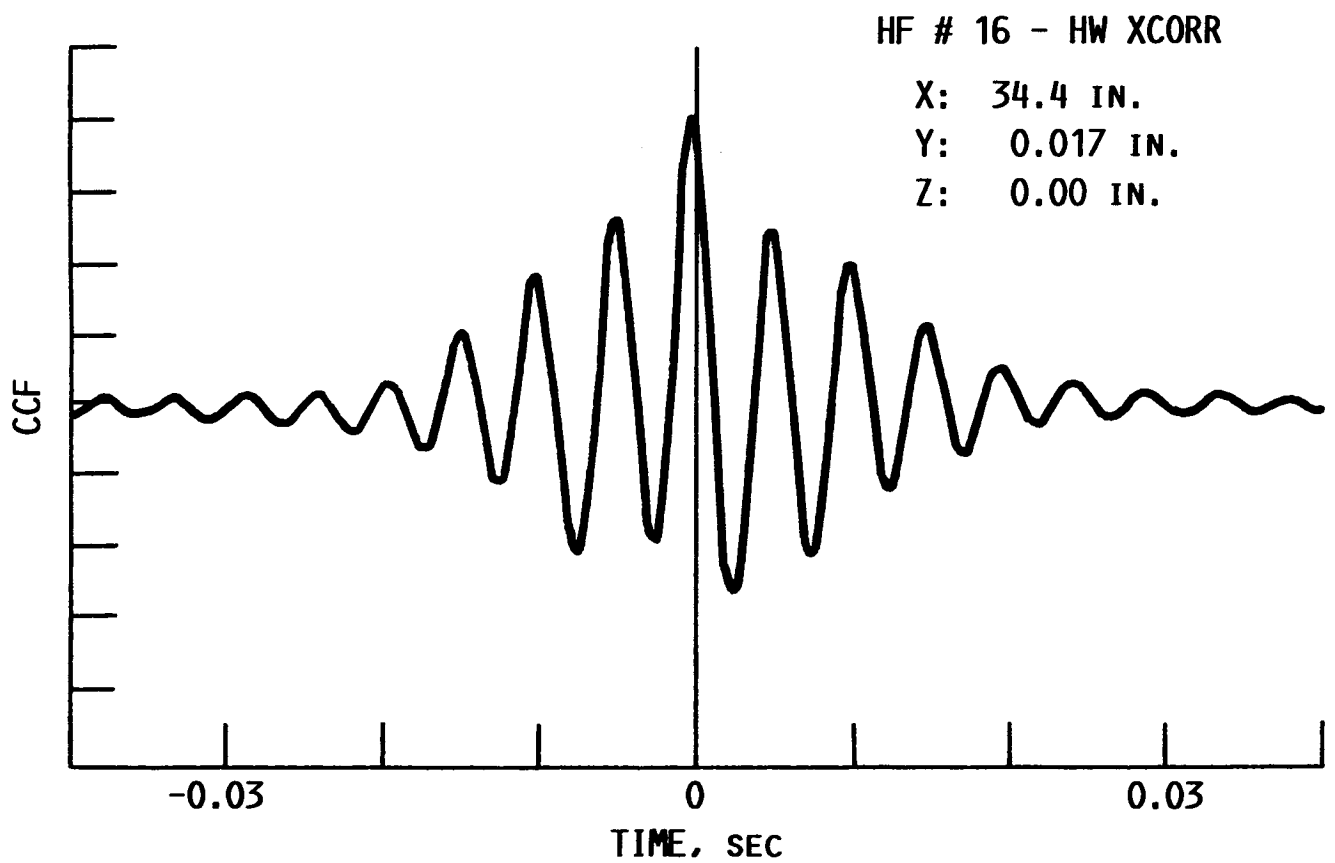

Fig. 72 Grid 0 – Crosscorrelation between two periodic signals.

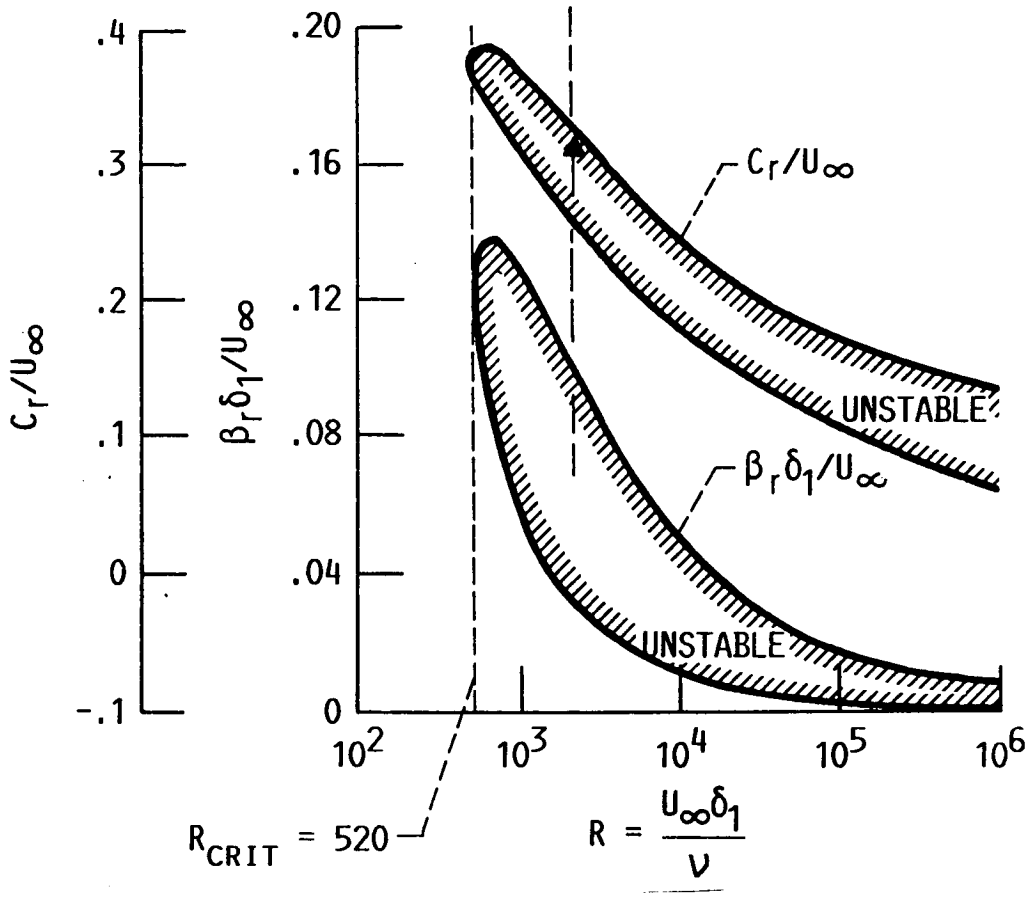

Fig. 73 Neutral stability curve – from Schlichting [5].

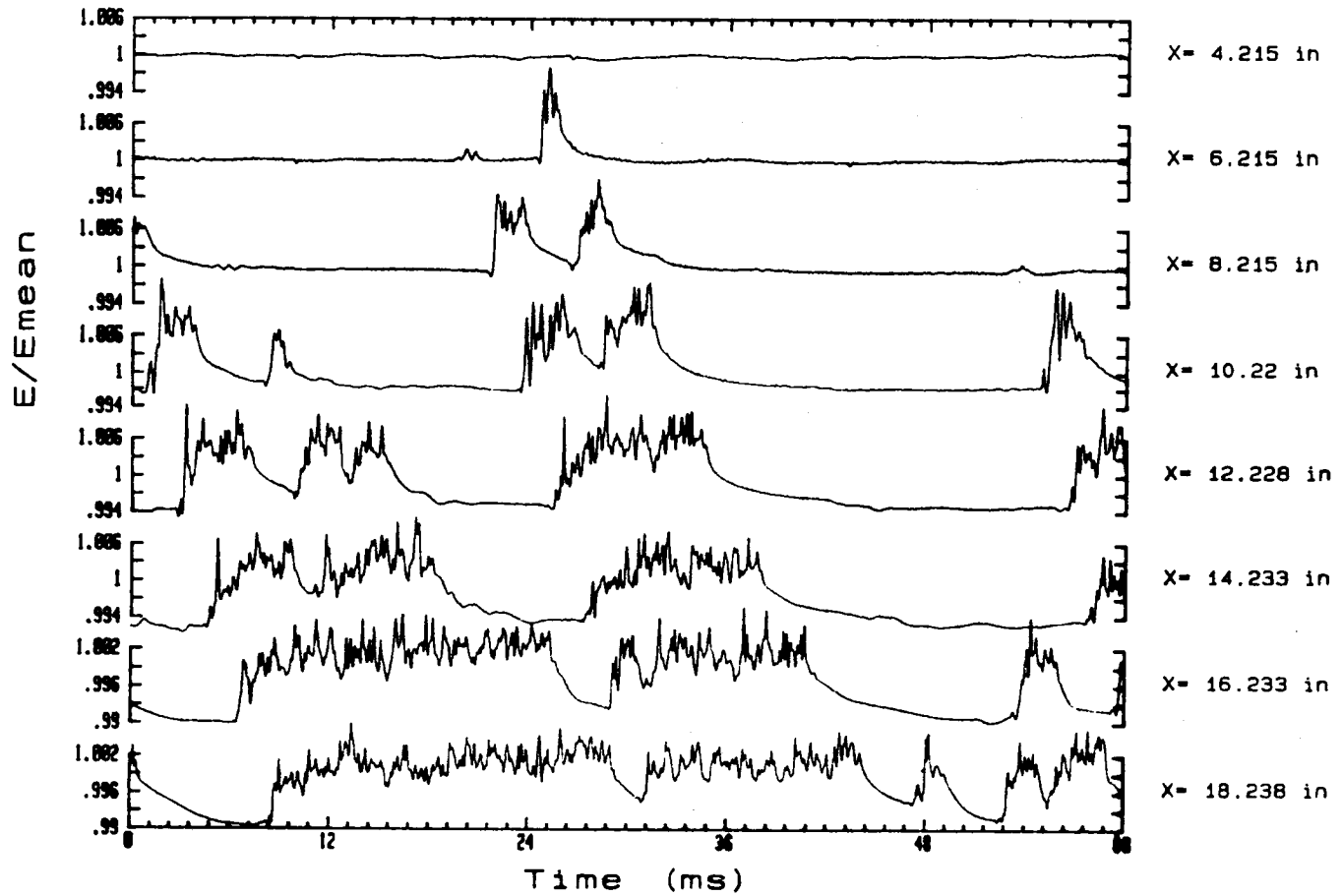

Fig. 74 Grid 0.5 – Simultaneous traces of the flush–mounted hot films encompassing the transition region.

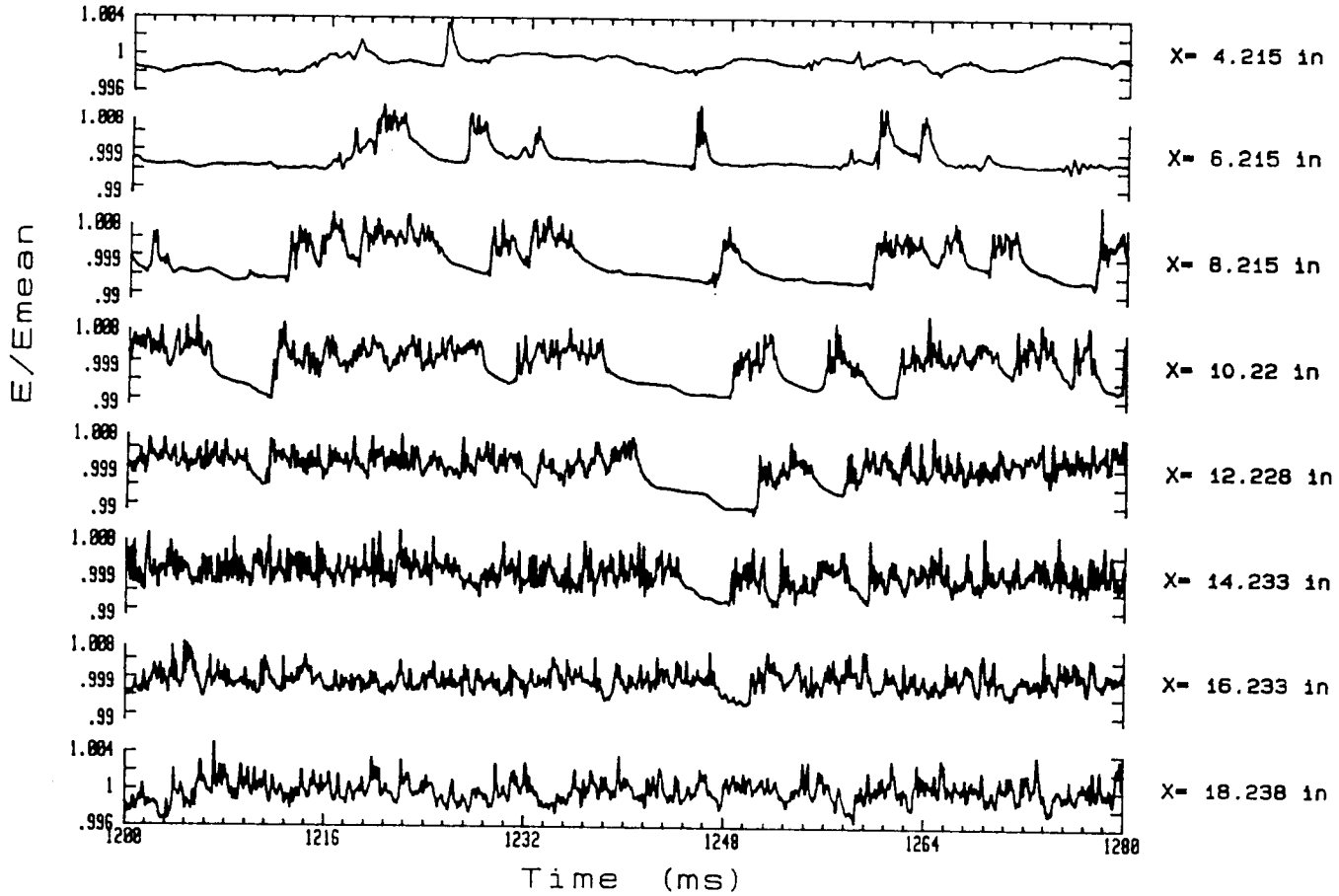

Fig. 75 Grid 1 – Simultaneous traces of the flush–mounted hot films encompassing the transition region.

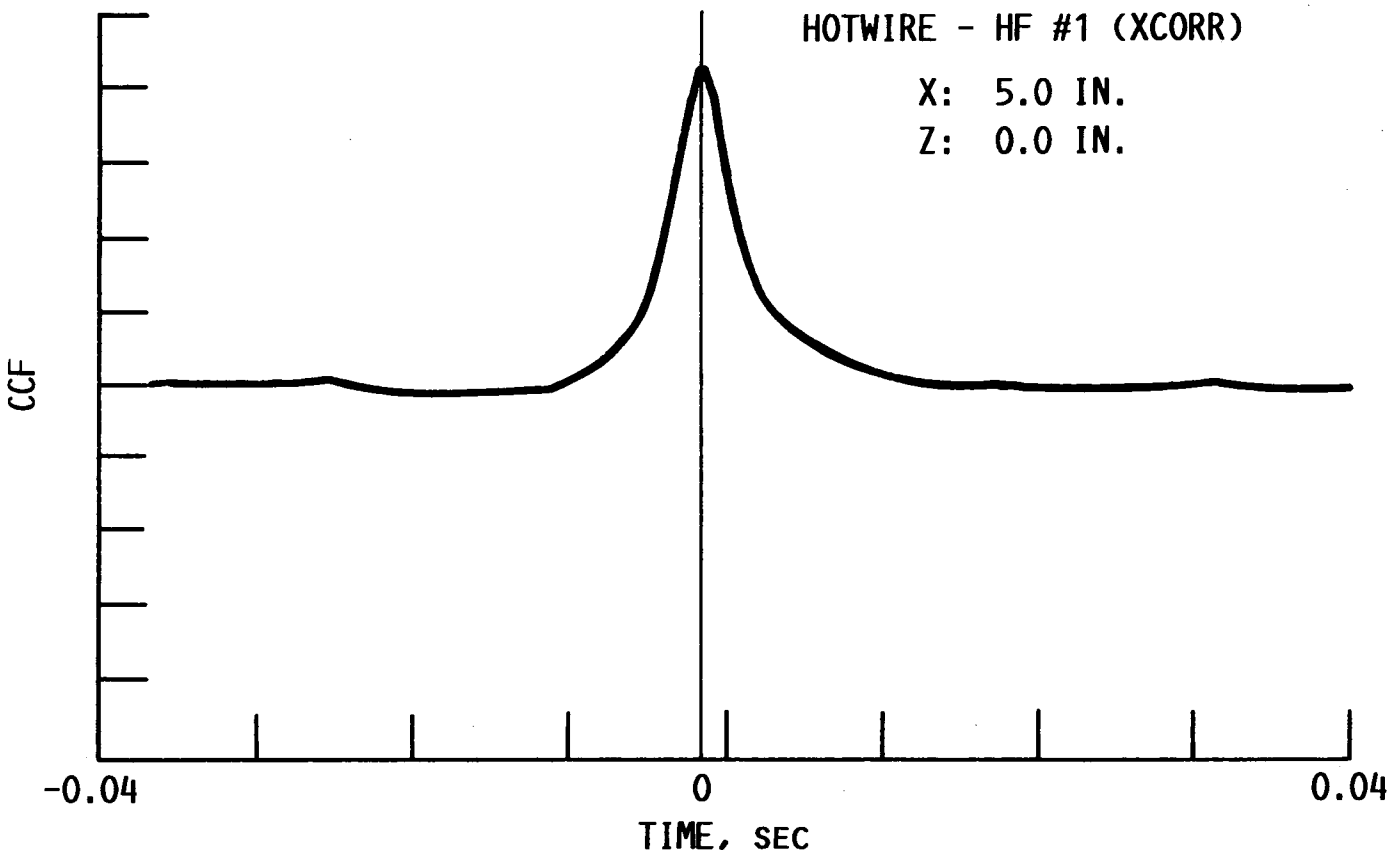

Fig. 76 Grid 1 – Crosscorrelation between hot film #1 and the hot wire positioned at x = 5 inches.

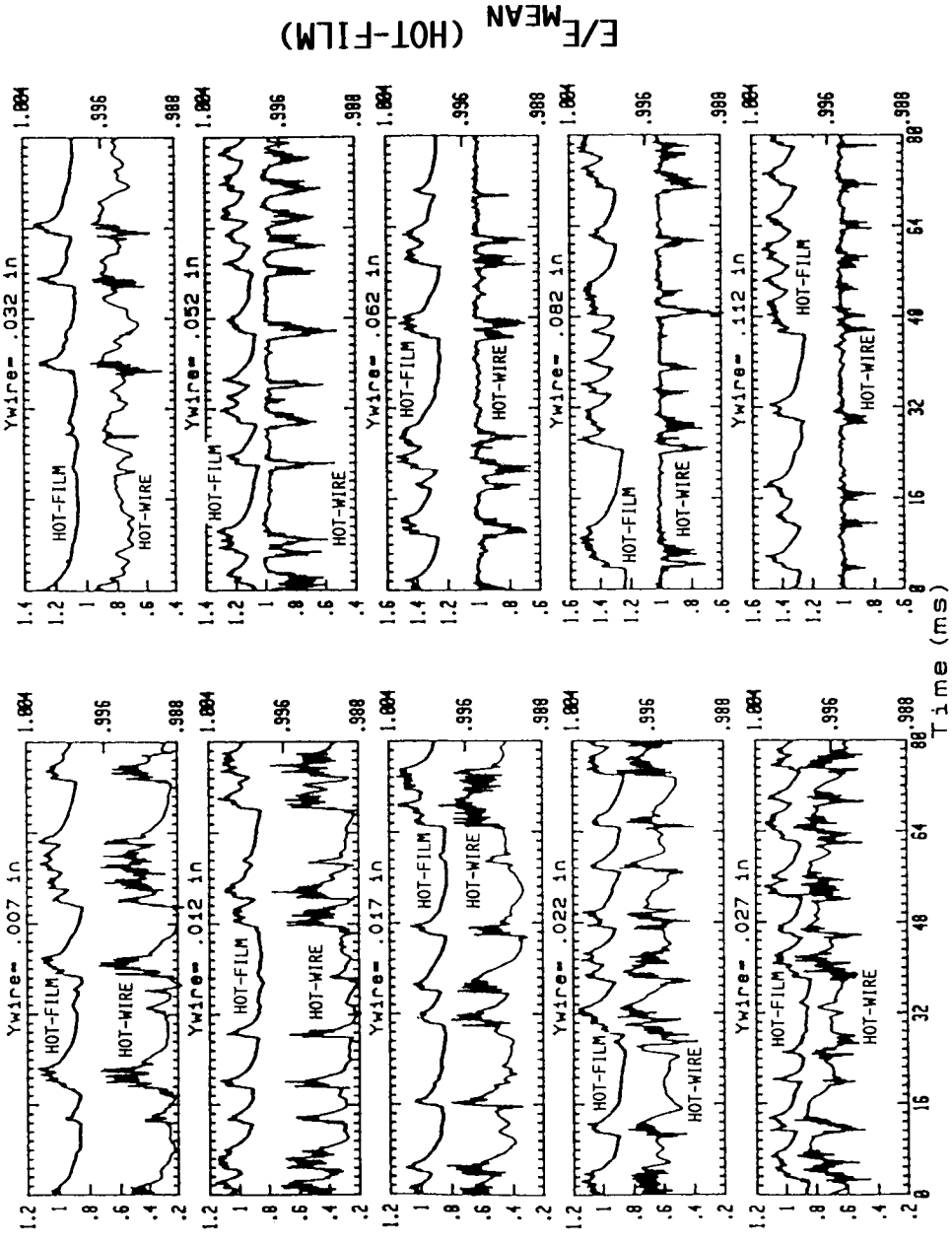

Fig. 77 Grid 1 – Simultaneous time traces of a flush–mounted hot film and a hot wire traversed throughout the boundary layer.

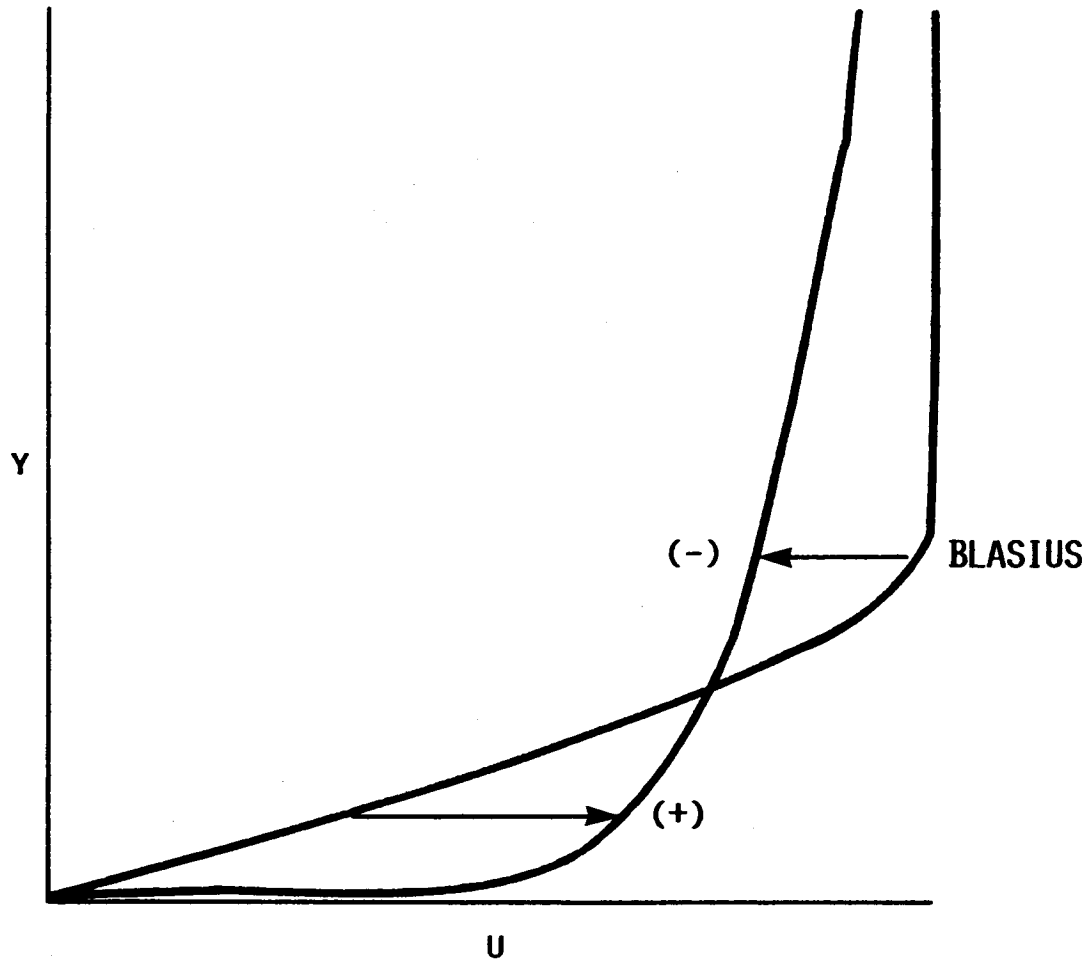

Fig. 78 Comparison between a typical laminar and turbulent boundary layer profile.

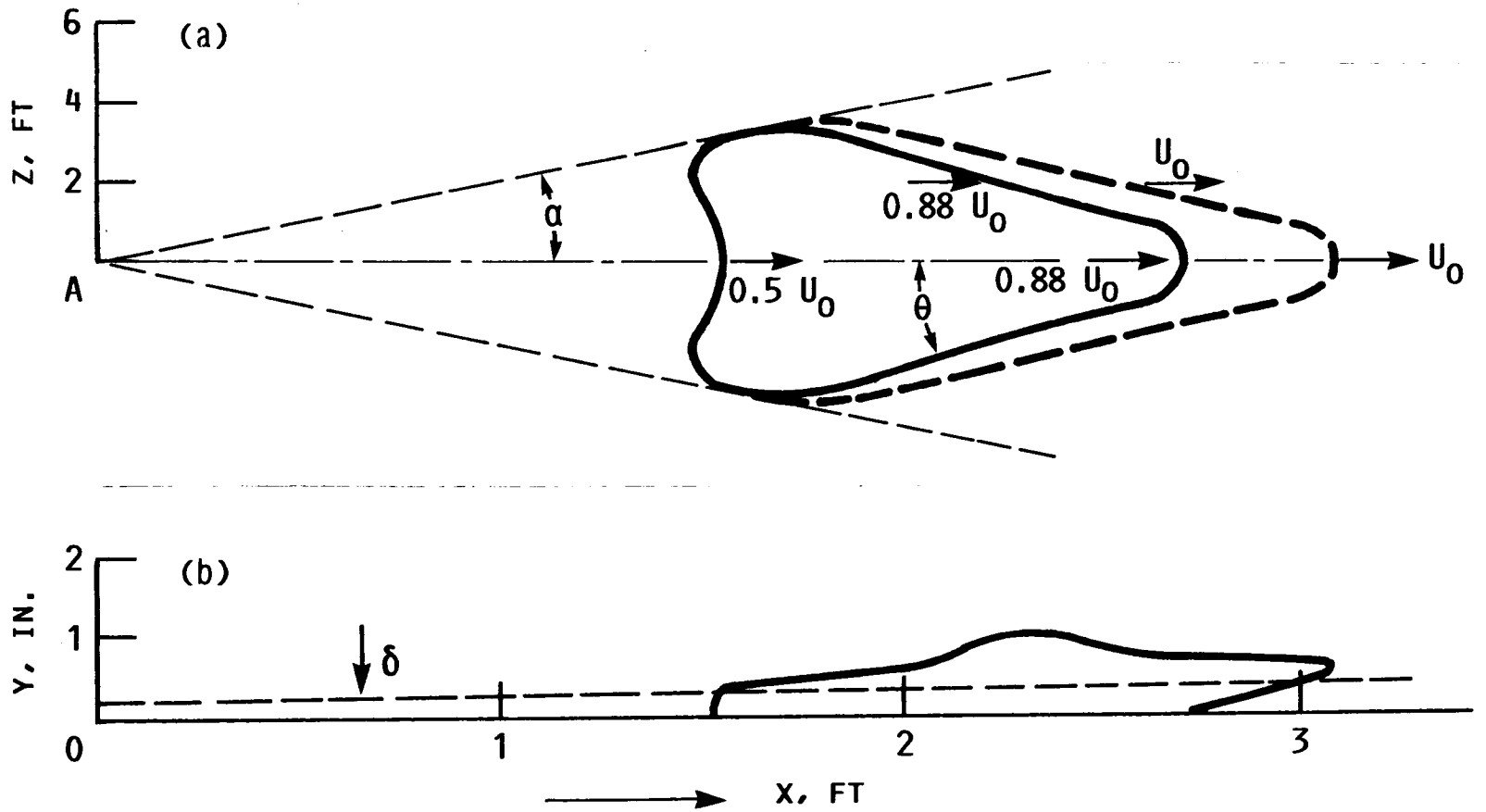

Fig. 79 Features of a turbulent spot–from Schlichting [5].

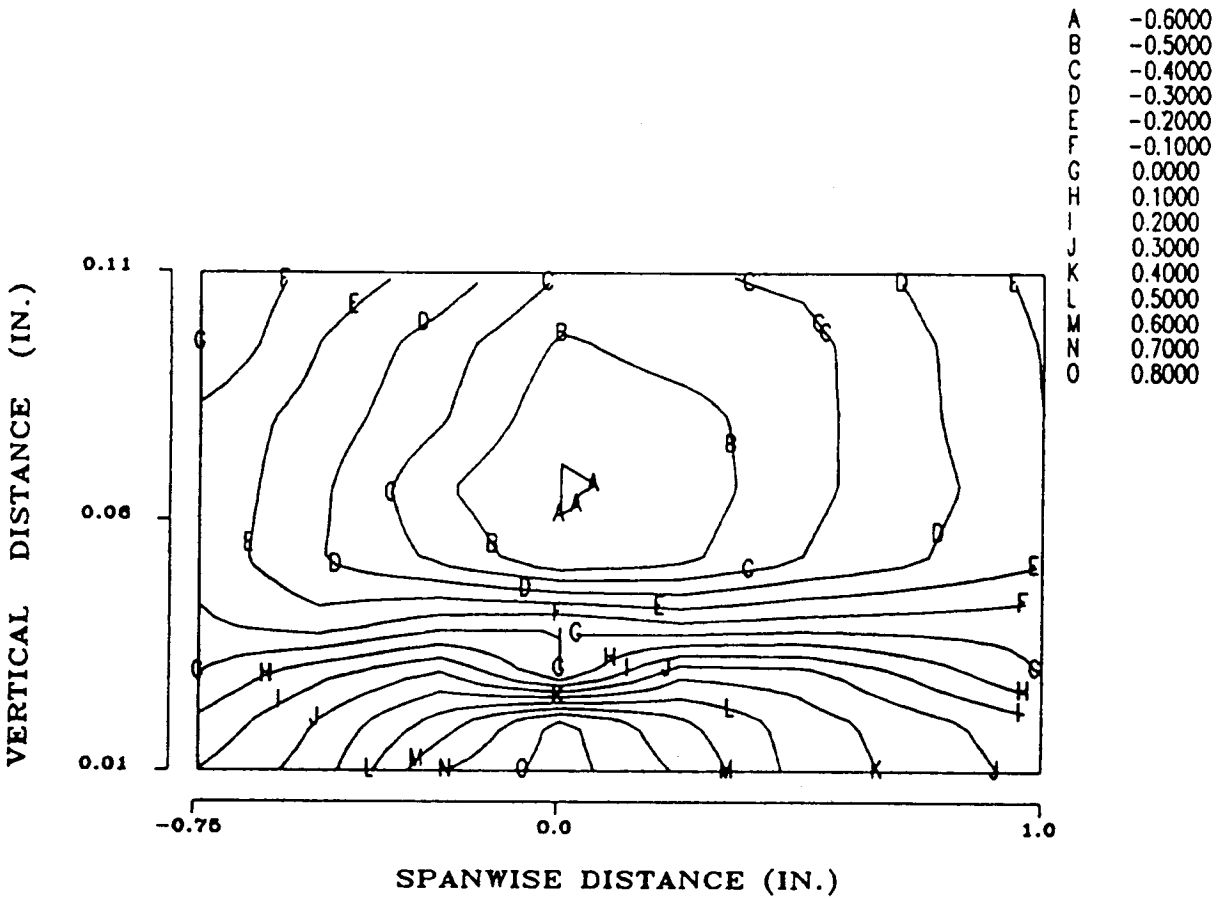

Fig. 80 Grid 1 – Contours of the maximum crosscorrelation between a flush–mounted hot film an a hot wire traversed throughout the y–z plane passing through the hot film.

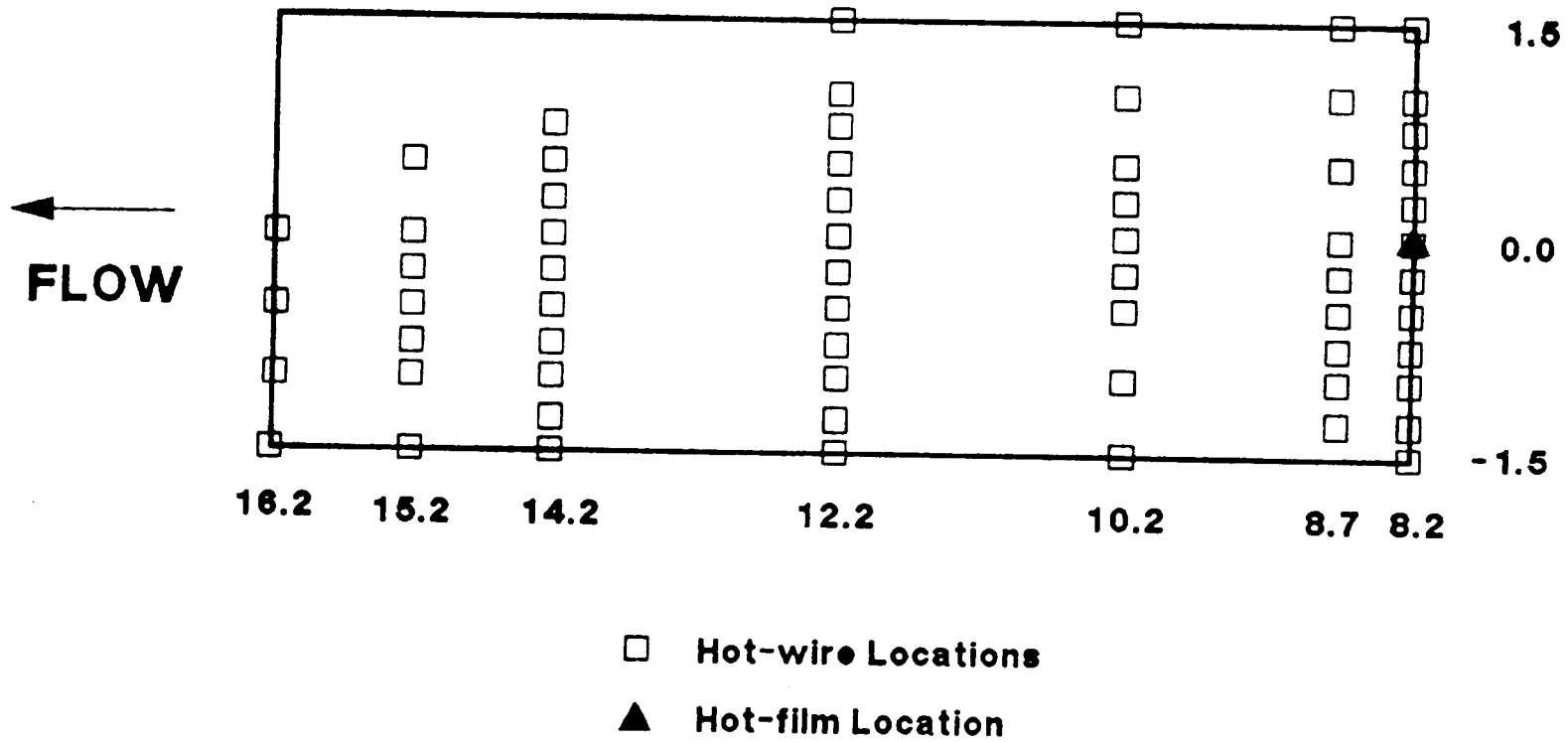

Fig. 81 Grid 1 – Hot–wire locations for the cross–correlations between a hot film and hot wire in the x – z plane.

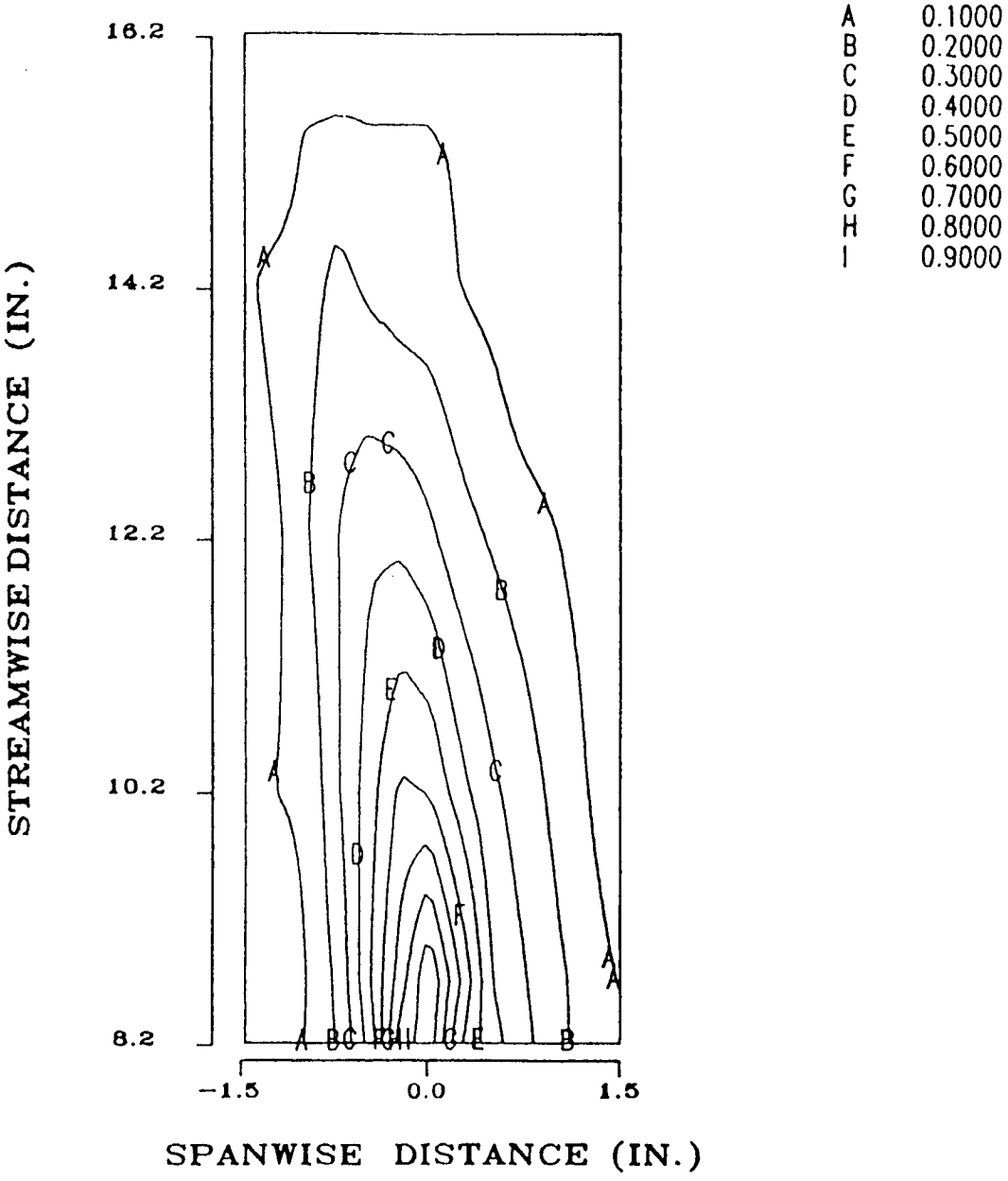

Fig. 82 Grid 1 – Contours of the maximum crosscorrelation between a flush–mounted hot film an a hot wire traversed throughout the x–z plane.

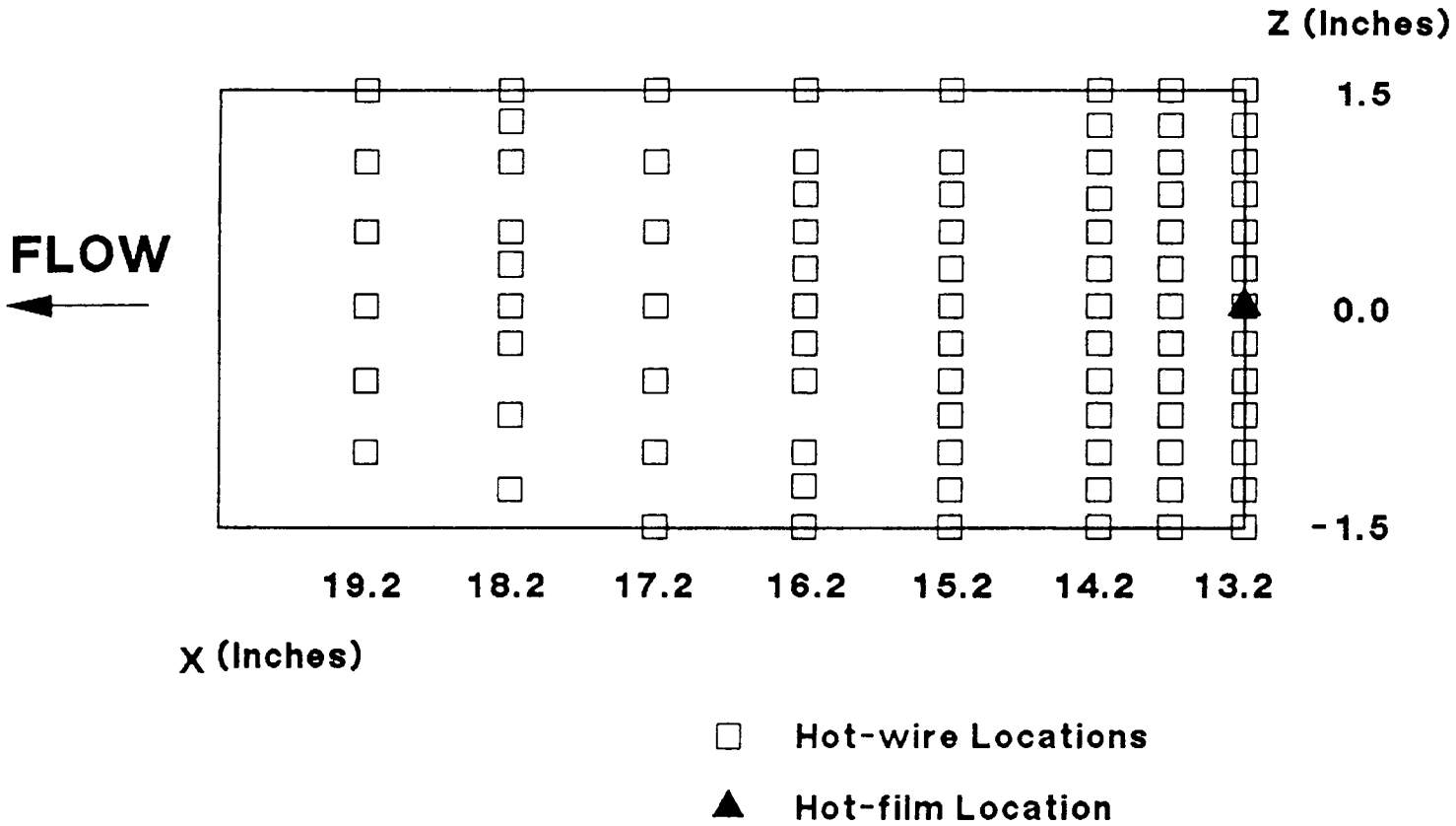

Fig. 83 Grid 0.5 – Hot–wire locations for the cross–correlations between a hot–film and hot wire in the x – z plane.

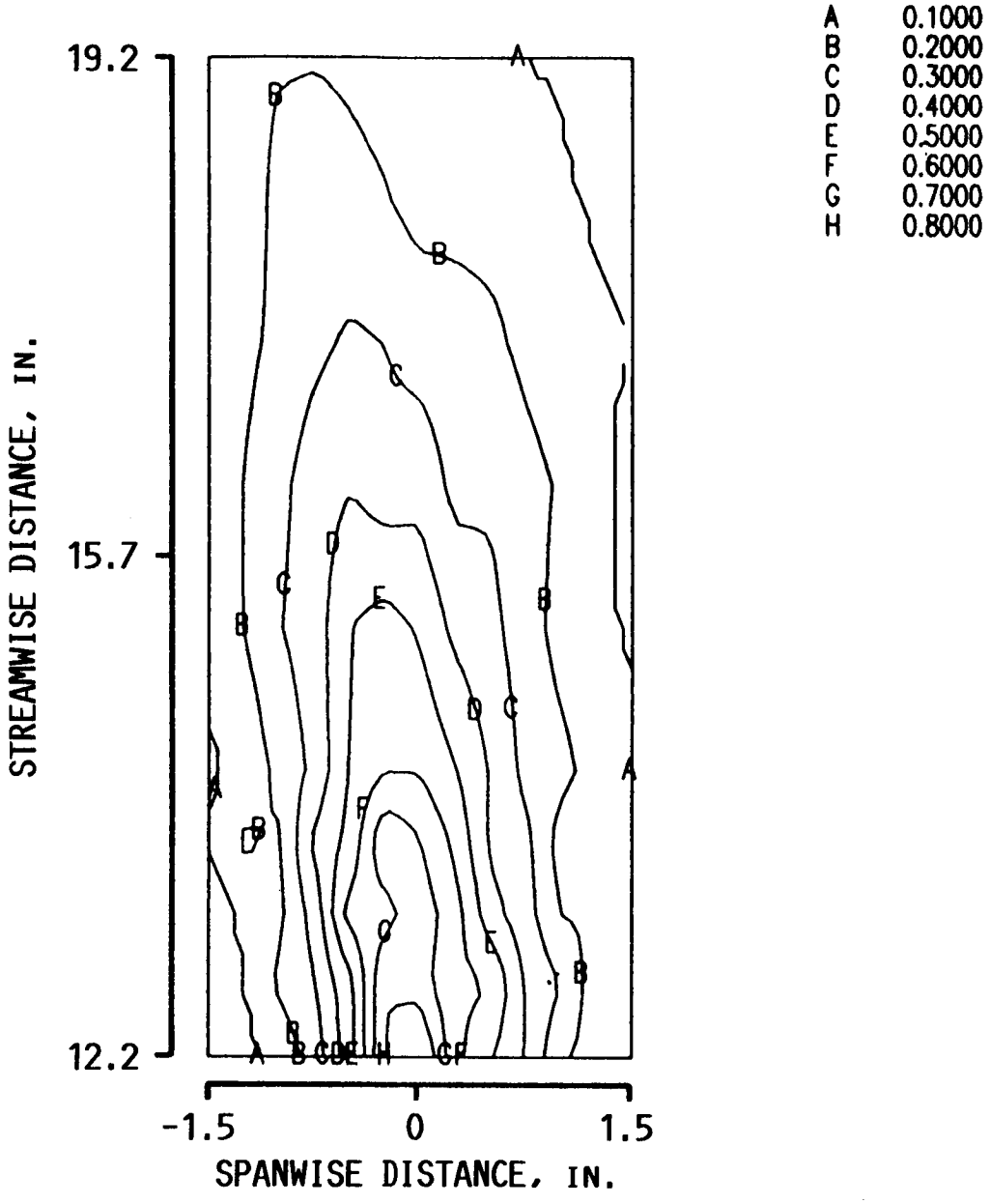

Fig. 84 Grid 0.5 – Contours of the maximum cross–correlation between a flush–mounted hot film and a hot wire traversed throughout the x–z plane.

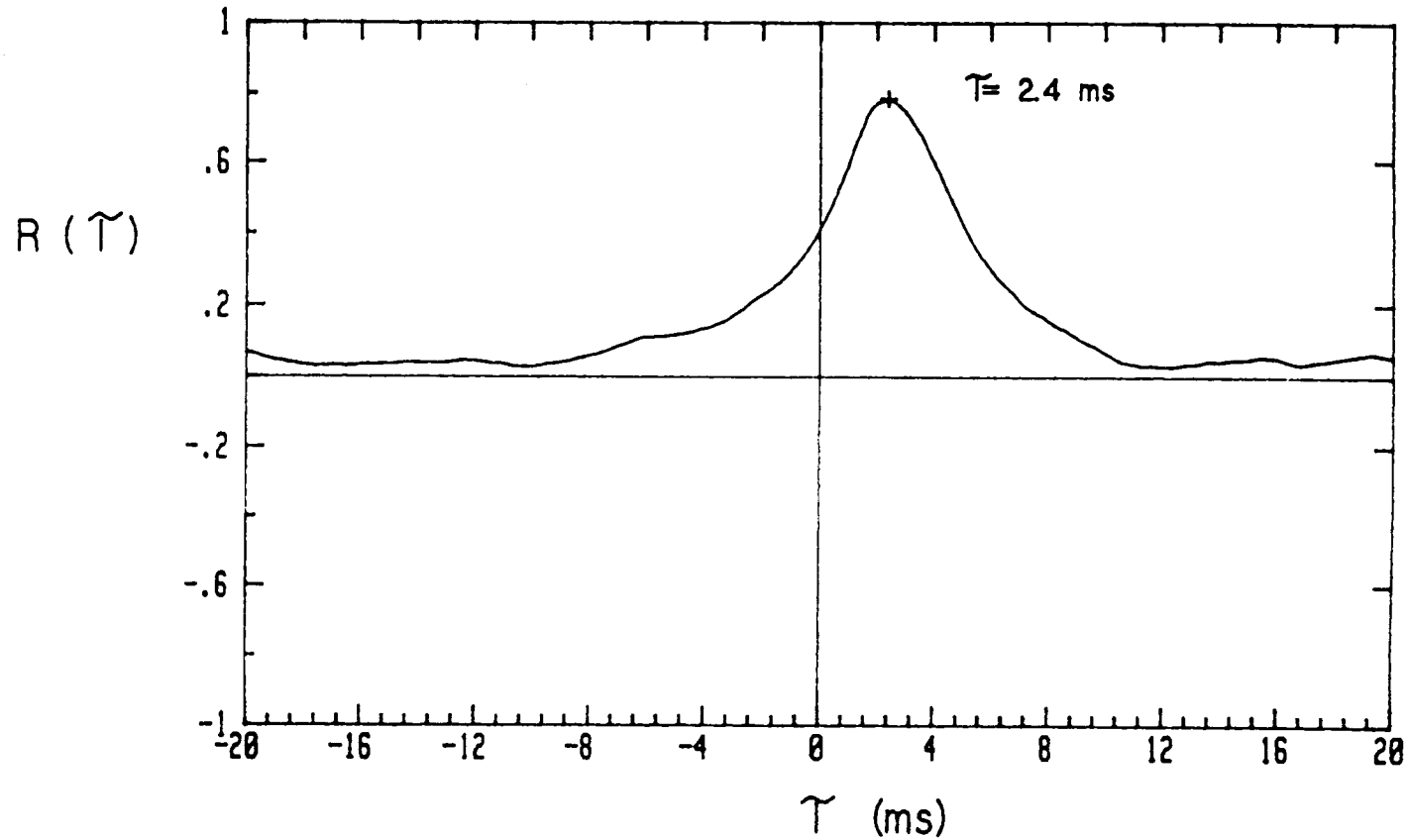

Fig. 85 A representative crosscorrelation between two succeeding flush–mounted hot films located in the boundary layer transition region (grid 0.5).

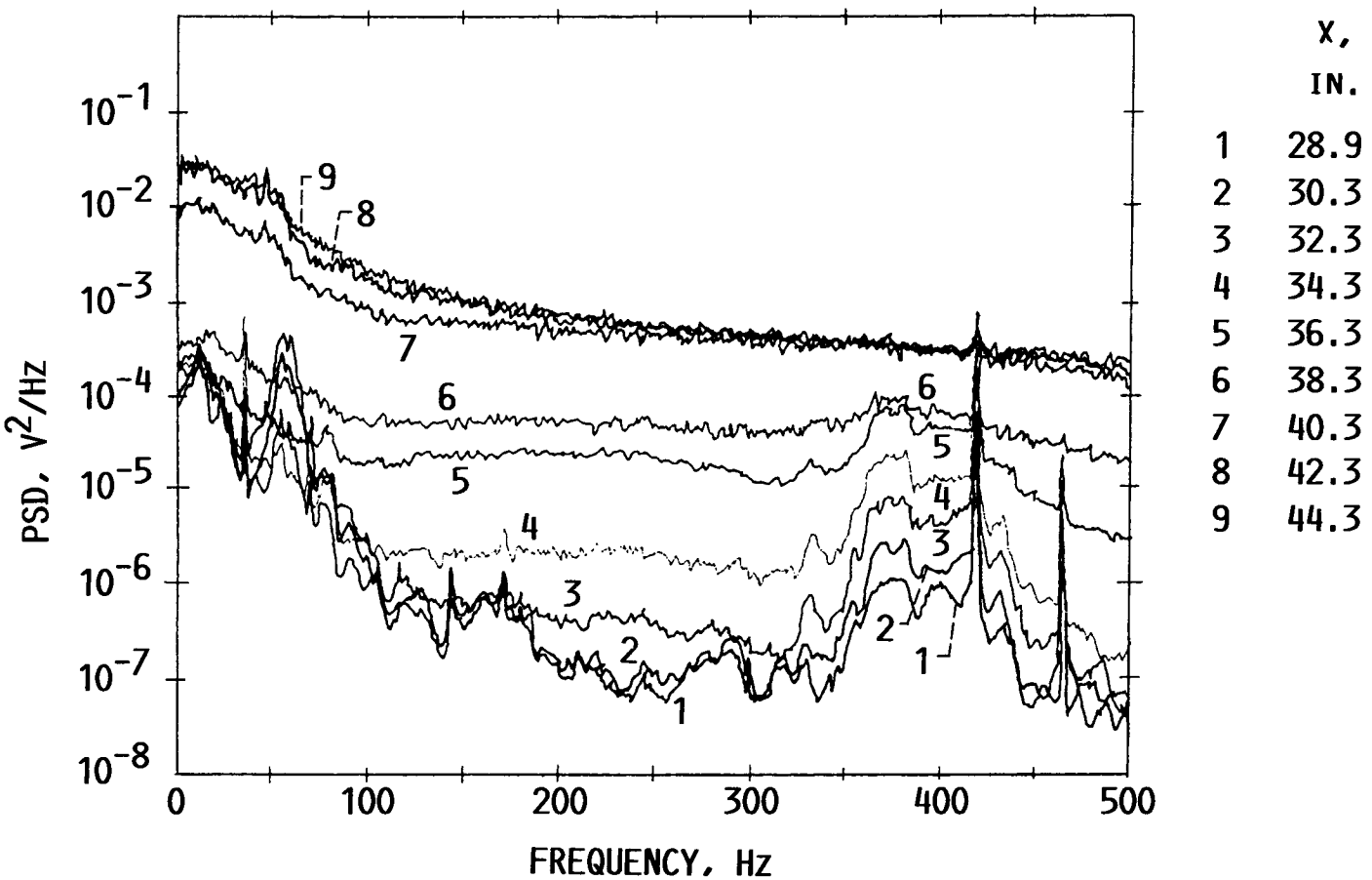

Fig. 86 Grid 0 – Boundary layer spectra acquired with the hot–wire location corresponding to the point of maximum RMS of the fluctuating velocities within the boundary layer.

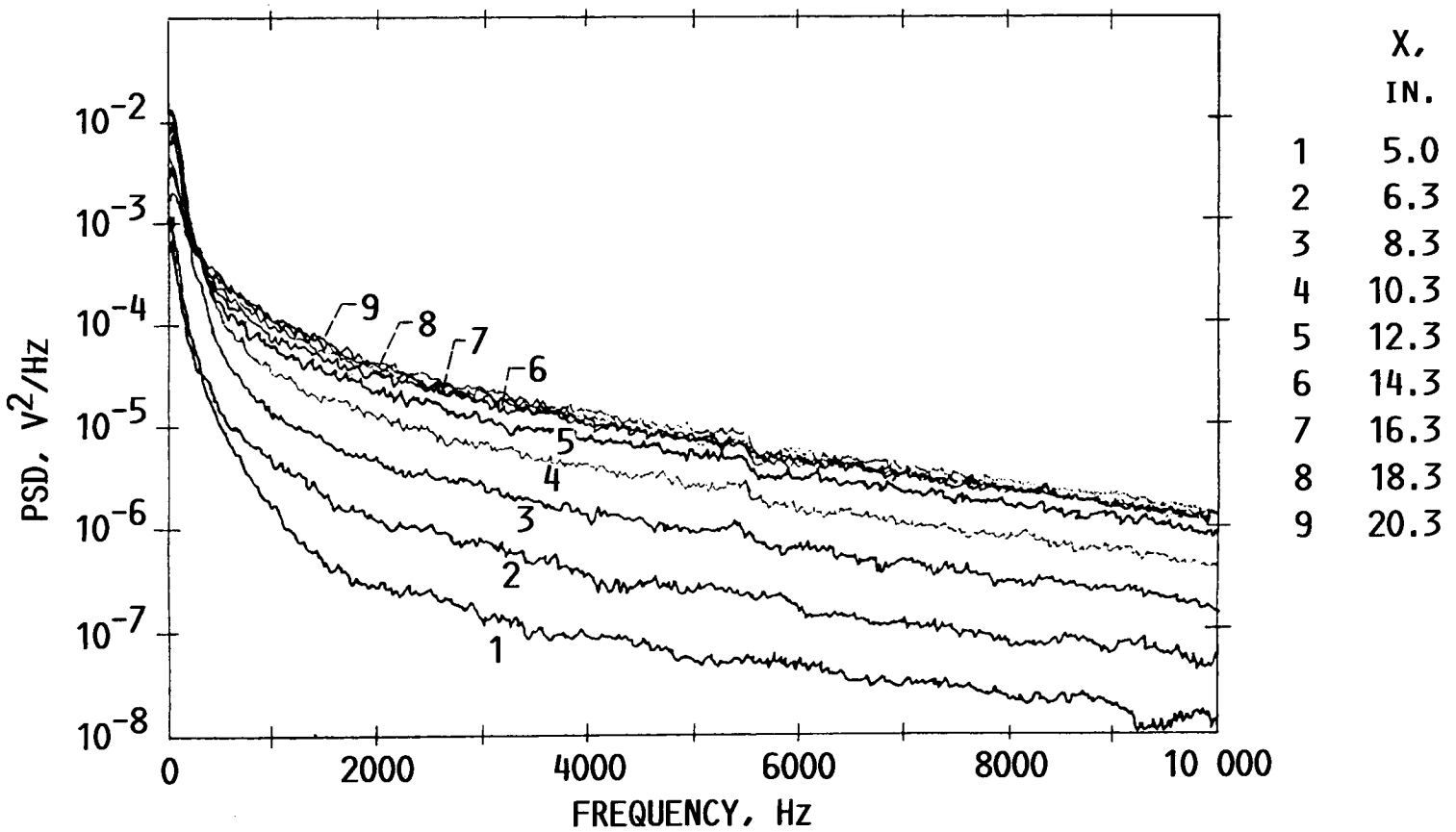

Fig. 87 Grid 0.5 – Boundary layer spectra acquired with the hot–wire location corresponding to the point of maximum RMS of the fluctuating velocities within the boundary layer.

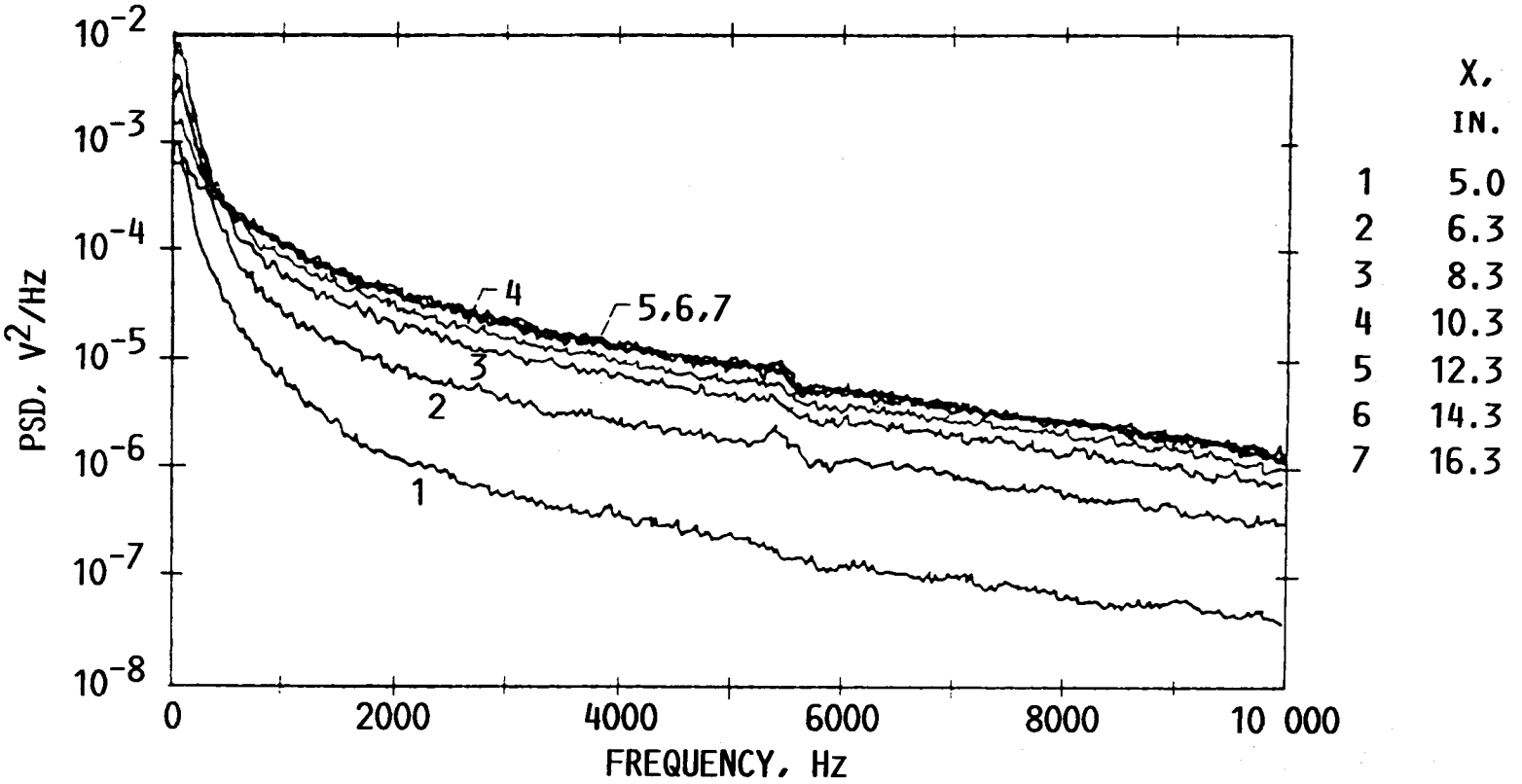

Fig. 88 Grid 1 – Boundary layer spectra acquired withthe hot–wire location corresponding to the point of maximum RMS of the fluctuating velocities within the boundary layer.

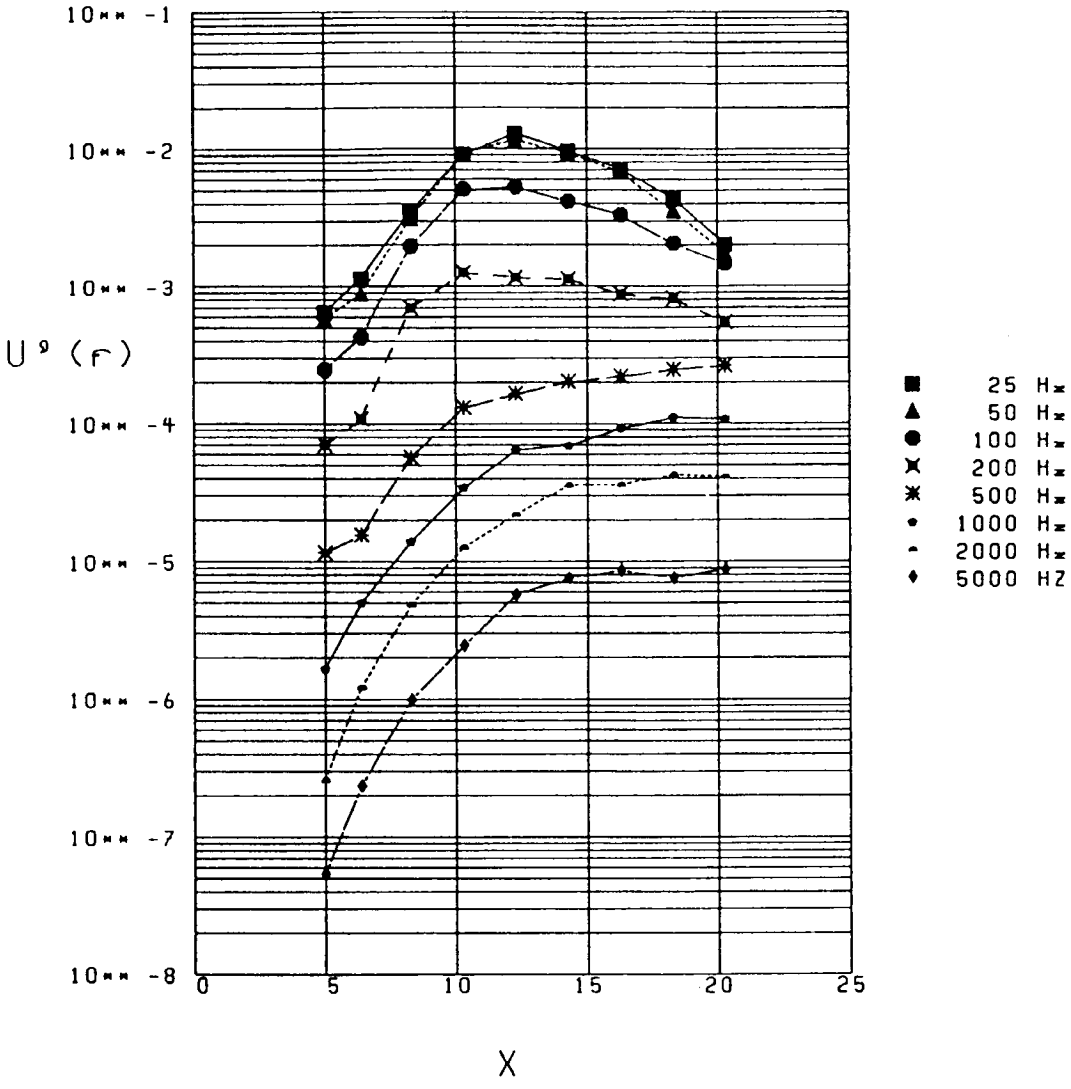

Fig. 89 Grid 0.5 – Streamwise distribution of the boundary layer disturbance amplitude at selected frequencies.

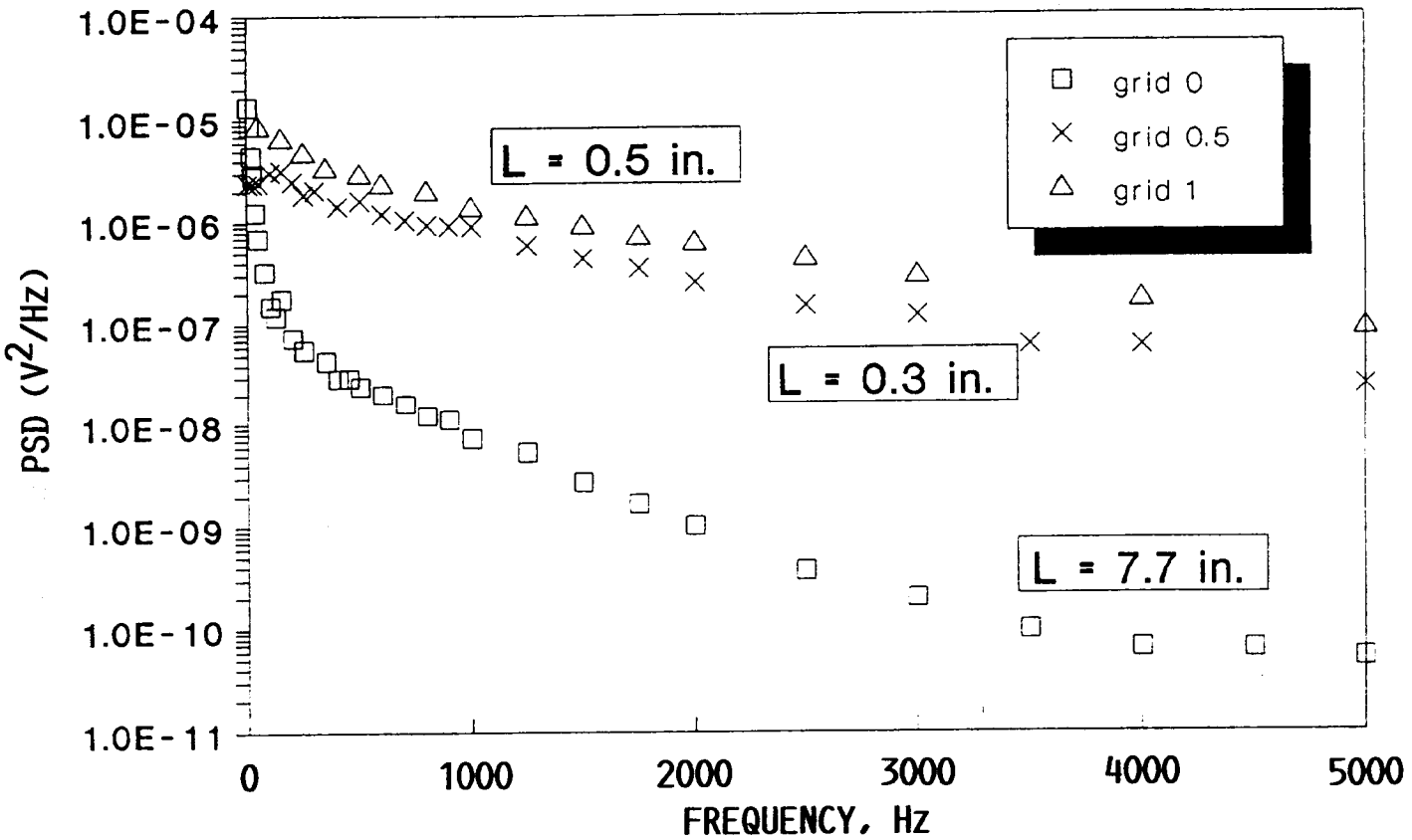

Fig. 90 Grid 0, grid 0.5, and grid 1 freestream spectra in dimensional coordinates – 0 to 5000 Hz frequency range.

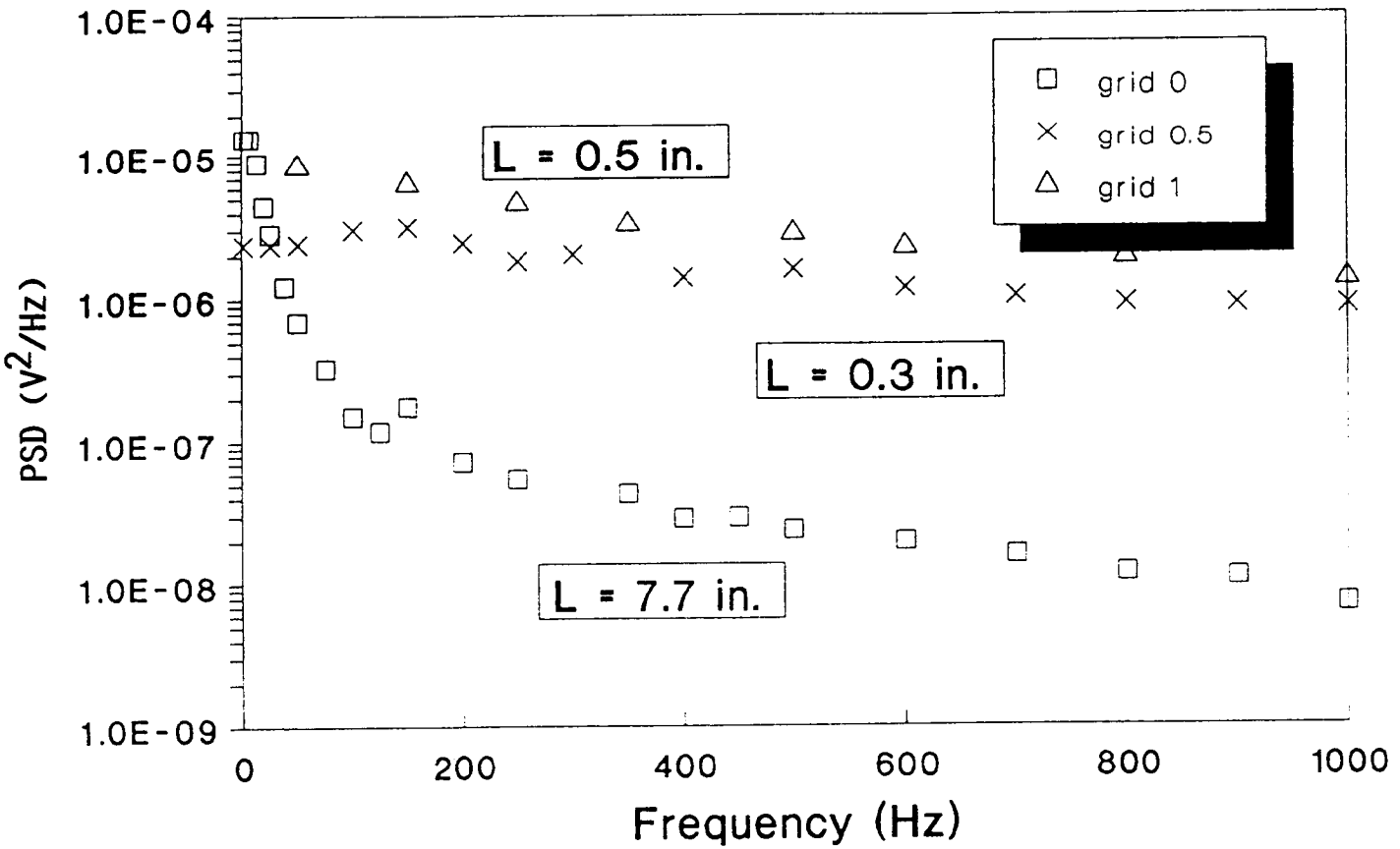

Fig. 91 Grid 0, grid 0.5, and grid 1 freestream spectra in dimensional coordinates – 0 to 1000 Hz frequency range.

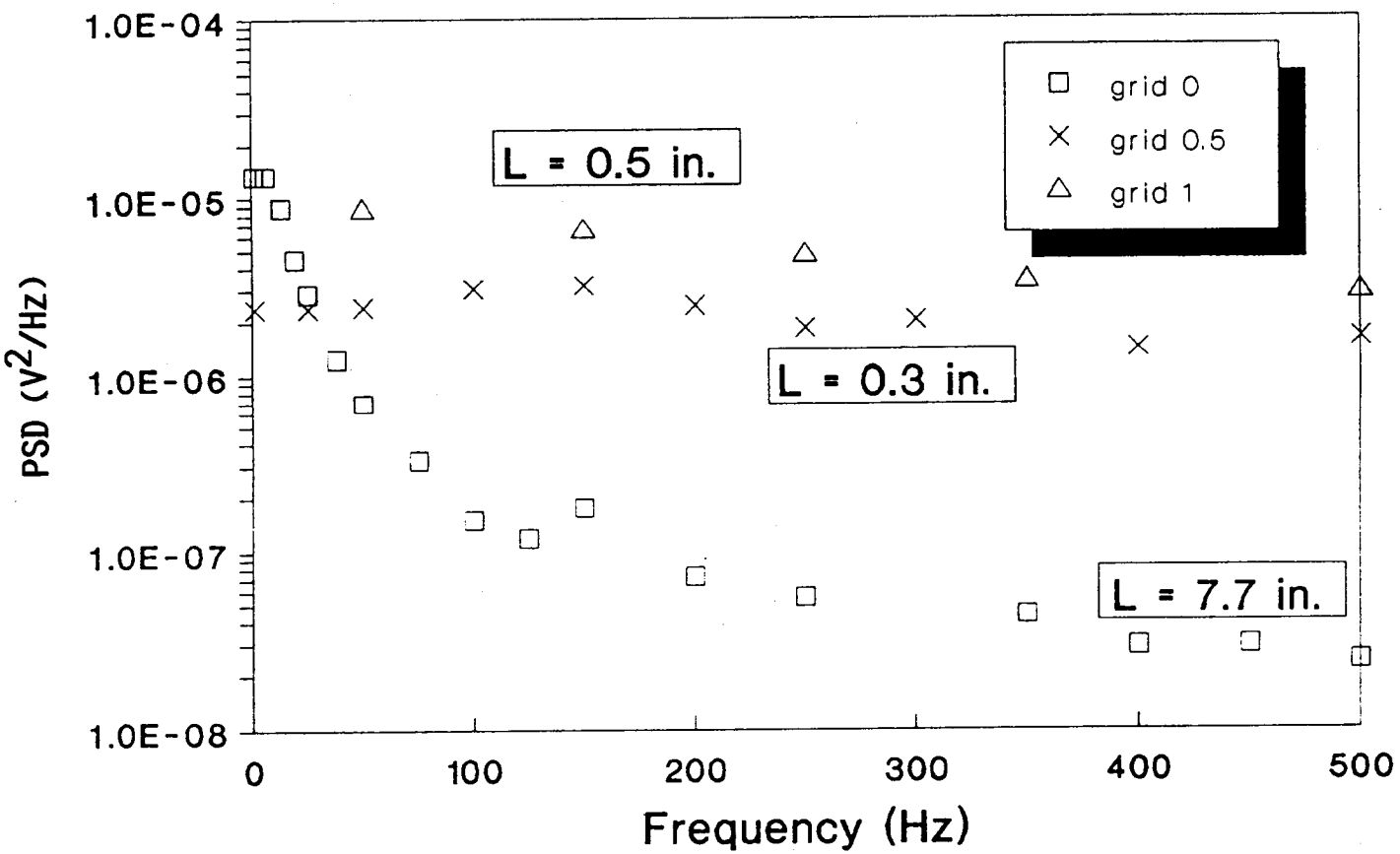

Fig. 92 Grid 0, grid 0.5, and grid 1 freestream spectra in dimensional coordinates – 0 to 500 Hz frequency range.

NASA
National Aeronautics and Space Administration

Report Documentation Page

1. Report No.	2. Government Accession No.	3. Recipient's Catalog No.
NASA TM-100913		

4. Title and Subtitle	5. Report Date
Experimental Study of Bypass Transition in a Boundary Layer	May 1988
	6. Performing Organization Code

7. Author(s)	8. Performing Organization Report No.
Kenneth L. Suder, James E. O'Brien, and Eli Reshotko	E-3953
	10. Work Unit No. 505-62-21

9. Performing Organization Name and Address	11. Contract or Grant No.
National Aeronautics and Space Administration Lewis Research Center Cleveland, Ohio 44135-3191	
	13. Type of Report and Period Covered Technical Memorandum
12. Sponsoring Agency Name and Address	14. Sponsoring Agency Code
National Aeronautics and Space Administration Washington, D.C. 20546-0001	

15. Supplementary Notes

Kenneth L. Suder and James E. O'Brien, NASA Lewis Research Center; Eli Reshotko, Case Western Reserve University, Dept. of Mechanical and Aerospace Engineering, Cleveland, Ohio 44106. This report was a thesis submitted by Kenneth L. Suder in partial fulfillment of the requirements for the degree of Master of Science to Case Western Reserve University, Cleveland, Ohio in May 1988.

16. Abstract

A detailed investigation to compare the boundary layer transition process in a low intensity disturbance environment to that in an environment in which the disturbances are initially non-linear in amplitude has been conducted using a flat plate model. Test section freestream turbulence values were varied from 0.3% to approximately 5% using rectangular-bar grids. The longitudinal integral length scale, intensity, and frequency spectra were acquired to characterize the freestream turbulence. For each level of freestream turbulence, boundary layer surveys of the mean longitudinal velocity and rms of the velocity fluctuations were obtained at several streamwise locations with a linearized hot-wire constant temperature anemometer system. From these surveys the resulting boundary layer shape factor, inferred skin friction coefficients, and distribution of the velocity fluctuations through the boundary layer were used to indentify the transition region corresponding to each level of freestream turbulence. Both the initially linear and initially non-linear transition cases were identified. Hereafter, the transition process initiated by the linear growth of Tollmien Schlichting (T-S) waves will be referred to as the T-S path to transition; whereas, the transition process initiated by finite non-linear disturbances will be referred to as the bypass transition process. The transition mechanism based on linear growth of T-S waves was associated with a freestream turbulence level of 0.3%; however, for a freestream turbulence intensity of 0.65% and higher, the bypass transition mechanism prevailed. The following detailed measurements were acquired to study and compare the two transition mechanisms: 1) simultaneous time traces of a flush-mounted hot film and a hot wire for the hot wire located at different depths within the boundary layer, 2) crosscorrelations between flush-mounted hot films, 3) two-point correlations between a flush-mounted hot film and a hot wire positioned at various locations throughout the flowfield, and 4) boundary layer spectra at various streamwise distances through the transition region. The results of these measurements indicate that there exists a critical value for the peak rms of the velocity fluctuations within the boundary layer of approximately 3 to 3.5% of the freestream velocity. Once the unsteadiness within the boundary layer reached this critical value, turbulent bursting initiated, regardless of the transition mechanism. The two point correlations and simultaneous time traces within the transition region illustrate the features of a turbulent burst and its effect on the surrounding flowfield.

17. Key Words (Suggested by Author(s))	18. Distribution Statement
Boundary layer transition; Bypass; Freestream turbulence Flat plate; Hot-wire anemometry; Hot films	Unclassified-Unlimited Subject Category 34

19. Security Classif. (of this report)	20. Security Classif. (of this page)	21. No of pages	22. Price*
Unclassified	Unclassified	198	A09

NASA FORM 1626 OCT 86

*For sale by the National Technical Information Service, Springfield, Virginia 22161